

University of Strathclyde  
Department of Chemical and Process Engineering

# Complex Flow of Concentrated Suspensions

Claire Forsyth

A thesis submitted to the Department of Chemical and Process Engineering in fulfilment of the requirements for the degree of Doctor of Philosophy.

2015

# Declarations

---

This thesis is the result of the author's original research. It has been composed by the author and has not been previously submitted for examination which has led to the award of a degree.

The copyright of this thesis belongs to the author under the terms of the United Kingdom Copyright Acts as qualified by University of Strathclyde Regulation 3.50. Due acknowledgement must always be made of the use of any material contained in, or derived from, this thesis.

Signed:

Date:

# Acknowledgements

---

I would like to thank my supervisor Mark Haw for all his help and ideas throughout the PhD and for reading through the thesis.

I would like to thank Leo Lue for his help with the simulations.

Thanks also to Jim Murphy for all his help in the lab and for his good chat. I would also like to thank Linda for keeping the lab clean and for her good chat too.

I would like to thank Joy, Sandy, Vincenzo and New Sandy for being good to sit next to in the office. Thanks to the office staff for their help too.

Thanks as well to the Carnegie Trust for funding the PhD.

Finally I would like to thank my sister Carol for all her help with various things throughout the PhD. I would also like to thank my wonderful cat Cindy for being inspirational, hilarious and the best. Thanks as well to my mum and dad for still letting me live at home.



# Publications and Conferences

---

## Publications

1. Forsyth, C. and S.V. Patwardhan, *Controlling performance of lipase immobilised on bioinspired silica*. Journal of Materials Chemistry B, 2013. **1**(8): p. 1164-1174.
2. Forsyth, C., T.W.S. Yip, and S.V. Patwardhan, *CO<sub>2</sub> sequestration by enzyme immobilized onto bioinspired silica*. Chemical Communications, 2013. **49**(31): p. 3191-3193.
3. Forsyth, C. and S. Patwardhan, *Bioinspired Silica for Enzyme Immobilisation: A Comparison with Traditional Methods*, in *Bio-Inspired Silicon-Based Materials*, P. Zelisko, Editor. 2014, Springer- Advances in Silicon Science. p. 39-62.
4. Forsyth, C., et al., *Influence of Controlled Fluid Shear on Nucleation Rates in Glycine Aqueous Solutions*. Crystal Growth and Design, 2015. **15**(1): p. 94-102.
5. Forsyth, C., M. Haw, and L. Lue, *Jamming in Concentrated Suspensions*. In preparation, 2015.

## Conferences

Imperial University Chemical Engineering Day 2013

Complex Flow of Concentrated Suspensions

25th-26th March 2013

Newcastle Chemical Engineering Conference 2013

Flow of Concentrated Suspensions in a Couette Geometry

8th-9th August 2013

Cambridge Soft Condensed Matter Conference 2014

Complex Flow of Concentrated Colloidal and Granular Suspensions

11<sup>th</sup>-14th April 2014

# Abstract

---

This thesis describes work done to investigate the effects of flow on concentrated suspensions. The work is largely about the effects of flow on concentrated colloidal suspensions, however, a short section on the effects of flow on concentrated granular suspensions is also given.

Concentrated suspensions show a variety of complex flow behaviour. They can show Newtonian, shear thinning or shear thickening behaviour, depending on the applied stress or shear rate and concentration. The shear thickening behaviour may be discontinuous and this is characterised by a dramatic increase in viscosity above a certain threshold of stress. This is thought to be closely related to flow induced jamming, which can be defined as the conversion of a liquid system into a solid by imposed stress. This behaviour is not well understood and can cause significant complications in industry. It also has potential applications, for example in shock absorption. Due to their complexities and potential applications, gaining a better understanding of how shear thickening and jamming materials behave is of interest and forms the basis of this thesis.

In this work, bespoke shear cells and a novel method to detect flow induced jamming were designed and utilised. This allowed jamming to be visualised and evaluated quantitatively. Conditions where jamming occurs were mapped out and the effects of parameters such as concentration, shear stress, system geometry and system confinement were investigated. This, and an analysis of jamming statistics, allowed ways to prevent and control jamming to be identified and a better understanding of the system to be achieved. Such an analysis is lacking in literature.

The conditions where jamming was detected using the novel equipment matched well with measurements using a commercial rheometer. This supported the idea of discontinuous shear thickening and flow induced jamming being closely related. The studies allowed a mechanism for flow induced jamming and discontinuous shear thickening to be proposed.

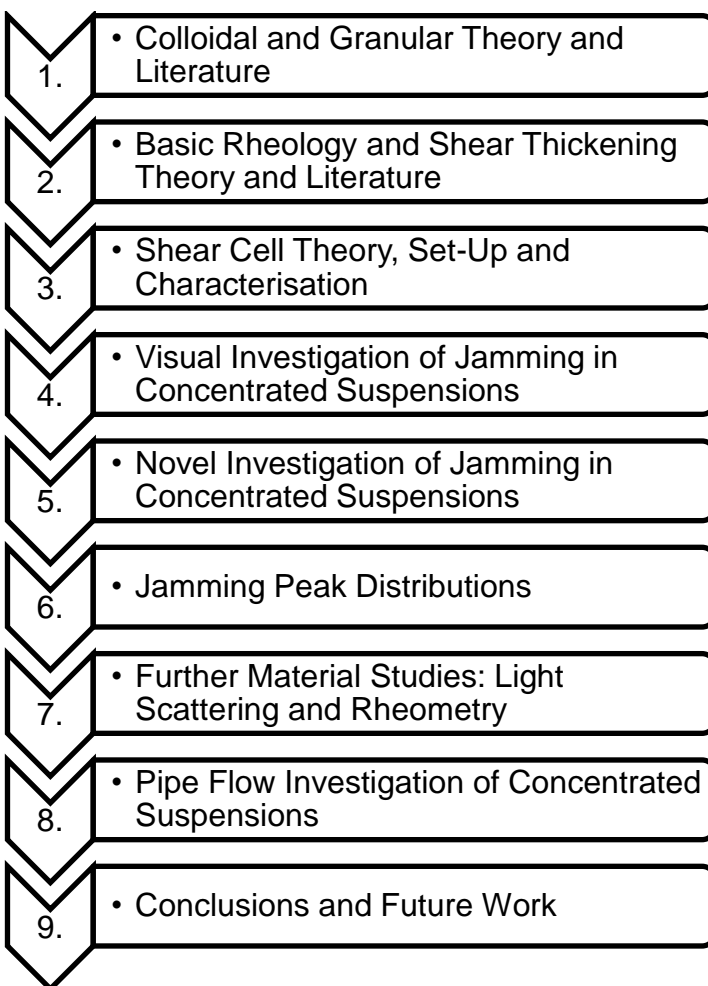
By designing and using novel equipment that is not commercially available, a better understanding of the effects of flow on concentrated suspensions was achieved.

This could ultimately lead to a better understanding of complex flow systems and lead to more efficient processes.

# Thesis Layout

---

This thesis is split into 9 chapters. Chapter 1 and Chapter 2 provide background theory and literature information relevant to the work done in this thesis. Chapter 3 covers background information and theory about the set-up and characterisation of the shear cells that were designed and used for the experimental work done in this thesis. Chapters 4-8 cover the main experimental and data analysis work done in this thesis. Chapter 9 details conclusions that can be drawn from this work and suggestions for future work. A chapter on preliminary molecular dynamics simulations that have been performed on a system similar to that investigated experimentally is included as an appendix.



## Chapter 1: Colloidal and Granular Theory and Literature

This chapter details the key characteristics of colloidal and granular systems which are relevant to the work done in this thesis. The importance and relevance of suspensions, both in an experimental and industrial context, is also discussed.

## Chapter 2: Basic Rheology and Shear Thickening Theory and Literature

Chapter 2 details the main rheological theory that is relevant to the work done in this thesis. This includes basic rheology theory and information about the effects of flow on concentrated suspensions. Discontinuous shear thickening and flow induced jamming, which are highly relevant to the results found experimentally, are discussed.

## Chapter 3: Shear Cell Theory, Set-Up and Characterisation

Chapter 3 begins by detailing the theory, methodology and characterisation of a rotating cylinder shear cell geometry that was designed for shearing concentrated colloidal suspensions. This design of shear cell is used in [Chapter 4](#) and [Chapter 5](#). The theory and methodology behind a capillary pipe flow shear cell that is used in [Chapter 8](#) for flowing concentrated granular suspensions is then detailed.

## Chapter 4: Visual Investigation of Jamming in Concentrated Suspensions

This chapter is about work done to visually analyse the effects of flow on concentrated colloidal suspensions. The chapter begins by detailing the experimental procedures for setting up the rotating cylinder shear cells detailed in [Chapter 3](#) and the experimental procedures for preparing concentrated colloidal suspensions. This is followed by the experimental procedures and results for visually analysing the flow of the concentrated suspensions.

## Chapter 5: Novel Investigation of Jamming in Concentrated Suspensions

This chapter details a more advanced jamming measurement system that was designed due to shortcomings of the visual analysis used in [Chapter 4](#). The chapter begins by detailing the methodology and characterisation of a novel technique that was designed to investigate jamming quantitatively using a force sensor. This is followed by the experimental procedures and results for analysing the flow under steady shear with the force sensor technique. This includes a comparison to the

visual results from [Chapter 4](#). The experimental findings and literature are then used to propose a mechanism for discontinuous shear thickening and flow induced jamming.

### Chapter 6: Jamming Peak Distributions

In this section of work, the data obtained from the force sensor used in [Chapter 5](#) is analysed further. Histograms and cumulative distributions of jamming peak magnitudes and the time gap between jams are produced for various conditions investigated. Their distributions are analysed, resulting in a greater understanding of the results in [Chapter 5](#).

### Chapter 7: Further Material Studies: Light Scattering and Rheometry

This chapter details the use of commercial instruments to further investigate the properties of the colloidal suspensions used in [Chapter 4](#) and [Chapter 5](#) and the cornflour-water suspensions used in [Chapter 8](#). It begins by detailing dynamic light scattering experiments that were performed on the supplied colloids to check particle size and polydispersity and to investigate the dynamics of the concentrated suspensions. This is followed by results obtained from using a commercial rheometer on the concentrated suspensions used in this thesis, with results obtained from this and the more novel techniques used being compared. Finally, details of a light scattering technique that was performed on the colloidal suspensions used in [Chapter 4](#) and [Chapter 5](#) to see if the particles were ordering under shear is given.

### Chapter 8: Pipe Flow Investigation of Concentrated Suspensions

This is the final experimental chapter of the thesis and details the set-up and results from experiments designed to investigating the effects of pipe flow on concentrated granular cornflour-water suspensions. Findings from these results are compared to those from the concentrated colloidal suspensions used in previous chapters.

### Chapter 9: Conclusions and Future Work

In this chapter, overall conclusions from the work done in this thesis are given. This is followed by a range of ideas for future work that may be worth pursuing.

# Contents

---

Declarations.....	i
Acknowledgements.....	ii
Publications and Conferences .....	iii
Abstract .....	iv
Thesis Layout .....	vi
Contents .....	ix
1. Colloidal and Granular Theory and Literature .....	1
1.1 Summary.....	2
1.2 Colloidal Materials .....	3
1.2.1 Soft Matter .....	3
1.2.2 Colloids and their Applications .....	3
1.2.3 Colloids as Hard Spheres .....	5
1.2.4 Volume Fraction and Phase Behaviour .....	6
1.2.5 Colloidal Glass Transition .....	8
1.2.6 Packing Characteristics .....	9
1.2.7 Forces and Interactions .....	12
1.2.7.1 Brownian Motion, Sedimentation, Particle Size and Péclet Number .	12
1.2.7.2 Colloidal Interparticle Interactions.....	16
1.2.8 Particle and Solvent Choice .....	21
1.2.9 Common Study Techniques.....	23
1.2.9.1 Optical Microscopy .....	23
1.2.9.2 Confocal Microscopy .....	24
1.2.9.3 Light Scattering (Dynamic and Static).....	24
1.2.9.4 Rheology .....	25

1.2.9.5 Computer Simulations .....	26
1.2.9.6 Combination of Approaches .....	26
1.3 Granular Materials.....	27
1.3.1 Overview.....	27
1.3.2 Packing Characteristics and Dilatancy .....	28
1.3.3 Forces.....	29
1.3.3.1 Brownian Motion and Gravitational Forces .....	29
1.3.3.2 Coulomb (Electrostatic) Repulsion and Van der Waals Forces.....	29
1.3.3.3 Contact Forces .....	29
1.3.4 Force Chains and Flow .....	30
1.3.5 Shear Induced Segregation .....	32
1.3.6 Angle of Repose .....	33
1.4 Conclusions.....	34
 2. Basic Rheology and Shear Thickening Theory and Literature.....	35
2.1 Summary.....	36
2.2 Basic Rheology Background and Theory.....	37
2.2.1 Newtonian Fluids .....	37
2.2.2 Elastic Solids .....	38
2.2.3 Non-Newtonian Fluids.....	39
2.2.3.1 Shear Dependent Behaviour: Shear Thinning and Shear Thickening .....	39
2.2.3.2 Time Dependent Behaviour .....	40
2.2.3.3 Viscoelastic/ Yield Stress Behaviour.....	41
2.2.3.4 Power Law Behaviour.....	42
2.2.3.5 Pipe Flow .....	43
2.2.3.6 Péclet Number.....	44
2.3 General Rheology of Concentrated Suspensions .....	45

2.4 Shear Thickening and Jamming .....	46
2.4.1 Overview.....	46
2.4.2 Continuous and Discontinuous Shear Thickening .....	49
2.4.3 Shear Thickening Mechanisms .....	51
2.4.3.1 Order-Disorder Transition.....	51
2.4.3.2 Hydroclustering .....	52
2.4.3.3 Dilatancy .....	55
2.4.3.4 Review of Proposed Mechanisms.....	58
2.4.4 Non Shear Thickening Materials .....	59
2.4.5 Shear/ Flow Induced Jamming.....	60
2.4.6 Jamming Transition.....	62
2.4.7 Jamming Phase Diagram.....	64
2.4.8 Unjamming and Controlling Shear Thickening .....	66
2.4.9 Two-fluid Behaviour and Self-filtration.....	68
2.5 Conclusions.....	68
 3. Shear Cell Theory, Set-Up and Characterisation .....	69
3.1 Summary.....	70
3.2 Rotating Cylinder Shear Cell Geometry.....	71
3.2.1 Geometry Overview .....	71
3.2.2 Geometries Used.....	72
3.2.3 Theory .....	74
3.2.3.1 Linear Approximation for Steady Flow .....	74
3.2.3.2 Non-Linear Approach for Steady Flow .....	75
3.2.3.3 Basic Oscillatory Flow Considerations .....	78
3.2.4 Geometry Characterisation .....	79
3.2.4.1 Shear Profiles for Steady-Flow .....	79
3.2.4.2 Flow Instabilities and Flow Visualisation .....	83

3.3 Motor Characterisation .....	90
3.3.1 Fixed Voltage Calibration .....	90
3.3.2 Motor Characteristics Derivation .....	94
3.3.3 Effect of Supplied Voltage on Motor Characteristics.....	95
3.4 Capillary/Pipe Flow Geometry .....	98
3.4.1 Geometry Overview .....	98
3.4.2 Theory for Newtonian Flow .....	99
3.4.2.1 Hagen-Poiseuille Derivation .....	99
3.4.2.2 Average and Maximum Velocities, Shear Rates and Shear Stresses .....	103
3.4.3 Theory for non-Newtonian Flow .....	105
3.5 Conclusions.....	105
 4. Visual Investigation of Jamming in Concentrated Suspensions.....	106
4.1 Summary.....	107
4.2 Experimental Procedures .....	108
4.2.1 Materials and Apparatus .....	108
4.2.1.1 Shear Cell Set-up and Calibration .....	108
4.2.1.2 Visual Observation Equipment .....	110
4.2.1.3 Concentrated Colloidal Suspension Preparation.....	111
4.2.2 Steady Shear Experiments .....	114
4.2.2.1 Effect of Volume Fraction, Shear Stress and Shear Rate .....	114
4.2.2.2 Effect of System Geometry.....	115
4.2.2.3 Minimum Voltage/ Stress for Motion .....	115
4.2.2.4 Velocity Decrease during Jamming .....	115
4.2.2.5 Effect of Rotating Outer Cylinder (rather than Inner).....	115
4.2.2.6 Effect of Particle Size .....	116
4.2.3 Oscillatory Shear Experiments .....	117

4.2.3.1 Effect of Volume Fraction, Shear Stress, Strain and Shear Frequency .....	117
4.2.4 Comment on Strengths and Weaknesses of Visual Analysis .....	117
4.3 Results and Discussion .....	118
4.3.1 Steady Shear Experiments .....	118
4.3.1.1 Effect of Volume Fraction, Shear Stress and Shear Rate .....	118
4.3.1.2 Shear Rate versus Shear Stress Flow Profiles .....	122
4.3.1.3 Effect of System Geometry.....	123
4.3.1.4 Minimum Voltage/ Stress for Motion .....	125
4.3.1.5 Velocity Decrease during Jamming .....	126
4.3.1.6 Effect of Rotating Outer Cylinder (rather than Inner).....	127
4.3.1.7 Effect of Particle Size .....	128
4.3.2 Oscillatory Shear Experiments .....	129
4.3.2.1 Effect of Volume Fraction, Shear Stress, Strain and Shear Frequency .....	129
4.4 Conclusions.....	130
 5. Novel Investigation of Jamming in Concentrated Suspensions .....	131
5.1 Summary.....	132
5.2 Experimental Procedures .....	133
5.2.1 Materials and Apparatus .....	133
5.2.1.1 Overview of Novel Technique.....	133
5.2.1.2 Sensor Details and Characterisation .....	134
5.2.1.3 Sensor Force Calibration.....	140
5.2.1.4 LabVIEW Code.....	141
5.2.2 Test with Newtonian Material .....	145
5.2.3 Steady Shear Experiments on Concentrated Colloidal Suspensions....	146
5.2.3.1 Effect of Volume Fraction .....	146

5.2.3.2 Effect of Shear Stress.....	147
5.2.3.3 Effect of System Geometry.....	147
5.2.3.4 Effect of Particle Size .....	147
5.2.3.5 Effect of Closed System .....	148
5.2.3.6 Effect of Soft Walls .....	148
5.3 Results and Discussion .....	149
5.3.1 Effect of Volume Fraction.....	149
5.3.1.1 General Profiles.....	149
5.3.1.2 Peak Magnitude .....	151
5.3.1.3 Count and Time Gap between Jams .....	152
5.3.1.4 Extent of Jamming.....	154
5.3.2 Effect of Shear Stress and the Link between Visual Observations, Flow Profiles and Novel Technique .....	155
5.3.3 Effect of System Geometry .....	158
5.3.4 Energy Dissipation per Unit Strain .....	162
5.3.5 Effect of Particle Size.....	165
5.3.6 Effect of Closed System.....	167
5.3.7 Effect of Soft Walls.....	170
5.3.8 Statistical Analysis of Precisions .....	173
5.3.9 Mechanism Summary .....	176
5.3.10 Additional Considerations .....	180
5.3.11 Wider Applications .....	186
5.4 Conclusions.....	187
 6. Jamming Peak Distributions.....	188
6.1 Summary.....	189
6.2 Analysis of Peak Magnitude Distributions- Effect of Volume Fraction .....	190

6.3 Analysis of Time Gap between Peaks Distributions- Effect of Volume Fraction .....	199
6.4 Relevance to Literature .....	205
6.5 Effect of Shear Stress on Distributions .....	209
6.6 Effect of System Geometry on Distributions .....	223
6.7 Effect of System Confinement (Soft Walls) on Distributions.....	230
6.8 Consideration of Observation Time .....	237
6.9 Overall Observations.....	241
6.10 Conclusions.....	242
7. Further Material Studies: Light Scattering and Rheometry .....	244
7.1 Summary.....	245
7.2 Dynamic Light Scattering.....	247
7.2.1 Light Scattering Theory.....	247
7.2.1.1 Light Scattering Background.....	247
7.2.1.2 Light Scattering Set-Up .....	248
7.2.1.3 Dynamic Light Scattering.....	248
7.2.2 Experimental Procedures.....	253
7.2.2.1 DLS of Colloid Particles.....	253
7.2.2.2 DLS of Concentrated Suspensions.....	253
7.2.3 Results and Discussion.....	254
7.2.3.1 DLS of Colloid Particles.....	254
7.2.3.2 DLS of Concentrated Suspensions.....	256
7.3 Rheometry.....	258
7.3.1 Rheometry Background and Theory .....	258
7.3.1.1 Rheometry Background.....	258
7.3.1.2 Parallel Plate Rheometer Theory.....	260
7.3.2 Experimental Procedures.....	262

7.3.2.1 Rheometer .....	262
7.3.2.2 Rheology of Concentrated Colloidal Suspensions .....	263
7.3.2.3 Rheology of Concentrated Cornflour-Water Suspensions.....	263
7.3.3 Results and Discussion.....	264
7.3.3.1 Rheology of Concentrated Colloidal Suspensions .....	264
7.3.3.2 Rheology of Concentrated Cornflour-Water Suspensions.....	271
7.3.3.3 Use of Rotating Cylinder Shear Cell as a Relative Rheometer .....	276
7.4 Light Scattering to Detect Ordering .....	278
7.4.1 Colloidal Ordering Under Shear: Background .....	278
7.4.2 Experimental Procedures.....	280
7.4.3 Results and Discussion.....	281
7.5 Conclusions.....	283
 8. Pipe Flow Investigation of Concentrated Suspensions.....	285
8.1 Summary.....	286
8.2 Cornflour Background .....	288
8.3 Experimental Procedures .....	291
8.3.1 Materials and Apparatus .....	291
8.3.1.1 Shear Cell Set-up .....	291
8.3.1.2 Concentrated Cornflour-Water Suspension Preparation.....	293
8.3.2 Steady Shear Experiments .....	294
8.3.2.1 Effect of Syringe Pump Bar Maximum Force (Shear Stress) on Jamming .....	294
8.3.2.2 Effect of Pipe Length on Jamming .....	294
8.3.2.3 Effect of Pipe Diameter on Jamming .....	294
8.3.2.4 Effect of Syringe Pump Bar Velocity (Shear Rate) on Jamming.....	295
8.3.2.5 Effect of Pipe Material on Jamming .....	295
8.3.2.6 Effect of Pipe Wall Thickness/Reinforcement .....	296

8.4 Results and Discussion .....	298
8.4.1 Effect of Syringe Pump Bar Maximum Force (Shear Stress) on Jamming .....	298
8.4.2 Effect of Pipe Length on Jamming .....	299
8.4.3 Effect of Pipe Diameter on Jamming .....	300
8.4.4 Effect of Syringe Pump Bar Velocity (Shear Rate) on Jamming .....	302
8.4.5 Effect of Pipe Material on Jamming.....	304
8.4.6 Effect of Pipe Wall Thickness/Reinforcement on Jamming.....	307
8.4.7 Summary of Findings .....	309
8.5 Conclusions.....	312
9. Conclusions and Future Work.....	313
9.1 Conclusions.....	314
9.2 Future Work .....	317

# 1. Colloidal and Granular Theory and Literature

## This section will cover:

- Examples of different colloidal materials.
  - An overview of colloid theory, including details of the effect of solid volume fraction and the forces that must be considered.
  - Details of different structures colloidal materials can take and information regarding packing characteristics.
  - Details of common techniques used to study colloidal materials.
  - Basic details of granular materials, including packing characteristics and forces that are involved.



## 1.1 Summary

Much of the work done in this thesis involved investigating how concentrated colloidal suspensions behave under flow. For this, it was necessary to understand the importance and relevance of colloidal suspensions both in an experimental and industrial context, as well as have an understanding of how colloids behave.

This chapter details the key characteristics of colloidal systems, many of which are relevant to the work done throughout the thesis. The properties of different colloidal systems and experimental techniques were investigated, allowing the strengths of the system used for the work in this thesis to be highlighted.

In [Chapter 8](#) of this thesis, the effects of flow on a granular system of concentrated cornflour suspensions were investigated. This chapter therefore contains some basic theory behind granular materials.

## **1.2 Colloidal Materials**

This section gives an overview of the relevance and importance of colloidal suspensions, as well as basic colloidal theory.

### **1.2.1 Soft Matter**

Colloids can be classified under the term ‘soft matter’. This is a term given to materials in states of matter that are not simple liquids or crystalline solids. They are described as ‘soft’ since they react more sensitively to disturbances (such as shear) than pure molecular materials [1, 2]. They involve length scales intermediate between atomic sizes and macroscopic scales and are therefore typically in the regime between a nanometre and micrometre. Brownian motion is important and most soft matter systems are able to be easily driven out of equilibrium and are often ‘trapped’ out of equilibrium. Subtle balances between energy and entropy exist and this can lead to the self-assembly of complex structures [2]. The definition of soft matter is relatively broad, and includes many classes of materials including polymer melts or solutions, biological macromolecules and colloids [1, 2]. Because of the ubiquitous nature of soft matter systems, research activities in the field are diverse and interdisciplinary [1].

### **1.2.2 Colloids and their Applications**

Colloids are multiphase substances consisting of particles, typically  $1\text{nm}-10\mu\text{m}$  in size, dispersed in a continuous phase [3, 4]. They can be divided into categories depending on the state of the dispersed and continuous phase (Table 1.1) and due to their broad description are ubiquitous in life. The word colloid comes from the Greek language; ‘coll’ means glue and ‘oid’ means like, hence colloid literally means ‘glue-like’ [4].

**Table 1.1- Common examples of various colloidal systems [3, 4]**

<b>Dispersed Phase</b>	<b>Continuous Phase</b>	<b>Term</b>	<b>Examples</b>
Solid	Liquid	Sol, suspension or dispersion	Industrial: Drilling muds, ink, toothpaste  Natural: Mud, magma
Solid	Solid	Solid suspension	Industrial: Chocolate, alloys  Natural: Granite
Solid	Gas	Solid aerosol	Industrial: Some antiperspirants  Natural: Smoke, dust, cloud
Liquid	Liquid	Emulsion	Industrial: Mayonnaise, hand cream  Natural: Milk
Liquid	Solid	Porous material, solid emulsion or gel	Industrial: Cheese, amalgam  Natural: Gelatine, agar
Liquid	Gas	Aerosol	Industrial: Aerosols  Natural: Fog, mist
Gas	Liquid	Foam	Industrial: Whipped cream, fire extinguisher foam  Natural: Vacuoles in cells
Gas	Solid	Solid foam	Industrial: Insulating foam  Natural: Dry sponge, pumice

Numerous natural and synthetic materials can be described as colloids, as highlighted in Table 1.1. In nature, blood is an example; it consists of blood cells suspended in liquid plasma. Soils and sediments in geology are also natural examples. Colloidal systems are highly relevant to many industrial processes. They are important final products in the manufacturing industries, and are involved in liquid and mineral purification and oil and gas recovery and processing, for example [3]. In everyday life, manufactured products such as paint, hand cream and hair spray are a few of the many examples.

Colloids are also very important research tools; colloidal structures can be treated as analogous to atomic and molecular systems, and as a result they are extensively used as models for such systems [5]. An advantage of colloids compared to atomic systems is that real-space and real-time experiments are feasible. Colloids can be prepared and characterised in a controlled way and interactions between particles can be readily tailored [1]. A combination of experimental, computer simulation and theoretical methods can be effective tools for studying such systems [1].

### 1.2.3 Colloids as Hard Spheres

Spherical particles without any additional structure possess the simplest and highest possible symmetry [6]. The simplest colloidal model is that of the ideal hard sphere system. This assumes that the colloid particles are effectively hard spheres: each particle has a physical volume prohibiting overlap with other particles [2, 7].

The hard sphere potential energy is therefore as follows:

$$P(r) = \begin{cases} \infty & \text{if } r_p \leq \sigma \\ 0 & \text{otherwise} \end{cases} \quad \text{Equation 1.1}$$

Here  $P$  is the hard-sphere potential,  $r_p$  is the distance between two sphere centres and  $\sigma$  is the sum of two sphere radii (i.e. the diameter if monodisperse).

This states that all allowable configurations have zero potential energy and that the only restriction on the system is that the particles cannot interpenetrate (i.e. they are infinitely repulsive on contact) [3]. From thermodynamics (Equation 1.2), this implies that the free energy is governed entirely by entropy, which in turn is determined by how much space there is between particles and how the space is arranged. This

means that for a monodisperse system, volume fraction is the key control parameter [3].

$$F = U - TS \quad \text{Equation 1.2}$$

Here F is the free energy, U is the internal energy, T is the absolute temperature and S is the entropy.

### 1.2.4 Volume Fraction and Phase Behaviour

Volume fraction ( $\phi$ ) is the key control parameter of colloids. It determines phase behaviour and has a significant effect on the flow characteristics of colloidal materials. It is defined as the fraction of the total volume that is occupied by the dispersed phase.

$$\Phi = \frac{V_{\text{particles}}}{V_{\text{available}}} = \frac{NV_p}{V_{\text{available}}} \quad \text{Equation 1.3}$$

For spherical particles this is:

$$\Phi_{\text{sphere}} = \frac{\frac{4}{3}\pi a^3 N}{V_{\text{available}}} \quad \text{Equation 1.4}$$

Here N is the number of particles,  $V_p$  is the particle volume,  $V_{\text{available}}$  is the total volume and a is the particle radius.

In dilute systems where  $\phi \sim 0$ , spheres/particles are disordered and typically far from each other (as in a gas). As the volume fraction is increased, solution viscosity increases and the states become more analogous to a liquid (or solid at even higher volume fractions) than a gas [5]. Non-Newtonian effects, such as shear-thinning, shear-thickening and/or yield stress behaviour, may also become apparent as particles come closer together [2]. For randomly packed monodisperse spheres, the maximum amorphous packing, or random close packing (RCP), corresponds to  $\Phi_{\text{RCP}} \approx 0.64$  [5]. A further consideration of different packing fraction definitions is given in 1.2.6.

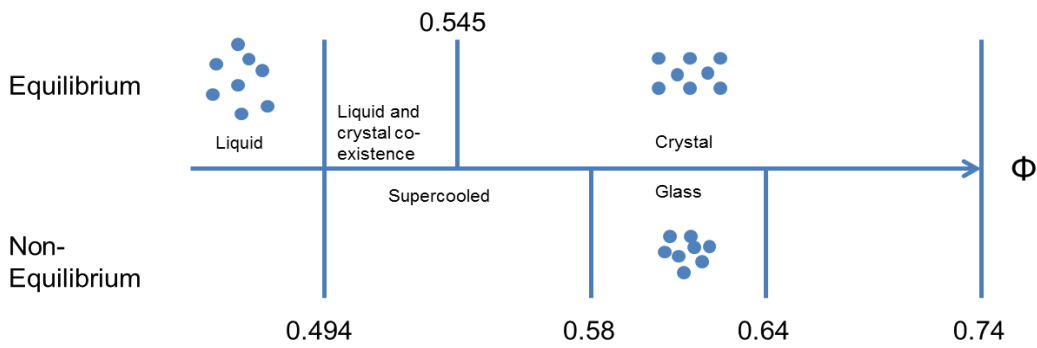


**Figure 1.1- Hard sphere phase diagram, with control parameter  $\phi$**

If a hard sphere system is allowed to equilibrate as the volume fraction is increased, the system can undergo an entropy driven phase transition that can turn it into an ordered crystalline state (Figure 1.1). The colloidal crystals are analogous to standard crystals whose repeating units are instead atoms or molecules.

From Figure 1.1, below  $\phi=0.494$ , a liquid region exists. Between  $\phi=0.494$  (freezing point) and  $\phi=0.545$  (melting point), crystal and liquid regions coexist [2, 8]. The liquid domains exist at  $\phi=0.494$  and the crystal domains exist at  $\phi=0.545$  [5]. As  $\phi$  is increased in this region, the amount of crystalline material present increases. As  $\phi$  is increased beyond 0.545, the crystalline state exists up until  $\phi_{\max}=0.74$ .  $\phi_{\max}$  is the volume fraction corresponding to the maximum packing possible of monodisperse (one size) spheres in a 3D system [5]. It is achieved through hexagonal close packing (HCP) or face centred cubic (FCC) arrangements (see 1.2.6) [3] .

Colloids undergo crystallisation since it results in increased system entropy. Although at first seeming counterintuitive due to the more ordered nature of the crystal structure, by forming an ordered arrangement, the colloidal spheres on average obtain a greater free volume to explore, compared to when arranged in a disordered state [2]. The system gains more entropy due to the increase in available volume than it loses through configurational entropy due to the system gaining long range order [2].

Non-equilibrium behaviour of colloids is also possible. This behaviour can be attained by increasing  $\phi$  quickly enough to avoid crystallisation (e.g. by centrifugation) [3]. In non-equilibrium conditions between  $\phi=0.494$  and  $\phi=0.58$ , a supercooled region exists; here the liquid is in a metastable state with the thermodynamically preferred state being crystal [3]. Between  $\phi=0.58$  and  $\phi_{RCP} \sim 0.64$ , the system undergoes a glass transition causing a glassy region to

exist. At volume fractions  $\geq 0.58$ , the growth of crystals is inhibited [9]. Here the amorphous liquid-like structure remains but all microscopic dynamics slow down significantly; particles are thought to be ‘caged-in’ (or jammed) by neighbours [3, 7, 10]. The glass transition is discussed in more detail in 1.2.5.

It is worth noting that the phase diagram of non-hard sphere systems can become more complicated due to interactions between particles. Three phase equilibria and even more complex non-equilibrium effects can become apparent [1, 11].

### 1.2.5 Colloidal Glass Transition

As mentioned, as the volume fraction approaches 0.58, colloids can undergo the colloidal glass transition. Here Brownian motion can no longer enable particles to move past their closest neighbours, and all microscopic dynamics slow down significantly [3]. This is because at these volume fractions, insufficient local free volume is present and in order for a given particle to move, it requires the co-operative movement of many other particles.

Glassy behaviour is thought to require a degree of polydispersity (multiple sized particles), since it inhibits crystallisation [12]. Polydispersity also influences the volume fractions where phase transitions occur [3, 5]. Theoretical and experimental work has found that there is a maximum polydispersity for hard-sphere crystallisation ( $\sim 11\%$ ) [9, 10].

Since glassy substances are not an equilibrium state, they are known to slowly ‘age’ (i.e. their structure slowly changes) as time proceeds, as the system evolves towards equilibrium conditions. As a result, their physical properties can change over sufficiently long time periods [2, 3].

This colloidal glass transition resembles the glass transition that takes place in simple molecular liquids, which occurs if the liquid is cooled at a rate sufficiently greater than the speed at which the liquid molecules can re-arrange into crystal positions. If molecules lack the vibrational energy required to jump out of their initial positions (i.e. due to the lower temperature), then they are effectively stuck in a trapped state, as are colloidal particles when at sufficiently high volume fractions [2]. Colloidal glasses are therefore a popular model system used to study the glass transition [12].

The colloidal glass transition also has important rheological implications; the material's relaxation time and viscosity increase significantly [12]. The glass transition is relevant to the discontinuous shear thickening and jamming of colloidal suspensions (detailed in [Chapter 2](#)), since it is at these high volume fractions that discontinuous shear thickening and jamming effects are most prominent [12].

### 1.2.6 Packing Characteristics

Colloidal suspensions have key packing characteristics that must be considered. They can have an important impact on suspension properties, such as flow behaviour.

#### Random Loose Packing

Random loose packing (RLP) is the least dense/ lowest volume fraction at which a particulate system is mechanically stable against gravity. This means that it can support its own weight. The actual value of RLP is poorly defined as it depends on the attractive forces between the particles, as well as the density difference between the continuous and dispersed phases. Experimental studies suggest a range of volume fractions, with estimates including 0.52-0.56 [13-15]. For spherical particle suspensions, many authors quote 0.55 [16].

#### Random Close Packing

Random close packing (RCP) is the densest packing fraction of spheres that has a random structure [17]. It is often defined as a jammed state since particles are unable to move relative to each other. The value of the RCP is typically quoted as  $\Phi=0.64$  for a system of monodisperse spheres [5, 17, 18]. The exact value, however, is unknown [17].

As RCP is approached, the viscosity diverges rapidly (tending to infinity) and the material is no longer able to flow [17]. As polydispersity is increased, the value of RCP increases, since particles are able to pack more closely [17].

#### Critical Jamming Packing Fraction

The critical jamming packing fraction corresponds to the jamming transition, above which the system has a yield stress like a solid [19, 20]. The value of this critical packing fraction can vary with particle shape and a number of other suspension

properties such as polydispersity [20, 21]. Studies suggest that the proximity of the volume fraction of a suspension to the critical point generally controls the slope/strength of the shear thickening regime; therefore the extent of shear thickening depends on the proximity to the critical jamming packing fraction [20]. This is discussed in more detail in [Chapter 2](#).

### Crystal Structures

Crystal arrangements lead to the maximum packing possible of monodisperse spheres in a 3D system, with  $\phi_{\max}=0.74$  [2]. As mentioned in 1.2.4, there are two different close-packed crystal structures for spheres that typically apply to hard sphere colloid crystallisation: face centred cubic (FCC) and hexagonal close packing (HCP).

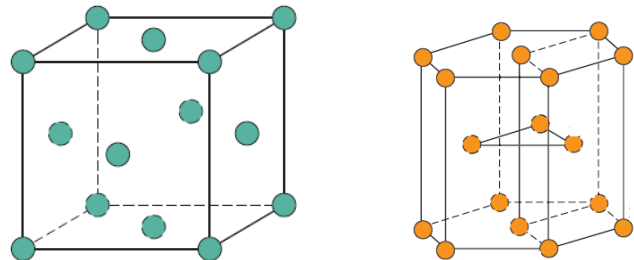


**Figure 1.2- Face centred cubic unit cell (left) and hexagonal close packing unit cell (right)** [22]

With FCC structures, a unit cell is cubic with particles located at each of the corners and the centres of all the cube faces (Figure 1.2). With HCP structures, the unit cell is hexagonal. The top and bottom faces of the unit cell each consist of six particles that form regular hexagons with a single particle in the centre. Another plane is situated between the top and bottom planes and provides three additional particles to the unit cell (Figure 1.2) [22].

Another difference between these configurations is the way in which close-packed planes (i.e. layers with the maximum packing density) stack upon each other as is shown in Figure 1.3. With FCC, layers alternate as abcabc. With HCP, layers alternate as ababab [2, 22].

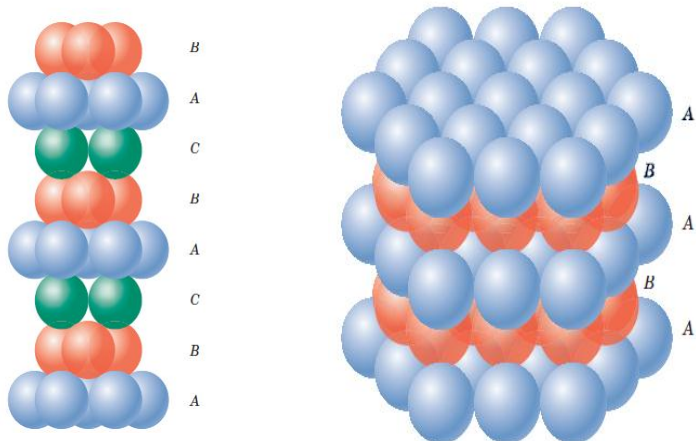


**Figure 1.3- Close-packed stacking sequence for face centred cubic structures (left) and hexagonal close packing structures (right) [22]**

Of the two structures, the face centred cubic structure is thought to have the lowest energy state and is therefore slightly more stable than hexagonal close packing [9, 11, 23]. Colloid crystals, however, usually show hexagonal close packing. This anneals to the more stable face centred cubic structure, but since the energy difference between the two is very small, the driving force is small. Therefore this step can be very slow [11].

## 1.2.7 Forces and Interactions

Colloids are characterised by an extremely high interfacial area per unit volume, and as a result have a substantial amount of interfacial energy. From energy considerations, particles will want to aggregate to reduce the overall interfacial area, and therefore reduce the free energy. A number of competing forces are involved in colloidal stability and often forces must be modified to prevent aggregation and bring about stabilisation.

Aggregation that is driven solely by diffusion is referred to as perikinetic aggregation, while aggregation that is enhanced by shear is referred to as orthokinetic aggregation [17]. Shear acts to bring particles together more quickly compared to just Brownian motion, resulting in a greater rate of aggregation [17].

### 1.2.7.1 Brownian Motion, Sedimentation, Particle Size and Péclet Number

Two important factors that affect colloidal systems are Brownian motion and sedimentation. When Brownian motion is significant, the effects of sedimentation are reduced.

#### 1.2.7.1.1 Brownian Motion

Brownian motion/ diffusion is the random jiggling motion of particles and is caused by the dispersed phase (e.g. colloid particles) constantly being randomly bombarded by molecules from the continuous phase (e.g. liquid) due to thermal motion [24]. For the size range of colloids, Brownian motion is very important [2].

The diffusion coefficient, which quantifies how quickly something diffuses, can be deduced from the Stokes-Einstein equation:

$$D = \frac{k_B T}{6\pi\eta a} \quad \text{Equation 1.5}$$

Here D is the diffusion coefficient,  $k_B$  is the Boltzmann Constant, T is the absolute temperature,  $\eta$  is the solvent viscosity and a is the particle radius.

The time scale for particle motion can be evaluated. This is typically the average time needed for a particle to diffuse its own radius and is known as the diffusion or Brownian time ( $\tau_D$ ). Its derivation comes from Equation 1.5 and 1.7 [3].

$$\tau_D = \frac{a^2}{6D} = \frac{\pi\eta a^3}{k_B T} \quad \text{Equation 1.6}$$

Because particle movements are random in magnitude and displacement, the average particle displacement in a particular direction is zero. Motion can therefore be quantified by the mean square displacement (MSD).

$$\langle \Delta x^2 \rangle = \langle [x(t + \Delta t) - x(t)]^2 \rangle = 2D\Delta t \quad \text{Equation 1.7}$$

Here  $\Delta x$  is the displacement in the x direction,  $x$  is position in x direction,  $D$  is the diffusion coefficient and  $t$  is the time.

Therefore in 3 dimensions, the MSD ( $\Delta r^2$ ) can be written as [3]:

$$\langle \Delta r^2 \rangle = 6D\Delta t = \frac{k_B T}{\pi\eta a} \Delta t \quad \text{Equation 1.8}$$

This shows that the smaller the particle size, the greater the distance travelled due to diffusion in a given time.

These relationships are often used to deduce particle sizes through the use of light scattering equipment. Light scattering equipment can be used to estimate diffusion coefficients, therefore allowing the particle's radius to be solved as an unknown (from Equation 1.5). Dynamic light scattering of the colloids used experimentally is detailed in [Chapter 7](#).

### 1.2.7.1.2 Sedimentation

The effect of sedimentation (particles settling) must also be considered. It is caused by gravity and is influenced by density differences between the phases (particles and surrounding medium). It is particularly important in systems with larger particle sizes (typically  $>0.1\mu\text{m}$ ), since it may be able to overcome the random thermal motion (Brownian motion) of the particles [4].

Sedimentation can limit the duration of experiments; since precise density matching is very difficult, over time particles will sink if their density is greater than the liquid or float if their density is less than the liquid, changing local volume fractions [3].

If a particle is placed in a liquid, with the particle density being greater than the liquid density, it will accelerate downwards due to gravity until the drag force, caused by

friction with the surrounding medium, balances the gravitational force. The velocity of the particle at this point is its terminal, or sedimentation, velocity [3].

The mechanism causing drag depends on the dimensionless particle Reynolds number ( $Re$ ) which is a ratio of inertia and viscosity [2].

$$Re = \frac{\rho v a}{\eta} \quad \text{Equation 1.9}$$

Here  $\rho$  is the liquid's density,  $\eta$  is the liquid's viscosity,  $v$  is the particle's velocity relative to the liquid and  $a$  is the particle's radius.

In colloids, the particle Reynolds number is usually small due to low velocities, small particle sizes and large viscosities when concentrated (as in this thesis). Therefore viscous forces greatly dominate and the drag force on a sphere ( $F_{drag}$ ) is given by Stokes' Law [2]:

$$F_{drag} = 6\pi\eta av \quad \text{Equation 1.10}$$

The gravitational force acting on a particle ( $F_{gravitational}$ ) is given by:

$$F_{gravitational} = \frac{4}{3}\pi a^3 \Delta \rho g \quad \text{Equation 1.11}$$

Here  $\Delta\rho$  is the density difference between the particles and liquid and  $g$  is the acceleration due to gravity.

The particle's terminal velocity ( $v_{terminal}$ ) can be deduced by equating the drag and gravitational forces [2].

$$F_{drag} = F_{gravitational}$$

$$v_{terminal} = \frac{2a^2 \Delta \rho g}{9\eta} \quad \text{Equation 1.12}$$

The terminal velocity is often much lower than this calculated value in practice. This is because these equations assume a single particle, with no effects from other particles. When multiple particles are present, they will influence each other, and the surrounding liquid, therefore having a notable impact on sedimentation. These effects will be more extreme at higher volume fractions [3].

For the colloidal experiments performed in [Chapter 4](#) and [Chapter 5](#), a calculation of the terminal velocity (Equation 1.12) suggested that it would take ~2100min for a

colloid particle at the top of the shear cell to sediment to the bottom (9mm fill height, 0.5 $\mu\text{m}$  particle radius, a solvent viscosity of 0.002 Pa.s, a PMMA density of 1180 kg/m<sup>3</sup> and a solvent density of 920 kg/m<sup>3</sup>). Sedimentation effects were therefore likely negligible, especially since these experiments involve concentrated systems in which sedimentation is significantly slower than this ‘free particle’ estimate.

#### **1.2.7.1.3 Effect of Particle Size and the Péclét Number**

Although not a control parameter in terms of phase transitions, it is clear that particle size is important and can greatly influence overall dynamics through the competing effects of Brownian motion and sedimentation which depend on particle size. Smaller particles will diffuse more rapidly than larger particles and the effect of sedimentation will be less significant and can often be ignored. This makes small particles favourable from a theoretical and analytical perspective [3].

The dimensionless gravitational Péclét number (Pe) can be used to compare a single particle’s gravitational energy to its thermal energy [25]. It therefore allows the importance of Brownian motion and sedimentation to be compared.

$$Pe = \frac{mga}{k_B T} \quad \text{Equation 1.13}$$

Where m is the particle mass.

When the Péclét number is small (<1), Brownian motion will dominate. When the Péclét Number is large (>1), sedimentation will dominate. Again, it highlights the importance of particle size.

For the system used experimentally in [Chapter 4](#) and [Chapter 5](#) (~1 $\mu\text{m}$  diameter particles at 20°C), the gravitational Péclét number was estimated to be ~0.7. The Péclét number is considered again in [Chapter 2](#).

### 1.2.7.2 Colloidal Interparticle Interactions

As well as the effects of sedimentation and Brownian motion, colloids also experience interactions between particles. These interparticle forces can be attractive or repulsive [2].

#### 1.2.7.2.1 Van der Waals Attraction

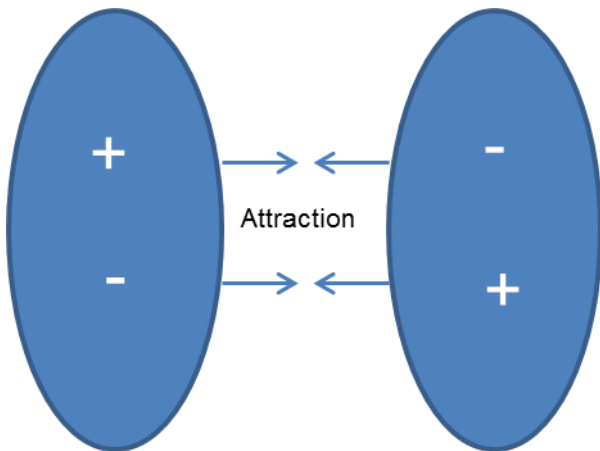


Figure 1.4- Van der Waals attraction [2]

Van der Waals attraction interactions are caused by fluctuating dipoles in particles (Figure 1.4). They are very strong at small separations (short-range ~10nm), but decay quickly as the separation is increased.

$$V(r) \propto \frac{1}{r^6} \quad \text{Equation 1.14}$$

Where V is the potential and r is the particle separation.

At small separations, van der Waals attraction forces often exceed thermal energy ( $k_B T$ ), explaining why particles that are not stabilised in some way (e.g. sterically or by charge) tend to stick together irreversibly [2]. The effect of van der Waals attractions can be greatly reduced by using a solvent with a similar refractive index to the colloid particles (see 1.2.8 and [Chapter 4](#)) [5].

### **1.2.7.2.2 Coulomb (Electrostatic) Repulsion**

Coulomb repulsion is caused by surface groups on colloidal particles dissociating or groups from the surrounding solution adsorbing, leaving particles charged. Overall charge neutrality is maintained by counter-ions in the solvent; these are attracted to the charged particle's surface, forming an electrostatic Debye double layer. At lengths greater than the double layer's length, the strength of electrostatic interactions between charged particles reduces to zero [2]. The length of the double layer greatly depends on the ion concentration of the surrounding medium. Ions act to screen repulsion, and increasing the ion concentration therefore reduces the length of the double layer and may lead to aggregation [5]. Stability of colloids is therefore highly dependent on the ion concentration of the surrounding medium [1, 2].

Since the charged particles and counter-ions are neutral overall, the repulsion is not caused directly through electrostatics. Instead it is the excess osmotic pressure of counter-ions at the surfaces that lead to the repulsive force [2]. Essentially the colloid particles are surrounded by a region in which the ion concentration is higher than the bulk solution. When these particles come close enough together, a region with an even higher ion concentration is created. This results in an osmotic pressure that acts to separate the colloidal particles [2, 26].

Direct electrostatic repulsion can occur if the surfaces of the particles are all either positively or negatively charged. This means that colloid particles are kept apart through electrostatics. This is significant when charged colloidal particles are dispersed in a non-polar solvent, where the double layer is insignificant [26].

### **1.2.7.2.3 Steric Stabilisation (Repulsion)**

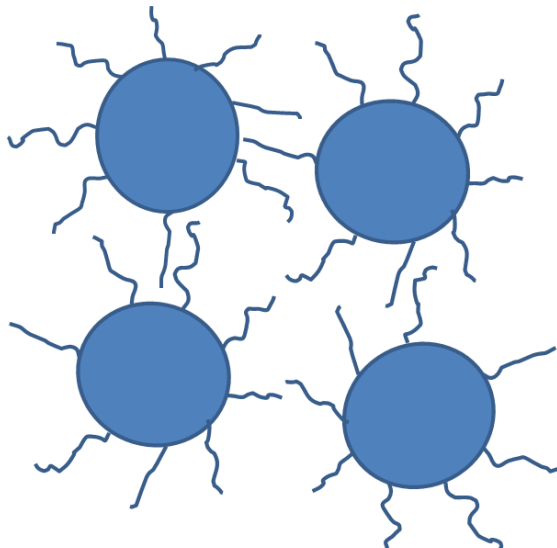


**Figure 1.5- Steric stabilisation [2]**

This is one of the most important methods of stabilising colloids and involves adding a boundary layer to the colloid particles, resulting in repulsive forces.

For example, a polymer layer may coat the particle, with one end of polymer chains being attached to the particle and the other sticking out. If two particles approach, the concentration of polymer in the gap between the particles increases (Figure 1.5). This leads to an increase in the osmotic pressure, resulting in a repulsive force which prevents the colloid particles approaching too closely [2].

The range of the interactions is dependent on the distance the polymer chains extend out from the colloid particle, and this itself depends on a number of parameters such as the solvent. If the polymer is in a 'good' solvent, it prefers to be surrounded by solvent and not close to other polymers. Therefore when other particles approach, a repulsive osmotic force occurs.

Using surfactants can have a similar effect. The hydrophobic tail of the surfactant can coat the colloid particles, while the hydrophilic head sticks into the water, therefore resulting in steric stabilisation [2].

#### 1.2.7.2.4 Depletion Interactions (Attraction)

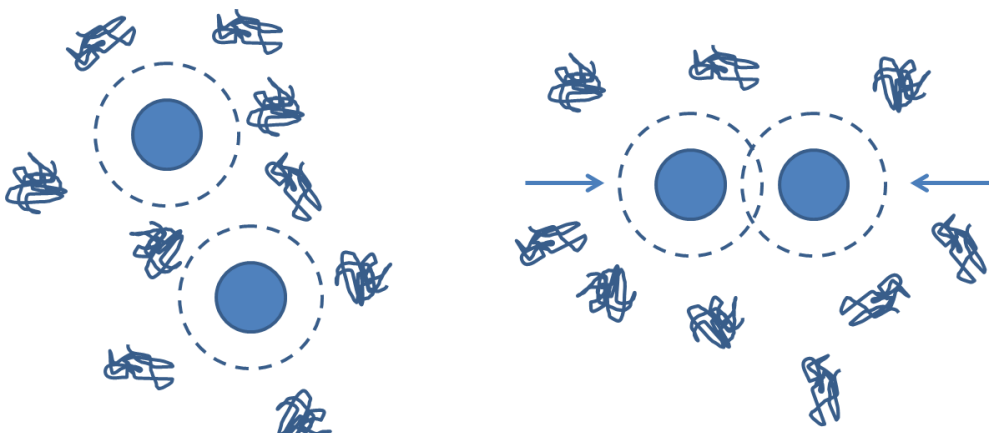


Figure 1.6- Depletion interactions [2]

Depletion interactions are attractive and arise when the solution also contains particles intermediate in size to the colloid particles and solvent molecules. This type of interaction is common when the suspension contains a dissolved polymer that does not adsorb on to the surface of the colloid particles [2].

The intermediate size particles are excluded from a region around the surface of the colloid particle: this is known as the depletion zone (dashed lines in Figure 1.6). As colloid particles approach, the concentration of intermediate particles between the approaching colloid particles (i.e. in the depletion zone) is less than the bulk concentration (Figure 1.6 right). This concentration difference causes a difference in osmotic pressure between the bulk solution and depletion zone, leading to a force that drives the colloid particles together.

The depletion interaction is always attractive [2]. The strength/depth of the interaction can be increased by increasing the amount of intermediate particles (e.g. by increasing the polymer concentration). If the intermediate particle concentration is high enough, the interaction energy can become comparable to, or exceed, the thermal energy ( $k_B T$ ). This can lead to phase separation, aggregation or gelation [2, 3]. The range of the interactions depends on the sizes of particles involved; typically the size of the intermediate species is limited to at most ~10% of the colloid particles. [3, 5, 8, 27, 28].

It is worth noting the approximate strengths of the interparticle interactions mentioned. All are typically of the order 1-5 kJ/mol (which is equal to ~1-2  $k_B T$  at

20°C). This is substantially less than the 200-1000kJ/mol typical strength of covalent bonds and the 500-4000kJ/mol typical strength of ionic bonds [29].

#### **1.2.7.2.5 Hydrodynamic Interactions**

Hydrodynamic interactions arise from disturbances in the flow field surrounding a particle, which were caused by another particle [17, 30, 31]. These interactions do not exist if the flow field is perfectly stationary. Hydrodynamic interactions are very important in the field of shear thickening and jamming of colloidal and granular suspensions and are explained in more detail in [Chapter 2](#).

#### **1.2.7.2.6 Frictional Interactions**

If the surfaces of neighbouring particles make physical contact, then friction can become significant depending on the friction coefficient of the particles. Additionally, in highly concentrated suspensions, interparticle friction can become the dominant form of interaction between particles within a suspension, as lubrication hydrodynamics between particles breaks down [20, 32]. Frictional interactions and lubrication hydrodynamics are very important in the field of shear thickening and jamming of colloidal and granular suspensions and are explained in more detail in [Chapter 2](#).

## 1.2.8 Particle and Solvent Choice

As mentioned briefly, the interactions between colloid particles can be readily tailored and this is largely done through the choice of particles and solvent.

Polymethylmethacrylate (PMMA) spheres coated with a steric stabilising agent (e.g. poly-(12 hydroxystearic acid)) are perhaps the most commonly used colloids in laboratory work, and are used in this thesis [33, 34]. Radii between 0.2-20 $\mu\text{m}$  are typical [9]. These spheres can readily be suspended in solvents, such as decahydronaphthalene (decalin) and tetrahydronaphthalene (tetralin), which are good refractive index matches and reasonable density matches. Their behaviour is thought to closely approximate that of hard spheres and as a result they are commonly used as model systems [9, 10, 12]. Recent studies, however, suggests that the particles may have a slight charge in certain solvents, making interactions more complex [5]. Tetralin is also absorbed by the particles and this can cause swelling over time, typically increasing particle radius by 1-20% [10, 18, 35].

Silica spheres are also often used for laboratory colloidal studies. The behaviour of charge stabilised colloidal silica particles in water is thought to closely represent hard spheres. Their main disadvantage is that they are difficult to density match. Sedimentation can be alleviated by using smaller particles, but this comes at the cost of greater polydispersity [18]. Charged stabilised polystyrene spheres can also be used. Their behaviour is hard sphere-like, and they are easy to density match. Unlike PMMA and silica, however, they are very difficult to refractive index match [18]. The choice of colloid particles is therefore generally a trade-off between interaction potential, index matching and density matching [5].

The choice of solvent is important and can help with control, as mentioned [3]. Miscible solvents can be readily mixed to allow close density matches with the colloid particles to be achieved. As mentioned briefly in 1.2.7.1.2, this can minimise gravitational effects i.e. sedimentation. Solvents can also be mixed to closely match the refractive index of the colloid particles. This minimises scattering, allowing optical microscopy or light scattering to be used as experimental techniques. Closely matching refractive indices between the particles and medium can also lessen van der Waals attractions, as mentioned [3]. The ion concentration of the solvent is also important, with ions acting to screen repulsive interactions.

In this thesis, PMMA particles sterically stabilised with poly-(12 hydroxystearic acid) and dispersed in a mixture of decalin and tetralin solvents were used. This system is a good representation of ideal hard spheres and the solvents could be mixed to allow close index matching. This allowed samples to be visualised and minimised interactions between particles. Close particle and solvent densities meant sedimentation was not significant. Particles could also be produced with a very low polydispersity (<5%). Details of colloid sample preparation are given in [Chapter 4](#).

## 1.2.9 Common Study Techniques

There are various analytical techniques that can be used to study colloidal systems. The size and thermal energy ( $k_B T$ ) of the particles largely dictates which instruments are suitable [5]. Often a combination of techniques is used and finding new methods is of interest.

### 1.2.9.1 Optical Microscopy

Conventional optical microscopy is a popular technique for studying colloids. This is largely due to its relative ease of use and low cost. It is able to resolve particles  $\sim 1\mu\text{m}$  in diameter, allowing ordering and distributions to be observed. It is often used alongside cameras, allowing images and videos to be recorded [5].

Bright field is the most common and basic optical microscopy illumination technique. It makes use of the absorption of light by the sample to produce image contrast. The technique is good for 2D imaging but is not well suited for 3D analyses. Limitations include poor image quality, low contrast and poor resolution. These problems are largely caused by multiple scattering from out of focus objects [5].

Fluorescence is another technique that is often used. With it, photons at a particular wavelength excite a dye (e.g. on the particles). The dye then emits photons at a larger wavelength (lower energy), allowing the particles to be viewed. A drawback of this technique is that the dyes can lose their ability to fluoresce with repeated light exposure (photobleaching). The dye can also modify interactions in the system, for example by leaving a slight charge on the particles [3]. It is also not well suited for concentrated systems; too much fluorescence may happen at the one time, giving a large background illumination and making the images unclear [36].

Optical microscopy can be combined with particle tracking. Particle tracking makes use of various image processing and computational techniques to deduce information about particle position and movement. In general, particle tracking accuracy increases with increasing particle size.

Particle tracking can work fairly well for dilute samples, but its performance can be very poor in more concentrated colloids. For example, if lots of particles are close together, it can be difficult to distinguish individual particles. It can also perform poorly if particle movements are very small [3].

### 1.2.9.2 Confocal Microscopy

Confocal microscopes are able to overcome many problems of optical microscopy. They are able to reject out of focus light, leading to clearer images, and are able to produce 3D images by scanning the sample quickly at various heights. They make use of fluorescence.

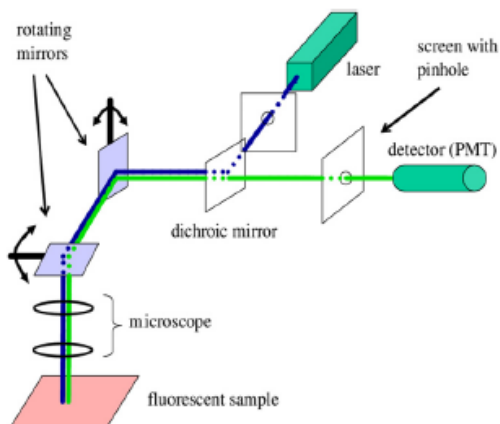


Figure 1.7- Confocal microscope layout [5, 13]

With a confocal microscope, laser light (blue in Figure 1.7) passes through a dichroic mirror and onto rotating mirrors that scan horizontally. The light then passes through the microscope optics and onto the sample, therefore exciting it. The emitted fluorescent light (green in Figure 1.7) then follows the reverse optical path back to the dichroic mirror. There it is reflected onto a screen with a pinhole. The in-focus light is then collected by a detector (photomultiplier tube/ PMT) [3].

Disadvantages of confocal microscopy include its cost and the fact that it relies on a laser since they are limited in terms of wavelength. The necessity of scanning the sample with the laser beam can limit the rate of image collection.

### 1.2.9.3 Light Scattering (Dynamic and Static)

Light scattering is useful for finding out average structural and dynamic information about a system, and the two main approaches are dynamic light scattering (DLS) and static light scattering (SLS). A typical experimental set- up involves illuminating a sample with an incident laser beam. Some of the light is scattered and this scattered light is measured by a detector at a given angle.

DLS experiments measure temporal variations of intensity at a fixed angle, and are based on the random Brownian motion of the particles in solution. Using this

technique, properties based on particle motion, such as diffusion coefficients, can be deduced. From this, particle sizes can be estimated.

Static (time averaged) light scattering experiments are based on measuring the intensity over an observation time, and then averaging the intensities measured. In general, the higher the intensity, the more light scattering and therefore, the larger the particles. By performing SLS at various angles, structural information can be obtained.

An important strength of light scattering is that it provides very good average information since measurements are based on an average of millions of particles. A disadvantage of this, however, is that local information is difficult to obtain. Light scattering is able to work with particles smaller than those required for microscopy. In general, light scattering instruments are able to work well with nanometre sized structures. Small angle light scattering (SALS) allows larger ~micron sized structures to be studied, by probing at a smaller angle [3, 5, 37].

Details of dynamic light scattering theory are given in [Chapter 7](#) where the technique is used to investigate particles sizes and suspension dynamics of the concentrated colloidal suspensions that are used experimentally in this thesis.

#### **1.2.9.4 Rheology**

Rheology is the study of how materials flow and how they deform in response to an applied force. More detailed information about rheology theory is given in [Chapter 2](#) and [Chapter 7](#) where a rheometer is used to analyse the materials used in this thesis. Rheometers/viscometers are typically used for this, and they work by applying a constant or oscillatory stress and measuring the resulting deformation, or by producing a shear rate/deformation and measuring the stress required for this. Since the measurements are macroscopic (i.e. based on the bulk solution), rheology as a technique provides little detail of microscopic subtleties [3].

### **1.2.9.5 Computer Simulations**

Computer simulations, such as molecular dynamics simulations, can be used to study colloidal systems. Computer simulations can be useful to verify experimental data (and vice-versa) if it has been possible to match simulation conditions closely to experimental. The results of simulations are determined solely by the nature of the model used [38]. As a result, comparison of simulation results with experimental data is a clear test of the model's accuracy and validity. If the experimental data are reliable, discrepancies between the experimental measurements and simulation data can be attributed to the model's failure to represent the system accurately [38].

### **1.2.9.6 Combination of Approaches**

Today, using a combination of the outlined techniques, or even developing a more novel technique, is typically favoured over using just one technique. By using a well thought out combination, it is possible to gain a greater understanding of complex systems than if only one technique alone was used. In the past, rheometry was often used as the sole technique to investigate the effects of shear on concentrated suspensions, but it is now widely accepted that rheometry alone cannot provide the detailed microscopic understanding required [39].

In this thesis, a combination of approaches was used to investigate flow complexities in concentrated suspensions: optical microscopy, light scattering, rheometry and a novel investigative technique. This allowed a better understanding of the systems investigated to be achieved than if only one technique was used.

Preliminary molecular dynamics simulations on a system similar to that investigated experimentally in this thesis have also been performed and are included as an appendix.

## 1.3 Granular Materials

In Chapter 8 of this thesis, the effects of flow on a granular system are investigated. This section therefore contains some basic theory behind granular materials.

### 1.3.1 Overview

Granular materials consist of discrete solid particles that are in direct physical contact with neighbouring particles most of the time [13, 15]. As a result, inter-particle collisions are very important [40]. Their properties are different from those commonly associated with solids, liquids, or gases [41].

Granulars are typically sized in the micron and millimetre diameter region, compared to colloids that typically range from a few nanometres to a few microns [13, 15]. Materials with diameters  $<100\mu\text{m}$  are typically referred to as powders, those with diameters  $<10\mu\text{m}$  are referred to as superfine powders and those with diameters below 1  $\mu\text{m}$  are hyperfine powders. Materials with diameters greater than this range are typically referred to as pebbles, aggregates or rocks, depending on size [13].

The external force of gravity is important in granulars due to their larger particle sizes and the usual density mismatch between the particles and the continuous phase [12].

Granular materials are commonly encountered in nature and in industrial applications; sand, gravel, seeds, sugar, food grains, pharmaceutical powders and coals are all examples [15]. Almost 80% of manufactured or grown goods exist as a granular material in at least one stage of their development, with granulars largely dominating the pharmaceuticals, agriculture and construction industries [13].

Despite their importance, the science and mechanics of granular materials is not well understood. As a result, studies of the area are becoming increasingly important [15]. Exploring links between colloidal and granular media under flow is an area of interest in recent literature [20, 25, 42].

It is worth noting that this work is largely concerned with dense granulars, rather than granular gases.

### 1.3.2 Packing Characteristics and Dilatancy

A granular material is called a ‘dry granular material’ if the fluid in the interstices or voids between particles is a gas (usually air). If the interstices are completely filled with a liquid (such as water), the material is said to be a ‘saturated granular material’. If there is liquid in some interstices and gas in the others, the material is said to be a ‘partially saturated granular material’. Sometimes both saturated and partially saturated materials are simply referred to as ‘wet granular materials’ [15]. The fluid present in the interstices has a significant impact on important parameters such as interparticle forces (see 1.3.3) [13].

The volume occupied by granular materials in a container depends on their configuration. This depends on forces between particles, forces between particles and the container, the container’s geometry and details of the system’s history [13]. External forces such as gravity are also important.

As for colloids, the maximum particle volume fraction possible for equal sized spheres is 0.74. It is typically achieved through regular hexagonal close packing. The maximum random close packing volume fraction for monodisperse granular spheres is ~0.64, as for colloids [13]. The least dense, loosest random packing that is mechanically stable is less clearly defined. Experimental results suggest a range of volume fractions, with estimates including 0.52-0.56 [13-15].

If a granular material is agitated, its volume fraction can decrease. This is because granular materials show ‘dilatancy’ when they experience shear; i.e. they volumetrically expand [13-15]. When granular materials experience shear, stable arches/force chains and voids may develop, resulting in a vertical load having a significant horizontal component. These arches and voids can increase the system’s volume, therefore decreasing the density [13]. An example of this is why footprints on sand appear dry. Upon pressure, the water-saturated sand underneath expands, developing new voids. The water drains into these, leaving the surrounding surface drier [13]. Agitation can also increase volume fraction, for example by enabling particles to find a denser, more stable arrangement under gravity.

### **1.3.3 Forces**

A range of forces are involved in granular systems, some of which are similar to those relevant to colloids (see 1.2.7). As mentioned, whether or not a fluid is present in the interstices has a significant impact on forces, and can dramatically alter both the statics and dynamics of the system.

#### **1.3.3.1 Brownian Motion and Gravitational Forces**

Due to close contact between particles in dense granulars, thermal energy is rapidly dissipated through inelastic interparticle collisions (friction). Gravitational effects are important, and these factors make Brownian motion negligible, therefore differing from colloidal materials [12]. For example, a grain of sand raised by its own diameter in atmospheric conditions at ambient temperature has a gravitational potential energy  $\sim 10^{12}$  times greater than its thermal energy  $k_B T$  [41]. Granular materials can therefore be considered as thermodynamically at zero degrees, and since  $k_B T$  is irrelevant, typical thermodynamics cannot be used to explain their behaviour [13, 41].

#### **1.3.3.2 Coulomb (Electrostatic) Repulsion and Van der Waals Forces**

These interactions arise for the reasons mentioned in 1.2.7. These interactions are, however, often insignificant compared to other forces involved, particularly with larger particles [15]. Powder processing in particular, however, is prone to producing large amounts of static electricity and equipment should be grounded.

#### **1.3.3.3 Contact Forces**

Due to the close proximity between particles in granular materials, particles are subjected to various contact forces. Frictional forces and cohesion are examples.

i)      Friction

Frictional forces arise when two bodies are in contact across an interface and friction is the tendency of the interface to resist the relative motion of these bodies. Various mechanisms have been proposed. One idea is that the frictional resistance arises because some of the applied mechanical energy is converted to heat, causing vibrations of the atoms at the interface. Another idea suggests that asperities or projections on the surfaces of the bodies adhere to form junctions. Work must then be done to break these junctions [15].

ii) Cohesion

Cohesion is the tendency of particles to stick together. It may arise if interparticle attractive forces such as van der Waals attractions are significant or if a liquid is present and causes liquid bridges to form between particles. A material is said to be cohesive if non-zero forces have to be applied in a direction normal to the interface to pull particles apart.

The presence of a liquid is very important in determining whether cohesion will apply. Coarse sand is cohesionless when dry, but cohesive when wet. Cohesion is also important for fine powders where interparticle forces such as van der Waals attractions are important [13, 15].

### 1.3.4 Force Chains and Flow

As mentioned, when a force is applied to granular materials, force chains may develop (Figure 1.8 and Figure 1.9). These are configurations of particles in close contact that are able to transmit part of the load. The force is then transmitted in directions that depend on the particle contacts and configurations, not just the direction of the load. Therefore the force can be transmitted partially horizontally when a vertical force is applied. This means that regions may be shielded from the applied force. Friction has a significant impact on how the chains develop [13].

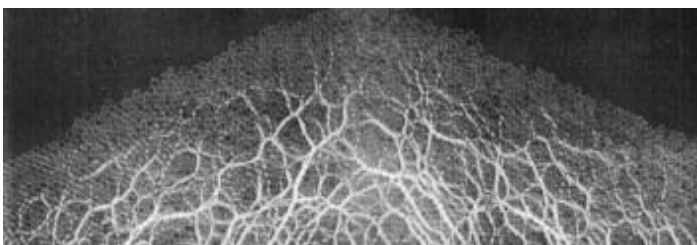


Figure 1.8- Force chains in a sandpile [13, 41]

Force chains have a significant impact on how granular materials flow [13]. If a granular material is flowing out of the bottom of an orifice in a tank, the flow behaviour is very different to that of a Newtonian liquid. For a Newtonian liquid such as water, the discharge rate will decrease with time as the height of the liquid (i.e. the pressure head) falls. With a granular material, however, the discharge rate will remain constant, regardless of the mass of material above it (at least until the tank is nearly empty).

This is due to force chains/arches forming. These lead to a fraction of the weight of the material above the orifice being transferred to the side (i.e. the tank walls), rather than towards the orifice. The pressure on the particles near the orifice arises only from a restricted, hemispherical volume approximately ten grains in radius from the opening. This is  $\sim$  independent of the amount of additional material in the container and this region is referred to as the “freefall arch”. It therefore forms a boundary separating particles that are not in direct contact and are accelerating freely due to gravity (i.e the particles leaving/about to leave the orifice), and the packed bed of compressed particles above [13].

It is this feature of granular materials that allows the sand in an hour glass to flow through the orifice at a nearly constant rate, therefore making an hour glass a useful instrument to measure elapsed time [41].

The flow of granular materials through pipes etc. is complex and it is estimated that in many industrial plants up to 40% of the plant's capacity is wasted due to difficulties transporting granular materials [41]. Their flow depends on parameters such as geometry, particle size, density and flow rate. When particles are large enough ( $>250\mu\text{m}$  diameter) and the surrounding fluid is not too viscous, particle interactions are dominated by friction between particles and collisions due to the applied force [43].

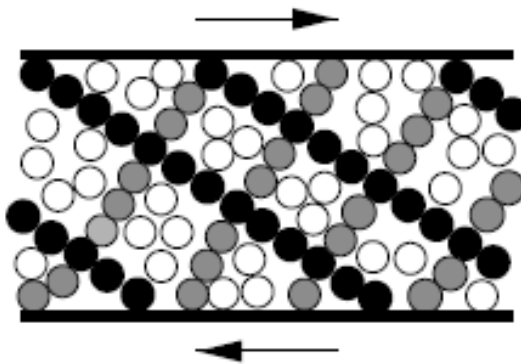


**Figure 1.9- Idealised schematic of force chain formation for system under shear stress (black=force chains, grey=other force-bearing particles, white=spectators) [44]**

Under certain conditions, force chains can form making flow complicated and difficult to predict [41]. When a force is applied to a granular material in a pipe, if force chains form, the applied force may be carried to the system's walls, rather than

making the material flow: i.e. force chains can result in the granular material ‘jamming’. More details about flow induced jamming are given in [Chapter 2](#).

### 1.3.5 Shear Induced Segregation

Size or mass segregation of granular media can occur when the system is externally agitated. In ‘normal’ systems, agitation would be thought to lead to improved mixing. With granular materials, however, spontaneous segregation of particles can be seen.

For example, when various sized granular materials are placed in a cylinder that is vertically shaken periodically, the larger particles will rise to the top. This is known as the ‘Brazil nut problem’, and the separation is thought to be due to a ratcheting mechanism. The vertical shaking causes an upward fluctuation of the larger particles. This causes voids to form directly beneath them. Other larger particles cannot fit into these voids but smaller particles can. This means that large particles are prevented from moving downwards, resulting in them eventually progressing to the top of the container [13].

An alternative idea suggests that convective rolls are instead responsible for the segregation. These are thought to be continuously present in the system when it is vertically shaken and are able to entrain larger particles, bringing them to the top of the container. Once at the top of the container, the larger particles are unable to follow the convective rolls of the smaller particles that move downwards [13, 43].

This segregation phenomenon has widespread industrial importance. For example, in the pharmaceuticals industry, drug powders need to be well mixed and homogeneous over the length scale of a pill [13, 14].

### 1.3.6 Angle of Repose

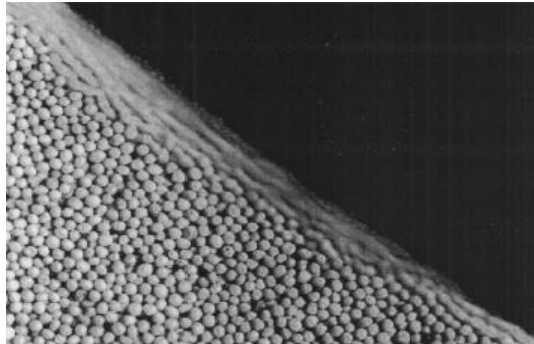


Figure 1.10- Avalanching mustard seeds [41]

When particles (e.g. sand) are dropped from a vertical height onto a horizontal surface, they come to rest through inelastic collisions with the surface and with each other. If a particle lands on another particle, it will most likely fall off, and in this way an approximately conical pile is formed. The angle a pile of granular material makes with the horizontal is very important. Below the maximum angle of stability ( $\theta_m$ ), the pile will be stable with interparticle forces and gravity holding the particles together. The pile will remain this way indefinitely, unless the surface is disturbed or more particles are added; in this respect, the pile can be considered as a solid [13, 14].

At angles greater than  $\theta_m$ , gravity can overwhelm the forces holding the particles together, and avalanches of particles from the pile's surface spontaneously flow down the slope like a fluid (Figure 1.10). This avalanching continues until the pile makes a smaller angle, the angle of repose  $\theta_r$ , with the surface [13-15].

The angle of repose depends on the density of the particles, particle size, coefficients of sliding and rolling friction, surface roughness and shape. Small amounts of interstitial liquid can greatly influence the pile due to the cohesive forces introduced by the liquid. Liquids generally allow much steeper slopes to be achieved before avalanching occurs. This explains why wet sand allows sandcastles almost perpendicular to the horizontal to be built [13].

The statistics of these 'sandpile' avalanches show power law behaviour in terms of avalanche size. This forms part of the theory of 'Self-Organized Criticality'. With this, it is suggested that systems such as sandpiles of grains evolve into a critical state by themselves and that this state shows power law behaviour [13]. When in this

state, small perturbations can result in chain reactions. For example, the addition of a single grain of sand to a pile can result in an avalanche of many particles [45].

## 1.4 Conclusions

The key characteristics of colloidal systems were investigated. The properties of different colloidal systems and experimental techniques were investigated, allowing the strengths of the system used for the work in this thesis to be highlighted.

Basic theory behind granular materials was investigated since in [Chapter 8](#) of this thesis, the effects of flow on a granular system of concentrated cornflour suspensions were investigated.

This chapter leads on to the work done in [Chapter 2](#) of this thesis, where basic rheology theory and information is given. This is followed by information about the rheological behaviour of concentrated suspensions.

a	Radius
d	Diameter
D	Diffusion coefficient
$E_{\text{gravitational}}$	Gravitational potential energy
$E_{\text{thermal}}$	Thermal energy
F	Free energy
$F_{\text{drag}}$	Drag force
$F_{\text{gravitational}}$	Gravitational force
FCC	Face centred cubic
g	Acceleration due to gravity
HCP	Hexagonal close packing
$k_B$	Boltzmann Constant
m	Particle mass
MSD	Mean square displacement
N	Number of particles
$\eta$	Solution viscosity
P	Hard-sphere potential
Pe	Péclet number
PHSA	poly-(12 hydroxystearic acid)
PMMA	polymethylmethacrylate
r	Particle separation
$r_p$	Distance between two sphere centres
RCP	Random close packing
Re	Reynolds number
$\langle \Delta r^2 \rangle$	Mean square displacement
S	Entropy
t	Time
T	Absolute temperature
$\Delta t$	Lag time
U	Internal energy
$v_{\text{terminal}}$	Terminal/sedimentation velocity
V	Total system volume
$V_p$	Single particle volume
$\Delta x$	Displacement in x direction
z	Height
$\sigma$	Sum of two sphere radii
$\phi$	Volume fraction of dispersed phase
$\phi_{\max}$	Maximal packing of monodisperse spheres in 3D system
$\phi_{\text{RCP}}$	Maximum amorphous packing/ random close packing volume fraction
$\theta_m$	Maximum angle of stability
$\theta_r$	Angle of repose
$\rho$	Density
$\Delta \rho$	Density difference between particle and liquid
$\tau_D$	Brownian time

1. Lowen, H., *Colloidal soft matter under external control*. Journal of Physics-Condensed Matter, 2001. **13**(24): p. R415-R432.
2. Jones, R., *Soft Condensed Matter*. 2011: Oxford.
3. Hunter, G.L. and E.R. Weeks, *The physics of the colloidal glass transition*. Reports on progress in physics. Physical Society (Great Britain), 2012. **75**(6): p. 066501.
4. Garvey, M., *The impact of colloid science*. Chemistry in Britain, 2003. **39**(2): p. 28-32.
5. Prasad, V., D. Semwogerere, and E.R. Weeks, *Confocal microscopy of colloids*. Journal of Physics-Condensed Matter, 2007. **19**(11): p. 25.
6. Blaak, R., et al., *Crystal nucleation of colloidal suspensions under shear*. Physical Review Letters, 2004. **93**(6).
7. Larson, R., *The Structure and Rheology of Complex Fluids*. 1999: Oxford University Press.
8. Lekkerkerker, H.N.W., et al., *Phase-Behavior Of Colloid Plus Polymer Mixtures*. Europhysics Letters, 1992. **20**(6): p. 559-564.
9. Vermant, J. and M.J. Solomon, *Flow-induced structure in colloidal suspensions*. Journal of Physics-Condensed Matter, 2005. **17**(4): p. R187-R216.
10. Poon, W.C.K., *The physics of a model colloid-polymer mixture*. Journal of Physics-Condensed Matter, 2002. **14**(33): p. R859-R880.
11. Anderson, V.J. and H.N.W. Lekkerkerker, *Insights into phase transition kinetics from colloid science*. Nature, 2002. **416**(6883): p. 811-815.
12. Weeks, E., *Soft Jammed Materials*. 2007, Tokohu University Press.
13. Kakalios, J., *Resource Letter GP-1: Granular physics or nonlinear dynamics in a sandbox*. American Journal of Physics, 2005. **73**(1).
14. Mehta, A., *Granular Physics*. 2007: Cambridge University Press.
15. Rao, K., *An Introduction to Granular Flow*. 2008: Cambridge.
16. Jenkins, M., et al., *Onset of mechanical stability in random packings of frictional spheres*. Physical Review Letters, 2008. **101**(1).
17. Mewis, J. and N. Wagner, *Colloidal Suspension Rheology*. 2012: Cambridge University Press.
18. Poon, W.C.K., E.R. Weeks, and C.P. Royall, *On measuring colloidal volume fractions*. Soft Matter, 2012. **8**(1): p. 21-30.
19. Liu, A.J. and S.R. Nagel, *Nonlinear dynamics - Jamming is not just cool any more*. Nature, 1998. **396**(6706): p. 21-22.
20. Brown, E. and H. Jaeger, *Shear thickening in concentrated suspensions: phenomenology, mechanisms, and relations to jamming*. Soft Condensed Matter, 2013.
21. Brown, E., et al., *Shear thickening and jamming in densely packed suspensions of different particle shapes*. Physical Review E, 2011. **84**(3).
22. Callister, W.D., *Materials Science and Engineering*. 7th ed. 2007: Wiley. 1000.
23. Woodcock, L.V., *Entropy difference between the face-centred cubic and hexagonal close-packed crystal structures*. Nature, 1997. **385**(6612): p. 141-143.
24. Rhodes, M., *Introduction to Particle Technology*. 2008: Wiley.
25. Jenkins, M.C., et al., *Does Gravity Cause Load-Bearing Bridges in Colloidal and Granular Systems?* Physical Review Letters, 2011. **107**(3).
26. Cosgrove, T., *Colloid Science: Principles, Methods and Applications*. 2010: Wiley-Blackwell.
27. Stradner, A., et al., *Equilibrium cluster formation in concentrated protein solutions and colloids*. Nature, 2004. **432**(7016): p. 492-495.

28. Illett, S.M., et al., *Phase-Behavior Of A Model Colloid-Polymer Mixture*. Physical Review E, 1995. **51**(2): p. 1344-1352.
29. Atkins, P., *Atkins' Physical Chemistry*. 2009: OUP Oxford.
30. Wagner, N.J. and J.F. Brady, *Shear thickening in colloidal dispersions*. Physics Today, 2009. **62**(10): p. 27-32.
31. Bossis, G. and J.F. Brady, *The Rheology Of Brownian Suspensions*. Journal of Chemical Physics, 1989. **91**(3): p. 1866-1874.
32. Seto, R., et al., *Discontinuous Shear Thickening of Frictional Hard-Sphere Suspensions*. Physical Review Letters, 2013. **111**(21): p. 5.
33. Pusey, P.N. and W. Vanmegen, *Phase-Behavior Of Concentrated Suspensions Of Nearly Hard Colloidal Spheres*. Nature, 1986. **320**(6060): p. 340-342.
34. Pusey, P.N. and W. Vanmegen, *Observation Of A Glass-Transition In Suspensions Of Spherical Colloidal Particles*. Physical Review Letters, 1987. **59**(18): p. 2083-2086.
35. Segre, P.N., O.P. Behrend, and P.N. Pusey, *Short-Time Brownian-Motion In Colloidal Suspensions - Experiment And Simulation*. Physical Review E, 1995. **52**(5): p. 5070-5083.
36. Cipelletti, L. and E. Weeks, *Glassy Dynamics and Dynamical Heterogeneity in Colloids* 2011: Oxford Science Publications.
37. Scirocco, R., J. Vermant, and J. Mewis, *Effect of the viscoelasticity of the suspending fluid on structure formation in suspensions*. Journal of Non-Newtonian Fluid Mechanics, 2004. **117**(2-3): p. 183-192.
38. Sadus, R., *Molecular Simulation of Fluids: Theory, Algorithms and Object-Orientation*. 2002, Elsevier.
39. Olmsted, P. *Flow-Microstructure Coupling: Instabilities and Shear Banding in Polymeric Fluids*. in AIChE 2014 Annual Meeting. 2014. Atlanta.
40. Mankoc, C., et al., *Role of vibrations in the jamming and unjamming of grains discharging from a silo*. Physical Review E, 2009. **80**(1): p. 7.
41. Jaeger, H.M., S.R. Nagel, and R.P. Behringer, *Granular solids, liquids, and gases*. Reviews of Modern Physics, 1996. **68**(4): p. 1259-1273.
42. Cates, M.E., M.D. Haw, and C.B. Holmes, *Dilatancy, jamming, and the physics of granulation*. Journal of Physics-Condensed Matter, 2005. **17**(24): p. S2517-S2531.
43. MiDi, G.D.R., *On dense granular flows*. European Physical Journal E, 2004. **14**(4): p. 341-365.
44. Cates, M.E., et al., *Jamming, force chains, and fragile matter*. Physical Review Letters, 1998. **81**(9): p. 1841-1844.
45. Winslow, N., *Introduction to Self-Organized Criticality & Earthquakes*. 1997, University of Michigan-Dept. of Geological Sciences.

## 2. Basic Rheology and Shear Thickening Theory and Literature

## This section will cover:

- Details of important rheological theory that is relevant to the work done in this thesis.
  - A consideration of the effects of flow on concentrated suspensions.



## **2.1 Summary**

Much of the work done in this thesis involved investigating how concentrated suspensions behaved under flow. For this, it was necessary to understand the theory and literature surrounding the area.

This chapter details the key rheological theory that is relevant to the work done in this thesis. This is followed by a section about the effects of flow on concentrated suspensions. It includes details about discontinuous shear thickening and flow induced jamming, which are highly relevant to the results found experimentally.

## 2.2 Basic Rheology Background and Theory

### 2.2.1 Newtonian Fluids

All gases and most simply structured liquids exhibit Newtonian behaviour. With Newtonian behaviour, the viscosity of a substance (which is a measure of its resistance to deformation by a shear stress or a measure of its rate of energy dissipation) is constant and is independent of what is done to the fluid (e.g. a stress applied) and time [1-3].

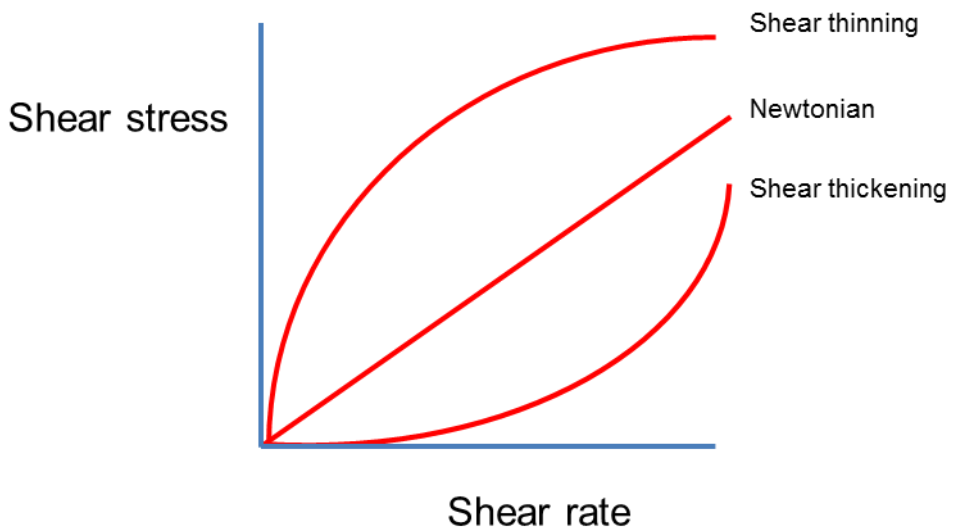


Figure 2.1- Shear stress versus shear rate profiles showing Newtonian, shear thinning and shear thickening behaviour

A linear relationship therefore exists between shear stress (the applied force per unit area) and shear rate (the rate of fluid deformation). Viscosity is the proportionality constant between the two and on a plot of shear stress versus shear rate, viscosity is the gradient of the slope (Figure 2.1). The profile passes through the origin: if no stress is applied, the fluid will not deform [4].

Newton's law of viscosity describes the relationship between shear stress ( $\tau$ ), shear rate or shear strain ( $\dot{\gamma}$ ) and viscosity ( $\eta$ ).

$$\tau = \eta \dot{\gamma} \quad \text{Equation 2.1} \quad \frac{N}{m^2} = \frac{Ns}{m^2} \times \frac{1}{s}$$

The shear rate describes 'how quickly' a fluid deforms. If a fluid is placed between two plates, with the bottom plate stationary, and a force is applied to the top plate,

the fluid will deform. The change of the velocity of the fluid with height is the shear rate. This can be seen in Figure 2.2 and can be defined as:

$$\dot{\gamma} = \frac{dv}{dz} \quad \text{Equation 2.2}$$

Where v is velocity and z is height.

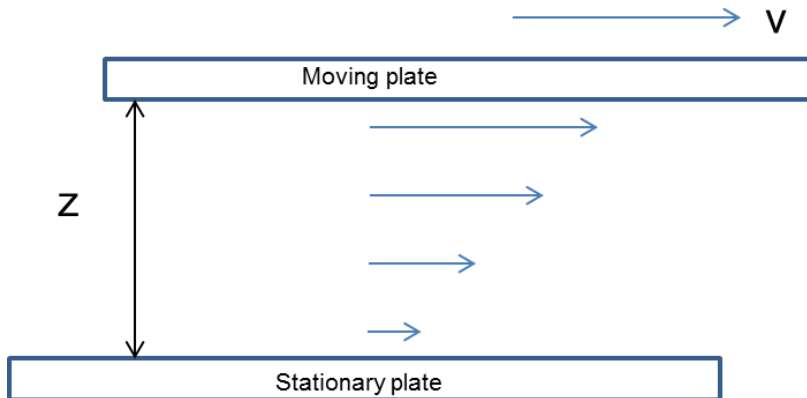


**Figure 2.2- Shear of a Newtonian fluid between two plates**

Newtonian fluids are purely viscous. They therefore have no elastic properties and no capacity to support a stress before yielding. Although shear stress and shear rate do not affect viscosity, factors such as temperature and pressure can. With liquids, an increase in temperature results in a decrease in viscosity. With gases, increases in temperature and pressure result in an increase in viscosity [1].

### 2.2.2 Elastic Solids

The behaviour of an ideal elastic solid can be described by Hooke's law. Here the elasticity modulus or Young's modulus (E) is used as a proportionality to relate stress ( $\sigma$ ) and strain ( $\epsilon$ ) and is analogous to viscosity [1].

$$\sigma = E\epsilon = E \frac{\Delta L}{L} \quad \text{Equation 2.3} \quad \frac{N}{m^2} = \frac{N}{m^2} \times \frac{m}{m}$$

Here  $\Delta L$  is the change in length and  $L$  is the length.

With elastic solids, input energy is stored and is therefore recoverable. This differs from purely viscous fluids where input energy is dissipated.

## 2.2.3 Non-Newtonian Fluids

Complex materials typically exhibit non-Newtonian behaviour and this causes a much more complicated response to flow. With a non-Newtonian fluid, the viscosity of the material may depend on what is done to the material and/or for how long the shear is applied. Non-Newtonian fluids may therefore be described as shear dependent and/or time dependent [1, 4]. A non-Newtonian fluid can also display a mixture of viscous and elastic properties [1].

### 2.2.3.1 Shear Dependent Behaviour: Shear Thinning and Shear Thickening

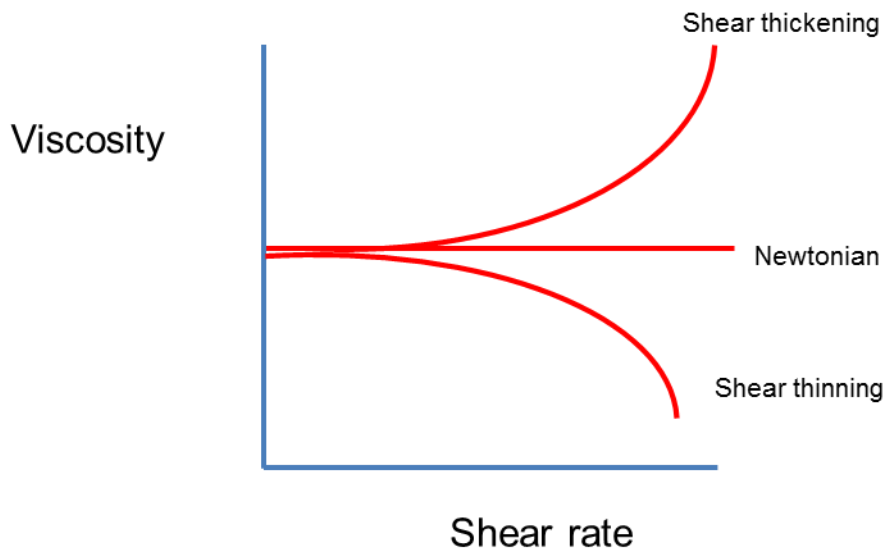


Figure 2.3- Viscosity versus shear rate profiles showing Newtonian, shear thinning and shear thickening behaviour

Since the viscosity of a non-Newtonian fluid is not independent of what is done to it, a linear relationship does not exist between the shear stress and shear rate.

A material whose viscosity decreases with increasing shear is said to be 'shear thinning' or a 'pseudoplastic' (Figure 2.3). Therefore on a plot of shear stress versus shear rate, the gradient of the curve (i.e. the viscosity) decreases with increasing shear rate (Figure 2.1) [1, 3, 4].

Paint is an example of a shear thinning material; when sheared onto a surface, the viscosity decreases allowing it to flow. When shearing stops, its viscosity increases, preventing the paint from dripping.

A material whose viscosity increases with increasing shear is said to be 'shear thickening' or a 'dilatant' (Figure 2.3). Therefore on a plot of shear stress versus shear rate, the gradient of the curve increases with increasing shear rate (Figure 2.1) [1, 3, 4].

A cornflour and water suspension is an example of a shear thickening fluid at high enough cornflour concentrations. When a stress is applied, the mixture's viscosity increases, therefore resisting deformation.

Often, a material displays Newtonian behaviour up until a particular shear rate- the critical shear rate- beyond which its behaviour is non-Newtonian. This critical shear rate is inversely proportional to the material's relaxation time. If the relaxation time is large (i.e. it takes a while for the material to return to its initial equilibrium state), the critical shear rate will be small [1, 3, 4].

### 2.2.3.2 Time Dependent Behaviour

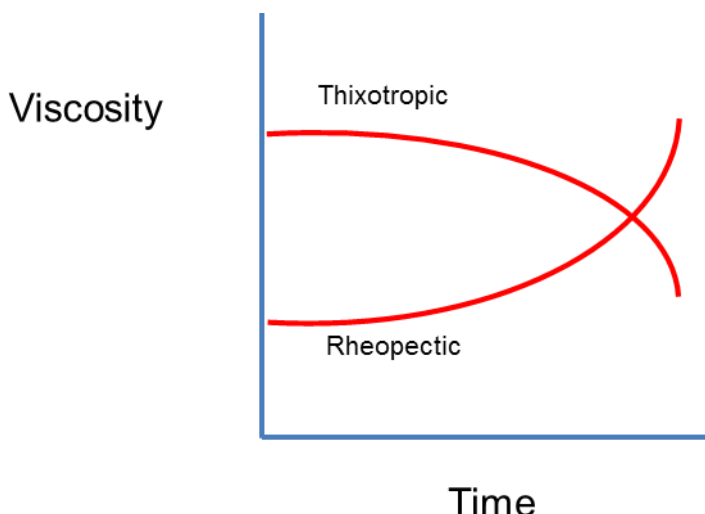


Figure 2.4- Response of time dependent fluids

The viscosity of time dependent fluids changes with time. Therefore, the shear rate depends upon the time the fluid has been subjected to a given shear stress and converse. If the viscosity of a fluid decreases over the duration of shear, it is 'thixotropic'. If the viscosity of a fluid increases over the duration of shear, it is 'rheopectic' or 'negative-thixotropic' (Figure 2.4) [1].

With all time dependent fluids, an 'equilibrium' condition (i.e. constant viscosity) will eventually be reached if the imposed condition (e.g. shear stress or shear rate) is

maintained for an adequate duration. Some fluids reach ‘equilibrium’ conditions so quickly that time-dependence can often be ignored. Others take much longer and in variable flow conditions may never reach ‘equilibrium’ [1].

### 2.2.3.3 Viscoelastic/ Yield Stress Behaviour

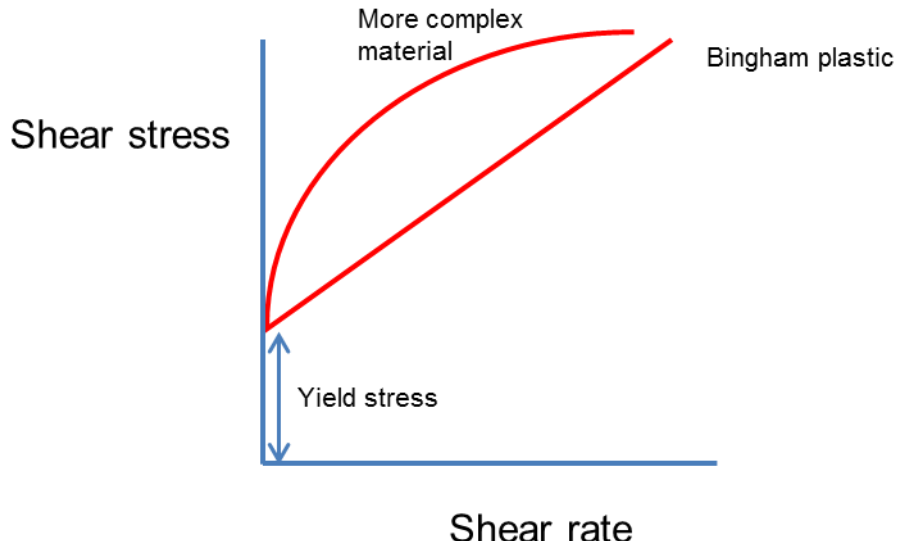


Figure 2.5- Yield stress behaviour

A viscoelastic material displays both viscous and elastic properties; it therefore has fluid and solid-like characteristics and input energy can either be dissipated through viscous forces or stored through elasticity. The elastic component can also be thought of as the fluid having infinite viscosity. Examples include polymer solutions and bituminous mixtures [1].

The type of response a viscoelastic material gives often depends on the type of deformation. For example, it may behave highly viscous in some situations but highly elastic in others. A yield stress material is viscoelastic; the material behaves as an elastic solid until a critical shear stress (the yield-stress) is reached (Figure 2.5). At stresses greater than the yield stress it behaves as a viscous fluid [1, 3, 4]. Therefore, it behaves as a solid at low shears and as a fluid at higher shears. Toothpaste is an example of a yield-stress material. It behaves as a solid in the tube, but by applying a force, it flows out of the tube as a liquid [1].

The simplest type of yield stress material is a Bingham plastic. Here at stresses beyond the yield stress, the shear stress and shear rate are directly proportional, as for a Newtonian fluid (Figure 2.5) [1, 2].

$$\tau = \tau_{yield} + \eta \dot{\gamma} \quad \text{Equation 2.4}$$

Some materials have more complex behaviour where beyond the yield stress, a plot of shear stress against shear rate approximates to a curve rather than a straight line. In this situation, the fluid behaves as a shear thinning or shear thickening material beyond the yield stress.

It is worth noting that the yield stress can be very low and it is therefore sometimes unclear whether a material has a yield stress or not.

#### 2.2.3.4 Power Law Behaviour

A common way of describing how a non-Newtonian fluid's viscosity varies with shear rate is through power law models. The two parameter Ostwald-de Waele model is often used: it makes use of a consistency coefficient ( $k$ ) and a power law index ( $n$ ), which indicates the amount of deviation from Newtonian behaviour [1, 2].

$$\tau = k \dot{\gamma}^n \quad \text{Equation 2.5}$$

The viscosity is therefore:

$$\eta = k \dot{\gamma}^{n-1} \quad \text{Equation 2.6}$$

When  $n > 1$ , the fluid's viscosity increases with increasing shear rate; this is therefore representative of a shear thickening material. When  $n < 1$ , the fluid's viscosity decreases with increasing shear rate and this represents a shear thinning material. When  $n = 1$ , the viscosity is constant, therefore representing a Newtonian material [1].

The units of  $k$  ( $\text{Ns}^n/\text{m}^2$ ) depend on  $n$  and therefore  $k$  values for fluids with different power law indices cannot be compared. The model only works well over a limited range of shear rates; i.e. where the rheological response such as shear thinning is constant [1].

Several alternative models relating shear stress and shear rate have been proposed which aim to overcome the mentioned shortcomings of the Ostwald-de Waele power law model. They are, however, considerably more complex and involve three or more parameters. A similar power law model accounting for yield stress behaviour also exists. It is called the Herschel-Bulkley equation or yield power law model [1, 2].

$$\tau = \tau_{yield} + k \dot{\gamma}^n \quad \text{Equation 2.7}$$

### 2.2.3.5 Pipe Flow

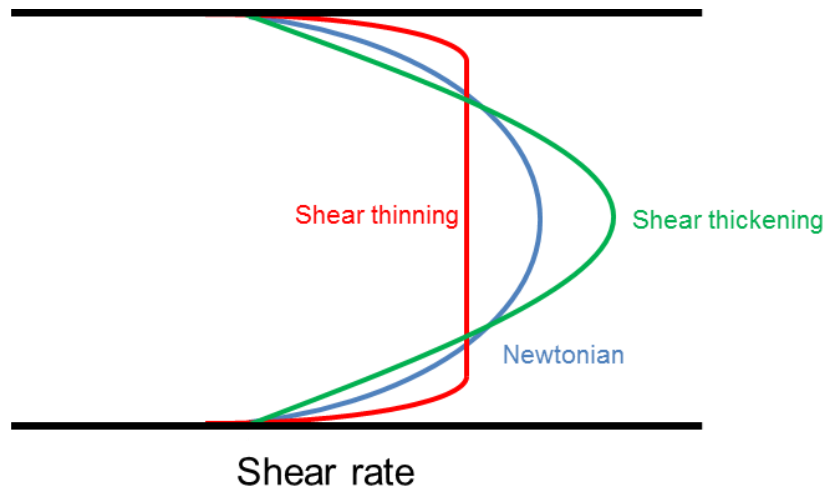


Figure 2.6- Pipe flow velocity profiles of Newtonian ( $n=1$  in blue), shear thinning ( $n<1$  in red) and shear thickening fluids ( $n>1$  in green)

Figure 2.6 shows the velocity profiles of Newtonian, shear thinning and shear thickening materials flowing through a pipe. When flowing, a material will travel such that energy dissipation is minimised [2]. Shear thinning materials therefore shear rapidly towards the walls since the large shear rate will result in a reduction in viscosity, minimising energy dissipation. On the other hand, shear thickening fluids flow so that the shear rate is minimised. Their velocity profiles are therefore more pointed than those for shear thinning materials.

### 2.2.3.6 Péclet Number

The Péclet number (detailed in [Chapter 1](#)) can also be used to estimate how much shear is likely to be required to disturb the structure of a colloidal system [5]. In this case, the Péclet number can be thought of as a ratio of two time scales: one related to diffusion and one related to the shear rate [5, 6]. It therefore expresses the relative importance of Brownian motion and shear [5].

For diffusion, the diffusion/ Brownian time ( $\tau_D$ ) detailed in [Chapter 1](#) can be used. It is the average time needed for a particle to diffuse its own radius [6]:

$$\tau_D = \frac{a^2}{6D} = \frac{\pi\eta a^3}{k_B T} \quad \text{Equation 2.8}$$

Here D is the diffusion coefficient,  $k_B$  is the Boltzmann Constant, T is the absolute temperature,  $\eta$  is the solvent viscosity and a is the particle radius.

The time scale for the shear rate ( $\tau_s$ ) can simply be defined as the inverse of the shear rate:

$$\tau_s = \frac{1}{\dot{\gamma}} \quad \text{Equation 2.9}$$

Therefore the shear Péclet number can be defined as [6]:

$$Pe = \frac{\tau_D}{\tau_s} = \frac{\pi\eta a^3 \dot{\gamma}}{k_B T} \quad \text{Equation 2.10}$$

When the shear Péclet number is small (<1), the time scale associated with diffusion is smaller than the time scale associated with shear/flow. Brownian motion will therefore be the dominant force for rearranging particles [7]. When the Péclet number is large (>1), shear will be able to rearrange particles and modify the structure and Brownian motion will be insufficient to influence this. Therefore to view shear induced behaviour, shear Péclet numbers greater than 1 should be used so that diffusion is insufficient to equilibrate the system [5, 6].

An estimation of the shear Péclet number for the shear rates encountered experimentally in this thesis suggested a Péclet number greater than 1. This suggested the effects of shear were significantly more influential than Brownian motion. For the range of shear rates encountered in the experiments in [Chapter 4](#) and [Chapter 5](#) ( $\sim 10\text{s}^{-1}$  to  $\sim 200\text{s}^{-1}$ ), the Péclet number varied from 2 to 40.

## 2.3 General Rheology of Concentrated Suspensions

Colloidal suspensions show a variety of complex non-Newtonian behaviour. The most distinctive feature of the rheology of concentrated colloidal suspensions is that an individual sample can show Newtonian, shear thinning or shear thickening behaviour, depending on the applied stress or shear rate. This is due to changes in the microstructure of the system, as shown in Figure 2.7.

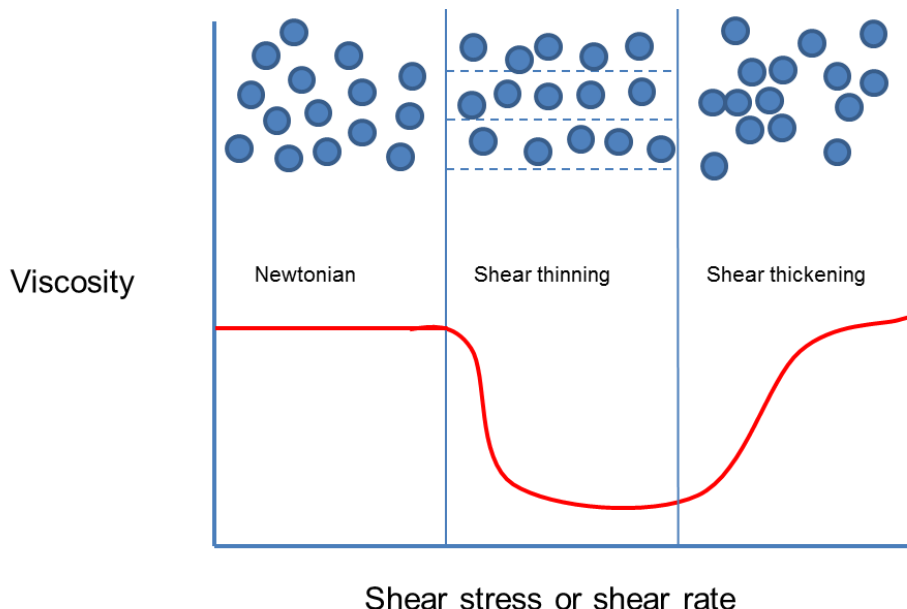


Figure 2.7- Colloid behaviour and microstructure as function of shear stress or shear rate [8]

Under suitably low shear rates, concentrated colloidal suspensions generally exhibit a constant viscosity and therefore behave as a Newtonian fluid. In some low shear cases, particle ordering may occur, with particles arranging in layers to comply with the flow (as illustrated in Figure 2.7). This results in shear thinning behaviour since less energy is dissipated through particle interactions [9-12].

Under higher stresses or shear rates, however, concentrated colloidal suspensions may exhibit shear thickening behaviour. This shear thickening behaviour, which may be continuous or discontinuous, is discussed in detail in section 2.4.

It is worth noting that at even higher shear rates and stresses, it is possible for some suspensions to undergo a change from shear thickening to shear thinning behaviour. This is typically due to deformation of particles within the system [13].

## 2.4 Shear Thickening and Jamming

In this section, shear thickening and flow induced jamming are discussed. These are thought to be closely related and are highly relevant to the work done in this thesis.

### 2.4.1 Overview

As detailed in 2.2, shear thickening is a type of non-Newtonian behaviour that is characterised by the viscosity of a substance increasing with shear stress/rate. Two main types of shear thickening exist: continuous and discontinuous [14, 15]. With continuous shear thickening, the increase in viscosity with shear rate is relatively gradual. On the other hand, discontinuous –or extreme- shear thickening (DST) is characterised by a dramatic increase in viscosity above a certain threshold of stress [14]. This is thought to be closely related to flow induced jamming, which can be defined as the conversion of a liquid system into a solid by imposed stress [11, 16-20]. Most shear thickening suspensions are immediately reversible upon flow cessation; once the stress is removed, the suspension relaxes and flows like a liquid [13, 14].

Although work has been done on the area, there is still considerable disagreement about the possible mechanisms of shear thickening [14]. The nature of shear thickening depends on a range of parameters of both the suspended and suspending phase. Particle volume fraction is particularly important and behaviour is also dependent on parameters such as particle size, particle shape, polydispersity, particle and fluid properties, interparticle forces, system geometry and details of the deformation (e.g. type of shear, time and rate of deformation) [8, 9, 16, 21]. In general, shear thickening occurs more readily (i.e. at a lower shear rate) with increasing particle size, particle roughness, medium viscosity and particle concentration and reduced particle polydispersity [13, 22].

#### Examples and Applications

Despite shear thickening typically receiving less interest than its shear thinning counterpart, shear thickening has been observed across a very wide range of colloidal and non-colloidal suspensions [14]. These include polymers, metals or oxides suspended in liquid (particularly when concentrated), inks, polymeric binders for paints, pastes, slurries, clay and blood. Such materials are frequently encountered in the oil and gas (e.g. drilling fluids, muds and slurries),

pharmaceutical (e.g. powders) and food processing industries. The complex behaviour of these materials has even been suggested to be related to earthquakes, volcanic eruptions, and landslides in geology, erratic unpredictable flow in biology (e.g. blood clots and strokes) and human stampedes [23-25].

Perhaps the most common example of a shear thickening material is a concentrated suspension of cornflour and water. It is referred to as a discontinuous shear thickener because of its apparent discontinuous jump in viscosity with increasing shear rate; above a certain volume fraction, at very low shears it acts like a liquid but at higher shear rates, its resistance to flow increases dramatically and it exhibits solid-like properties [14].

Materials that exhibit shear thickening behaviour, such as concentrated suspensions, can lead to processing problems in industry due to their complicated behaviour and the fact that they are not well understood. Transporting the materials is complex. For example, the transformation of the flow to a solid state can cause the flow to unexpectedly stop. The flow may then start up again, and this jamming cycle may repeat, leading to erratic flow patterns, density waves and a fluctuating viscosity. Pattern formation and particle segregation may also occur during the transport of shear thickening materials. This complicated flow is not well understood, but is thought to be caused by the way in which forces are transmitted through the materials [16]. Such materials may also jam when extruded through small openings and can lead to the breaking and blockage of process equipment (e.g. mixers and pumps) [14]. Pipe fouling and spraying applications are also particularly troublesome [8].

As a few examples, in oil and gas, an increase in the concentration of suspended hydrated particles in flows through pipelines is a major issue and prevents the flow from behaving like a liquid, resulting in clogging [26, 27]. In other industries, blockages and jamming of powdered and granular materials in silos can result in production lines needing to stop temporarily [27, 28]. It is therefore clear that these shear thickening and jamming materials can have a significant detrimental impact in industry.

Shear thickening materials do, however, have a range of useful applications. Their special property of increasing energy dissipation with shear makes them particularly useful for damping and shock absorption applications. For example, studies have

shown that shear thickening fluids could be used alongside Kevlar to produce enhanced protective clothing. These clothes could be flexible at rest, allowing freedom of movement, but could become more rigid in response to an impact [8, 14]. Studies suggest that a system containing Kevlar formulated with shear thickening colloids would require 1.5-2.5 times the impact velocity of Kevlar alone to penetrate the material [8].

Shear thickening fluids could prove useful for applications in the oil and gas industry. For example, they could be used to protect wells from blowouts (uncontrolled releases of crude oil and/or natural gas from wells), which can cause major equipment damage and result in fatalities. Blowouts typically occur when a drill reaches a gas pocket and it has been proposed that using drilling fluids with shear thickening properties could minimise damage. The increase in pressure during the blowout, particularly around the blowout area, would result in the fluid thickening and effectively patching the blowout [24].

In recent years, there has been renewed interest in shear thickening materials by connecting shear thickening systems to other soft-matter and granular systems through the universal concept of 'jamming' [14]. Due to their complexities and potential applications, gaining a better understanding of how shear thickening and jamming materials behave, particularly under flow, is of interest.

## 2.4.2 Continuous and Discontinuous Shear Thickening

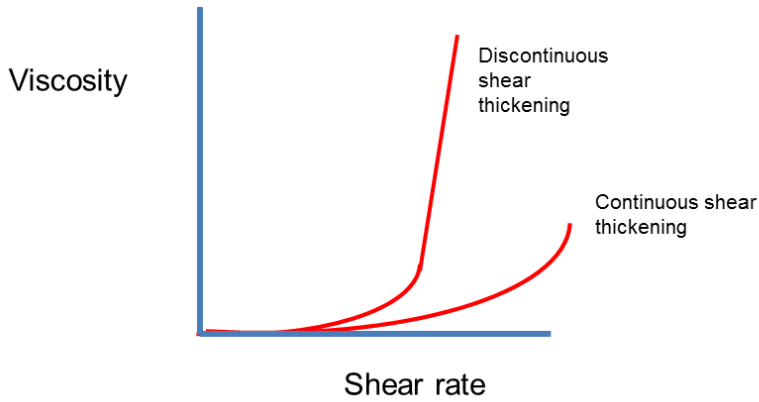


**Figure 2.8- Comparison between continuous and discontinuous shear thickening**

### i) Continuous

With continuous shear thickening, the increase in viscosity with shear rate is relatively gradual (Figure 2.8), the extent of which depends on the volume fraction of particles. Shear thickening generally is not observed in dilute suspensions. At volume fractions between 0.3 and 0.4, shear thickening begins to appear in suspensions of solid spheres [8, 14]. At these intermediate volume fractions, the increase in viscosity with shear rate is relatively low but becomes increasingly larger with increased volume fraction. Typically, the shear thickening regime begins at a critical minimum shear stress,  $\tau_{\min}$ , (that is thought to be ~independent of volume fraction) [14]. Below this stress, Newtonian or shear thinning behaviour may be found depending on the material [8].

As mentioned, shear thickening (continuous and discontinuous) occurs more readily (i.e. at a lower shear rate and shear stress) with increasing particle size [13]. It has been found that the maximum particle size that shear thickening can occur at is ~1mm diameter [20]. The optimal size, where shear thickening occurs most readily, is thought to be ~10 $\mu\text{m}$  diameter. Here the largest stress range for the shear thickening regime can be found and the shear stress required for shear thickening is at its minimum [14]. This particle size is similar to cornflour [20]. The optimal region corresponds to the colloid /granular transition, where the dominance of Brownian motion in the colloidal regime switches to the dominance of gravity and friction in the granular regime [14].

## ii) Discontinuous

In some cases, particularly at higher volume fractions and stresses, the viscosity increase with shear rate becomes significantly steeper. Eventually, there becomes a point where the viscosity and shear stress jump discontinuously by several orders of magnitude beyond a certain shear rate (Figure 2.8). Therefore increasing volume fraction can cause continuous shear thickening to change to discontinuous shear thickening. Examples of materials that display DST include cornflour and water suspensions (as mentioned) and concentrated hard particle suspensions (e.g. hard spheres in a solvent) [8, 13, 14, 19, 20, 29, 30].

As with continuous shear thickening, DST becomes apparent at a critical minimum shear stress ( $\tau_{\min}$ ). This regime ends at a maximum shear stress ( $\tau_{\max}$ ), beyond which shear thinning, cracking, granulation and suspension break-up become apparent [14, 31]. As volume fraction is increased, the onset of shear thickening is shifted to lower shear rates and the degree of shear thickening increases [8].

DST is typically only observed over a small range of volume fractions in concentrated colloidal suspensions. This is typically around  $\phi=0.6$  for concentrated suspensions, but has been observed at lower volume fractions ( $\sim\phi=0.5$ ) [13, 14, 17, 32]. In more granular media, DST had been observed at lower volume fractions, for example DST in cornflour suspensions has been reported in volume fractions as low as 0.3 [33].

DST is associated with large fluctuations in stress and viscosity [14]. When discontinuous shear thickening occurs, increasing the power to a rheometer, for example, leads to such a dramatic increase in viscosity and fluctuations in stress that the suspension either refuses to flow any faster (i.e. a limiting shear rate is reached) or it solidifies [8].

## iii) Distinguishing between Continuous and Discontinuous

Although perhaps obvious experimentally, a practical way of distinguishing between the different types of shear thickening behaviour is to fit a power law  $\tau \propto \dot{\gamma}^\alpha$  to the data and determine the exponent. If Newtonian,  $\alpha=1$ . If continuous,  $1 < \alpha \leq 2$ . If discontinuous,  $\alpha > 2$ .  $\alpha$  increases with increasing volume fraction [14].

## 2.4.3 Shear Thickening Mechanisms

Although much work has been done on the area, there is still considerable disagreement about the possible mechanisms of shear thickening. Three main mechanisms have been proposed yet none have been able to fully explain shear thickening behaviour.

### 2.4.3.1 Order-Disorder Transition

The order-disorder transition mechanism was proposed by Hoffman in the 1970s. His pioneering work used light scattering equipment to probe the underlying microstructural transitions that occurred during shear thickening in concentrated latex suspensions. This resulted in his proposal of a model for shear thickening based on a flow induced order-disorder transition [8, 29, 30].

With the order-disorder mechanism, the flow microstructure changes from ordered layers at lower shear rates, to a disordered structure at higher shear rates. This results in increased drag forces between particles, resulting in increased energy dissipation [13, 14, 29, 30]. Hoffman suggested that a flow instability (controlled by a balance between the stabilising forces of repulsion between particles and hydrodynamic forces) caused the particles to break out of their ordered layers at some critical level of shear, causing them to jam into one another, thereby causing the rise in viscosity [30].

The model has been shown to successfully predict the onset shear rate for shear thickening, however, it has been shown that shear thickening can occur without an order-disorder transition. Therefore, although an order-disorder microstructure transition may occur alongside shear thickening in some cases, it is not a required mechanism [8, 14]. Microstructural changes are also unable to explain the large increases in viscosity seen with discontinuous shear thickening [14].

### 2.4.3.2 Hydroclustering

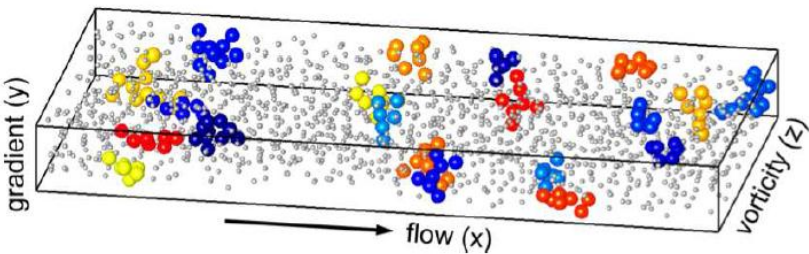


Figure 2.9- Configurations of transient clusters in the shear thickening regime [14, 34]

The development of Stokesian dynamics simulations led to the development of a fundamentally different proposed mechanism for shear thickening in the 1980s by researchers including Brady and Bossis [13, 35, 36]. This idea proposes that under shear, particles tend to be driven together into clusters (hydroclusters). These result in increased hydrodynamic interactions, resulting in increased viscosity.

The idea behind this mechanism is that shear pushes particles close together resulting in increased lubrication drag forces between particles [13, 14]. For particles to move away from each other they must overcome the large viscous drag forces from the small lubrication gap between neighbouring particles [14]. This makes it difficult for a particle to leave a cluster, particularly by diffusion. As a result, the movements of particles that are driven into close proximity remain strongly correlated and can show closed trajectories.

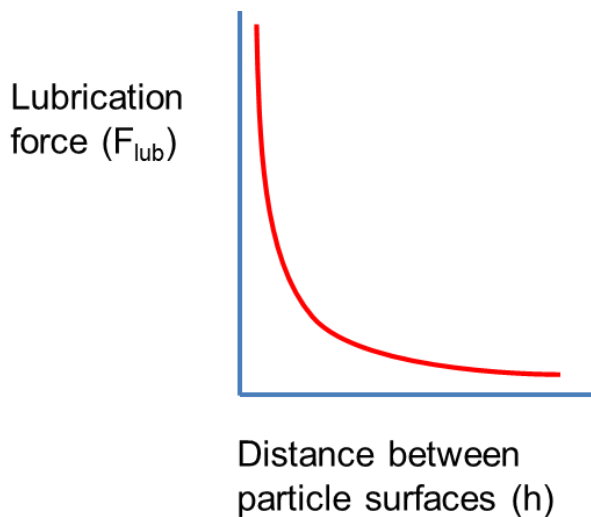


Figure 2.10- Lubrication force acting to keep particles together diverges inversely with particle surface separation

Lubrication hydrodynamics describes the behaviour of particles interacting via the suspending medium at a very close range. As two particles approach, the rising hydrodynamic pressure between them squeezes fluid from the gap. The hydrodynamic lubrication force diverges inversely with the distance between the particle surfaces (Figure 2.10) [8]. Therefore when particles are in very close contact, a large lubrication force holds them together, meaning that a large force would be required to separate them. This therefore results in hydrocluster formation since it is difficult for particles to separate [8].

Various forms of the lubrication force expression can be found in literature. Typically only the squeeze lubrication term is included (which considers motion along the line of centres) but other modes of lubrication do exist (e.g. shear, pump and twist) [37]. The Reynolds squeeze lubrication term for hard spheres which is often seen in literature is defined as [37]:

$$\mathbf{F}_{lub} = -\frac{3\pi\eta d^2}{8h_{ij}} (\mathbf{v}_i - \mathbf{v}_j) \cdot \mathbf{n}_{ij} \mathbf{n}_{ij} \quad \text{Equation 2.11}$$

Here  $\mathbf{F}_{lub}$  is the lubrication force,  $\eta$  is the solvent viscosity  $d$  is the particle diameter,  $h$  is the distance between the surfaces of particles 'i' and 'j',  $\mathbf{v}$  is the particle velocity and  $\mathbf{n}$  is the unit vector along the line between particle centres.

The presence of hydroclusters results in fluctuating stresses and increases dissipative hydrodynamic interactions; with clusters present, the microstructure is significantly different from that near equilibrium, resulting in increased energy dissipation and therefore a higher viscosity [8]. Hydrodynamic forces dominate systems at high shear rates, typically at Péclet numbers  $>1$ , as the effect of interparticle forces and Brownian motion becomes negligible [8].

These hydroclusters (Figure 2.9) are local transient fluctuations in particle density, not aggregates or coalesced particles [13]. They are more densely packed than the bulk (higher  $\phi$ ) and are anisotropic with very high stresses [13]. Hydroclusters are sustained and driven by the applied shear [8]. Upon flow cessation with hard sphere systems, samples have been shown to relax instantaneously, suggesting that hydrodynamic interactions are dominant and that hydrocluster formation is reversible [8, 13].

It has been proposed that a critical shear rate exists, above which the particles 'stick' together transiently by short-range lubrication forces, as mentioned, and they

can then grow into larger clusters. Larger clusters result in a larger effective viscosity (due to greater hydrodynamic interactions/effects) and so the critical shear rate at which hydroclusters begin to form can be viewed as the onset shear rate for shear thickening [14]. It has been proposed that as concentration and the shear rate is increased, the effective volume of hydroclusters becomes larger (more, larger clusters) and they may eventually span the system, causing discontinuous shear thickening [13, 14].

As well as through simulations, evidence for hydrocluster formation has been found experimentally. Increased turbidity has been recorded and confocal rheology measurements and measurements from light scattering equipment (such as small angle neutron scattering) have provided strong evidence [13, 14, 34, 38, 39]. For continuous shear thickening, the mechanism has produced critical shear rates/stresses and viscosities that match well with experiments. Calculations and simulations, however, have so far been unable to produce the significant increase in viscosity seen with discontinuous shear thickening through the hydroclustering mechanism. It is therefore still an open question as to whether the hydroclustering mechanism alone is viable [14]. If not applicable to DST, the hydrocluster model could still be valid for continuous shear thickening right up until the onset of discontinuous shear thickening [14].

To help explain DST, it has been suggested that at higher volume fractions and stresses, rather than lubrication hydrodynamics keeping particles in clusters together, frictional contacts between particles may instead occur. This is due to particles being driven into very close proximity and lubrication breaking down. This transition from lubrication to frictional contacts is thought to correspond to a transition from continuous to discontinuous shear thickening. In this situation, clusters may be thought of more as force transmitting hydroclusters and these may play an important role in discontinuous shear thickening, along with the idea of dilatancy, as outlined below [14, 40-42].

### 2.4.3.3 Dilatancy

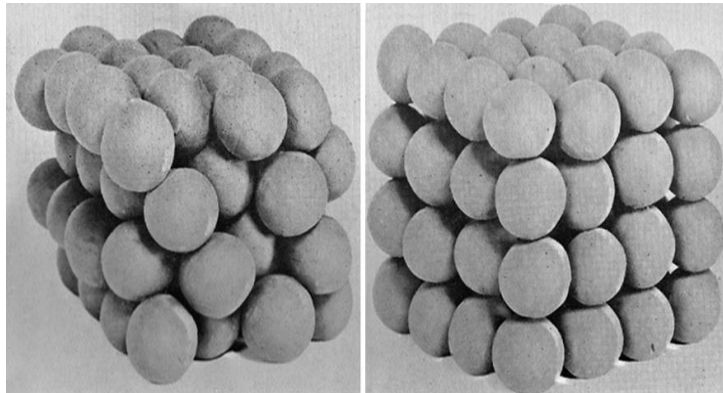


Figure 2.11- Arrangement of spheres subjected to deformation that required a volumetric expansion to shear [13, 15]

Dilatancy involves the volumetric increase/expansion of the material under shear (Figure 2.11). This allows concentrated systems to flow by effectively reducing the volume fraction, giving particles more room to move [14]. The expansion causes the material to push against the system's boundaries and this can result in additional stresses from solid-solid friction [14]. Dilatancy can be observed along with discontinuous shear thickening, and recent literature has suggested that it may play a crucial part in the discontinuous shear thickening mechanism [13, 14, 32].

The concept of dilatancy is well known with respect to granular flows [8, 43]. When sheared, particles try to go around each other, but often cannot take direct paths and their packing volume must therefore expand to allow them to flow and roll over each other [43]. This expansion leads to normal stresses being exerted [14].

In the past, dilatancy was used as a synonym for shear thickening, with shear thickening materials often being referred to as 'dilatants' [14]. This, however, came out of practice when a study confirmed that volumetric dilatancy (i.e. expansion under shear) can occur quite separately from rheological dilatancy (i.e. shear thickening) [44]. Therefore while the onset of dilatancy and shear thickening are often found to coincide, dilatancy can occur without shear thickening [13, 14, 44]. Since it was clear that dilatancy and shear thickening did not have a simple correspondence, it was concluded that dilatancy should not be directly thought of as related to shear thickening [14].

This viewpoint has, however, changed in recent years, with a different interpretation of these earlier findings and new studies being considered [14, 45]. This suggests that dilatancy can occur without shear thickening, but shear thickening cannot occur

without dilatancy [20]. This has resulted in ideas suggesting that dilation can help explain discontinuous shear thickening: what the other models have been unable to explain. Work suggests that dilation is necessary, but not sufficient, for discontinuous shear thickening. It is thought that for the large increases in viscosity seen with discontinuous shear thickening, frustrated dilatancy against a stiff boundary is required.

Dilation in concentrated suspensions (e.g. colloidal) is thought to be similar to that in granulars [14]. When dilation is frustrated by boundary conditions that confine the suspension (e.g. surface tension at a liquid–air interface, the stiffness of walls surrounding the system, or the particle stiffness [20]), shear results in normal stresses against the boundaries being measured that correspond to the material being pushed against the boundary as it attempts to expand. Confinement provides equal and opposite restoring confining stresses (from Newton's 3<sup>rd</sup> law), and these can be transmitted along solid-solid frictional contacts between neighbouring particles that form part of a network of force chains or force transmitting clusters (these networks may arise due to hydroclusters with frictional contacts growing in size and eventually spanning the system- see 2.4.3.2) [13, 14, 46].

These frictional contacts are therefore able to produce shear stresses that are proportional to the normal stresses, resulting in coupling of the shear and normal stress. This allows the dramatic increases in shear stress with shear rate, that are associated with discontinuous shear thickening, to be achieved [14, 20].

### Boundaries and Confinement

In a system where the boundaries are not fixed/frustrated (e.g. the flow geometry can expand), no shear thickening behaviour may be observed [14]. This suggests that DST is not a bulk property of a fluid and depends very much on system boundaries and confinement, as outlined below [14].

The growth and evolution of this frictional contact network has not yet been confirmed via direct experiments on concentrated suspensions. There have, however, been many observations of its consequences, particularly concerning the dilation of concentrated suspensions during DST [8, 14, 31, 32, 47]. This has led to an awareness of the importance of the role of confining capillary stresses at boundaries (i.e. the air-suspension interface) [14, 31].

When dilating, a material can typically dilate most successfully out of an open surface since it is the place where additional volume can most readily be obtained [14]. In wet systems (e.g. a concentrated suspension) this causes particles to encounter and deform the air-liquid interface. This generates a large confining capillary stress at the surface (which depends on the particle size and suspending medium surface tension). If particles are between 1-100 microns in diameter, the surface appears drier, rougher and more opaque than the rest of the sample (i.e. it changes from glossy to matt). This is because partially exposed particles at the surface scatter light diffusely [14]. The confining capillary stress pushes surface penetrating particles towards the sample interior. The fact that the particles continue to penetrate the surface, as observed during DST, means forces must be transmitted all the way through the material via force chains/clusters to balance this [20]. The surface capillary stress can therefore be considered a confining stress which is transmitted and redirected through the suspension [20].

For dilating concentrated suspensions, the confining capillary stress ( $\tau_{capillary}$ ) is much larger than that of a Newtonian liquid. The capillary stress is typically defined as the liquid surface tension ( $\gamma$ ) divided by the radius of curvature of the interface ( $r$ ):

$$\tau_{capillary} = \frac{\gamma}{r} \quad \text{Equation 2.12}$$

Since the interface is deformed by particles with dilating concentrated suspensions, the radius of curvature is reduced to the particle diameter ( $d$ ):

$$\tau_{capillary} = \frac{\gamma}{d} \quad \text{Equation 2.13}$$

This results in much larger confining stresses [13, 14].

The confining capillary stress is typically the weakest confining stress in the system (i.e. compared to the solid system boundaries or particle stiffness) [14, 20]. It therefore determines the maximum shear stress at which shear thickening can occur [14]. In systems without any air-suspension interface, the stiffness of the particles or solid boundary wall is likely the weakest confining stress [20]. Above the weakest confining stress (or maximum shear stress at which shear thickening can occur), shear thinning, cracking, granulation and suspension break-up becomes apparent [14, 31].

Concentrated suspension systems with no open surface may or may not discontinuously shear thicken. With soft system boundaries, although the material

must dilate under shear to flow, the soft system boundaries are likely unable to provide sufficient confinement to frustrate dilation and discontinuous shear thickening is therefore unlikely [14]. If the walls are hard, complete jamming would be expected as there would be no dilation since the hard walls would be able to completely frustrate dilatancy, resulting in extremely large confining stresses [14]. The material could therefore not flow, unless the walls gave way or the particles could deform. Further compression would increase the confining stress further [14].

In an open system with a suspension-air interface, the capillary confining stress is limited by  $\tau_{capillary} = \frac{\gamma}{d}$  and further applied forces could result in this being exceeded [14]. These examples highlight the importance of dilation and the fact that the dilation must be frustrated by some form of confining boundary to produce discontinuous shear thickening [14].

The frustrated dilatancy mechanism has been able to accurately predict the minimum and maximum shear stresses of the shear thickening regime. It has also been able to explain normal force measurements made in discontinuous shear thickening and the dependence of boundary conditions and confinement. It has, however, so far been unable to quantitatively predict the slope of viscosity curves [14].

#### **2.4.3.4 Review of Proposed Mechanisms**

Frustrated dilatancy appears to be essential to explain discontinuous shear thickening. Hydroclusters alone, as mentioned, are insufficient to explain the large stresses measured during discontinuous shear thickening. They are also unable to explain the strong coupling between shear and normal stresses and the strong dependence on boundary conditions and confinement seen with DST. These, however, can be explained more clearly through (frustrated) dilatancy and frictional contacts between particles [14]. As mentioned in 2.4.3.2, the hydrocluster mechanism could still be valid for continuous shear thickening, right up until the onset of discontinuous shear thickening.

#### 2.4.4 Non Shear Thickening Materials

Although possible mechanisms for shear thickening are based on generic phenomena, such as dilatancy, friction and lubrication forces, not all concentrated suspensions are reported to shear thicken [14]. This can partly be explained by the relative importance of different stresses. Shear thickening behaviour may only become apparent when stresses from shear thickening mechanisms dominate [14].

For example, shear thickening may appear hidden by a yield stress or shear thinning behaviour [14]. In such cases, no shear thickening will occur if the minimum stress required for shear thickening exceeds the maximum stress where shear thickening can occur [14]. In such a case, the stress scale of particle interactions exceeds the stresses that cause shear thickening so shear thickening cannot occur. This situation is thought to be quite common. Discontinuous shear thickening also only occurs readily over a small range of particle sizes and volume fractions, as mentioned [14].

Dry hard particles in an open container are known not to shear thicken. Although they dilate under shear, the free surface does not provide any confining force. Shear thickening can only be found in such a system when it is completely confined by solid walls (i.e. a closed system). Wet particles on the other hand would shear thicken in an open container. This shows that the surface tension of the liquid provides a confining stress and that confinement is essential for discontinuous shear thickening [14].

Discontinuous shear thickening is not found in emulsions, foams and suspensions of deformable particles; they often show shear thinning behaviour, even when confined. These soft particles can easily deform to shear past each other. This means that, even when concentrated, they do not need to dilate to flow [14]. As a result, they can shear without pressing hard against the boundaries, meaning confining stresses are very low and shear thickening is highly unlikely [14].

## 2.4.5 Shear/ Flow Induced Jamming

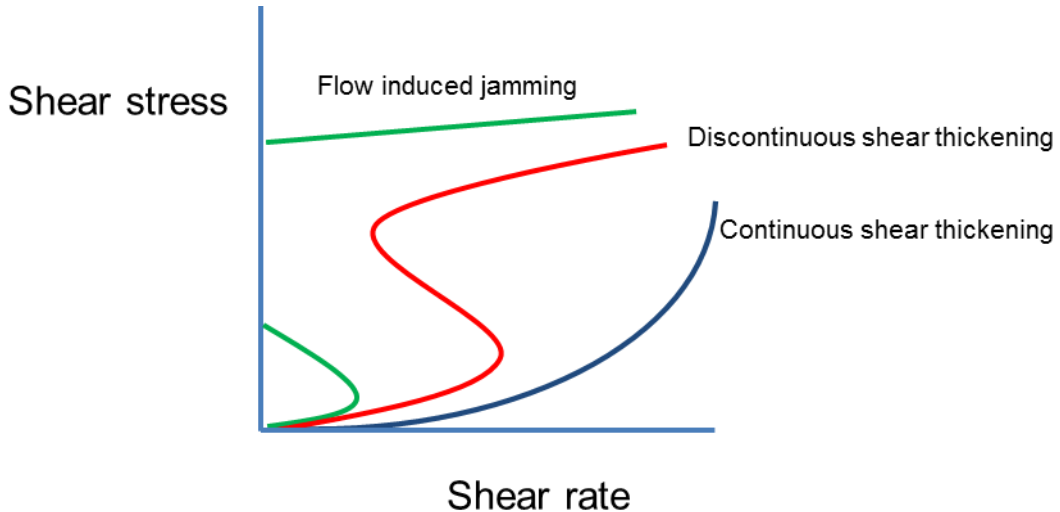


**Figure 2.12- Example flow curves for different regimes. Continuous shear thickening=blue; discontinuous shear thickening=red; flow induced jamming=green [31]**

In literature, there are various definitions of ‘jamming’, so it is important to understand which type is being referred to [46]. The jamming transition mentioned in 2.4.6 refers to systems where the particle concentration becomes sufficiently high (beyond a critical value) that a structurally disordered amorphous solid with a yield stress forms [13, 46, 48]. In this case jamming occurs due to the volume fraction being sufficiently high, and this definition of jamming is regularly encountered in literature [46].

In this thesis, however, an alternative definition of jamming that is regularly encountered in literature is used [46]. Here jamming refers to a set of conditions where, despite applying a stress to a fluid, no flow will occur. At stresses above and below this region, the material will flow. In this case, jamming is caused by an applied stress and can be defined as the conversion of a liquid system into a solid by imposed stress [11, 16-20]. This is referred to as flow induced jamming or shear induced jamming.

Discontinuous shear thickening is thought to be closely related to flow induced jamming, as mentioned [11, 16-20]. Jamming refers to a system that is fluid at rest but jams beyond a critical shear stress/rate. When jammed, the material is fully arrested with no flow (i.e. a zero shear rate). It remains jammed until another critical stress is reached, above which it unjams [31]. This is similar to DST, since DST occurs between a minimum and maximum stress. With DST, however, the shear

rate has a non-zero value when able to dilate [8, 19]. Typical flow curves for continuous shear thickening, discontinuous shear thickening and jamming are shown in Figure 2.12.

It is possible that the fully jammed state therefore simply occurs in DST systems that are unable to dilate. Dilation allows systems to continue flowing by reducing the overall volume fraction. If dilation is not possible (i.e shear forces cannot overcome confining stresses from the boundaries), the material would undergo a complete jamming transition since the volume fraction could not be reduced [45]. If a material is able to dilate, it may be sheared without completely jamming [45].

Flow induced jamming may therefore be viewed as DST where flows becomes fully arrested due to being unable to successfully dilate, for example in a closed system with no suspension-air interface and very hard walls and particles. This idea is similar to that suggested by Cates who says that jamming can be viewed as the constant volume counterpart of dilatancy [18].

## 2.4.6 Jamming Transition

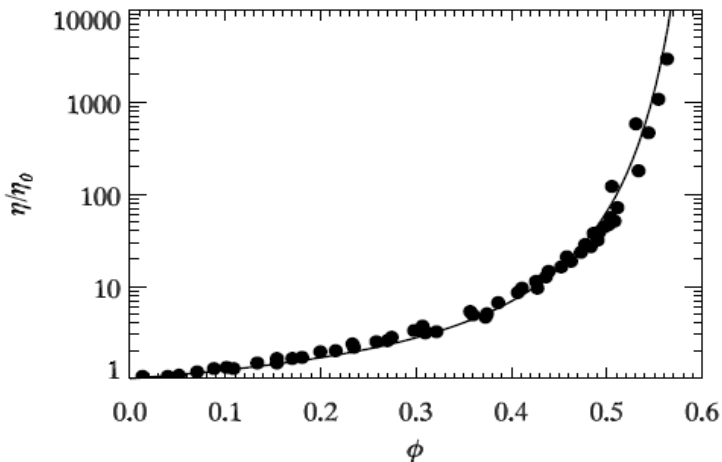


Figure 2.13- Relative viscosity as a function of volume fraction for monodisperse hard spheres [6]

As mentioned in 2.4.5, another definition of jamming found in literature is related to the effect of increasing the volume fraction [14]. This definition of jamming refers to systems where the particle concentration becomes sufficiently high (beyond a critical value) that a structurally disordered amorphous glassy solid with a yield stress forms [13, 46]. This glass has a yield stress like a solid; at stresses below the yield stress, the material will not flow [14, 19, 46].

Jamming is therefore typically characterised by the onset of a yield stress [49]. Practically, the onset of jamming is measured as the packing fraction where the largest increase in the yield stress occurs [49]. The onset of jamming is referred to as the jamming transition.

Studies have proposed that this jamming transition can be thought of as similar to the glass transition seen in glass forming liquids [6, 46]. Here decreasing the temperature (or increasing the pressure) of a liquid can cause it to become kinetically arrested while retaining its liquid-like structure [6, 46].

For the jamming transition, as  $\phi$  approaches a critical value, the viscosity diverges (Figure 2.13) [14]. In colloids, this critical volume fraction is thought to be around  $\phi_c=0.58$  for spherical particles [6, 49]. This is in the region of the colloidal glass transition, detailed in Chapter 1. Here at volume fractions between  $\phi=0.58$  and  $\phi_{RCP} \sim 0.64$ , a glassy region exists. The material retains an amorphous liquid-like structure, but all microscopic dynamics slow down significantly, rendering it

kinetically frozen; particles are thought to be ‘caged-in’ (or jammed) by neighbours [6, 50, 51].

For spherical particles, the development of a yield stress (i.e. the material undergoing the jamming transition) has been observed at volume fractions as low as  $\phi=0.56$  [49]. In some cases, however, it has been reported that, despite being at the glass transition volume fraction ( $\phi=0.58$  for spherical particles), the glass may not have a yield stress. In this case a volume fraction greater than 0.58 is required for the jamming transition to occur. This suggests that the glass transition and jamming transition are not the same, despite some literature suggesting this [46].

The critical volume fraction at which the jamming transition occurs can vary with factors such as particle shape and a number of other suspension properties such as polydispersity [14, 49]. For example, rods with an aspect ratio of 9 have a critical volume fraction of  $\phi_c =0.35$  [49]. This is thought to be due to rods being able to entangle with one another, similarly to entangled polymers [46].

As detailed in [Chapter 1](#), studies suggest that the proximity of the volume fraction to the critical jamming packing fraction of a suspension generally controls the slope/strength of the shear thickening regime; therefore the extent of shear thickening depends on the proximity to the jamming transition [14]. This suggests some form of relationship exists between the jamming transition mentioned here and discontinuous shear thickening and flow induced jamming.

## 2.4.7 Jamming Phase Diagram

It has been suggested that jamming systems can be described by means of a phase or state diagram in three dimensions [52, 53]. This is more pertinent to the type of jamming described in 2.4.6 associated with increasing volume fraction, rather than flow induced jamming described in 2.4.5 [46].

### i) Original Phase Diagram

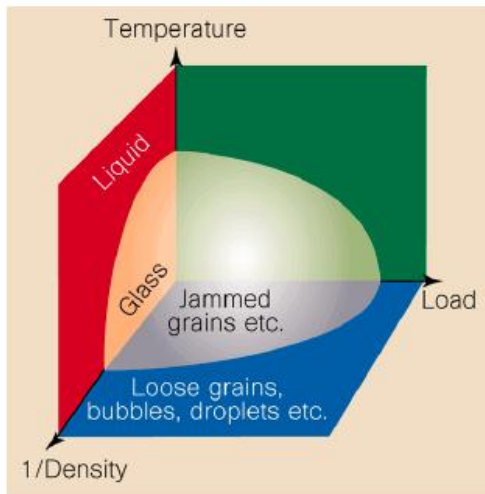


Figure 2.14- Liu's proposed jamming phase diagram [53]

The idea that jamming could be represented by a phase diagram was proposed by Liu in the 1990s [53]. From Figure 2.14, along the axes are the inverse of density (inverse volume fraction), temperature and applied load. In theory, increases in any of these parameters could transform/unjam a solid-like state into a fluid. Within the curved surface in Figure 2.14, the material is in a jammed state.

The plane formed by temperature and 1/density represents the regular glass transition for glass forming liquids, where the inverse of density represents the inverse of pressure [46]. At high temperatures or low pressures, the material will exist as a liquid. By lowering the temperature or increasing the pressure a glass will form. The applied load axis represents the idea that if the load is above the yield stress of the jammed material (e.g. colloidal or granular), the material will unjam and flow [46].

The diagram is able to represent key facts about the systems. For example, a jammed colloidal suspension or granular media may be unjammed by reducing the

volume fraction/density or increasing/inducing an applied force [21, 54]. These systems could be described as athermal since thermal energy alone is insufficient to unjam the material [54]. Increasing the temperature of a thermally arrested glass can similarly result in the glass unjamming to a molecular liquid state, as mentioned [21]. Such a system could be described as thermal [54].

From the phase diagram, all jammed states are formed by crossing the jamming transition surface. The continuity of the surface implies that there is a universal jamming transition and a universal jammed state, with perhaps differences that vary smoothly as a function of the axis parameters [46]. This original phase diagram does, however, have faults and this has led to the development of revised phase diagrams [46].

## ii) Revised Phase Diagram

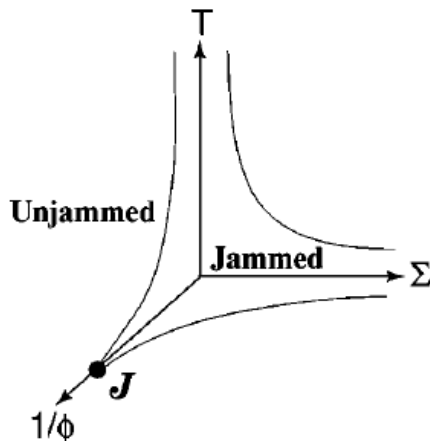


Figure 2.15- Revised phase diagram [55]

The phase diagram in Figure 2.14 has generally been replaced by a revised phase diagram, shown in Figure 2.15. The three axes are similar: temperature, inverse volume fraction (instead of inverse density), and applied stress  $\Sigma$  (instead of load). The main differences are the curvature and the addition of point J [55].

The curvature has been changed to show the idea that a material will remain in a jammed state if the density is sufficiently high, even if the temperature is increased dramatically. It also shows that a material will remain jammed at a very high applied stress if the temperature is sufficiently low and the density is sufficiently high [46].

Point J reflects the fact that below a certain volume fraction, likely that of random loose packing, particles no longer touch each other and therefore the system cannot be jammed at all [46].

## 2.4.8 Unjamming and Controlling Shear Thickening

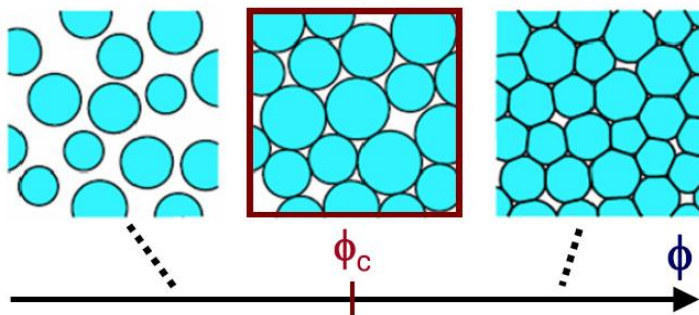


Figure 2.16- Effect of volume fraction on jamming. Left=unjammed; centre=at jamming transition where particles only just touching; right=jammed [56]

Due to the problems shear thickening and jamming can cause in industry, ways of controlling them are of interest. Means to prevent shear thickening in the first place are of interest and so are ways to unjam (transform from solid to liquid behaviour) the material when jammed.

Strategies often involve modifying systems so that they operate out with conditions where shear thickening and jamming occur (e.g. lower volume fractions (Figure 2.16) and lower flow rates) [8].

Changing the applied forces may also be used to unjam materials. Jammed materials can be classed as fragile matter [18]. With a fragile matter system, the system can support applied shear stresses (within some compatible load range), due to a self-organised internal structure which has evolved to support the applied load [18]. In fragile matter systems, however, slight disturbances in the applied load (e.g. a change in size, direction or an additional force) can cause significant structural rearrangements, resulting in the structure no longer being able to support the ‘incompatible’ load. This results in unjamming [18]. This can be done through shaking or vibrations for example [16, 57, 58]. Vibrations are thought to decrease the probability of force chains forming and/or break chains when they do form [58]. An example of this idea is a pile of sand. Undisturbed, it appears solid and sustains its shape despite gravity. If the pile is tilted or vibrated, however, the grains will move and the solid ‘melts’ [18, 53, 56].

If the applied stress is changed to exceed the jammed material's yield stress or exceed the maximum stress in the region where flow induced jamming occurs, the viscosity may drop (due to shear thinning or sample break-up), allowing the material to flow again [8, 19].

Under particular conditions, experiments on concentrated jamming suspensions in a converging flow geometry have shown the formation of rotating vortices in the flow pattern that lead to a 'self-lubrication' effect and unjamming. Vortices were thought to form due to force chain rotation which prevented the formation of stable force chains and transmission of pressure to the system's walls [17]. Therefore changing system geometry is an option for reducing jamming. The work done in this thesis highlights the importance of geometry and confinement considerations.

On a smaller scale, the separation between hydrocluster particles it thought to be on the order of nanometres for a typical colloidal suspension. Manipulating these nanoscale short-range forces could therefore be used to control shear thickening [8].

Modifying the particles is an option. For example, the addition of a polymer brush grafted or adsorbed onto the particles' surface can prevent particles becoming close together. Studies have shown that by tuning parameters such as polymer density, molecular weight and the solvent, shear thickening can be moved out of the desired processing conditions range. Although this technique can reduce the material's viscosity at high flow rates, it may result in an increased viscosity at lower rates [8].

Particle size, shape and polydispersity can also be considered. It is generally found that introducing polydispersity makes shear thickening more difficult and jamming less likely (higher stresses and higher volume fractions are required) [13, 46]. Similarly, reducing particle size often makes shear thickening and jamming less likely [22]. This is discussed in more detail in [Chapter 4](#) and [Chapter 5](#). Parameters such as fluid slip, adsorbed ions, surfactants, polymers and surface roughness can also significantly affect the onset of shear thickening [8]. For example, increased particle roughness has been shown to decrease the critical shear rate at which jamming occurs [10]. Roughness leads to increased anisotropy of the particles. This can make the effective volume fraction of the particles much greater than the real volume fraction. This results in jamming and shear thickening occurring at lower 'real' volume fractions [11].

### **2.4.9 Two-fluid Behaviour and Self-filtration**

It has been proposed that jamming in colloidal and granular media can both be linked with a ‘two-fluid-like’ picture [16, 57]. This idea splits the suspensions into the ‘particulate part’ (the particles) and the ‘liquid part’ (the solvent). It has been observed experimentally that for convergent flows, the volume fraction downstream from the point of jamming was lower than that upstream. This was thought to be caused by a self-filtration mechanism: the particulate part of the system jammed and therefore stopped flowing but the liquid part still continued to flow through the pores of the jammed solid. As a result, there was an increased flow rate of solvent relative to particles, resulting in a reduced downstream particle volume fraction [16].

This could also be interpreted in terms of ‘dilation’. To allow flow in response to the applied pressure drop, the region of sample just downstream from the convergence must dilate. This means that it must decrease its volume fraction by taking in more solvent. This solvent must come from somewhere and therefore it must have come from the upstream region. This would have resulted in an increased upstream volume fraction and would have led to jamming [16].

This effective phase separation (i.e. changes in the solid-liquid phase ratio) could cause problems in industry. For example with concentrated pharmaceuticals, if the liquids flow more than the particles, dosages may change during processing or even injection. Similar effects may be seen in food processing, leading to variable consistency.

## **2.5 Conclusions**

This chapter detailed important rheological theory that is relevant to the work done throughout the thesis. This included basic information about the behaviour of non-Newtonian materials.

This was followed by a significant section about the effects of flow on concentrated suspensions. This is relevant to the work done throughout this thesis. This section included information about discontinuous shear thickening and flow induced jamming, which are highly relevant to the results found experimentally in this thesis. Possible mechanisms for this behaviour were considered along with its industrial relevance and possible applications.

1. Coulson, J. and J. Richardson, *Coulson and Richardson Volume 1: Fluid Flow, Heat Transfer and Mass Transfer*. 1999.
2. Rhodes, M., *Introduction to Particle Technology*. 2008: Wiley.
3. Mackley, M., *Rheology and Processing*. 2011, Cambridge University.
4. Barnes, H., *A Handbook of Elementary Rheology*. 2000: The University of Wales Institute for Non-Newtonian Fluid Mechanics.
5. Jones, R., *Soft Condensed Matter*. 2011: Oxford.
6. Hunter, G.L. and E.R. Weeks, *The physics of the colloidal glass transition*. Reports on progress in physics. Physical Society (Great Britain), 2012. **75**(6): p. 066501.
7. Vermant, J. and M.J. Solomon, *Flow-induced structure in colloidal suspensions*. Journal of Physics-Condensed Matter, 2005. **17**(4): p. R187-R216.
8. Wagner, N.J. and J.F. Brady, *Shear thickening in colloidal dispersions*. Physics Today, 2009. **62**(10): p. 27-32.
9. Bertrand, E., J. Bibette, and V. Schmitt, *From shear thickening to shear-induced jamming*. Physical Review E, 2002. **66**(6): p. 3.
10. Lootens, D., et al., *Dilatant flow of concentrated suspensions of rough particles*. Physical Review Letters, 2005. **95**(26): p. 4.
11. Hebraud, P. and D. Lootens, *Concentrated suspensions under flow: Shear-thickening and jamming*. Modern Physics Letters B, 2005. **19**(13-14): p. 613-624.
12. Ianni, F., et al., *Relaxation of jammed colloidal suspensions after shear cessation*. Physical Review E, 2006. **74**(1): p. 6.
13. Mewis, J. and N. Wagner, *Colloidal Suspension Rheology*. 2012: Cambridge University Press.
14. Brown, E. and H. Jaeger, *Shear thickening in concentrated suspensions: phenomenology, mechanisms, and relations to jamming*. Reports on Progress in Physics, 2013. **77**(4): p. 046602.
15. Scott Blair, G.W., *An Introduction to Industrial Rheology*. 1938.
16. Haw, M.D., *Jamming, two-fluid behavior, and "self-filtration" in concentrated particulate suspensions*. Physical Review Letters, 2004. **92**(18).
17. Campbell, A.I. and M.D. Haw, *Jamming and unjamming of concentrated colloidal dispersions in channel flows*. Soft Matter, 2010. **6**(19): p. 4688-4693.
18. Cates, M.E., et al., *Jamming, force chains, and fragile matter*. Physical Review Letters, 1998. **81**(9): p. 1841-1844.
19. Brown, E. and H.M. Jaeger, *Dynamic Jamming Point for Shear Thickening Suspensions*. Physical Review Letters, 2009. **103**(8): p. 4.
20. Brown, E. and H.M. Jaeger, *The role of dilation and confining stresses in shear thickening of dense suspensions*. Journal of Rheology, 2012. **56**(4): p. 875-923.
21. Kakalios, J., *Resource Letter GP-1: Granular physics or nonlinear dynamics in a sandbox*. American Journal of Physics, 2005. **73**(1).
22. Barnes, H.A., *Shear-Thickening (Dilatancy) In Suspensions Of Nonaggregating Solid Particles Dispersed In Newtonian Liquids*. Journal of Rheology, 1989. **33**(2): p. 329-366.
23. Ding, J., W. Li, and S. Shen, *Research and Applications of Shear Thickening Fluids*. 2011: Faculty of Engineering Papers Archive- University of Wollongong.
24. Hamburger, C., et al., *Development and application of a new fluid for stopping unwanted flows in and around wellbores*. Soc. Pet. Eng. AIME-Exon Production Research Co., 1983.

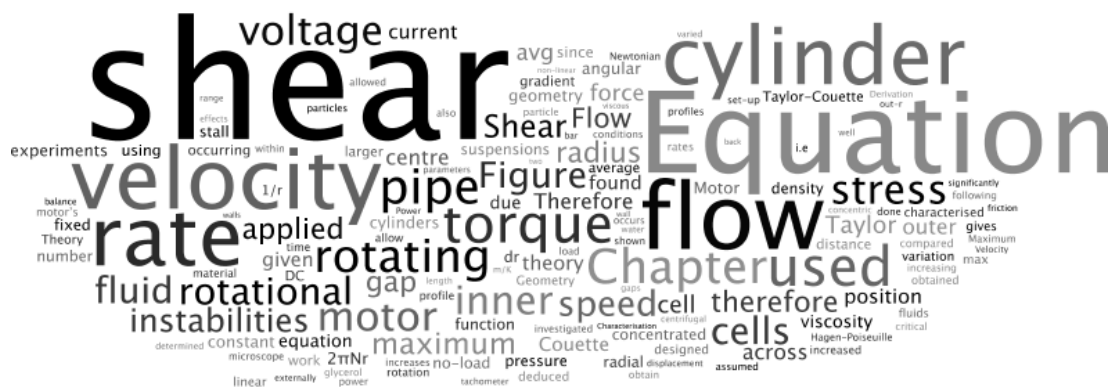
25. Zuriguel, I., et al., *Clogging transition of many-particle systems flowing through bottlenecks*. Scientific Reports, 2014. **4**: p. 8.
26. Moradpour, H., A. Chapoy, and B. Tohidi. *Transportability of particles at higher water cut systems and optimisation of anti-agglomerant concentration*. in *7th International Conference on Gas Hydrates*. 2011. Edinburgh: Heriot-Watt University.
27. Zuriguel, I., *Clogging of granular materials in bottlenecks*. Papers in Physics, 2014. **6**(060014).
28. Zuriguel, I., et al., *Jamming during the discharge of granular matter from a silo*. Physical Review E, 2005. **71**(5): p. 9.
29. Hoffman, R.L., *Discontinuous And Dilatant Viscosity Behavior In Concentrated Suspensions .1. Observation Of A Flow Instability*. Transactions of the Society of Rheology, 1972. **16**(1): p. 155-&.
30. Hoffman, R.L., *Explanations for the cause of shear thickening in concentrated colloidal suspensions*. Journal of Rheology, 1998. **42**(1): p. 111-123.
31. Cates, M.E., M.D. Haw, and C.B. Holmes, *Dilatancy, jamming, and the physics of granulation*. Journal of Physics-Condensed Matter, 2005. **17**(24): p. S2517-S2531.
32. O'Brien, V.T. and M.E. Mackay, *Stress components and shear thickening of concentrated hard sphere suspensions*. Langmuir, 2000. **16**(21): p. 7931-7938.
33. Fall, A., et al., *Shear thickening of cornstarch suspensions as a reentrant jamming transition*. Physical Review Letters, 2008. **100**(1).
34. Cheng, X., et al., *Imaging the Microscopic Structure of Shear Thinning and Thickening Colloidal Suspensions*. Science, 2011. **333**(6047): p. 1276-1279.
35. Bossis, G. and J.F. Brady, *The Rheology Of Brownian Suspensions*. Journal of Chemical Physics, 1989. **91**(3): p. 1866-1874.
36. Brady, J.F. and G. Bossis, *The Rheology Of Concentrated Suspensions Of Spheres In Simple Shear-Flow By Numerical-Simulation*. Journal of Fluid Mechanics, 1985. 155(JUN): p. 105-129..
37. Melrose, J.R. and R.C. Ball, *Continuous shear thickening transitions in model concentrated colloids - The role of interparticle forces*. Journal of Rheology, 2004. **48**(5): p. 937-960.
38. Bender, J.W. and N.J. Wagner, *Optical Measurement Of The Contributions Of Colloidal Forces To The Rheology Of Concentrated Suspensions*. Journal of Colloid and Interface Science, 1995. **172**(1): p. 171-184.
39. Bender, J. and N.J. Wagner, *Reversible shear thickening in monodisperse and bidisperse colloidal dispersions*. Journal of Rheology, 1996. **40**(5): p. 899-916.
40. Seto, R., et al., *Discontinuous Shear Thickening of Frictional Hard-Sphere Suspensions*. Physical Review Letters, 2013. **111**(21): p. 5.
41. Wyart, M. and M.E. Cates, *Discontinuous Shear Thickening without Inertia in Dense Non-Brownian Suspensions*. Physical Review Letters, 2014. **112**(9).
42. Fall, A. and F. Bertrand, *Macroscopic Discontinuous Shear Thickening vs Local Shear Jamming in Cornstarch*. Soft Condensed Matter, 2015. Under review.
43. Reynolds, O., *On the dilatancy of media composed of rigid particles*. Philosophical Magazine, 1885. **20**(127): p. 469.
44. Metzner, A.B. and M. Whitlock, *Flow Behavior Of Concentrated (Dilatant) Suspensions*. Transactions of the Society of Rheology, 1958. **2**: p. 239-253.
45. Fall, A., et al., *Shear thickening of cornstarch suspensions*. Journal of Rheology, 2012. **56**(3): p. 575-591.

46. Weeks, E., *Soft Jammed Materials*. 2007, Tokoku University Press.
47. Smith, M.I., et al., *Dilatancy in the flow and fracture of stretched colloidal suspensions*. Nature Communications, 2010. **1**: p. 5.
48. Bi, D., et al., *Jamming by shear*. Nature, 2011. **480**(7377): p. 355-358.
49. Brown, E., et al., *Shear thickening and jamming in densely packed suspensions of different particle shapes*. Physical Review E, 2011. **84**(3).
50. Poon, W.C.K., *The physics of a model colloid-polymer mixture*. Journal of Physics-Condensed Matter, 2002. **14**(33): p. R859-R880.
51. Larson, R., *The Structure and Rheology of Complex Fluids*. 1999: Oxford University Press.
52. Prasad, V., et al., *Universal features of the fluid to solid transition for attractive colloidal particles*. Faraday Discussions, 2003. **123**: p. 1-12.
53. Liu, A.J. and S.R. Nagel, *Nonlinear dynamics - Jamming is not just cool any more*. Nature, 1998. **396**(6706): p. 21-22.
54. O'Hern, C.S., et al., *Force distributions near jamming and glass transitions*. Physical Review Letters, 2001. **86**(1): p. 111-114.
55. O'Hern, C.S., et al., *Jamming at zero temperature and zero applied stress: The epitome of disorder*. Physical Review E, 2003. **68**(1).
56. van Hecke, M., *Jamming of soft particles: geometry, mechanics, scaling and isostaticity*. Journal of Physics-Condensed Matter, 2010. **22**(3).
57. Holmes, C.B., et al., *Glass transitions and shear thickening suspension rheology*. Journal of Rheology, 2005. **49**(1): p. 237-269.
58. Mankoc, C., et al., *Role of vibrations in the jamming and unjamming of grains discharging from a silo*. Physical Review E, 2009. **80**(1): p. 7.

# 3. Shear Cell Theory, Set-Up and Characterisation

## This section will cover:

- The theory, methodology and characterisation of a rotating cylinder shear cell geometry that was designed for shearing concentrated colloidal suspensions. This design of shear cell is used in [Chapter 4](#) and [Chapter 5](#).
  - The characterisation of the shear cell's motor.
  - The theory and methodology behind a capillary pipe flow shear cell that is used in [Chapter 8](#) for flowing concentrated granular suspensions.



Note: Experiments were performed at 20°C in this thesis, unless stated otherwise.

## 3.1 Summary

A main aim of the research in this thesis was to investigate the effects of flow on concentrated suspensions. An initial stage of the research involved designing and characterising suitable flow geometries for this.

The primary geometry designed was a rotating cylinder shear cell geometry to allow the effects of Couette flow to be investigated. The shear cells consisted of two concentric cylinders; for the main set-up the inner cylinder was allowed to rotate while the outer cylinder was kept fixed. Different gap sizes between the inner and outer cylinder could be achieved by changing the size of the cylinders. The shear cells were designed so that they could be placed under an optical microscope, therefore allowing samples to be viewed on a microscopic level while undergoing shear. They were also designed to allow the material to be visualised macroscopically while being sheared to allow larger scale features to be identified.

The flow within the shear cells was characterised and it was checked that flow instabilities were not occurring. The motor used in the shear cells was also characterised to allow a better understanding of the set-up.

This design of shear cell is used significantly in [Chapter 4](#) and [Chapter 5](#) where it was used to investigate the effects of flow on concentrated colloidal suspensions. It is also further characterised in [Chapter 4](#) where its input voltage is converted to a shear stress and its rotational rate is used to obtain a shear rate.

In [Chapter 8](#), the effects of pipe/capillary flow on concentrated granular suspensions are investigated. Therefore, basic theory and set-up methodology of a pipe flow geometry is given.

## 3.2 Rotating Cylinder Shear Cell Geometry

### 3.2.1 Geometry Overview

Rotating concentric cylinder shear cells (resulting in Couette flow) were designed that could readily be placed under an optical microscope for observation, therefore allowing samples to be viewed on a microscopic level while undergoing shear. They were also designed to allow the material to be visualised macroscopically while being sheared to allow larger scale features to be identified.

The shear cells consisted of two custom made concentric cylinders with a gap between them for fluid to be sheared. Two main arrangements were designed: one with a rotating inner cylinder and fixed outer cylinder (Figure 3.1 and Figure 3.2) and a second with a rotating outer cylinder and fixed inner cylinder. The rotating inner cylinder geometry was used for the majority of the work done in [Chapter 4](#) and [Chapter 5](#). Reasons for this are given in [Chapter 4](#).

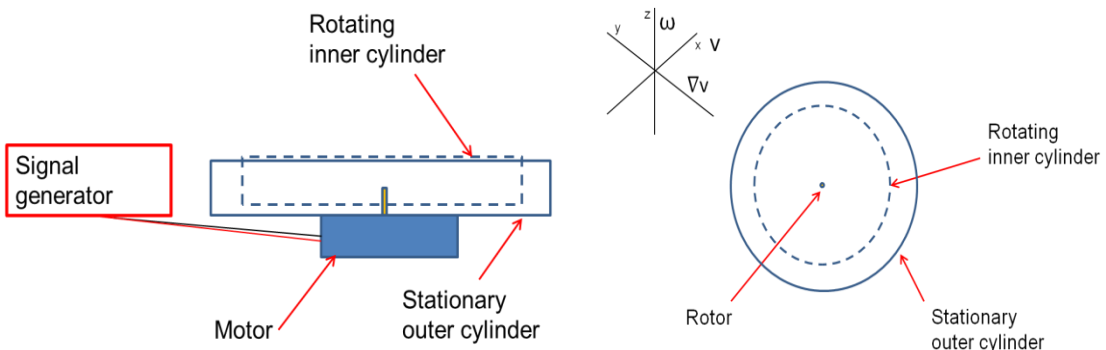


Figure 3.1 Shear cell set-up

Figure 3.2- Top view of shear cell. Velocity ( $v$ ) in  $x$  direction; velocity gradient ( $\nabla v$ ) in  $y$  direction and vorticity ( $\omega$ ) in  $z$  direction.

The rotating cylinder was mounted on a motor's shaft (GM-300C DC Micro Motor) and its movement was controlled by the voltage supplied by a signal generator (TTi TG320 Function Generator). The signal could be controlled to allow the cylinder to rotate steadily or to oscillate.

It was found that the velocity of the motor (and rotating cylinder) was proportional to the voltage supplied by the signal generator. For steady operation, increasing the voltage resulted in an increase in the rotational rate of the motor and rotating cylinder. For oscillatory operation, increasing the peak to peak voltage amplitude

resulted in larger amplitudes of oscillation, since increases in velocity resulted in larger displacements in a given time.

The diameter of the cylinders could be varied to allow different gaps between the cylinders to be achieved. The space between the rotating and stationary cylinder bases was kept as small as possible to minimise the liquid present between the bases since this could complicate flow. This space between the cylinder bases was kept fixed.

A range of fluids of varying viscosity (such as water and glycerol) were tested in the shear cells to check the performance across a range of viscosities and to characterise the shear cells' performance.

Many shear cell materials were tested for compatibility with the concentrated colloidal suspensions that were ultimately used in the shear cells. As detailed in [Chapter 4](#), the colloid particles were made from PMMA and were dispersed in the solvents decalin and tetralin. These solvents are highly corrosive and finding a suitable material was challenging. Ultimately, shear cells made from Perspex (which is PMMA) were used. These were compatible with the solvents and had good optical properties.

### 3.2.2 Geometries Used

A range of shear cell set-ups were tested for effectiveness in terms of design, ergonomics and microscope compatibility. Ultimately it was decided that the following geometries would meet the necessary requirements.

**Table 3.1- Cylinder shear cell set-up examples. Dimensions were measured using a ruler, with the errors denoting  $\pm$  half the ruler's smallest division.**

Shear Cell	Inner Cylinder Diameter [mm]	Outer Cylinder Diameter [mm]	Gap [mm]
1	25 $\pm$ 0.5	35 $\pm$ 0.5	5.0 $\pm$ 0.5
2	30 $\pm$ 0.5	35 $\pm$ 0.5	2.5 $\pm$ 0.5
3	15 $\pm$ 0.5	35 $\pm$ 0.5	10.0 $\pm$ 0.5

The available height of the outer cylinder was 10mm while the inner was 8mm, resulting in a 2mm gap between the cylinder bases. In experiments, shear cells

were typically filled to a 9mm fill height to prevent spillage. Example dimensions are shown in Figure 3.3.

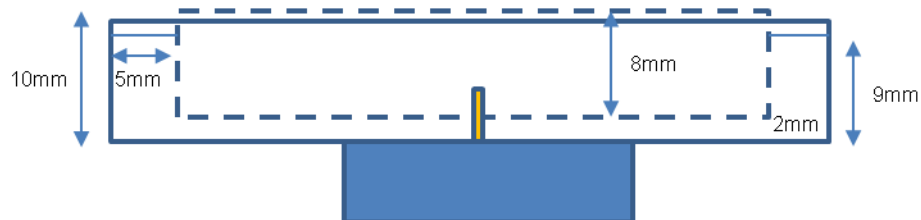


Figure 3.3- Example dimensions of 5mm gap shear cell

Shear cells with larger gaps were easiest to use; the gaps were easily imaged with the microscope (Figure 3.4) and the cells were easy to fill. Problems with the larger gaps included that the gap could not all be imaged at once under the microscope and theory for Couette flow becomes more complex for larger gaps, as subsequently detailed. With smaller gaps, images were not so clear and the shear cells were also more difficult to fill and operate. The chosen gap sizes were therefore a compromise between the two- the gaps were small enough that simple Couette theory was still applicable and the shear cells were easy to fill and image.

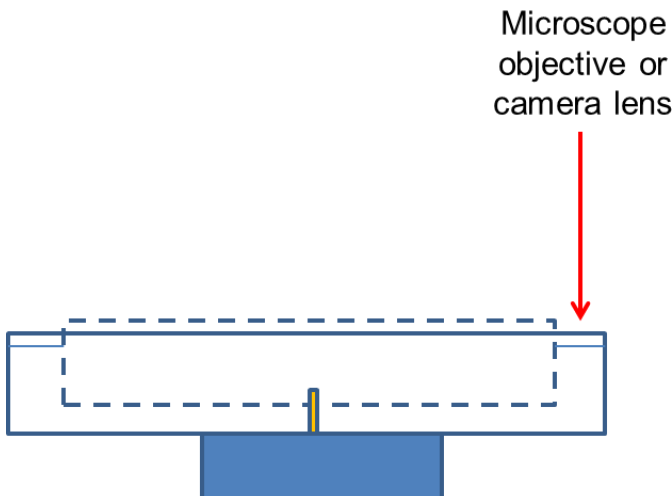


Figure 3.4- Diagram showing where images were taken from with microscope or high speed camera. Microscope objective or camera lens was placed above the gap between the cylinders.

### 3.2.3 Theory

The theory given is for the rotating inner cylinder arrangement, as was used for the majority of the work. It can, however, be easily adjusted for the rotating outer cylinder arrangement. Theory is based on Newtonian Flow.

#### 3.2.3.1 Linear Approximation for Steady Flow

Two main approaches can be considered for steady flow in the rotating cylinder shear cell geometry. The first is an approximation that assumes the velocity profile is linear across the gap. This therefore allows the shear rate across the gap to be assumed constant (Figure 3.5). This is typically valid when the gap between the cylinders is sufficiently small [1].

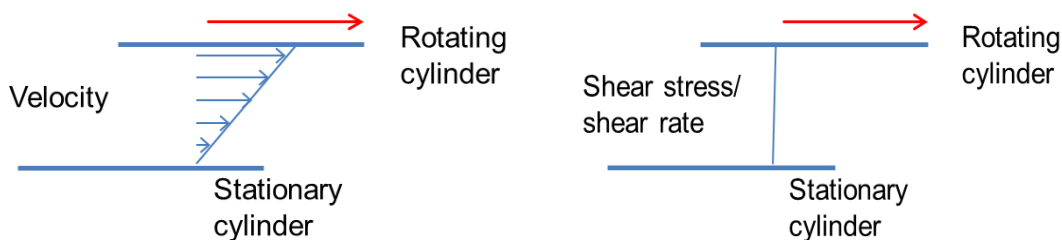


Figure 3.5- Variation of velocity (left) and shear stress/shear rate (right) across gap, with linear approximation

The theoretical velocity as a function of position in the gap (assuming velocity profile is linear) can be determined from the following, where  $r$  is the radial distance from the centre:

$$v(r) = 2\pi N r_{in} \frac{r_{out}-r}{r_{out}-r_{in}} \quad \text{Equation 3.1}$$

Here  $v$  is the velocity,  $N$  is the rotational rate,  $r_{in}$  is the inner cylinder radius,  $r_{out}$  is the outer cylinder radius and  $r$  is the radial distance from the centre. No slip conditions were assumed.

The shear rate ( $\dot{\gamma}$ ) across the gap (assuming the velocity profile is linear and the shear rate is constant) is therefore:

$$\dot{\gamma} = \frac{\text{rotational speed of inner cylinder}}{\text{gap between cylinders}} = \frac{2\pi N r_{in}}{r_{out}-r_{in}} \quad \text{Equation 3.2}$$

### 3.2.3.2 Non-Linear Approach for Steady Flow

For the second approach, it is assumed that the velocity is not a linear function of position in the gap. For this, the non-linear variation of velocity with position is given by:

$$v(r) = 2\pi N r_{in} \frac{r_{in}}{r} \frac{\left(1 - \frac{r^2}{r_{out}^2}\right)}{\left(1 - \frac{r_{in}^2}{r_{out}^2}\right)} \quad \text{Equation 3.3}$$

This allows the shear rate as a function of position to be obtained.

$$\dot{\gamma}(r) = \frac{dv(r)}{dr} = 2\pi N r_{in} \frac{\left(\frac{1}{r^2} - \frac{1}{r_{out}^2}\right)}{\left(\frac{1}{r_{in}^2} - \frac{1}{r_{out}^2}\right)} \quad \text{Equation 3.4}$$

Example flow profiles for the non-linear variation of velocity and therefore non-constant shear rate are shown in Figure 3.6.

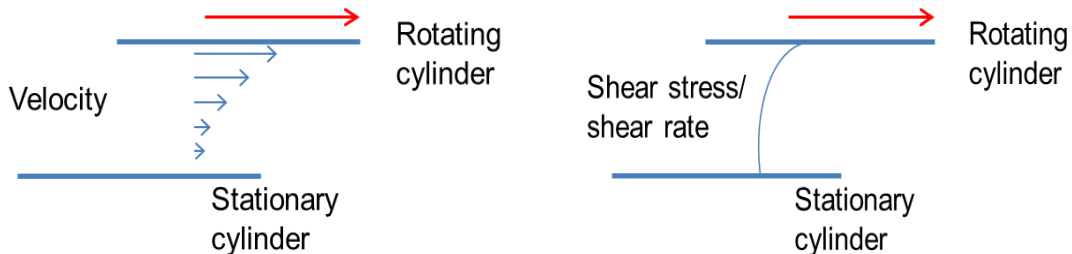


Figure 3.6- Variation of velocity (left) and shear stress/shear rate (right) across gap, with non-linear approach

#### 3.2.3.2.1 Velocity Derivation

The velocity and shear rate equations just detailed are derived from a momentum balance across the system (from the Navier-Stokes equation):

$$\frac{\partial v}{\partial t} = \eta_k \left[ \frac{\partial}{\partial r} \left( \frac{1}{r} \frac{\partial}{\partial r} (rv) \right) \right] \quad \text{Equation 3.5}$$

Here  $\eta_k$  is the kinematic viscosity and  $t$  is time.

When the inner cylinder is rotating at a constant speed, as with steady-shear, the following steady-state limit is applied:

$$\eta_k \left[ \frac{\partial}{\partial r} \left( \frac{1}{r} \frac{\partial}{\partial r} (rv) \right) \right] = 0$$

Integrating this once gives:

$$\frac{\partial}{\partial r}(r\nu) = Cr \quad \text{where } C \text{ is a constant.} \quad \text{Equation 3.6}$$

Integrating again gives:

$$r\nu = Ar^2 + B \quad \text{where } A \text{ and } B \text{ are constants} \quad \text{Equation 3.7}$$

Therefore, the velocity profile takes the following form:

$$\nu(r) = Ar + \frac{B}{r} \quad \text{Equation 3.8}$$

The constants A and B can then be determined by using boundary conditions (i.e  $\nu = 0$  when  $r = r_{out}$  and  $\nu = 2\pi N r_{in}$  when  $r = r_{in}$  assuming no slip conditions) to give Equation 3.3.

Outer boundary condition:

When  $r = r_{out}$ ,  $\nu = 0$ . Therefore Equation 3.8 becomes:

$$0 = Ar_{out} + \frac{B}{r_{out}}$$

Rearranging for constant A gives:

$$A = -\frac{B}{r_{out}^2} \quad \text{Equation 3.9}$$

Substituting back into the velocity equation (Equation 3.8) gives:

$$\nu(r) = -\frac{Br}{r_{out}^2} + \frac{B}{r}$$

$$\nu(r) = B \left( \frac{1}{r} - \frac{r}{r_{out}^2} \right) \quad \text{Equation 3.10}$$

Inner boundary condition:

When  $r = r_{in}$ ,  $\nu = 2\pi N r_{in}$ . Therefore Equation 3.10 becomes:

$$\nu(r) = B \left( \frac{1}{r_{in}} - \frac{r_{in}}{r_{out}^2} \right) = 2\pi N r_{in}$$

Rearranging for B gives:

$$B = \frac{2\pi N r_{in}}{\left( \frac{1}{r_{in}} - \frac{r_{in}}{r_{out}^2} \right)}$$

Substituting back into the velocity equation (Equation 3.8) with A and B now known gives:

$$v(r) = 2\pi N r_{in} \frac{\left(\frac{1}{r} - \frac{r}{r_{out}^2}\right)}{\left(\frac{1}{r_{in}} - \frac{r_{in}}{r_{out}^2}\right)}$$

$$v(r) = 2\pi N r_{in} \frac{r_{in} \left(1 - \frac{r^2}{r_{out}^2}\right)}{r \left(1 - \frac{r_{in}^2}{r_{out}^2}\right)} \quad \text{Equation 3.3}$$

### 3.2.3.2.2 Shear Rate Derivation

An expression for the shear rate as a function of position can be found by differentiating the velocity profile (Equation 3.3) with respect to radius to obtain Equation 3.4.

$$\dot{\gamma}(r) = \frac{dv(r)}{dr} = 2\pi N r_{in} \frac{\left(-\frac{1}{r^2} - \frac{1}{r_{out}^2}\right)}{\left(\frac{1}{r_{in}} - \frac{r_{in}}{r_{out}^2}\right)} \quad \text{Equation 3.4}$$

The average shear rate across the gap can be calculated from:

$$\dot{\gamma}_{avg} = \frac{1}{r_{out} - r_{in}} \int_{r_{in}}^{r_{out}} \dot{\gamma}(r) dr = \frac{2\pi N r_{in}}{r_{out} - r_{in}} \quad \text{Equation 3.11}$$

This gives the same expression as Equation 3.2.

### 3.2.3.2.3 Shear Stress Derivation

From Newton's Law of Viscosity:

$$\tau = \eta \dot{\gamma}$$

Here  $\tau$  is the shear stress,  $\eta$  is the viscosity and  $\dot{\gamma}$  is the shear rate.

Therefore the expression for the shear rate can simply be multiplied by the viscosity to obtain how the shear stress varies across the gap.

$$\tau(r) = \eta 2\pi N r_{in} \frac{\left(-\frac{1}{r^2} - \frac{1}{r_{out}^2}\right)}{\left(\frac{1}{r_{in}} - \frac{r_{in}}{r_{out}^2}\right)} \quad \text{Equation 3.12}$$

The average shear stress that occurs across the gap can be found from:

$$\tau_{avg} = \frac{\eta 2\pi N r_{in}}{r_{out} - r_{in}} \quad \text{Equation 3.13}$$

Further calibration of the shear cells is done in [Chapter 4](#) where the input voltage to the shear cell is converted to a shear stress and the rotational rate is used to obtain a shear rate.

### 3.2.3.3 Basic Oscillatory Flow Considerations

The majority of work done in the thesis is based on steady flow. One piece of oscillatory work is done in [Chapter 4](#). A very basic outline of the necessary considerations is therefore included here.

The velocity of the shear cell motor (and rotating cylinder) was proportional to the voltage supplied by the signal generator. When the shear cells were operated in oscillatory mode, the voltage signal to the motor, and therefore the velocity of the rotating cylinder, was set to oscillate sinusoidally. Therefore, the displacement of the rotating inner cylinder as a function of time was given as:

$$y(t) = -A\cos(\omega t) \quad \text{Equation 3.14}$$

Where:  $A = r_{in}\theta$  i.e. the arc length

Here  $y$  is the displacement,  $\omega$  is the angular frequency,  $\theta$  is the angle of oscillation,  $r_{in}$  is the inner cylinder radius and  $t$  is time.

The velocity at the inner rotating cylinder as a function of time was therefore given by:

$$\frac{dy}{dt} = v(t) = v_{max}\sin(\omega t) \quad \text{Equation 3.15}$$

Where:

$$v_{max} = A\omega = r_{in}\theta\omega$$

For oscillatory operation, increasing the peak to peak voltage amplitude resulted in larger amplitudes of oscillation, since increases in velocity resulted in larger displacements in a given time.

### **3.2.4 Geometry Characterisation**

The flow in the rotating cylinder shear cells was characterised so that their behaviour could be established.

#### **3.2.4.1 Shear Profiles for Steady-Flow**

The shear cells were characterised by obtaining velocity and shear rate profiles for different arrangements.

##### 3.2.4.1.1 Procedure

The flow profiles of the shear cells were investigated by studying the motion of tracer particles via optical microscopy (Zeiss Axioskop FS) under various conditions. Video clips of the particles under motion were made (using an Edmund Optics EO-3122C camera) and analysed using Image J.

Rotating inner cylinder shear cells (2.5mm, 5mm and 10mm gap) were used and the inner cylinder was rotated steadily at a known rotational rate (0.5RPM or 2RPM) which was measured using a tachometer (DT-2236B Photocontact Tachometer). The tachometer worked by shining a laser at a strip of reflective tape that was placed on the rotating cylinder. When the laser struck the reflective tape, it bounced back and was detected by a sensor. This allowed the rotational rate to be determined. According to the manufacturer, the tachometer was accurate to  $\pm 0.5\%$ . Measurements using this tachometer were compared to another tachometer (DT-2234C+) and both compared very closely (within 3%), suggesting the tachometer was accurate and suitable for the experiments.

The displacements of tracer particles in a given time, at various positions within the gap, were measured (assuming their displacement followed a linear path). This allowed a velocity profile to be obtained by accounting for the particle displacements in a known time. An average shear rate was deduced from the velocity profile. Experimental velocities and shear rates were compared to those deduced from theory.

The tracer particles used were 20 $\mu\text{m}$  polystyrene spheres. They were density matched in a water/glycerol mixture. When placed in water alone, the polystyrene particles were found to sink (due to their density being higher than water), and when in pure glycerol, they were found to rise (due to their density being lower than glycerol).

$$x_1 \rho_{\text{water}} + x_2 \rho_{\text{glycerol}} = \rho_{\text{polystyrene}} \quad \text{Equation 3.16}$$

Here x is the volume fraction and ρ is the density. The density of water was taken as 998 kg/m<sup>3</sup>, the density of glycerol was 1264 kg/m<sup>3</sup> and the density of polystyrene was 1050 kg/m<sup>3</sup> [2].

This led to the following v/v mixture being required to balance the solvent density and particle density:

20% glycerol/ 80% water

### 3.2.4.1.2 Results

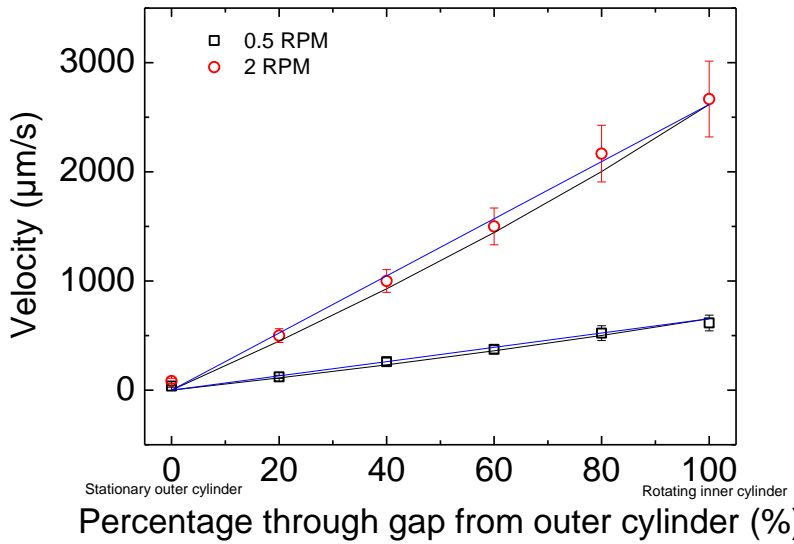
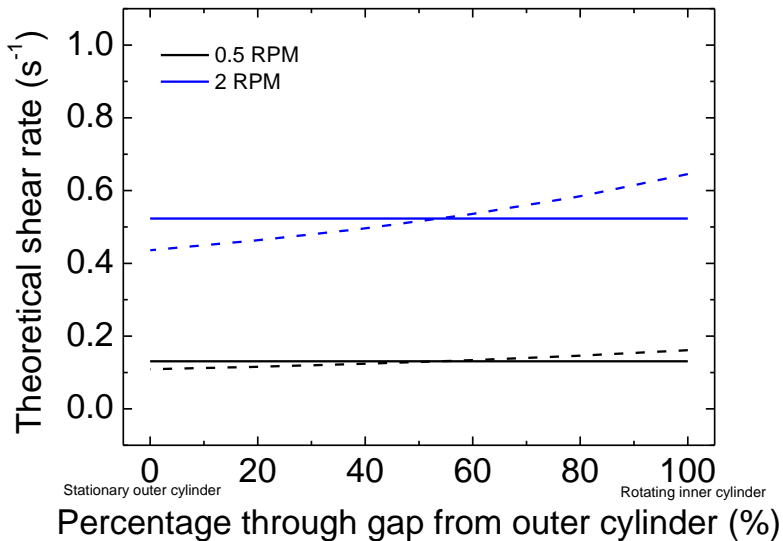


Figure 3.7- Example velocity profiles for 5mm gap shear cell. Points show those measured experimentally. Lines show theoretical linear velocities from Equation 3.1 (blue) and theoretical non-linear velocities from Equation 3.3 (black). Error bars show standard deviation of repetitions.

As expected, the velocity was at a maximum at the rotating inner cylinder wall and decreased while moving towards the stationary outer cylinder. The velocity profiles across the gap appeared approximately linear for the conditions studied for all shear cells investigated, suggesting the shear rate did not vary substantially across the gap. Example velocity profiles for the 5mm shear cells are shown in Figure 3.7. These showed that by accounting for the error in measurements, there was no appreciable difference between the experimental and theoretical linear and non-linear profiles.

There were several sources of error in imaging the velocity profiles. For example, it was assumed that the times associated with frames were accurate. Due to the field of view size available with the microscope and microscope camera, particles covered this displacement in less than 1 second, resulting in short measurement time periods. It was assumed that the particles followed a linear displacement. This was reasonable considering the small particle displacement observed with the microscope, relative to the whole shear cell.



**Figure 3.8- Theoretical shear rates across the gap for the 5mm shear cells. Dashed lines show non-constant shear rates from Equation 3.4. Solid lines show constant, or average, shear rate from Equation 3.2 and 3.11.**

The velocities estimated experimentally compared well to those deduced from the non-linear theoretical approach (Equation 3.3). The theoretical shear rates were calculated using this non-linear approach (Equation 3.4). Shear rates did not vary significantly, but did increase towards the rotating inner cylinder (Figure 3.8). With the non-linear approach, the shear rate varied  $\pm 15\%$  of the average shear rate across the shear cell, at its maximum deviation from the average. This was within the typical margin of error encountered in the experiments in this thesis.

Due to the shear rate variation not being significant, for the rest of the work in the thesis, the average shear rate is quoted. This is that obtained from Equation 3.11 (and Equation 3.2). The shear rate obtained from this compared very well to that obtained experimentally.

It is worth noting that the rotational rates used for obtaining velocity profiles were significantly lower than those used in the experiments in [Chapter 4](#) and [Chapter 5](#). This was due to limitations of the speed the cameras used for imaging could operate at. The results do, however, suggest that the shear cells operated as would be expected for Newtonian fluids.

### **3.2.4.2 Flow Instabilities and Flow Visualisation**

While reviewing theory on the rotating cylinder shear cell geometries, it became evident that there was a possibility of flow instabilities occurring. These instabilities are referred to as Taylor-Couette instabilities/flow or Taylor vortex flow.

It was therefore necessary to look into their theory and ultimately deduce whether or not they were occurring in the shear cells used. For this, a combination of calculations and flow visualisation were done.

#### 3.2.4.2.1 Taylor- Couette Flow

##### Overview

Beyond a critical angular velocity, Couette flow may become unstable, resulting in the formation of vortices. These vortices cause high-speed fluid near the rotating inner cylinder to be carried outwards, and low-speed fluid near the stationary outer cylinder to be carried inwards. This can cause energy redistributions within the gap [3]. These instabilities are referred to as Taylor-Couette instabilities/flow or Taylor vortex flow.

The presence of these instabilities can change the hydrodynamic, mass transfer and heat transfer characteristics of processes when this type of flow occurs. It is therefore important to be able to predict the onset of these instabilities [4].

##### Basic Theory

Taylor-Couette flow occurs in the annulus between rotating concentric cylinders when the angular velocity exceeds a critical value. It typically occurs when the inner cylinder is rotating and the outer cylinder is fixed [5]. The problem was first investigated by Couette (1890) and Mallock (1896) who were investigating ways to measure viscosity. Couette rotated the outer cylinder and kept the inner fixed while Mallock did the converse. They observed different results and this prompted further investigation. By 1923 Taylor was able to relate theory and experiments for stability in cylindrical Couette flow, and put the differences due to Taylor vortices occurring [5, 6].

With simple Couette flow, the torque needed to rotate the rotating cylinder increases linearly with rotation speed. Beyond a critical value of rotation speed, however, the torque increases more rapidly due to the loss of stability of the stable Couette flow

[7]. When the angular velocity ( $\Omega = 2\pi N$ , where  $N$  is the rotational rate) exceeds a critical value, the flow becomes unstable to infinitesimal perturbations/disturbances, resulting in the formation of pairs of counter-rotating, axisymmetric, toroidal (ring shaped) vortices that fill the annulus superimposed on the Couette flow [5, 7, 8]. These can be seen in Figure 3.9.

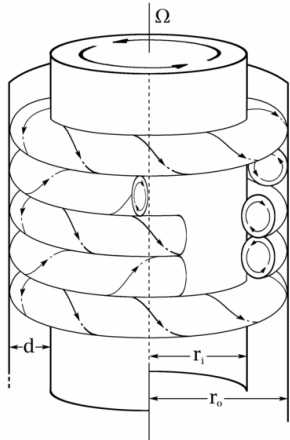


**Figure 3.9- Taylor-Couette flow arrangement [5]**

The vortices cause high-speed fluid near the rotating inner cylinder to be carried outwards, and low-speed fluid near the stationary outer cylinder to be carried inwards. This redistributes the angular momentum/energy of the fluid in the gap [3, 5].

The origin of the vortical flow comes from centrifugal instability. In simple Couette flow, the centrifugal force acting to push fluid away from the rotating inner cylinder is balanced by the radial pressure gradient force pushing fluid inwards (Figure 3.10) [5]. From Bernoulli's equation, increases in velocity result in decreases in pressure. Therefore since the velocity increases when moving from the outer to inner cylinder, the pressure gradient pushes in this direction.

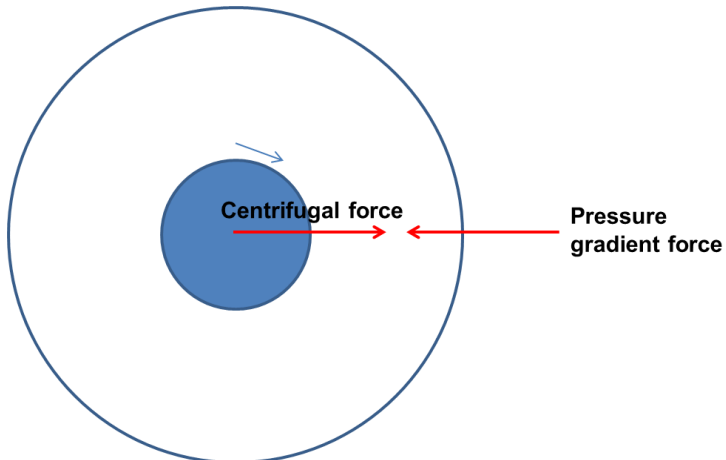


Figure 3.10- Force diagram showing centrifugal force and pressure gradient force [8]

If a fluid particle is moved outwards slightly (i.e. is perturbed even by an infinitesimal amount) from its initial radius, it reaches a region where the inward force due to the pressure gradient is slightly less than the outward centrifugal force on the particle, since the outward force is based on the particle's initial position because its angular momentum is conserved. As a result, the particle will continue outwards. Conversely, a fluid particle moved slightly inwards from its initial radius will continue inwards as the inward force due to the pressure gradient is slightly greater than the outward force on the particle [5].

At low rotational speeds, these instabilities can be suppressed by viscosity; this damps out the perturbations, rather than allowing them to continue. Viscosity therefore delays the onset of centrifugal instabilities [5, 8].

The instabilities only occur when the pressure gradient force decreases with increasing radius. This is the case when the inner cylinder is rotating and the outer cylinder is fixed, since the velocity decreases with increasing radius. When the outer cylinder is rotating and the inner cylinder is fixed, the pressure gradient force increases with increasing radius, and the flow remains stable [5].

## Taylor Number and Reynolds Number

The onset of loss of stability can be estimated through the Taylor number (Ta) which increases with increasing rotational speed. It is a dimensionless number, and when it exceeds a critical value ( $Ta_{crit}$ ), Taylor-Couette instabilities occur.

There are various forms of the Taylor number, but all represent the ratio of centrifugal (or inertial) forces to viscous forces. Above the critical Taylor number, centrifugal forces exceed viscous forces, and as a result, the flow becomes unstable.

When the inner cylinder is rotating and the outer cylinder is stationary, the Taylor number can be defined as [5, 7]:

$$Ta = 4Re^2 \frac{1 - \frac{r_{in}}{r_{out}}}{1 + \frac{r_{in}}{r_{out}}} \quad \text{Equation 3.17}$$

Re is the Reynolds number based on the surface velocity of the inner cylinder (v) and the gap width (d) [5].

$$Re = \frac{\rho v d}{\eta} = \frac{\rho (2\pi N r_{in}) d}{\eta} \quad \text{Equation 3.18}$$

where:  $d = (r_{out} - r_{in})$

Estimates suggest that the critical Taylor number is around 1700 for concentric cylinders with the inner cylinder rotating and outer fixed [8, 9].

## Instabilities in Shear Thinning and Shear Thickening Fluids

Few studies have been carried out regarding the onset of instabilities in shear thickening fluids, and those that are available are largely theoretical. A slightly larger number are available for shear thinning fluids, but again, information on the area is lacking [4].

Theoretical studies have found that in shear thickening fluids, the critical Taylor number required for loss of stability of Couette flow increased as shear thickening effects increased. This was thought to be due to increased viscous effects. The opposite has been found for shear thinning fluids: smaller Taylor numbers were required for instabilities as shear thinning behaviour increased [10-12].

#### 3.2.4.2.2 Experimental Taylor Number

The Taylor Number was deduced for various experimental conditions to see whether instabilities could theoretically have been occurring. For this, the viscosity and density of water-glycerol mixtures were used and various rotation rates were investigated. After this, flow visualisation with a rheoscopic fluid and dye was done for further verification.

Considering the 5mm gap shear cell geometry, with water in the shear cells, instabilities were expected to occur when the rotational rate was greater than 50RPM. As the viscosity of the solution increased, the rotational rate required for instabilities increased. For example, when pure glycerol was used, a rotational rate of 70,000RPM would have been required for instabilities to occur. This was well out with the rotational rates used in the experiments. For these calculations it was assumed that the density and viscosity of water were  $998 \text{ kg/m}^3$  and  $0.001 \text{ Ns/m}^2$  respectively and for glycerol, the density was  $1264 \text{ kg/m}^3$  and the viscosity was  $1.4 \text{ Ns/m}^2$  [2].

Due to the highly viscous nature of the concentrated suspensions used in the experiments in [Chapter 4](#) and [Chapter 5](#) (see [Chapter 7](#)), and the rotational rates encountered, it was deduced that flow instabilities would not have been occurring in the experiments according to theory.

#### 3.2.4.2.3 Flow Visualisation

To verify that flow instabilities were not occurring in the experiments, flow visualisation with a rheoscopic fluid and dye was done. For this, water-glycerol mixtures of varying compositions were used and different rotation rates were investigated.

For the dye analysis method, a needle was used to inject a dye into the fluid as it was being sheared and its path was monitored visually.

With the rheoscopic fluid method, a rheoscopic fluid (Pearl Swirl) was used to visualise flow within the shear cells. Microscopy and IR analyses of the fluid showed that it contained anisotropic reflective platelets/flakes of a material thought to be mica. These generally varied between  $5\text{-}20\mu\text{m}$  at the largest cross section.

Rheoscopic fluids work due to the flakes aligning with the flow; depending on orientation, different amounts of incident light are reflected, making flow patterns visible. The flakes align with their larger dimension parallel to the flow (to minimise energy dissipation). Therefore if the flow direction is along the observer's line of sight, the flakes' largest dimension will not be facing the observer and the area will appear darker since less light will be reflected (Figure 3.11 left). Conversely, if the flow is perpendicular to the observer's line of sight, the 'face' of the flake will be facing the observer. This will result in more light being reflected back and a lighter area will be observed (Figure 3.11 right) [13, 14].



Figure 3.11- Rheoscopic fluid mechanism. Flow along observer's line of sight (left). Flow perpendicular to observer's line of sight (right).



Figure 3.12- 80% v/v glycerol-water mixture at 500RPM with dye injected



Figure 3.13- 80% v/v glycerol-water mixture at 500RPM with rheoscopic fluid

As shown in Figure 3.12 and Figure 3.13, no signs of flow instabilities were seen with an 80% v/v glycerol-water mixture at 500RPM. Since the concentrated suspensions used in [Chapter 4](#) and [Chapter 5](#) were more viscous than this (and were sheared at lower rotational rates), flow instabilities were therefore highly unlikely to have been occurring. This agreed with the Taylor number calculations in 3.2.4.2.2.



**Figure 3.14-** 20% v/v glycerol-water mixture at 500RPM with dye injected



**Figure 3.15-** 20% v/v glycerol-water mixture at 500RPM with rheoscopic fluid

To show an example with instabilities occurring, Figure 3.14 and Figure 3.15, show flow instabilities occurred with a 20% v/v glycerol-water mixture at 500RPM. This showed that when instabilities were present, they were clearly visible.

Overall, the work on flow instabilities and visualisation confirmed that, despite using a rotating inner cylinder geometry, flow instabilities were highly unlikely to have occurred in the concentrated suspension experiments in [Chapter 4](#) and [Chapter 5](#).

### 3.3 Motor Characterisation

A range of experiments were performed to produce calibration curves and equations for the DC motors used in the shear cells. This was to see how parameters such as torque, current and power varied with the load and applied voltage, therefore allowing a better understanding of the set-up.

The following sources were used for reference: [15-17]

#### 3.3.1 Fixed Voltage Calibration

The following motor calibration was performed at a fixed voltage of 10.8V (the maximum that could be supplied by the power supply used with the motor). This supply voltage to the shear cell was used significantly in [Chapter 4](#) and [Chapter 5](#).

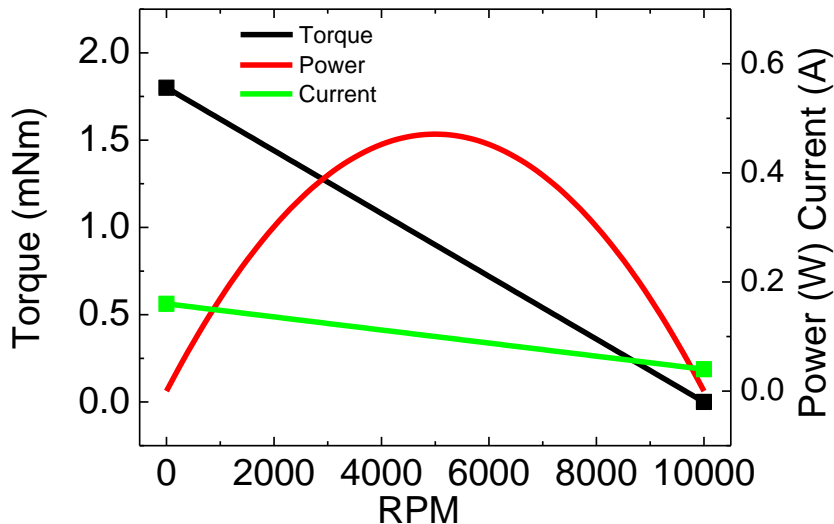


**Figure 3.16- Motor torque, power and current calibration curves. Measured data given as points. Error bars are within size of points.**

#### Variation of Torque with Rotational Speed

At a constant applied voltage, the torque externally applied ( $T$ ) by the motor varies approximately linearly (inversely) with angular rotational speed ( $\omega$ ). As the load is increased, the rotational speed decreases. This results in the torque increasing. This relationship is characterised by two parameters: the stall torque ( $T_s$ ) and the no-load speed ( $\omega_n$ ).

The no-load speed is the fastest possible rotational speed at a particular voltage. This occurs when there is no load on the shaft and no torque is applied to the shaft. The stall torque occurs when the shaft is fully loaded and is unable to move (i.e. the rotational speed is zero). Here the torque is at its maximum.

This allows the relationship between torque and angular velocity to be written as:

$$T = -\left(\frac{T_s}{\omega_n}\right)\omega + T_s \quad \text{Equation 3.19}$$

$$T = T_s \left(1 - \frac{\omega}{\omega_n}\right) \quad \text{Equation 3.20}$$

Here  $T$  is the torque,  $T_s$  is the stall torque,  $\omega$  is the angular rotation speed and  $\omega_n$  is the no-load speed.

The no-load speed was found by measuring the rotation rate (RPM) of the motor, using a tachometer, when there was no load. The stall torque was found by attaching a bar of known length to the shaft perpendicularly. The motor was then arranged so that the bar hit the plate of a balance when it rotated. This prevented the motor from spinning (i.e. causing it to stall). The mass on the balance was noted and this along with the length of the bar allowed the stall torque to be calculated.

The variation of torque with rotational rate is plotted in Figure 3.16 from Equation 3.19, since the stall torque and no-load speed were now known.

#### Variation of Power with Rotational Speed

Power (output),  $P$ , is the product of torque and angular velocity.

$$P = T\omega \quad \text{Equation 3.21}$$

$$P = -\left(\frac{T_s}{\omega_n}\right)\omega^2 + T_s\omega \quad \text{Equation 3.22}$$

Power is therefore a quadratic function, with the maximum occurring at half the stall torque and half the no-load speed.

The variation of power with rotational rate is plotted in Figure 3.16 from Equation 3.22.

#### Variation of Current with Torque

The torque generated by a DC motor is directly proportional to the current. At the stall torque, the current is at its maximum. At the torque corresponding to the no-

load speed (zero applied torque), the current is at its minimum. The no-load current has a non-zero value as it takes a certain amount of current to overcome internal friction in the motor.

The no-load current and stall torque current were found by placing a multimeter in series. This allowed the relationship between torque and current to be found (Figure 3.17).

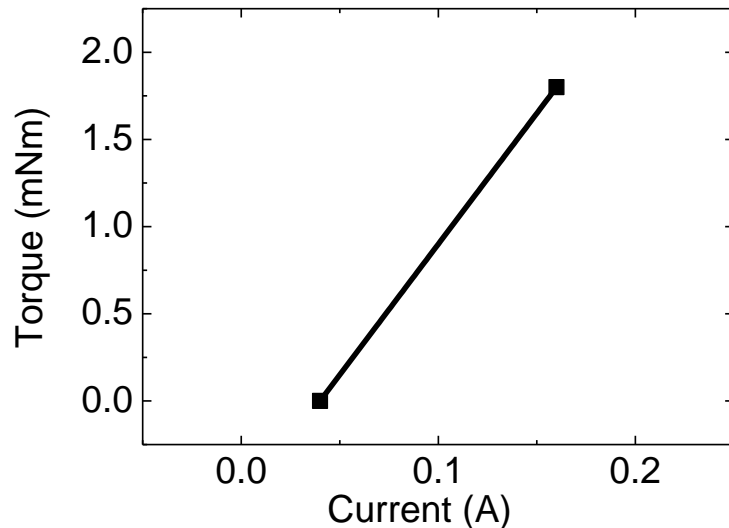


**Figure 3.17- Motor's relationship between current and torque. Measured data given as points. Error bars are within size of points.**

The variation of current with rotational speed is plotted in Figure 3.16.

## Efficiency

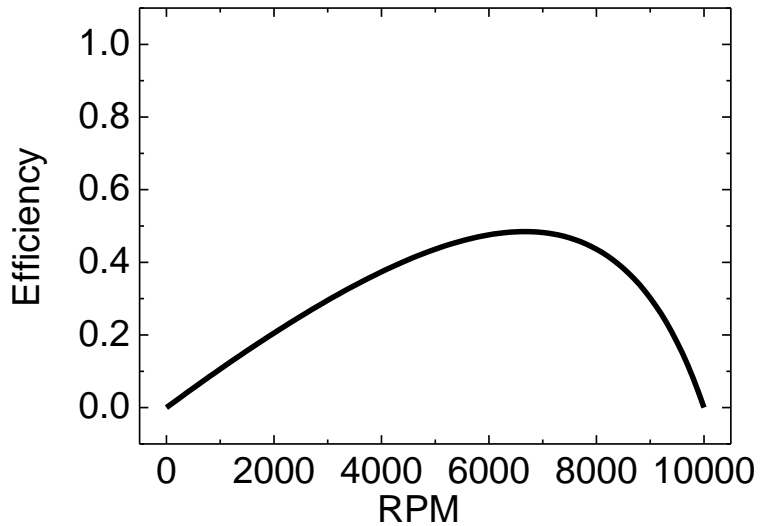


Figure 3.18- Motor efficiency curve

The efficiency is defined as:

$$\text{Efficiency} = \frac{\text{Power out}}{\text{Power in}} \quad \text{Equation 3.23}$$

The output power is the product of torque and angular velocity, as mentioned. The input power is the product of the current and applied voltage.

This therefore allowed the motor's efficiency to be plotted to see how it was affected by the applied load. This showed that the motor's efficiency peaked at around 50% (Figure 3.18). This is in the range of the typical efficiency of a DC motor, suggesting the procedure used was reasonable [18].

## Conclusions

From this fixed voltage calibration, it could be concluded that when the rotational rate of the inner cylinder did not differ too substantially between experiments (which is shown in [Chapter 4](#) where the rotational rate generally varied between 0 and 400RPM) at a fixed voltage, the motor's torque, current, power and efficiency did not vary significantly. For example, the torque varied by just 4% across the range from 0 to 400RPM. This meant that the motor operated consistently for all conditions studied and that further considerations of the motor's performance were not necessary when comparing experimental results.

### 3.3.2 Motor Characteristics Derivation

Parameters such as the no-load speed, stall torque and therefore torque vary with supplied voltage. The motor characteristic equation below describes the relationship between voltage, externally applied torque and angular velocity (Equation 3.24).

$$V = \frac{R_m}{K_m} (T + T_f) + K_b \omega \quad \text{Equation 3.24}$$

Here  $V$  is the voltage,  $R_m$  is the motor resistance,  $K_m$  is a constant of the motor,  $T$  is the torque (externally applied),  $T_f$  is the torque from internal friction,  $K_b$  is a constant of the motor and  $\omega$  is the angular rotation speed.

Equation 3.24 can be derived from some key features of DC motors, as follows. The voltage drop across a DC motor is made up of two components. The first is due to motor resistance ( $R_m$ ), and the second is the back emf, or electromotive force, ( $E_b$ ) generated by the spinning rotor. Since  $V=IR$  (here  $V$  is voltage,  $I$  is current and  $R$  is resistance):

$$V = R_m I + E_b \quad \text{Equation 3.25}$$

The torque generated ( $T_0$ ) by a DC motor is proportional to the current running through it:

$$T_0 = K_m I \quad \text{Equation 3.26}$$

Here  $K_m$  is a constant of the motor and  $I$  is the current.

If an external load is present, the torque generated by the motor is balanced by the sum of the externally applied torque ( $T$ ) and the torque from internal friction ( $T_f$ ).

$$T_0 = T + T_f \quad \text{Equation 3.27}$$

The back emf ( $E_b$ ) of the motor is directly proportional to the rotational speed and is given by:

$$E_b = K_b \omega \quad \text{Equation 3.28}$$

Here  $K_b$  is a constant of the motor.

Therefore, combining equations 3.25-3.28 gives:

$$V = \frac{R_m}{K_m} (T + T_f) + K_b \omega \quad \text{Equation 3.24}$$

### 3.3.3 Effect of Supplied Voltage on Motor Characteristics

$$V = \frac{R_m}{K_m} (T + T_f) + K_b \omega \quad \text{Equation 3.24}$$

To use Equation 3.24, the parameters  $R_m/K_m$ ,  $T_f$  and  $K_b$  must be specified- these describe the motor's characteristics. They can be found by solving Equation 3.24 with the motor's limits ( $T_s$  and  $\omega_n$ ).

Stall torque limit:

When  $T=T_s$ ,  $\omega=0$ .

Therefore:

$$V = \frac{R_m}{K_m} (T_s + T_f)$$

$$T_s = \left(\frac{K_m}{R_m}\right) V - T_f \quad \text{Equation 3.29}$$

No load speed limit:

When  $\omega=\omega_n$   $T=0$ .

Therefore:

$$V = \frac{R_m}{K_m} (0 + T_f) + K_b \omega_n$$

$$\omega_n = \frac{V - \left(\frac{R_m}{K_m}\right) T_f}{K_b} \quad \text{Equation 3.30}$$

Therefore:

$$\frac{T_s}{\omega_n} = K_b \left(\frac{K_m}{R_m}\right) \quad \text{Equation 3.31}$$

To solve for these parameters, the stall torque was measured and plotted as a function of voltage. From Equation 3.29, this allowed  $R_m/K_m$  and  $T_f$  to be obtained. The final parameter,  $K_b$ , was then determined using Equation 3.31.

**Table 3.2- Motor characteristic constants for motors used in the shear cells**

$R_m/K_m$ [V/Nm]	$10000 \pm 1200$
$T_f$ [Nm]	$0.0001 \pm 0.00005$
$K_b$ [Vs]	$0.01 \pm 0.003$

Equation 3.30 was then used with the parameters (Table 3.2) to see how the no-load speed varied with voltage. This was compared to no-load speeds determined experimentally. As can be seen in Figure 3.19, these compared well, suggesting the parameters that were deduced were accurate and could describe the motor's behaviour well. This also confirmed that the motor's voltage was directly proportional to the shaft's velocity.

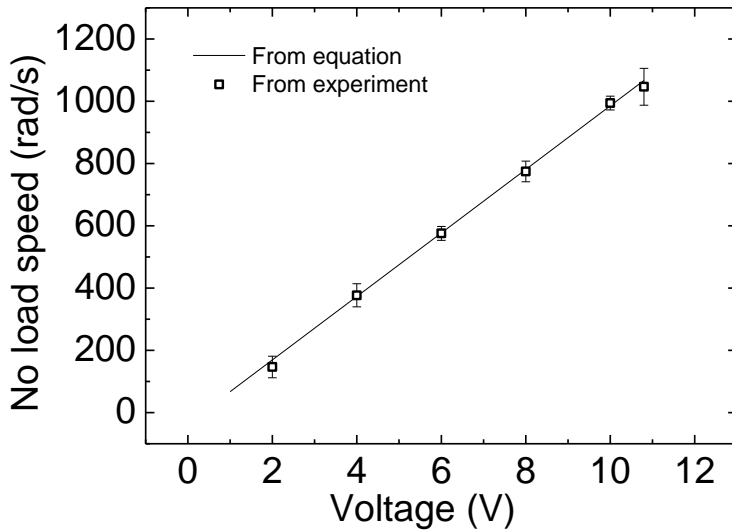


**Figure 3.19- Comparison between no load speeds obtained using derived motor characteristic parameters with those found experimentally. Error bars show standard deviation of repetitions.**

Knowing these parameters therefore allows the externally applied torque to be determined when the applied voltage and rotational speed of the motor are known.

$$V = \frac{R_m}{K_m} (T + T_f) + K_b \omega \text{ rearranges to give:}$$

$$T = \frac{K_m}{R_m} (V - K_b \omega) - T_f \quad \text{Equation 3.32}$$

The externally applied torque could then be used to obtain an applied shear stress since:

$$T = \tau 2\pi r_{in}^2 L \quad \text{Equation 3.33}$$

Here  $T$  is the torque,  $\tau$  is the shear stress,  $r_{in}$  is the inner cylinder radius and  $L$  is the fill height.

This allowed the shear stress as a function of voltage to be estimated. The equations suggested that the torque applied by the motor (and therefore the shear

stress) increased approximately linearly with voltage for the voltage ranges considered experimentally. At the maximum voltage, 10.8V, it was estimated that a shear stress of  $96 \pm 27 \text{ N/m}^2$  was applied when using a rotational rate within the range of those encountered in the experiments (0 to 400 RPM) and the motor characteristic constants.

This compared well to that deduced in [Chapter 4](#) where a shear stress-voltage calibration suggested that at 10.8V, a shear stress of  $72 \pm 5 \text{ N/m}^2$  was applied. For this, a calibration with Newtonian glycerol and water-glycerol mixtures was performed to see how the rotational rate of the shear cell's inner cylinder varied with the supplied voltage. Since this allowed the shear rate as a function of voltage to be determined, and the viscosity was known (from literature), this allowed the shear stress as a function of voltage to be deduced. More details of this are given in [Chapter 4](#).

In [Chapter 4](#), it was deduced that overall:

$$\tau \left[ \frac{\text{N}}{\text{m}^2} \right] = 6.7 \pm 0.4 \times \text{voltage [V]} \quad \text{Equation 3.34}$$

From the motor calibration, this was deduced to be:

$$\tau \left[ \frac{\text{N}}{\text{m}^2} \right] = 8.7 \pm 1.2 \times \text{voltage [V]} \quad \text{Equation 3.35}$$

The calibrations compared reasonably well given the different approaches used to determine them.

It is worth noting that these motor calibrations were performed assuming a 'steady-state', where the rotation rate for a fixed load remained constant. In practice, the rotation rate varied due to the material in the shear cell jamming, as detailed in [Chapter 4](#). This likely affected the angular acceleration and therefore the externally applied torque (since the externally applied torque is the product of the angular acceleration and moment of inertia). This may have resulted in the possibility of the rate of change of shear rate being proportional to the shear rate, leading to the potential for oscillations. No evidence of this was found experimentally.

## 3.4 Capillary/Pipe Flow Geometry

### 3.4.1 Geometry Overview

The work in [Chapter 8](#) involved pumping concentrated cornflour-water suspensions through cylindrical piping. A brief overview of the general theory surrounding cylindrical pipe flow is given in this section.

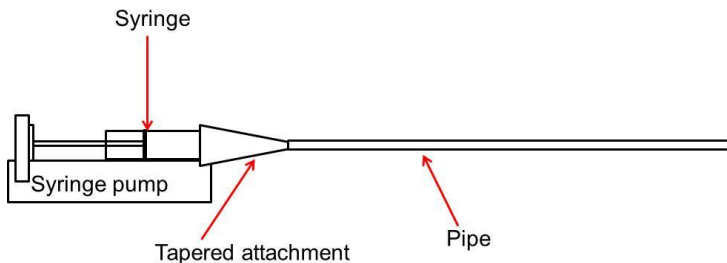


**Figure 3.20- Pipe flow geometry set-up**

For the set-up, a syringe pump (Cole Parmer 74905-54) was used to control the flow of the material through the piping (Figure 3.20). A tapered attachment was designed to provide a more gradual constriction to the material as it exited the syringe barrel and entered the piping to minimise entrance and exit effects. More details about this are given in [Chapter 8](#).

The maximum force that could be applied by the syringe pump's bar and the bar's velocity could be adjusted (Table 3.3). The bar's velocity could be used to control the shear rate in the pipe since it controlled the volumetric flow rate of the suspension exiting the syringe barrel and entering the pipe. The maximum force that could be applied by the bar controlled the maximum shear stress that could be applied to the fluid in order to achieve the desired flow rate.

It is worth noting that only the maximum force that could be applied by the bar was known- what it was instantaneously operating at was not. During operation, the actual force applied by the bar could vary from zero up to the set maximum. For the pump to run, the maximum force that could be applied by the bar and the desired flow rate (which controlled that bar's velocity) had to be set by the user. More details of this are given in [Chapter 8](#).

**Table 3.3- Syringe pump details**

<b>Maximum linear force of bar [N] (100%)</b>	330
<b>Maximum bar speed [mm/s]</b>	3.2

### 3.4.2 Theory for Newtonian Flow

An overview of general theory related to the pipe flow of a Newtonian material is given in this section.

#### 3.4.2.1 Hagen-Poiseuille Derivation

For fluid flowing through a pipe, due to the geometry, the velocity, shear rate and shear stress are functions of radial position i.e. distance from the pipe axis. The shear stress and shear rate are highest at the walls of the pipe and lowest at the centre. The velocity is highest at the pipe centre and lowest at the walls.

Much of the theory behind the flow of a Newtonian material through a pipe is centred on the derivation of the Hagen-Poiseuille equation which relates pressure drop to flow rate.

##### 3.4.2.1.1 Force Balance

The derivation of the Hagen-Poiseuille equation starts with a force balance over a horizontal length of pipe:

$$(-\Delta P)\pi R^2 = 2\pi R l \tau_w \quad \text{Equation 3.36}$$

Here  $\Delta P$  is the pressure drop due to friction,  $R$  is the pipe radius,  $l$  is the pipe length and  $\tau_w$  is the wall shear stress.

This relates the pressure drop due to friction to the wall shear stress.

A force balance can also be done over a central core of fluid of radius  $r$ .

$$(-\Delta P)\pi r^2 = 2\pi r l \tau_r \quad \text{Equation 3.37}$$

Here  $\tau_r$  is the shear stress at radius  $r$ .

### 3.4.2.1.2 Variation of Velocity with Radial Position

The velocity over the cross-section of a pipe is not uniform: the velocity varies parabolically with radius, from a minimum at the pipe walls to a maximum at the centre, as shown in Figure 3.21. This is because the shear stress applied to the fluid varies linearly with distance from the pipe centre as detailed in 3.4.2.1.3.

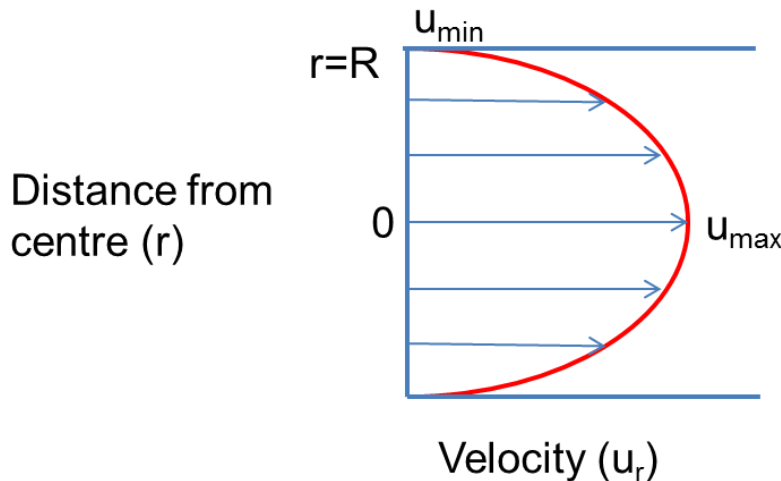


**Figure 3.21- Variation of velocity with radial position in pipe flow**

An equation describing the relationship between fluid velocity and radial position can be derived as follows.

The shear stress in terms of the distance from the pipe axis can be written as:

$$\tau_r = -\eta \frac{du_r}{dr} \quad \text{Equation 3.38}$$

Here  $\tau_r$  is the shear stress at radius  $r$ ,  $\eta$  is the viscosity,  $u_r$  is the velocity at radius  $r$  and  $r$  is the radius of the core of fluid.

The negative sign is used since the velocity gradient is negative: as the distance from the centre is increased, the velocity decreases.

Equation 3.38 can then be substituted into the force balance for a central core of fluid (Equation 3.37):

$$(-\Delta P)\pi r^2 = 2\pi r l \left( -\eta \frac{du_r}{dr} \right) \quad \text{Equation 3.39}$$

Rearranging this gives:

$$\Delta P r = 2l\eta \frac{du_r}{dr} \quad \text{Equation 3.40}$$

This can now be separated and integrated to obtain an expression for the variation of velocity with radial position.

For this, no slip boundary conditions are assumed ( $u_r=0$  when  $r=R$ ).

$$\int_0^{u_r} du_r = \frac{\Delta P}{2\eta l} \int_R^r r dr \quad \text{Equation 3.41}$$

$$u_r = \frac{(-\Delta P)}{l} \frac{1}{4\eta} (R^2 - r^2) \quad \text{Equation 3.42}$$

This shows the parabolic variation of velocity with distance from the pipe centre as shown in Figure 3.21. The maximum velocity ( $u_{max}$ ) occurs at the pipe centre (where  $r=0$ ) and the minimum occurs at the pipe wall (where  $r=R$ ).

$$u_{max} = \frac{(-\Delta P)}{4\eta l} R^2 = \frac{(-\Delta P)}{16\eta l} d^2 \quad \text{Equation 3.43}$$

The ratio of the velocity at position  $r$  to the maximum velocity can be written as:

$$\frac{u_r}{u_{max}} = 1 - \frac{r^2}{R^2} \quad \text{Equation 3.44}$$

#### 3.4.2.1.3 Variation of Shear Stress and Shear Rate with Radial Position

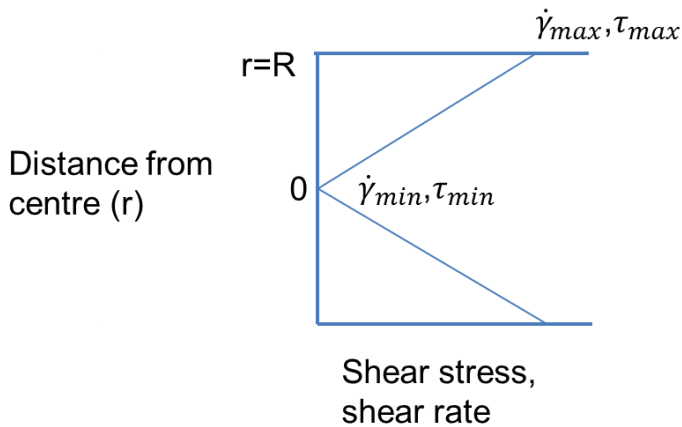


**Figure 3.22- Variation of shear stress and shear rate with radial position**

As mentioned, the shear rate and shear stress are functions of radial position in a pipe. This is expected since from 3.4.2.1.2, the velocity profile across a pipe is a parabolic function of radial position. Since the shear rate is equal to the velocity gradient (i.e. the derivative of parabolic velocity profile), the shear stress and shear rate are linear functions of radial position.

The ratio of the shear stress at distance  $r$  from the pipe centre ( $\tau_r$ ) to the shear stress at the wall ( $\tau_w$ ) is:

$$\frac{\tau_r}{\tau_w} = \frac{r}{R} \quad \text{Equation 3.45}$$

The same can be said for the shear rate's variation with radial position.

$$\frac{\tau_r}{\tau_w} = \frac{\dot{\gamma}_r}{\dot{\gamma}_w} = \frac{r}{R} \quad \text{where } \dot{\gamma}_w = \dot{\gamma}_{max} \quad \text{Equation 3.46}$$

Since from Newton's Law of Viscosity:

$$\tau = \eta \dot{\gamma}$$

Therefore the shear stress and shear rate increase linearly from zero at the centre of the pipe (where the velocity is at its maximum) to a maximum at the pipe walls (where the velocity is at its minimum). This is shown in Figure 3.22.

#### 3.4.2.1.4 Determination of Pipe Volumetric Flow Rate

As mentioned, the Hagen-Poiseuille equation relates pressure drop to flow rate. Therefore a final part of the derivation, using the term for the radial velocity variation, must take place to obtain the Hagen-Poiseuille equation in its final form.

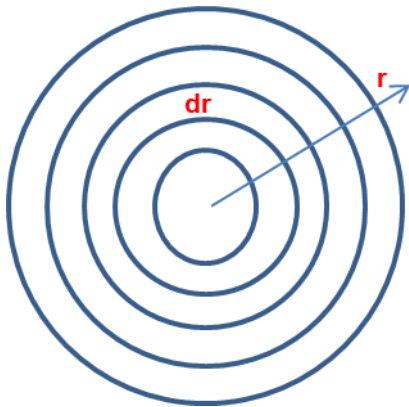


Figure 3.23- Cross-section of pipe showing division into annular regions in which the volumetric flow rate is evaluated

To determine the volumetric flow rate ( $Q$ ), the pipe's cross-section is split into annular elements (Figure 3.23). An annulus has the area of a ring between radius  $r$  and  $(r+dr)$ . If each annulus is sufficiently thin, it can be assumed that the velocity is constant in each ring.

The volumetric flow rate in an annulus can be determined from:

$$dQ = u_r 2\pi r dr \quad \text{Equation 3.47}$$

The total volumetric flow rate can therefore be found by integrating this equation across the whole pipe. For this, Equation 3.42 is substituted in for  $u_r$ .

$$\int_0^Q dQ = 2\pi \int_0^R u_r r dr \quad \text{Equation 3.48}$$

This now gives the Hagen-Poiseuille equation:

$$Q = \frac{\pi(-\Delta P)}{8\eta l} R^4 \quad \text{Equation 3.49}$$

### 3.4.2.2 Average and Maximum Velocities, Shear Rates and Shear Stresses

#### 3.4.2.2.1 Average and Maximum Velocity

The average velocity ( $u_{avg}$ ) in a pipe is the volumetric flow rate divided by the cross-sectional area. Therefore

$$u_{avg} = \frac{Q}{\pi R^2} \quad \text{Equation 3.50}$$

The Hagen-Poiseuille equation can be substituted into this giving:

$$u_{avg} = \frac{(-\Delta P)}{8\eta l} R^2 \quad \text{Equation 3.51}$$

As detailed in 3.4.2.1.2, the maximum velocity (i.e. at the centre of the pipe) is given by:

$$u_{max} = \frac{(-\Delta P)}{4\eta l} R^2$$

Therefore:

$$u_{avg} = \frac{u_{max}}{2} \quad \text{Equation 3.52}$$

The velocity in the pipe at a particular distance from the centre can therefore be written in terms of the average velocity.

$$u_r = 2u_{avg} \left(1 - \frac{r^2}{R^2}\right) \quad \text{Equation 3.53}$$

### 3.4.2.2 Average and Maximum Shear Rates

Since the shear rate is the velocity gradient, a term for the shear rate at any point from the pipe centre can be obtained by differentiating Equation 3.53 with respect to  $r$ .

$$\dot{\gamma}(r) = -\frac{du_r}{dr} = \frac{4ru_{avg}}{R^2} \quad \text{Equation 3.54}$$

At the pipe walls, the shear rate is at its maximum.  $r=R$  therefore:

$$\dot{\gamma}_{max} = \frac{4u_{avg}}{R} = \frac{8u_{avg}}{d} \quad \text{Equation 3.55}$$

The average shear rate across the pipe can be found from:

$$\dot{\gamma}_{avg} = \frac{1}{R-0} \int_0^R \dot{\gamma}(r) dr = \frac{2u_{avg}}{R} = \frac{4u_{avg}}{d} \quad \text{Equation 3.56}$$

### 3.4.2.2.3 Average and Maximum Shear Stresses

Since  $\tau = \eta\dot{\gamma}$  for a Newtonian fluid, the equations for the maximum and average shear stress, and how it varies as a function of position, can be obtained by multiplying those deduced for the shear rate by the viscosity.

Shear stress as a function of position from the pipe centre:

$$\tau(r) = \frac{4\eta ru_{avg}}{R^2} \quad \text{Equation 3.57}$$

At the pipe walls, the shear stress is at its maximum.  $r=R$  therefore:

$$\tau_{max} = \frac{4\eta u_{avg}}{R} \quad \text{Equation 3.58}$$

The average shear stress across the pipe can be found from:

$$\tau_{avg} = \frac{1}{R-0} \int_0^R \tau(r) dr = \frac{2\eta u_{avg}}{R} \quad \text{Equation 3.59}$$

### 3.4.3 Theory for non-Newtonian Flow

For non-Newtonian flows, such as those used in this work (concentrated colloidal suspensions in [Chapter 4](#) and [Chapter 5](#) and concentrated cornflour-water suspensions in [Chapter 8](#)), the theory in section 3.4.2 must be adjusted.

The equation for the maximum shear rate can be adjusted by adding a correction (C).

$$\dot{\gamma}_{max} = C \left( \frac{8u_{avg}}{d} \right) \quad \text{Equation 3.60}$$

For a power-law fluid (detailed in [Chapter 2](#)), the following correction can be used to estimate the maximum shear rate [1, 19, 20]:

$$C = \left( \frac{3n+1}{4n} \right) \quad \text{Equation 3.61}$$

Therefore, the wall shear rate of a power law fluid can be written as:

$$\dot{\gamma}_{max} = \left( \frac{3n+1}{4n} \right) \frac{8u_{avg}}{d} \quad \text{Equation 3.62}$$

This is the Rabinowitsch-Mooney relation and for power-law fluids, n is the power-law index of the fluid [19]. For shear thickening fluids, n>1, as detailed in [Chapter 2](#). For cornflour-water suspensions of the concentrations used in this work, power law indices in the region of 2-4 are typical [21]. This means the maximum shear rate would be ~80-90% of the maximum shear rate obtained with a Newtonian fluid.

## 3.5 Conclusions

Two suitable flow geometries were designed and characterised. The primary geometry designed was a rotating cylinder shear cell. The flow within this geometry was characterised and it was checked that flow instabilities were not occurring. The motor used in the shear cells was characterised to allow a better understanding of the set-up.

This design of shear cell is used significantly in [Chapter 4](#) and [Chapter 5](#). It is also further characterised in [Chapter 4](#) where its input voltage is converted to a shear stress and its rotational rate is used to obtain a shear rate.

The second geometry involved simple pipe flow. Basic theory and set-up methodology for it was investigated. This geometry is used significantly in [Chapter 8](#).

A	Arc length (maximum displacement)
C	Correction factor
d	Diameter
DC	Direct current
$E_b$	Back EMF
I	Current
$K_b$	Motor constant
$K_m$	Motor constant
l	Pipe length
N	Rotational rate
n	Power law index
PMMA	Poly(methyl methacrylate)
P	Power
$\Delta P$	Pressure drop due to friction
Q	Volumetric flow rate
R	Resistance
R	Pipe radius
r	Radius of core of fluid (i.e. distance from pipe centre) Or radial distance from shear cell centre
$R_m$	Motor resistance
Re	Reynolds number
$r_{in}$	Inner cylinder radius
$r_{out}$	Outer cylinder radius
T	Torque (externally applied)
$T_f$	Torque from internal friction
$T_0$	Torque generated by motor
$T_s$	Stall torque
t	Time
Ta	Taylor number
u	Velocity
$U_r$	Velocity at radius r
$U_{avg}$	Average pipe velocity
V	Voltage
v	Velocity
$\nabla v$	Velocity gradient (shear rate)
$v_{max}$	Maximum velocity
x	Volume fraction
y	Displacement
$\dot{\gamma}$	Shear rate
$\eta$	Viscosity
$\eta_k$	Kinematic viscosity
$\theta$	Angle of oscillation in radians (1/2 of peak-to-peak rotation degrees)
$\rho$	Density
$\tau_r$	Shear stress at radius r
$\tau_w$	Wall shear stress
T	Shear stress
$\omega$	Vorticity
$\omega$	Angular rotation speed
$\omega_n$	No load speed

1. Barnes, H., *A Handbook of Elementary Rheology*. 2000: The University of Wales Institute for Non-Newtonian Fluid Mechanics.
2. Cheng, N.S., *Formula for the viscosity of a glycerol-water mixture*. Industrial & Engineering Chemistry Research, 2008. **47**(9): p. 3285-3288.
3. Wereley, S.T. and R.M. Lueptow, *Spatio-temporal character of non-wavy and wavy Taylor-Couette flow*. Journal of Fluid Mechanics, 1998. **364**: p. 59
4. Coronado-Matutti, O., P.R.S. Mendes, and M.S. Carvalho, *Instability of inelastic shear-thinning liquids in a Couette flow between concentric cylinders*. Journal of Fluids Engineering-Transactions of the Asme, 2004. **126**(3): p. 385-390.
5. Lueptow, R., *Taylor-Couette flow*. 2009: Scholarpedia.
6. Taylor, G.I., *Stability of a viscous liquid contained between two rotating cylinders*. Philosophical Transactions of the Royal Society of London Series a-Containing Papers of a Mathematical or Physical Character, 1923. **223**: p. 289-343.
7. Brenner, M. and T. Katopodes, *Classical Physics through the work of G.I. Taylor*. 1998, Harvard University.
8. Avila, M. *Taylor-Couette Flow*, Universitat Politècnica de Catalunya. 2005; Available from: <http://www-fa.upc.es/websfa/fluids/marc/tc.php?lang=eng>.
9. Dou, H.S., B.C. Khoo, and K.S. Yeo, *Instability of Taylor-Couette flow between concentric rotating cylinders*. International Journal of Thermal Sciences, 2008. **47**(11): p. 1422-1435.
10. Ashrafi, N. and R.E. Khayat, *Shear-thinning-induced chaos in Taylor-Couette flow*. Physical Review E, 2000. **61**(2): p. 1455-1467.
11. Ashrafi, N. *Stability of shear thickening flow between rotating cylinders*. in *15th International Congress on Rheology/80th Annual Meeting of the Society-of-Rheology*. 2008. Monterey, CA.
12. Ashrafi, N., *Stability of Shear-Thickening and Shear-Thinning Fluids in Narrow Gap between Rotating Cylinders*. Majlesi Journal of Mechanical Engineering, 2011. **4**(2): p. 65.
13. Weisberg, A.Y., I.G. Kevrekidis, and A.J. Smits, *Delaying transition in Taylor-Couette flow with axial motion of the inner cylinder*. Journal of Fluid Mechanics, 1997. **348**: p. 141-151.
14. Andereck, C.D., S.S. Liu, and H.L. Swinney, *Flow Regimes In A Circular Couette System With Independently Rotating Cylinders*. Journal of Fluid Mechanics, 1986. **164**: p. 155-183.
15. MIT. *Understanding DC Motor Characteristics*. 1999; Available from: <http://lancet.mit.edu/motors/motors3.html>.
16. University of Minnesota, *Understanding DC Motors*. 2014; Available from: <http://www.me.umn.edu/courses/me2011/arduino/technotes/dcmotors/motor-tutorial/>.
17. Micromo. *DC Motor Calculations*. 2013; Available from: <http://www.micromo.com/motor-calculations>.
18. Simple-Motors, *Torque and Efficiency Calculations*. 2014, Simple Electric Motors.
19. Coulson, J. and J. Richardson, *Coulson and Richardson Volume 1: Fluid Flow, Heat Transfer and Mass Transfer*. 1999.
20. Secco, R., *Fluid Viscosity Measurement*. 1999: The University of Western Ontario.
21. Steffe, J., *Rheological Methods in Food Process Engineering*. 1996: Freeman Press.

# 4. Visual Investigation of Jamming in Concentrated Suspensions

## This section will cover:

- The experimental procedures for setting up the rotating cylinder shear cells detailed in **Chapter 3**.
  - The experimental procedures for preparing concentrated colloidal suspensions.
  - The experimental procedures for visually analysing the flow under steady and oscillatory shear.
  - The results obtained from steady and oscillatory shear experiments.



Note: In this work, discontinuous shear thickening and jamming are often used interchangeably. Strictly speaking, jamming should only be used when the flow is completely arrested, resulting in complete jamming. More details of this are given in Chapter 2 and 5.3.9.

## 4.1 Summary

As an initial stage of the work, the effects of flow on concentrated colloidal suspensions were investigated visually. As outlined in [Chapter 3](#), the rotating cylinder shear cells used for flowing the concentrated colloidal suspensions were designed to be placed under an optical microscope, therefore allowing samples to be visualised while undergoing shear. The flow could also be visualised macroscopically to allow larger scale features to be identified. A comprehensive analysis of the effects of flow on concentrated suspensions and how it may be seen visually is lacking in literature hence the purpose of this work [1].

In this work the flow of concentrated colloidal suspensions was visually analysed for a range of different conditions, for example different sample volume fractions and shear stresses. Main findings included macroscopically seeing the sample dilating (volumetrically expanding) at the open surface (fluid-air interface) and characterising the extent of this. Microscopically, interesting results were seen as the sample dilated. The flow appeared to slow down notably, and this was followed by significant cracking and breaking. These visual effects were thought to be signatures of flow induced jamming/ discontinuous shear thickening. The conditions required for this dilating/jamming behaviour were investigated and mapped.

To our knowledge, such clear microscopic images of a sample undergoing jamming have not been reported. A systematic visual study, such as the following, is also lacking in literature.

The shear cells were also calibrated further from the work done in [Chapter 3](#) to allow shear stresses and shear rates to be obtained. A calibration was performed to allow the shear cell input voltage to be converted to a shear stress. This suggested a linear relationship between shear stress and supplied voltage. The rotational rate of the rotating cylinder could be used to obtain a shear rate.

The work done in this chapter leads onto the work done in [Chapter 5](#) where a novel technique to investigate jamming was designed and used to overcome the limitations of visual experiments (e.g. they rely on human judgement and are difficult to quantify). The findings of this chapter are also referred to in [Chapter 7](#), where the results are compared to those found using a commercial rheometer.

## 4.2 Experimental Procedures

### 4.2.1 Materials and Apparatus

Details of how the shear cells discussed in [Chapter 3](#) were operated and how the concentrated colloidal suspensions used were prepared are given in this section.

#### 4.2.1.1 Shear Cell Set-up and Calibration

Volume fractions ( $\Phi$ ) ranging from 0.54-0.61 of PMMA (488 $\pm$ 5 nm radius) suspensions, index matched in decalin and tetralin, were sheared in rotating cylinder shear cell geometries to investigate the effects of Couette flow on concentrated suspensions. A description of the colloid preparation procedure is given in 4.2.1.3. Details of particle sizing are given in [Chapter 7](#) where dynamic light scattering was used to analyse samples.

The main details of shear cell set-up and characterisation are given in [Chapter 3](#). To summarise, the shear cells consisted of two concentric cylinders; the inner cylinder was allowed to rotate while the outer cylinder was kept fixed. The rotating inner cylinder was mounted on a motor's shaft and its movement was controlled by the voltage supplied by a signal generator (which could be varied between 0 and 10.8V). Different gap sizes between the inner and outer cylinder could be achieved by changing the size of the cylinders. The space between the cylinder bases was kept fixed. The shear cells were designed so that they could be placed under an optical microscope, therefore allowing samples to be viewed on a microscopic level while undergoing shear. The flow could also be visualised macroscopically simultaneously to allow larger scale features to be identified. Shear cells had an open top surface to aid visualisation.

As mentioned in [Chapter 3](#), the shear cells were characterised and calibrated further to allow the shear stress and shear rate to be determined from a given supply voltage and rotational rate respectively. The rotational rate was used to determine the shear rate and the input voltage was used to determine the shear stress, as follows.

The rotational rate of the inner cylinder was measured using a tachometer. This allowed an average shear rate across the gap to be estimated from Equation 4.1:

$$\dot{\gamma} = \frac{2\pi N r_{in}}{r_{out} - r_{in}}$$

**Equation 4.1**

Here  $\dot{\gamma}$  is the shear rate,  $N$  is the rotational rate,  $r_{in}$  is the inner cylinder radius and  $r_{out}$  is the outer cylinder radius.

To allow the shear stress as a function of supplied voltage to the shear cell to be determined, a calibration with Newtonian glycerol and water-glycerol mixtures was performed to see how the rotational rate of the inner cylinder varied with the supplied voltage. A linear relationship was found, with the rotational rate increasing with increased voltage (as was expected from [Chapter 3](#)). Since this allowed the shear rate as a function of voltage to be determined, and the viscosity was known (from literature), this allowed the shear stress as a function of voltage to be deduced since from Equation 4.2:

$$\tau = \eta \dot{\gamma}$$

**Equation 4.2**

Here  $\tau$  is the shear stress,  $\eta$  is the viscosity and  $\dot{\gamma}$  is the shear rate.

Calibration Example: With pure glycerol in the shear cell, the rotation rate (and therefore shear rate) increased linearly with voltage. Since glycerol is Newtonian, the viscosity was constant at a given temperature ( $1.4 \text{ Ns/m}^2$  at  $20^\circ\text{C}$ ) [2]. Therefore the shear stress varied linearly with voltage, since  $\tau = \eta \dot{\gamma}$  (Figure 4.1).

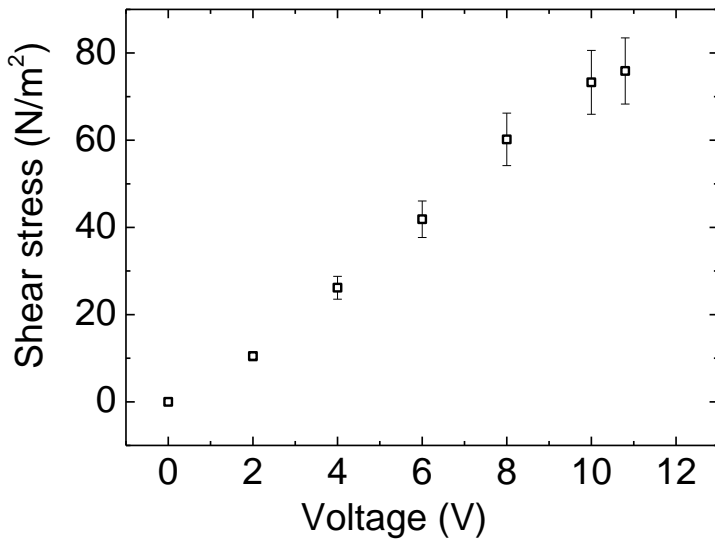


**Figure 4.1- Variation of shear stress with voltage with glycerol in shear cell. Shear stress was calculated from Equation 4.2. Error bars show standard deviation of repetitions.**

On average, it was deduced that:

$$\tau \left[ \frac{N}{m^2} \right] = 6.7 \pm 0.4 \times \text{voltage } [V] \quad \text{Equation 4.3}$$

This meant that the shear stress could have varied by  $\pm 6\%$  of its quoted value. For example, at a voltage of 10.8V, while a shear stress of 72.4 N/m<sup>2</sup> was quoted, it could have varied from 68.0 N/m<sup>2</sup> to 76.7 N/m<sup>2</sup>.

This was repeated with an 80% glycerol-water mixture and its calibration lay within the error bars of pure glycerol's calibration ( $\tau=6.6 \pm 0.2 \times \text{voltage}$ ). This suggested the calibration was reliable, and for the remainder of this thesis, Equation 4.3 is used as the relationship between voltage and shear stress.

It is worth noting that at a fixed voltage (and shear stress), when the shear cell was filled, the rotational rate of the inner cylinder (and therefore shear rate) decreased as the mixture became more concentrated (e.g. colloid volume fraction increased). This was due to the increased viscosity of the suspensions with increasing concentration.

The viscosity of glycerol (1.4 Ns/m<sup>2</sup>) was close to the zero shear viscosity of  $\Phi=0.56-0.59$  colloid samples, where the zero shear viscosity varied from 0.85-2.0 Ns/m<sup>2</sup>. Details of this are given in [Chapter 7](#) where a rheometer was used to analyse samples.

#### 4.2.1.2 Visual Observation Equipment

Macroscopic visual observations were performed using a high speed digital camera (Casio EX-ZR1000). Measurements at 480 frames per second were made. Microscope observations were made using a microscope camera (Edmund Optics EO-3122C) attached to an optical microscope (Zeiss Axioskop FS 5x magnification). The camera's maximum speed was 24 frames per second. Images were processed using Image J. As shown in [Chapter 3](#), the microscope objective or camera lens was placed above the gap between the rotating and stationary cylinders, allowing fluid within the gap to be visualised.

#### **4.2.1.3 Concentrated Colloidal Suspension Preparation**

The colloid particles used were monodisperse polymethylmethacrylate (PMMA) spheres. These were sterically stabilised with poly-(12 hydroxystearic acid) (PHSA) polymer hairs, which were approximately 10nm in length [3].

Particles were dispersed in a refractive index matched solvent to minimise van der Waals interactions, as explained below and in [Chapter 1](#). Colloidal suspensions of this type are commonly used throughout literature since the colloids are a good representation of ideal hard spheres: particles can be assumed to only interact through the hard sphere potential [4-7]. This is detailed in [Chapter 1](#).

#### Chemicals

Poly(methyl methacrylate) (PMMA), decahydronaphthalene (decalin) mixture of cis and trans isomers and 1,2,3,4-tetrahydronaphthalene (tetralin).

#### Procedure

A PMMA/decalin pre-prepared mixture (obtained from the Soft Matter Physics Department at Edinburgh University [8-11]) was centrifuged for 2 hours at 3000 RPM. The supernatant was discarded and the mass of sediment was determined (mass of tube plus sediment- mass of empty tube).

The mass of solid (PMMA) and solvent present in the sediment was determined; for this it was assumed that the solid volume fraction of the sediment was 0.64: that corresponding to random close packing. Tetralin (filtered using a 0.45 $\mu$ m PTFE filter) was added to the sediment to get the refractive indices of the PMMA and overall solvent to closely match. For this, the solvent was ~33% v/v tetralin and 67% v/v decalin overall. This was shaken and mixed by a vortex mixer to ensure that all PMMA particles were dispersed.

The solution was centrifuged again (2 hours at 3000RPM) and the supernatant was discarded. Again, the mass of solid and solvent present in the sediment was determined. A calculated volume of filtered refractive index matched solvent (~33% v/v tetralin and 67% v/v decalin) was then added to this to obtain the desired solid volume fraction. This was shaken and mixed by a vortex mixer to ensure that all PMMA particles were dispersed and the sample was homogeneous.

By matching refractive indices, van der Waals interactions between colloid particles are minimised. Close matching also minimises light scattering [12].

Particle sizes were obtained from dynamic light scattering (DLS) based on a dilute PMMA and decalin mixture. Particles were  $488 \pm 5$  nm in radius unless stated otherwise. Further details of particle sizes and particle size distributions are given in [Chapter 7](#).

### Uncertainty in Solid Volume Fraction

Despite care being taken to ensure volume fraction consistencies, work suggests that the actual volume fraction is unlikely to be known any better than  $\pm 3\text{--}6\%$  [3, 13]. With the experimental procedure for preparing the colloids detailed above, errors are likely to have come from the following:

- The actual value of random close packing is not known exactly [3, 14]. The 0.64 value used may therefore not have been correct.
- The effect of polydispersity on random close packing is not well understood [3]. Since the colloids used were highly monodisperse (as detailed in [Chapter 7](#)), the effect of this is likely to have been small.
- The solvents used may have caused particle swelling which could have influenced volume fractions [13]. Tetralin in particular is known for this [3, 5, 9].
- Centrifugation may have caused the sediment to compress and it may then have expanded after the cessation of centrifugation [3, 13]. This would have introduced additional uncertainty.
- Little is known about the dependence of sediment structure on centrifugation protocol [3].

So long as a consistent procedure was followed in preparing the suspensions (e.g. in terms of centrifugation), then the volume fraction of the sediment likely took on a reproducible value [3]. This meant there was essentially a systematic error in knowing the true value of the solid volume fraction, but all experiments performed were based on the same assumption.

Volume fraction inconsistencies likely occurred when transferring the stock sample to the equipment. If a narrow opening or high shear pipette for example, was used to transfer a high volume fraction sample, self-filtration may have occurred [15]. This

would have meant the volume fraction of the collected sample was lower than the stock. To avoid this, gentle pouring of the sample into the shear cells was done.

It was also important to ensure samples were homogeneous before being transferred for use. Within a stock container, the local volume fractions may have differed from the global volume fraction, which may have led to errors when obtaining samples from the stock [16]. Samples were well mixed by a vortex mixer prior to use to ensure homogeneity.

To minimise the effects of these sources of error, care was taken to ensure consistent procedures were followed. This meant that sample volume fractions should have been consistent and comparable, even though their absolute value could not be exactly known. As mentioned, work suggests that the actual volume fraction is unlikely to be known any better than  $\pm 3\text{-}6\%$  [3, 13]. This meant that what was stated as a  $\Phi=0.55$  sample, for example, may have actually had a volume fraction as low as 0.52 or as high as 0.58.

## 4.2.2 Steady Shear Experiments

This section outlines the main experiments that were performed to investigate the effects of steady shear on the concentrated colloidal suspensions.

### 4.2.2.1 Effect of Volume Fraction, Shear Stress and Shear Rate

In the first set of experiments, various volume fractions (ranging from 0.54-0.61) of the concentrated colloidal suspensions (488 $\pm$ 5nm radius) were sheared in the rotating inner cylinder shear cells. A shear cell with a 5mm gap and ~9mm fill height was used. The shear cell's inner cylinder had a 25mm diameter and the outer was 35mm. Further experiments used different gap sizes to see the role of geometry (see 4.2.2.2 and [Chapter 5](#)).

For the visual experiments, conditions that resulted in what appeared to be some form of visible jamming/dilatancy/discontinuous shear thickening were investigated. This involved gradually increasing the voltage supplied to the motor and noting the voltage where jamming became visually evident. The rotational rate at this point was determined using a tachometer. This allowed the minimum shear stress and shear rate required for jamming to be determined. This was repeated at various volume fractions to allow trends to be identified.

The rotational rate as a function of supplied voltage (from 0 to 10.8V) was also determined for each volume fraction. This allowed shear rate versus shear stress profiles to be deduced.

The rotational rate quoted was an average, since when jamming occurred, the rotational rate was not constant. At a particular set of conditions, the rotational rate was measured at regular time intervals (every minute) and an average of the readings was determined. It was not possible to measure an instantaneous shear rate as the rotating cylinder had to complete a full revolution to allow a rotational rate to be determined by the tachometer. During measurements, the rotational rate varied due to the jamming and unjamming of the suspensions, as later detailed. An average was therefore deemed as the most suitable way to present the shear rate. It was found that despite the rotational rate of the inner cylinder varying, measured averages appeared consistent throughout an experiment, typically varying by a maximum of 15%. This was within the error of repeat experiments.

#### **4.2.2.2 Effect of System Geometry**

A procedure similar to the above was performed, however, this time colloid samples were sheared in shear cells with different gap sizes between the inner and outer cylinders (2.5mm and 10mm), compared to the 5mm arrangement previously used. Different gaps were obtained by changing the diameter of the rotating inner cylinder.

#### **4.2.2.3 Minimum Voltage/ Stress for Motion**

The minimum voltage/ stress required to get the inner cylinder to rotate (and therefore shear the material) was measured for various volume fractions (0.56-0.61), including when the shear cell was empty. The difference between this stress and the minimum stress required to observe jamming was determined.

#### **4.2.2.4 Velocity Decrease during Jamming**

Macroscopic video clips of the colloids being sheared at the maximum voltage were analysed to estimate the reduction in velocity of the rotating inner cylinder during jamming. It was hoped that analysing the velocity reduction would give an insight into how ‘extreme’ jams were. Estimations were approximate due to possible inaccuracies in measuring the rotating cylinder’s displacement in a given time; it was assumed that the displacement was linear. This was reasonable given that only small displacements were considered.

#### **4.2.2.5 Effect of Rotating Outer Cylinder (rather than Inner)**

A set-up where the outer cylinder was rotating and the inner was fixed was also used for comparison (Figure 4.2).

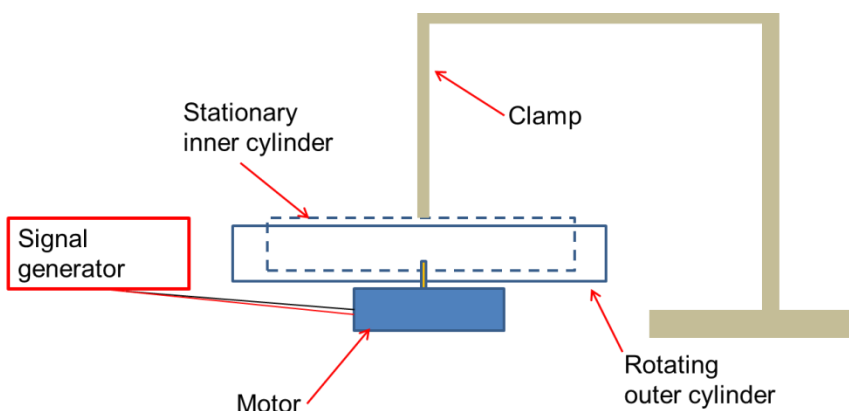


**Figure 4.2- Rotating outer cylinder shear cell set-up**

As before, conditions required for jamming were investigated (volume fraction, shear stress, shear rate etc.). These conditions were then compared to those required with the inner cylinder rotating. A shear cell with a 5mm gap and ~9mm fill height was used. The shear cell's inner cylinder had a 25mm diameter and the outer was 35mm.

A voltage/shear stress calibration was performed with glycerol for the rotating outer cylinder geometry. The results differed slightly from the rotating inner cylinder arrangement.

$$\text{For the rotating outer cylinder: } \tau \left[ \frac{N}{m^2} \right] = 5.3 \times \pm 0.4 \text{ voltage [V]} \quad \text{Equation 4.4}$$

$$\text{For the rotating inner cylinder: } \tau \left[ \frac{N}{m^2} \right] = 6.7 \pm 0.4 \times \text{voltage [V]} \quad \text{Equation 4.5}$$

This may have been due to a number of reasons. For example, weight, frictional and fill height differences may have contributed. For the rotating outer cylinder arrangement, a clamp was used to hold the inner cylinder stationary. This made alignment difficult and it was difficult to ascertain if the inner cylinder was truly stationary. The gap between the inner cylinder and the base may also have differed slightly to the previous arrangement, due to the clamp not holding the inner cylinder entirely flat. The rotating inner cylinder arrangement was considerably simpler to set-up since parts were machined to fit together concentrically and no additional clamp was required.

#### **4.2.2.6 Effect of Particle Size**

The effect of particle size was investigated by performing a range of experiments with  $287 \pm 4$  nm radius PMMA particles and comparing results to those with the  $488 \pm 5$  nm radius particles used previously. Samples were investigated across a range of conditions (different volume fractions, various supply voltages to the motor and with different shear cell gap sizes).

### **4.2.3 Oscillatory Shear Experiments**

This section outlines the main experiments that were performed to investigate the effects of oscillatory shear on the concentrated colloidal suspensions.

#### **4.2.3.1 Effect of Volume Fraction, Shear Stress, Strain and Shear Frequency**

A similar procedure to steady shear was performed, but now with oscillatory shear. Sinusoidal voltage oscillations were used.

Various volume fractions (ranging from 0.54-0.61) of the concentrated colloidal suspensions (488±5 nm radius) were sheared in the rotating inner cylinder shear cells. A shear cell with a 5mm gap and ~9mm fill height was used. The shear cell's inner cylinder had a 25mm diameter and the outer was 35mm.

Conditions (volume fraction, peak to peak voltage amplitude, strain amplitude and frequency) required for what appeared to be some form of visible jamming were investigated. This involved gradually increasing the peak to peak amplitude of oscillations (i.e. the voltage) and altering the frequency for a range of different concentrations.

#### **4.2.4 Comment on Strengths and Weaknesses of Visual Analysis**

The visual method used had various strengths and weaknesses that should be mentioned. Strengths included that information that could not readily be obtained with a commercial rheometer was obtained, for example visually seeing the material jam. This helped better understand possible mechanisms into why the observed behaviour was occurring. Weaknesses included that the technique relied on human judgement and the visual results were difficult to quantify. For example, without advanced video processing software, manual counting of jams/dilating regions was necessary. This was cumbersome and error prone. The visual results were, however, a good starting point for the work and by combining and using their findings with subsequent chapters, more robust findings were made.

For all experiments, typically three to five repetitions were done. Error bars represent ± one standard deviation.

## 4.3 Results and Discussion

### 4.3.1 Steady Shear Experiments

#### 4.3.1.1 Effect of Volume Fraction, Shear Stress and Shear Rate

For Figure 4.3, Figure 4.4 and Figure 4.5, the rotating inner cylinder was towards the top of the images and the stationary outer cylinder was towards the bottom.



Figure 4.3- Example macroscopic observation in 5mm gap shear cell showing spanning dilating region.  $\Phi=0.59$ ;  $72.4 \text{ N/m}^2$  stress.

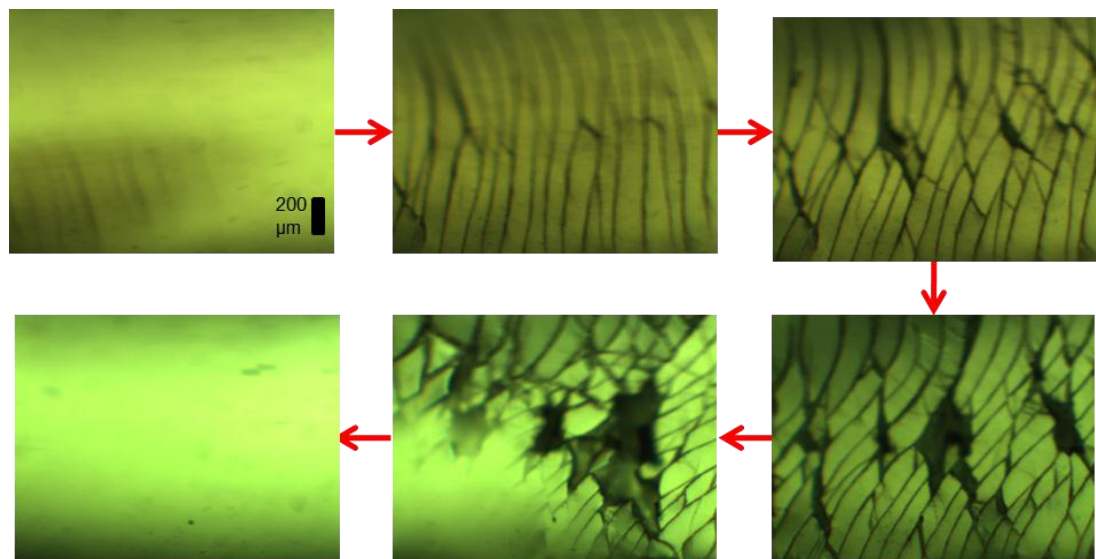
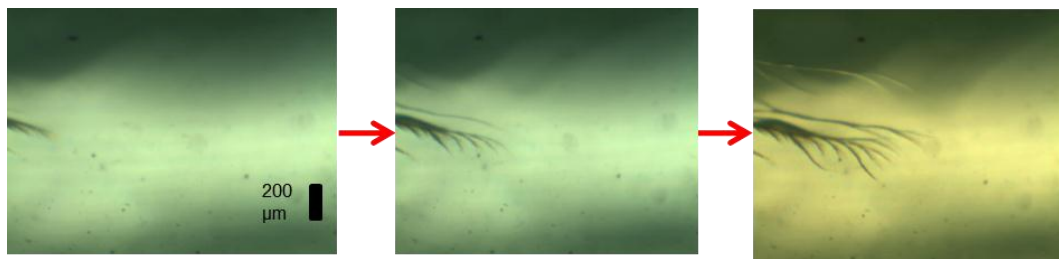


Figure 4.4- Example microscopic observation (5x magnification) in 5mm gap shear cell showing formation and destruction of jammed region.  $\Phi=0.59$ ;  $72.4 \text{ N/m}^2$  stress. Time gap between images was approximately 0.05s.



**Figure 4.5- Example microscopic observation (5x magnification) in 5mm gap shear cell showing growing cracks.  $\Phi=0.59$ ;  $72.4 \text{ N/m}^2$  stress. Time gap between images was approximately 0.05s.**

For the conditions investigated, jamming was only evident during the shearing of samples beyond a particular volume fraction ( $\phi \geq 0.56$ ). This behaviour was identified by the sample showing signs of dilatancy at the open surface [14, 17-21]. Macroscopically (Figure 4.3), a region on the top of the sample began to look drier, rougher and more opaque than the rest of the sample (i.e. it changed from glossy to matt). This is because expansion causes particles to encounter and deform the air-liquid interface and partially exposed particles at the surface scatter light diffusely [1].

This was followed by the material in this region appearing to bulge out of the sample, causing the surface of the region to crack open and fracture. This behaviour could also be seen microscopically (Figure 4.4 and Figure 4.5), where the material changed from flowing like a fluid to solid-like, with signs of fracturing being visible. Patterns observed appeared random and no two jams looked the same. Sometimes jammed regions spanned the entire gap, and sometimes just partially jammed/dilating regions were observed.

As dilatancy became apparent, for example when ‘drier’ regions appeared on the surface macroscopically, the rotating inner cylinder (and therefore flow) slowed down. Slowing down occurred as the dilating regions first became evident. As the regions broke up, e.g. through cracking as shown in Figure 4.4, the rotating cylinder returned to its initial speed. The extent the rotating cylinder slowed down varied throughout an experiment.

In this chapter, a ‘jam’ refers to the sighting of an individual dilated region (e.g. Figure 4.3) or fractured region seen microscopically (e.g. Figure 4.4 and Figure 4.5).

## Possible Mechanism

As mentioned in [Chapter 2](#), dilatancy that is frustrated is thought to be a possible mechanism for jamming [1, 22]. Hydroclusters may form (via the hydroclustering mechanism). The presence of hydroclusters could lead to continuous shear thickening due to their hydrodynamic impact. At certain volume fractions and beyond a critical shear rate, however, discontinuous shear thickening or jamming may occur. Here force transmitting hydroclusters with frictional contacts (due to very close particle proximity and the breakdown of lubrication) may span the system (e.g. across the gap) and these must dilate in order to flow [1, 23-25]. Dilation of the frictional force transmitting hydroclusters against a frustrated system boundary may therefore lead to the large fluctuations in stress and dramatic increases in viscosity associated with discontinuous shear thickening and jamming.

In the shear cells, attempted expansion towards the solid system boundaries would result in large confining stresses, causing resistance to motion. Therefore, the material dilates most successfully out of the open surface since it is here that additional volume can most readily be obtained (the confining capillary stress at the open surface is the weakest confining stress) [1].

As the growth (and expansion) of the clusters causes particles to encounter and deform the air-liquid interface, a large confining capillary stress at the surface is generated. This confining stress depends on the particle size and suspending medium surface tension ( $\tau_{capillary} = \frac{\gamma}{d}$  where  $\gamma$  is the liquid surface tension and  $d$  is the particle diameter) and this (combined with the stronger confining effects of the solid boundaries and particle stiffness) can balance out interparticle and shear forces, resulting in the region resisting motion. Forces and further dilation may then cause the jammed material to fracture if the confining capillary stress at the surface is overcome (it is the weakest of the confining stresses) [14, 17]. Flow may therefore continue, until the next 'jam' occurs.

The presence of the visible dilating regions provides evidence of the formation of frictional force transmitting hydroclusters or a network of force chains. Since there is a confining capillary stress at the air-liquid interface acting to push particles into the fluid, the fact that the particles penetrate the surface is evidence that the forces must be transmitted through the interior via the frictional contacts in the clusters/force chains [1].

It was found that as volume fraction was increased, the average number of jams for a fixed rotation of the inner cylinder increased and the maximum time gap between jams decreased. Further consideration of the count, intensity and time gap between jams is given in [Chapter 5](#) since measuring these parameters was challenging and prone to error visually.

#### Minimum Shear Stress and Shear Rate for Jamming

It was found that a critical shear stress (Figure 4.6) and a critical shear rate (Figure 4.7) were required for jamming/dilation to be visible. These decreased with increasing volume fraction. These critical shear rates were found to compare closely to measurements made using a rheometer (TA Discovery HR-2) for the onset conditions for discontinuous shear thickening. This is detailed in [Chapter 7](#).

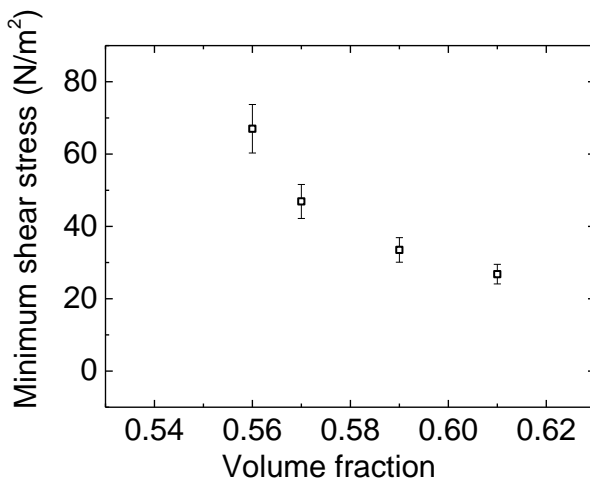


**Figure 4.6- Minimum shear stress required for visible dilation for various volume fractions.**  
Error bars show standard deviation of repetitions.

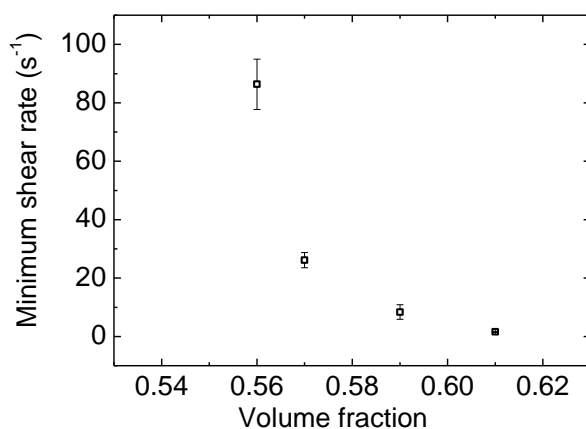


**Figure 4.7- Minimum shear rate required for visible dilation for various volume fractions.**  
Error bars show standard deviation of repetitions.

### 4.3.1.2 Shear Rate versus Shear Stress Flow Profiles

By measuring the rotational rate of the inner cylinder as a function of voltage, shear rate versus shear stress profiles were produced (Figure 4.8). It was found that in systems that showed jamming behaviour, the profiles were curved: beyond a critical point, increasing the supplied voltage (i.e. the shear stress) did not result in the material flowing more quickly (i.e. an increased shear rate). This idea of a material refusing to flow faster beyond a critical rate or load demonstrates discontinuous shear thickening behaviour/jamming [14, 26-28]. The critical point corresponded very closely to the onset of visual signs of dilatancy and jamming. Beyond the point of the visual onset of dilatancy, the profiles flattened and further increases in shear stress did not result in the shear rate steadily increasing.

Dilatancy/jamming may have been a means of energy dissipation; additional energy supplied through increasing the voltage may have been consumed through jamming, hence no increase in speed. This is discussed in more detail in [Chapter 5](#).

In the systems that did not jam visually ( $\phi < 0.56$ ), this curved behaviour was not found, suggesting no strong shear thickening. As detailed in [Chapter 7](#), these flow profiles compared well to those produced using the commercial rheometer.

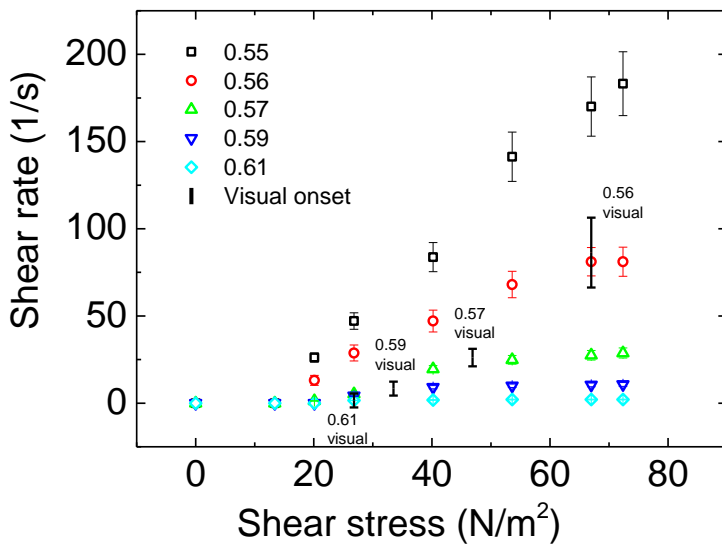


**Figure 4.8-** Shear rate versus shear stress profiles for various volume fractions. Solid lines show where visual onset of dilatancy began from Figure 4.6 and Figure 4.7. Error bars show standard deviation of repetitions.

### 4.3.1.3 Effect of System Geometry

A voltage/shear stress calibration was performed for the geometries with different gaps between the cylinders and it was found that the previous relationship for the 5mm gap geometry was still valid. When the shear cell was filled, with a bigger gap the rotation rate at a particular voltage was larger, but accounting for the geometry, the shear rate was still approximately equal. Since  $\tau = \eta\dot{\gamma}$  and  $\dot{\gamma} = \frac{2\pi N r_{in}}{r_{out} - r_{in}}$ , a larger gap resulted in a larger rotation rate to maintain the same shear rate for a fixed shear stress and viscosity.

For  $\Phi=0.59$  and  $\Phi=0.61$ , with all the gap sizes, the voltage (and therefore shear stress) required to get jamming remained constant (Figure 4.9). At this voltage, the rotation rate required for jamming increased with increasing gap size, but accounting for the geometry, the shear rate required for jamming did not vary substantially (Figure 4.10). This suggested that a particular shear stress/rate was required for jamming at a particular volume fraction, and this was independent of the gap size.

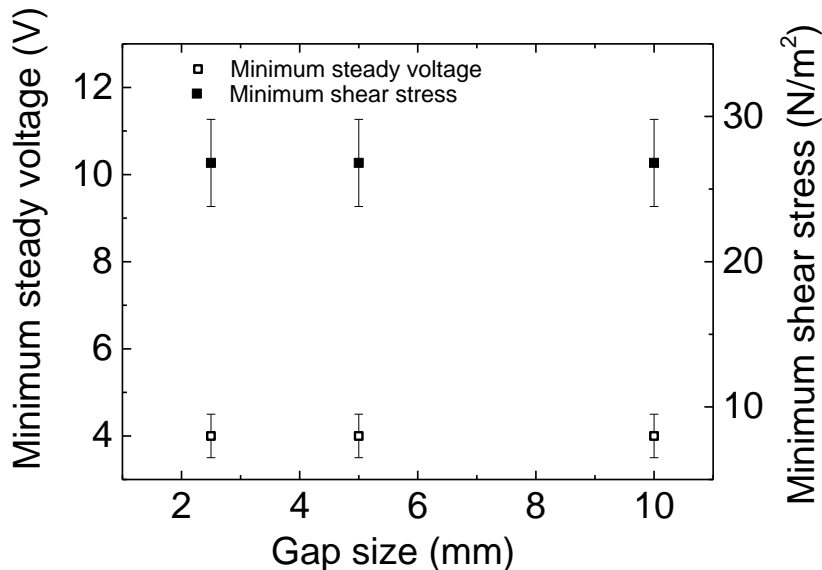
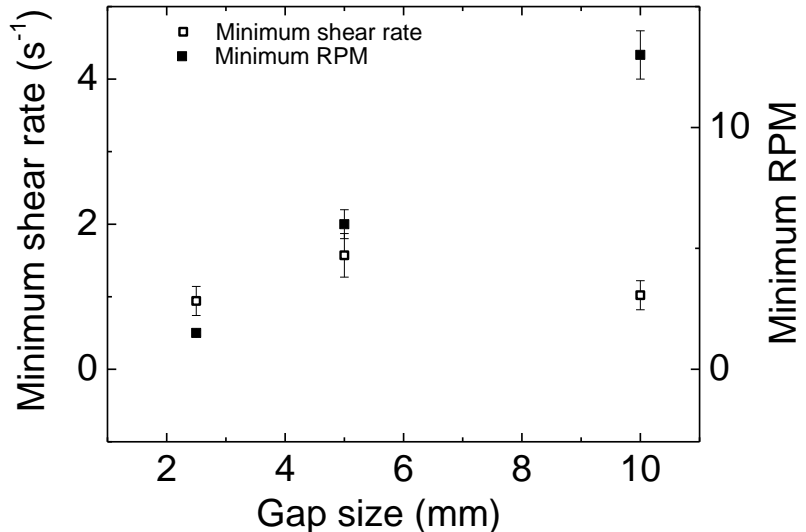


Figure 4.9- Minimum voltage and shear stress required for jamming with different gap sizes ( $\Phi=0.61$ ). Error bars show standard deviation of repetitions.



**Figure 4.10- Minimum RPM and shear rate required for jamming with different gap sizes ( $\Phi=0.61$ ).** Error bars show standard deviation of repetitions.

As gap size was increased, the average number of jams in a given time decreased and the maximum time between jams increased. As the shear cell gap size increased, although the average number of jams decreased, the jams that did occur appeared larger and more obvious; due to the larger gap size, they had to span a greater distance, making them larger and more distinct. Further consideration of the count and extent of jamming, and its dependence on gap size, is given in [Chapter 5](#).

The effect of gap size was then investigated using a sample volume fraction of 0.56 and 0.57. The results for the 2.5mm gap and 5mm gap experiments were as expected from what was found for the  $\phi=0.59$  and  $\phi=0.61$  experiments. The shear stress and shear rate required for jamming remained ~constant for the two gap sizes. This suggested that a particular shear stress/rate was required for jamming at a particular volume fraction

With the 10mm gap, however, no jamming was seen at any of the conditions studied for the  $\Phi=0.56$  and 0.57 samples. It was possible that jamming was occurring at too low a frequency for it to be seen in the observation time (5 minute experiments), or that the time gap possible between jams exceeded the observation time. As previously mentioned, results showed that the number of jams in a given time decreased with increasing gap size and decreased with decreasing volume fraction for a fixed rotation of the inner cylinder. The average and maximum time gap

between jams was shown to increase with increasing gap size and increase with decreasing volume fraction for a fixed rotation of the inner cylinder. This explanation was therefore possible given that this was a larger gap with lower volume fractions. This is considered in more detail in [Chapter 5](#).

#### 4.3.1.4 Minimum Voltage/ Stress for Motion

At  $\phi=0.56$  and  $\phi=0.57$ , a minimum stress of  $20\text{N/m}^2$  was required to get the inner cylinder to start rotating (Figure 4.11). At  $\phi=0.59$  and  $\phi=0.61$ ,  $27\text{N/m}^2$  was required.  $6\text{N/m}^2$  was required to get the inner cylinder to rotate when the shear cell was empty. This suggested that with more viscous suspensions in the shear cell, a greater shear stress was required to overcome initial inertia to motion.

The range of stresses where the cylinder rotated (i.e. the material was sheared) but jamming was not present decreased as volume fraction increased. When  $\phi=0.56$ , the inner cylinder rotated at  $20\text{N/m}^2$ , but it wasn't until  $\sim 70\text{N/m}^2$  that jamming occurred. At  $\phi=0.61$ , however, the inner cylinder began rotating at a stress of  $27\text{N/m}^2$  and jamming also occurred at this point.

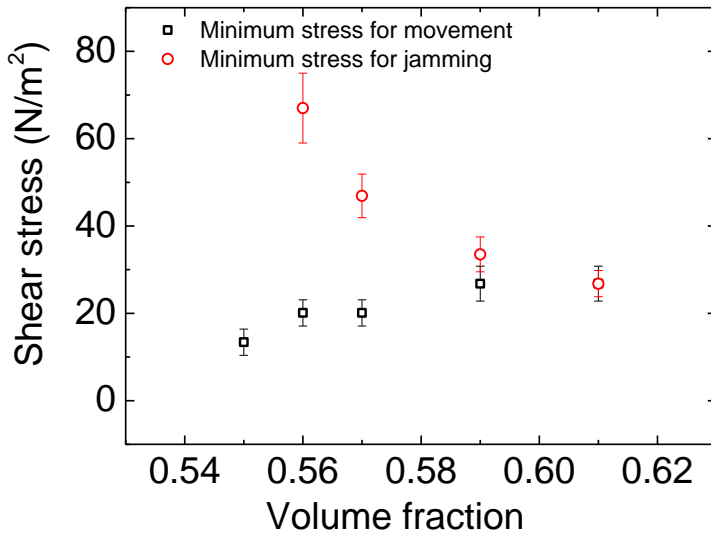


**Figure 4.11-** Minimum stress required for movement (shearing) and jamming with 5mm gap shear cell. Error bars show standard deviation of repetitions.

#### 4.3.1.5 Velocity Decrease during Jamming

Table 4.1- Velocity reduction during jamming for when large dilating regions spanned gap. 72.4 N/m<sup>2</sup> stress. 5mm shear cell gap size.

$\Phi$	Typical jammed velocity for when large dilating regions spanned gap (expressed as % of initial velocity)
0.56	~20-30
0.57	~25-35
0.59	~30-40
0.61	~30-50

The velocity reduction during jamming was estimated by calculating the velocity of the rotating inner cylinder prior to a jam and at the most extreme point of a jam. This was done for events where large dilating regions clearly spanned the entire gap since this was more obvious to observe macroscopically and was associated with large velocity reductions that were easier to measure. Microscope measurements were not possible due to the small field of view and large rotation rates involved. Values presented in Table 4.1 are averages of the velocity reductions in 10 large, spanning dilating region events for each volume fraction.

As mentioned, the velocity of the rotating cylinder decreased during jamming (Table 4.1). As the jammed region broke up, it returned to its initial speed. As volume fraction increased, the extent of velocity reduction decreased. This may have been due to the rotating inner cylinder going at a lower velocity initially due to the more viscous suspension.

Since the inner cylinder was rotating more rapidly in the lower volume fraction experiments, jams must have been more extreme as the amount of speed lost was much more significant. For example, for  $\Phi=0.57$ , the velocity decreased from ~0.15m/s to ~0.05m/s during a large jam. This reduction in speed was significantly more than the decrease from ~0.01m/s to ~0.005m/s seen with the  $\Phi=0.61$  suspensions during a large jam.

This may explain why, as mentioned previously, jams appeared more obvious in the lower volume fraction experiments. One possible picture is that the extent of velocity reduction was related to the intensity/magnitude of the jam; as volume fraction

decreased, there were fewer jams for a fixed rotation of the inner cylinder, but jams had a greater magnitude.

It is worth noting again that the constant jamming and unjamming of the suspensions meant the shear rate was not constant. As explained earlier, shear rates quoted are averages. This seemed the most reliable way to present the shear rate data, given the difficult circumstances.

As mentioned in the experimental procedures section, the velocity decreases measured were approximate. Further consideration of the magnitudes of jams is given in [Chapter 5](#).

#### 4.3.1.6 Effect of Rotating Outer Cylinder (rather than Inner)

With a rotating outer cylinder, in general, it was found that jamming occurred slightly more readily than with the rotating inner cylinder set-up used previously. Slightly lower shear stresses and shear rates were required for the first signs of jamming to become evident (Figure 4.12). The difference, however, did not appear to be statistically significant.

Since in [Chapter 3](#) it was found that instabilities were not occurring with the rotating inner cylinder arrangement and the rotating inner cylinder arrangement was more straight forward to manufacture and use (e.g. with the microscope), it was decided to continue using the rotating inner cylinder arrangement.

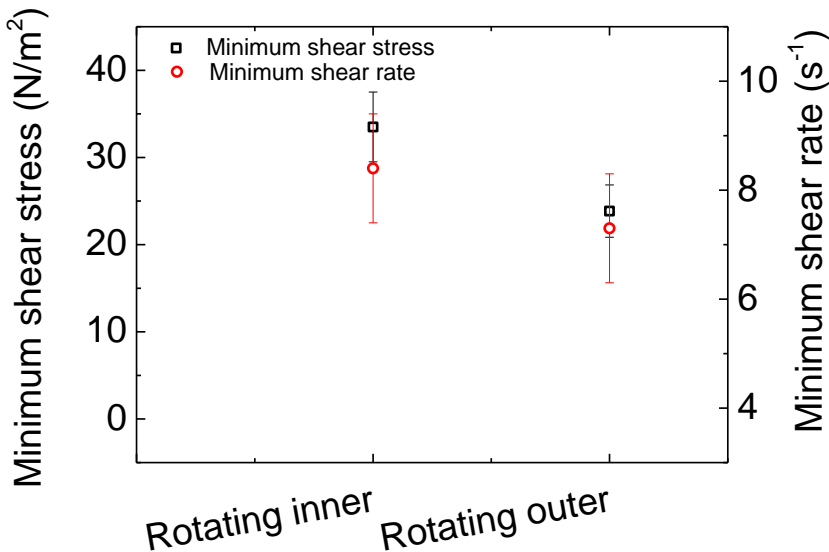


**Figure 4.12-** Minimum shear stress and shear rate required for jamming with rotating inner/outer comparison ( $\Phi=0.59$ ). Error bars show standard deviation of repetitions.

#### 4.3.1.7 Effect of Particle Size

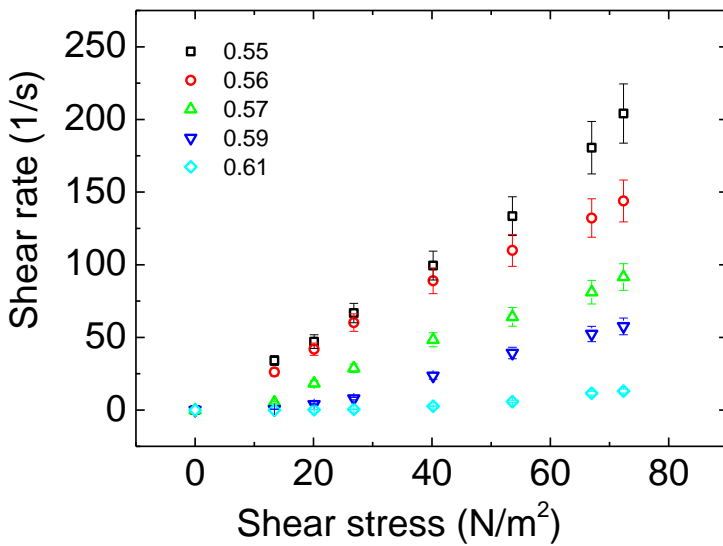


Figure 4.13- Shear rate versus shear stress profiles for 287nm radius particles. Error bars show standard deviation of repetitions.

With  $287 \pm 4$  nm radius particles (compared to  $488 \pm 5$  nm used previously), in the 5mm gap shear cell, no jamming was seen, even at the highest shear stresses and shear rates and with the highest volume fraction used experimentally. This was then repeated in the 2.5mm gap shear cell (previous results showed that a smaller gap size increased the likelihood of jamming). Again, no jamming was seen in any of the conditions studied.

Shear rate versus shear stress profiles similar to those detailed in 4.3.1.2 were obtained for the smaller particle size (Figure 4.13). The curved behaviour that signified jamming/discontinuous shear thickening detailed previously was no longer found. This suggested that shear thickening was not strong in these systems, hence the lack of jamming. The effects of particle size are discussed in more detail in Chapter 5.

## 4.3.2 Oscillatory Shear Experiments

### 4.3.2.1 Effect of Volume Fraction, Shear Stress, Strain and Shear Frequency

Similar trends with oscillatory shear using  $488\pm 5$  nm radius particles were found, with increasing volume fractions resulting in lower peak shear stresses being required for jamming (Figure 4.14). The corresponding peak-peak strain also appeared important: as volume fraction increased, smaller oscillations were required for jamming. As with the steady shear experiments, only samples at  $\Phi \geq 0.56$  showed jamming behaviour.

The effect of frequency was also investigated. In a region where jamming was occurring at 1Hz, increasing the frequency resulted in jamming so long as the strain amplitude remained sufficient. Increasing the frequency eventually resulted in a decrease in the peak to peak amplitude of the rotating cylinder's displacement, and therefore strain amplitude, hence significant increases in frequency (at a fixed peak to peak voltage/stress amplitude) could inhibit jamming. At  $\phi=0.59$  and  $\phi=0.61$ , only very slight strain amplitudes were required for jamming to occur.

It is worth noting that the dilatancy/jams did not appear as pronounced with oscillatory shear compared to steady. Due to this and the wider applications of steady shear, it was decided to concentrate on steady shear experiments for the remainder of the work.

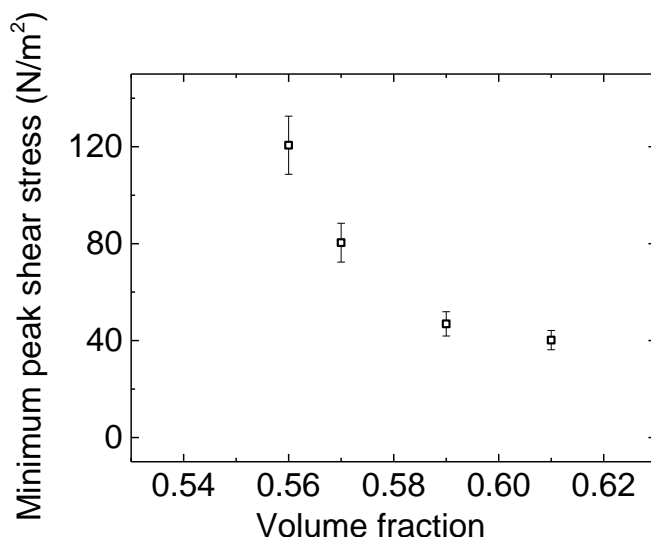


Figure 4.14- Minimum peak shear stress required for jamming for various volume fractions. 5mm gap shear cell with 488nm radius particles at 1Hz. Error bars show standard deviation of repetitions.

## 4.4 Conclusions

Visible signs of discontinuous shear thickening and jamming could be seen when shearing concentrated colloidal suspensions in a rotating cylinder shear cell geometry. Macroscopically, the sample could be seen to dilate at the open surface. Microscopically, interesting results were seen as the sample dilated- the flow appeared to slow down as dilation became visible and this was followed by significant cracking and breaking of the sample. These visual effects were thought to be signatures of flow induced jamming.

Suspension concentration was very important: jamming was only seen at  $\Phi \geq 0.56$ . As volume fraction was increased, the minimum shear stress and shear rate required for jamming decreased. Concentration also appeared to have an important impact on the frequency of jamming.

Flow geometry and particle size appeared to be important. While gap size did not appear to affect the minimum shear stress and shear rate required for jamming at a particular volume fraction, jamming was less likely to occur with larger gap geometries. Jamming did not occur at all with smaller particles ( $287 \pm 4$  nm radius) in the conditions studied.

Due to the limitations of visual experiments (e.g. they rely on human judgement and are difficult to quantify), an idea for a more advanced jamming measurement system was postulated. This forms the basis of [Chapter 5](#) and it overcomes the limitations of the visual experiments.

d	Diameter
N	Rotation rate
r	Radius
$\eta$	Viscosity
$\tau$	Shear stress
$\dot{\gamma}$	Shear rate
$\gamma$	Liquid surface tension

1. Brown, E. and H. Jaeger, *Shear thickening in concentrated suspensions: phenomenology, mechanisms, and relations to jamming*. Reports on Progress in Physics, 2013. **77**(4): p. 046602.
2. Cheng, N.S., *Formula for the viscosity of a glycerol-water mixture*. Industrial & Engineering Chemistry Research, 2008. **47**(9): p. 3285-3288.
3. Poon, W.C.K., E.R. Weeks, and C.P. Royall, *On measuring colloidal volume fractions*. Soft Matter, 2012. **8**(1): p. 21-30.
4. Vermant, J. and M.J. Solomon, *Flow-induced structure in colloidal suspensions*. Journal of Physics-Condensed Matter, 2005. **17**(4): p. R187-R216.
5. Poon, W.C.K., *The physics of a model colloid-polymer mixture*. Journal of Physics-Condensed Matter, 2002. **14**(33): p. R859-R880.
6. Hunter, G.L. and E.R. Weeks, *The physics of the colloidal glass transition*. Reports on progress in physics., 2012. **75**(6): p. 066501.
7. Prasad, V., D. Semwogerere, and E.R. Weeks, *Confocal microscopy of colloids*. Journal of Physics-Condensed Matter, 2007. **19**(11): p. 25.
8. Antl, L., et al., *The Preparation Of Poly(Methyl Methacrylate) Lattices In Nonaqueous Media*. Colloids and Surfaces, 1986. **17**(1): p. 67-78.
9. Segre, P.N., O.P. Behrend, and P.N. Pusey, *Short-Time Brownian-Motion In Colloidal Suspensions - Experiment And Simulation*. Physical Review E, 1995. **52**(5): p. 5070-5083.
10. Pusey, P.N. and W. Vanmegen, *Detection Of Small Polydispersities By Photon-Correlation Spectroscopy*. Journal of Chemical Physics, 1984. **80**(8): p. 3513-3520.
11. Pusey, P.N. and W. Vanmegen, *Observation Of A Glass-Transition In Suspensions Of Spherical Colloidal Particles*. Physical Review Letters, 1987. **59**(18): p. 2083-2086.
12. Ackerson, B.J. and P.N. Pusey, *Shear-Induced Order In Suspensions Of Hard-Spheres*. Physical Review Letters, 1988. **61**(8): p. 1033-1036.
13. Royall, C.P., W.C.K. Poon, and E.R. Weeks, *In search of colloidal hard spheres*. Soft Matter, 2013. **9**(1): p. 17-27.
14. Mewis, J. and N. Wagner, *Colloidal Suspension Rheology*. 2012: Cambridge University Press.
15. Haw, M.D., *Jamming, two-fluid behavior, and "self-filtration" in concentrated particulate suspensions*. Physical Review Letters, 2004. **92**(18): p. 185506.
16. Haw, M.D., *Volume fraction variations and dilation in colloids and granulars*. Philosophical Transactions of the Royal Society a-Mathematical Physical and Engineering Sciences, 2009. **367**(1909): p. 5167-5170.
17. Smith, M.I., et al., *Dilatancy in the flow and fracture of stretched colloidal suspensions*. Nature Communications, 2010. **1**: p. 5.
18. Fall, A., et al., *Shear thickening of cornstarch suspensions as a reentrant jamming transition*. Physical Review Letters, 2008. **100**(1): p. 018301.
19. Fall, A., et al., *Shear thickening of cornstarch suspensions*. Journal of Rheology, 2012. **56**(3): p. 575-591.
20. Brown, E. and H.M. Jaeger, *The role of dilation and confining stresses in shear thickening of dense suspensions*. Journal of Rheology, 2012. **56**(4): p. 875-923.
21. Cates, M.E., M.D. Haw, and C.B. Holmes, *Dilatancy, jamming, and the physics of granulation*. Journal of Physics-Condensed Matter, 2005. **17**(24): p. S2517-S2531.
22. Bi, D., et al., *Jamming by shear*. Nature, 2011. **480**(7377): p. 355-358.

23. O'Brien, V.T. and M.E. Mackay, *Stress components and shear thickening of concentrated hard sphere suspensions*. Langmuir, 2000. **16**(21): p. 7931-7938.
24. Seto, R., et al., *Discontinuous Shear Thickening of Frictional Hard-Sphere Suspensions*. Physical Review Letters, 2013. **111**(21): p. 5.
25. Wyart, M. and M.E. Cates, *Discontinuous Shear Thickening without Inertia in Dense Non-Brownian Suspensions*. Physical Review Letters, 2014. **112**(9).
26. Williamson, R.V. and W.W. Heckert, *Some properties of dispersions of the quicksand type*. Industrial and Engineering Chemistry, 1931. **23**: p. 667-670.
27. Wagner, N.J. and J.F. Brady, *Shear thickening in colloidal dispersions*. Physics Today, 2009. **62**(10): p. 27-32.
28. Freundlich, H. and H.L. Roder, *Dilatancy and its relation to thixotropy*. Transactions of the Faraday Society, 1938. **34**(1): p. 0308-0315.

# 5. Novel Investigation of Jamming in Concentrated Suspensions

## This section will cover:

- The methodology and characterisation of a novel technique designed to investigate jamming quantitatively using a force sensor.
  - The experimental procedures for analysing the flow under steady shear with the force sensor technique.
  - The results obtained from analysing the flow under steady shear with the force sensor technique.
  - A comparison of the results obtained visually in **Chapter 4** with the force sensor technique to allow a link to be deduced.
  - The use of the experimental findings and literature to propose a likely mechanism for discontinuous shear thickening and flow induced jamming.



Note: In this work, discontinuous shear thickening and jamming are often used interchangeably. Strictly speaking, jamming should only be used when the flow is completely arrested, resulting in complete jamming. More details of this are given in Chapter 2 and 5.3.9.

## 5.1 Summary

Due to the mentioned shortcomings of the visual investigations in [Chapter 4](#) (e.g. they rely on human judgement and are difficult to quantify), a more advanced jamming measurement system was designed. This forms the basis of [Chapter 5](#) and it overcomes the limitations of the visual experiments.

This novel technique was designed to measure intermittent forces in the sample that were only present when jamming occurred. The set-up consisted of a probe that was inserted into the gap between the rotating and stationary cylinders in the shear cell. When the material jammed, the probe struck a piezo sensor. A piezo sensor converts an applied stress to a voltage. Therefore, when the material jammed, a voltage peak was seen in the piezo's output. A peak in the piezo's output voltage was therefore taken as analogous to a jam. The piezo's output voltage was calibrated to allow an output voltage to be converted to a force. The jams were thought to be closely related to discontinuous shear thickening (DST), as detailed in [Chapter 2](#) and [Chapter 4](#).

The new technique was used to investigate similar conditions to those investigated visually, for example different sample volume fractions and shear stresses. The output peaks were analysed to allow jamming trends to be identified, such as the effect of concentration on the size and count of peaks. Links between the visual and novel technique were made. The effect of confinement on the sample was also investigated. Based on the experimental findings, a mechanism for discontinuous shear thickening and flow induced jamming was proposed.

The investigative technique designed was highly novel. No such instruments are reported in literature to the best of our knowledge. The data obtained allowed a more thorough and quantifiable investigation of jamming to be made and was more robust and reliable than the visual investigation in [Chapter 4](#). It also led to a further analysis of the statistical distributions of the jamming peaks being considered and that forms the basis of [Chapter 6](#). The findings of this chapter are also referred to in [Chapter 7](#), where the results are compared to those found using a commercial rheometer.

## 5.2 Experimental Procedures

### 5.2.1 Materials and Apparatus

#### 5.2.1.1 Overview of Novel Technique

A drawback of the visual experimental procedure was that it relied on the human eye and judgement. Due to error associated with these, a new jamming detection method that did not rely so heavily on these was developed (Figure 5.1).

It had been noticed that in systems that jammed (i.e. showed visible dilation), when a needle or spatula was placed in the flow and held, intermittent forces were felt that could knock the inserted object out of place temporarily. These were thought to be related to jamming since they were not observed in systems that did not jam visually. A system that made use of this feature was therefore designed.

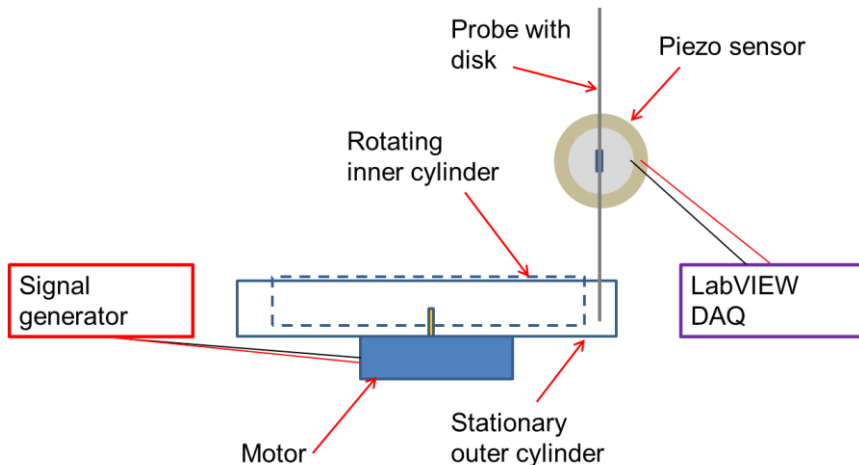


Figure 5.1- Novel force sensor technique set-up

The set-up consisted of a metal probe (0.23mm diameter) inserted into the sample in the gap between the rotating and stationary cylinders in the shear cell. The probe was held tightly enough so that small forces applied to the probe resulted in a reasonable displacement (~1mm) and when the applied forces stopped, the probe would spring back to its initial position.

When the probe moved, a metal disk attached to it struck a piezo sensor (Maplin Electronics YU82D). A piezo sensor converts an applied stress to a voltage.

Therefore, when the probe struck the sensor, for example when an intermittent force was applied to the probe (i.e. the material jammed), a voltage peak was seen in the piezo's output. A peak in the piezo's output voltage was therefore taken as analogous to a jam.

The piezo sensor was connected to a computer via LabVIEW data acquisition (NI BNC-2120 and NI PCI-6221). A LabVIEW code was written that recorded how the piezo's output voltage varied with time (see 5.2.1.4). The piezo's output voltage was calibrated to allow an output voltage to be converted to a force (see 5.2.1.3).

The peaks recorded in an experiment were analysed (via MATLAB) to allow jamming trends to be identified. These included studies of the frequency and magnitude of jamming peaks, as well as the time gaps between them. A further statistical analysis of the peak data is given in [Chapter 6](#).

### **5.2.1.2 Sensor Details and Characterisation**

A brief overview of how piezo sensors work is given, followed by details of the characterisation of the piezo sensors used in the experiments. Understanding how the piezo sensors behaved was vital to ensure results obtained from the sensors were understood.

#### Overview of Piezo Sensor Theory

A piezoelectric sensor makes use of the piezoelectric effect and therefore generates a voltage/charge that is proportional to the applied stress/strain/force/pressure [1]. The effect is reversible: a mechanical deformation can produce an electrical charge/voltage and conversely, an electrical charge/voltage can produce a mechanical deformation [1, 2].

The piezoelectric effect can occur in crystals with no inversion symmetry in the unit cell. With inversion symmetry, for every point  $(x,y,z)$  in the unit cell there is a point  $(-x,-y,-z)$ . Normally, piezoelectric crystals are electrically neutral. Mechanical stress can, however, disrupt the balance and bring about a change in polarisation, resulting in net charges on opposing surfaces, causing a voltage. Examples of piezoelectric materials include quartz and lead zirconium titanate (PZT) which is the most common piezoelectric ceramic [1].

Piezoelectric sensors are well suited to dynamic applications but are not so well suited for static applications [3]. This is because the voltage/charge produced when a static/constant force is applied is not constant and decays exponentially with time due to resistance. Therefore if a static force is applied, the voltage/charge initially generated will eventually dissipate to zero. The rate at which the voltage decays depends on the resistance, with larger resistances taking longer to decay [1].

The rate of decay can be characterised through a discharge time constant. This is the time taken for the signal to go to 37% ( $1/e$ ) of its initial value [1, 3].

$$v = V e^{\frac{-t}{\tau}} \quad \text{Equation 5.1}$$

Here  $v$  is the voltage at time  $t$ ,  $V$  is the initial voltage,  $t$  is time and  $\tau$  is the time constant.

#### Voltage Profiles from Piezo Sensor Used in Novel Technique

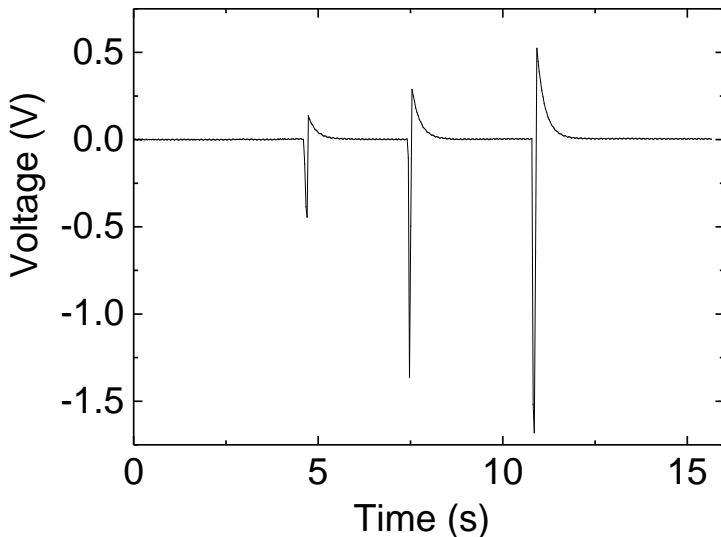


**Figure 5.2- Example voltage peaks from piezo sensor as sensor was struck with increasing force. This force was applied crudely by striking the sensor with a metal rod. The force was increased by striking the sensor ‘harder’.**

When the probe struck the sensor, a profile with a shape similar to those in Figure 5.2 was seen. When the force striking the sensor increased (i.e. the probe struck the sensor with a greater velocity due to a greater acceleration), a larger peak was seen. The signal's sign depended on how the circuit was set-up. Switching the wires simply resulted in the profiles being inverted. When analysing the profiles, the peak

magnitude was taken as the distance from zero to the trough (since this peak was due to the probe striking the sensor).

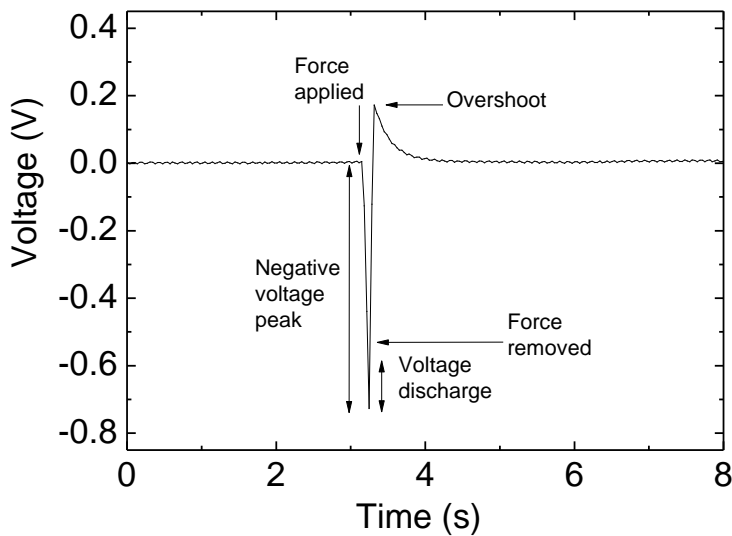


**Figure 5.3- Diagram showing various parts of the peaks produced when sensor was struck**

As shown in Figure 5.3, when the probe struck the sensor (i.e. compressed/deformed it), the voltage peaked negatively. When the probe sprung back, the voltage went in the other direction towards zero. This corresponded to the sensor returning back to its initial arrangement since the compressive force of the probe was no longer present.

On its return, the signal overshot zero. This was likely caused by the charge (produced due to the probe's force) discharging, reducing the magnitude of the voltage without recovery of the piezo's deformation. This meant that for the piezo to recover fully to its initial state, the signal would have to overshoot zero. After overshooting zero, the signal decayed back to zero, again due to the charge/voltage discharging. The positive peaks were typically 5-30% of the larger negative peaks' magnitudes.

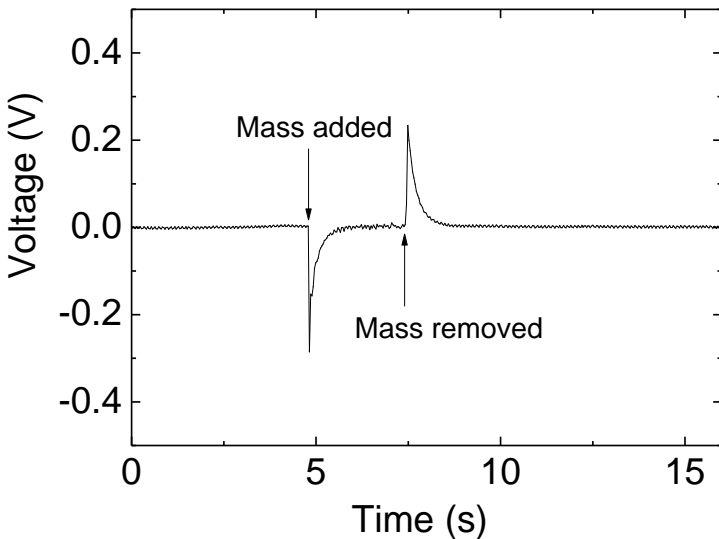


**Figure 5.4- Example peak when mass placed on piezo sensor and then removed**

This effect could be seen more clearly when a fixed mass was placed on the sensor, the signal was allowed to settle and the mass was then removed (Figure 5.4). As the mass was placed on the sensor, a strong negative peak was seen (i.e. the sensor was compressed). When the mass was kept there, the signal's magnitude decayed back to zero due to charge discharge. This resulted in a zero voltage output, despite the fixed mass (and therefore force) still being present. When the mass was removed, a positive peak was seen (i.e. as the sensor returned to its initial state before deformation). This was of a similar magnitude to the initial negative peak since complete charge discharge had taken place.

Differences between Figure 5.3 and Figure 5.4 were likely due to the amount of time the applied force was in contact with the sensor, resulting in different extents of the charge/voltage discharging (i.e. the fixed mass experiment was static compared to the striking experiment which was much more dynamic). In Figure 5.3, since the force was only in contact with the sensor for a very short time, only small levels of discharge would have occurred, hence the small positive peaks. In Figure 5.4, however, the charge was fully discharged, with the voltage returned to zero, before the mass/force was removed. This meant that a positive peak of a similar magnitude to the initial negative peak occurred after the force was removed.

### Discharge Time Constant

A discharge time constant was found for the peaks in the fixed mass experiments by fitting an exponential decay to the decay data (Equation 5.1 and Figure 5.4), giving  $\tau=0.2 \pm 0.05$  s. This suggested that it would take ~1s for the voltage to decay to zero ( $5\tau$ ) when a constant force was applied/removed.

From the data obtained for the probe simply striking the sensor, the signal took a much shorter time to return to zero (0.03-0.06s) after being struck. The slight positive peaks formed, however, took longer to return to zero (~1s). Therefore when jams were close together, the decay of the positive peak would likely have influenced the magnitude of the next peak measured. Since the positive peaks were small relative to the negative peaks caused by the initial strike (typically a maximum of 15% of the negative peak magnitude), the effect of this is likely to have been small and within the error range that was determined through repeat experiments.

Assuming the positive peaks from the previous jam had not decayed at all, the size of the next jamming peak would really have been the sum of the positive peak magnitude from the previous jam plus the current jam's negative peak magnitude. Therefore when a peak size is quoted, it may actually have been larger than its quoted value. This, however, was within the error bars of repeat experiments and applied to all data that were processed making this a systematic error. As shown in Figure 5.10 and Figure 5.11, only very small positive peaks were typically measured in the concentrated colloidal experiments. This suggested that the dynamics of the jams were fast compared to the piezo's decay constant, such that little charge discharge actually occurred.

### Force Proportionality to Charge or Voltage

Literature suggests that the voltage generated by a piezo sensor is directly proportional to the applied force. A piezo sensor has a very high output impedance and can therefore be treated as a proportional voltage source. For the work in this chapter, the magnitude of the voltage peak was treated as related to the intensity of a jam, with larger peaks suggesting larger jams.

There was also the possibility of considering the force applied to the sensor as being proportional to the charge, rather than the voltage. By considering Figure 5.4, this would lead to the following force, charge and voltage profiles with time when a mass was placed on the sensor and then removed (Figure 5.5).

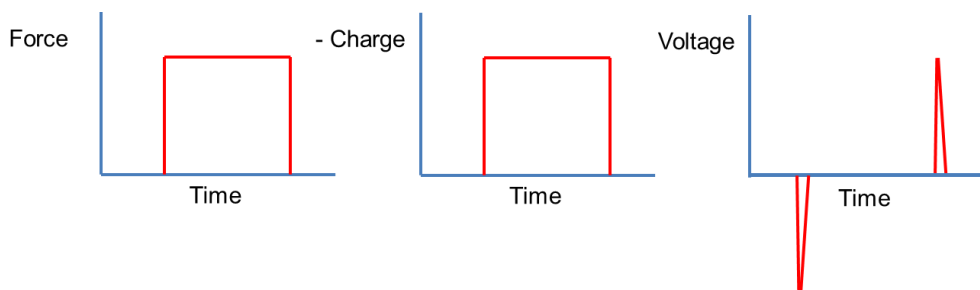


**Figure 5.5- Variation of force, charge and voltage with time when mass placed on sensor and then removed**

This shows the charge being proportional to the force and the voltage being proportional to the rate of change of charge since  $V=IR$  and  $I=dQ/dt$  where  $V$  is voltage,  $I$  is current,  $R$  is resistance,  $Q$  is charge and  $t$  is time. In this case, it may be worthwhile considering the area under the voltage peaks, rather than the size of the peaks, to get an idea of the intensity of jamming.

Due to uncertainties in the validity of this argument, and the general agreement in literature that the voltage generated by a piezo sensor can be treated as directly proportional to the applied force, it was decided to treat the force as being proportional to the voltage. Therefore the magnitude of the voltage peak was treated as related to the intensity of a jam. If peaks had a similar base width, larger peaks would have resulted in larger areas under the peaks, suggesting larger jams, even if the alternative viewpoint was considered. This suggested that both methods would have produced similar trends.

### 5.2.1.3 Sensor Force Calibration

To calibrate the piezo sensor, various masses were placed on the sensor to see how the initial peak voltage signal varied with applied force. As the mass (and therefore force) increased, larger voltage peaks were seen (Figure 5.6). The voltage varied approximately linearly with force.

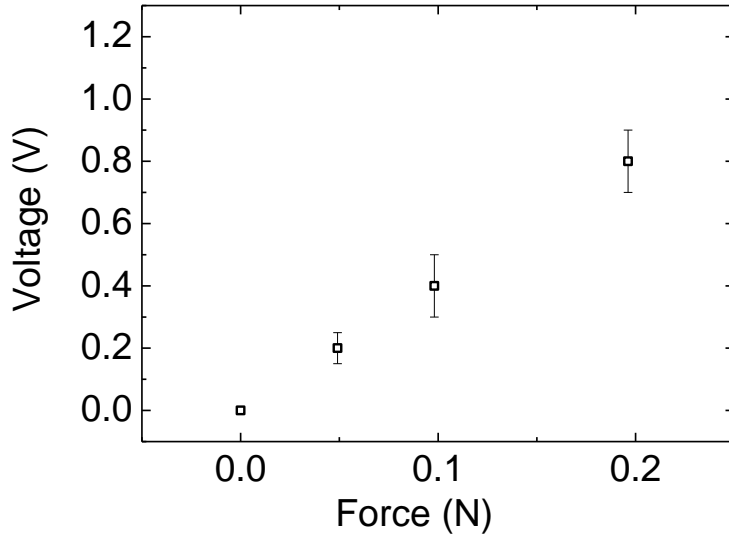


Figure 5.6- Piezo force calibration. Error bars show standard deviation of repetitions.

By performing a linear fit to the force calibration, it was found that:

$$Voltage [V] = 4 \pm 0.5 \times Force [N]$$

This therefore allowed the forces associated with jams to be estimated from the voltage peaks.

This meant that the force could have varied by  $\pm 13\%$  of its quoted value. For example, at a voltage of 0.5V, while a force of 0.13 N was calculated, it could have varied from 0.11 N to 0.14 N.

### 5.2.1.4 LabVIEW Code

*Carol Forsyth assisted with LabVIEW.*

The piezo sensor was connected to a computer using a LabVIEW connector block (BNC-2120) and signals were digitised using a data acquisition card (National Instruments PCI-6221). These were recorded using LabVIEW.

A brief overview of the LabVIEW code that was written to collect the piezo data is given.

The LabVIEW front panel that was produced is shown in Figure 5.7. The user could choose a sampling rate (number of measurements per minute) on the front panel and when the code was run (by clicking the start/stop button), the code recorded the voltage output from the piezo as a function of time. The code plotted the voltage as a function of time on the front panel as the code ran so that progress could be monitored. Once the code was stopped, the time and voltage data were saved.

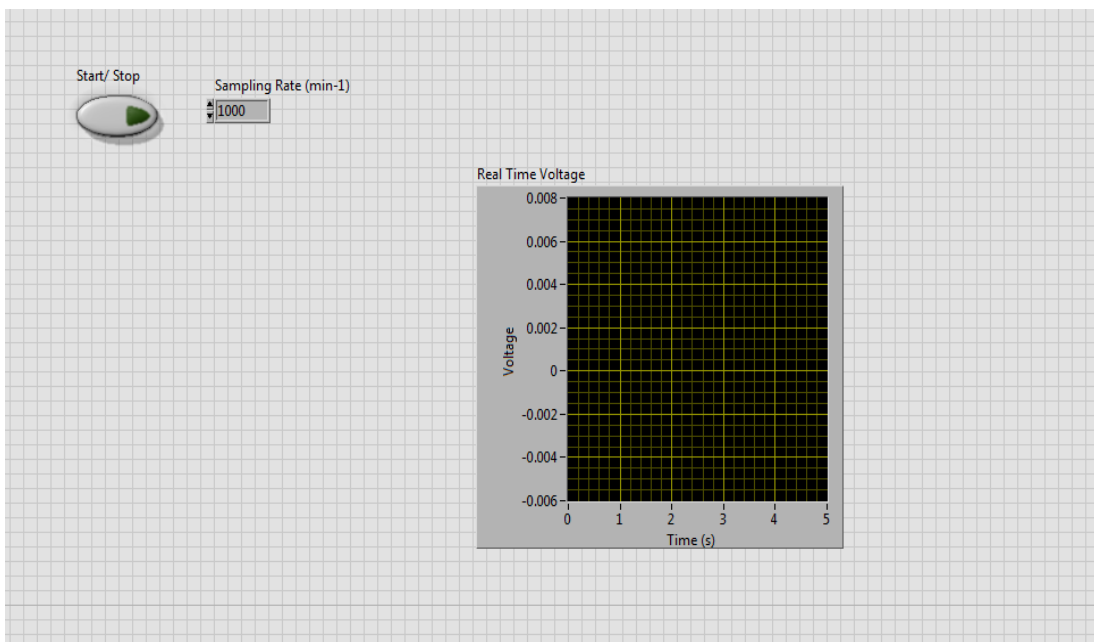


**Figure 5.7- LabVIEW front panel**

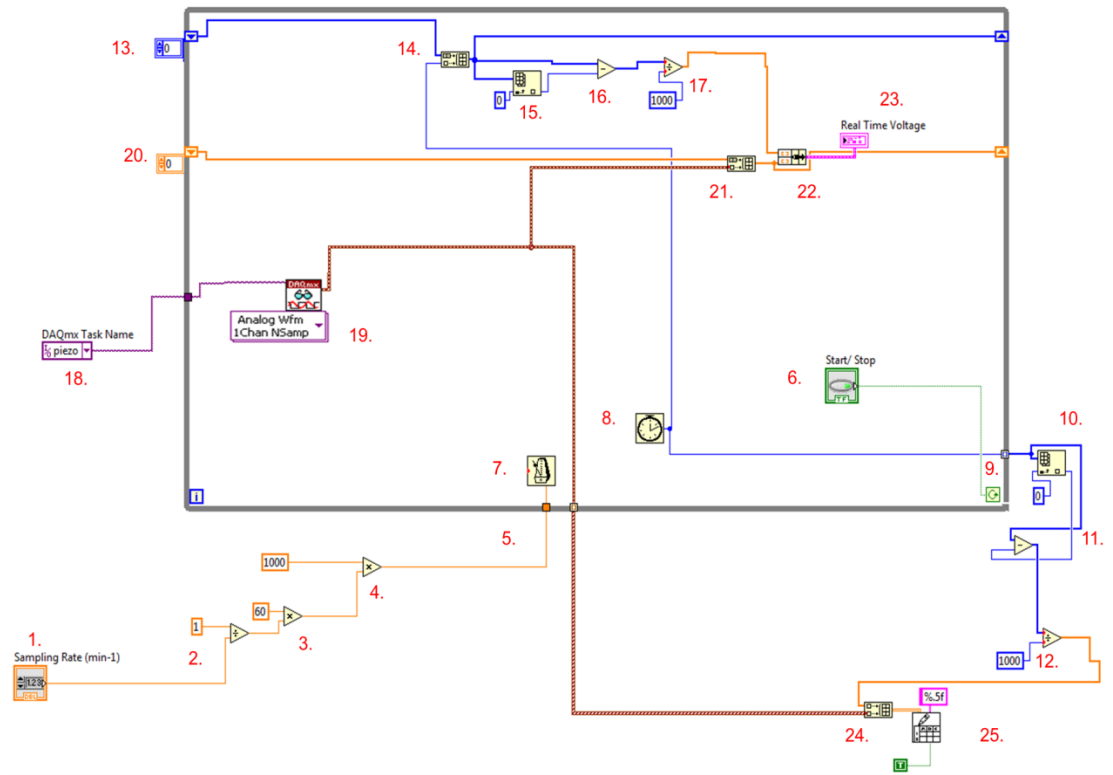


**Figure 5.8- Labelled LabVIEW block diagram code**

Figure 5.8 shows the LabVIEW block diagram code. The main features are labelled and their purpose is summarised in Table 5.1. More detailed descriptions and explanations of the workings of LabVIEW can be found on the National Instruments website or from relevant textbooks [4].

**Table 5.1- LabVIEW code main features summary**

<b>Number</b>	<b>Summary of purpose</b>
1.	Obtains the sampling rate from the front sheet.
2.	Uses the sampling rate to calculate the time between measurements (in minutes).
3.	Converts the time between measurements from minutes to seconds.
4.	Converts the time between measurements from seconds to milliseconds.
5.	This time is the ‘millisecond multiple’ and is fed to the while loop.
6.	Obtains the status of ‘on’ or ‘off’ from the front panel. The loop only runs if the status is on.
7.	Code waits until the time is a millisecond multiple before executing the next loop. This means the loop only runs when the timer’s value is a multiple of the millisecond multiple. This means the while loop runs according to the sampling rate set by the user.
8.	This is a millisecond timer within the while loop which gets the time from the computer’s clock at the start of each loop.
9.	These computer clock values exit the loop and form an array.
10.	An index array function is used to obtain the computer’s clock value for the first loop. This is at index zero.
11.	The clock value from the first loop is subtracted from the clock value for each loop to deduce the time (in milliseconds) associated with each loop.
12.	The times are converted from milliseconds to seconds and represent all the time data.
13.	Shift registers are used to pass information from one execution of the loop to subsequent executions. In this case, the time from the computer’s clock at the start of each previous loop is passed to the subsequent loops. This allows graphs that contain the results from the previous loops, plus the current loop, to be plotted on the front panel. The graphs update with each loop, allowing ‘live’ monitoring.
14.	The time from the computer’s clock at the start of a loop is added to an array that contains the time from computer’s clock at the start of each previous loop.
15.	An index array function is used to obtain the computer’s clock value for the first loop. This is at index zero.

16.	The clock value from the first loop is subtracted from the clock value for each loop to deduce the time (in milliseconds) associated with each loop.
17.	The times are converted from milliseconds to seconds and represent the time data for the current loop and all previous loops.
18.	This is used to set the data acquisition task to record the voltage output from the piezo. Here the number of measurements taken during sampling and the sampling rate can be defined.
19.	Each time the while loop is run, the data acquisition task is run to obtain the voltage data from the piezo.
20.	Shift registers are used to pass information from one execution of the loop to subsequent executions. In this case, the voltage data from previous loops are passed to the subsequent loops.
21.	The voltage data from the current loop is added to an array that contains the voltage data from each previous loop.
22.	The voltage data and time data from the previous loops and current loop are bundled into clusters.
23.	These voltage-time clusters are plotted on the front panel. This allows 'live' monitoring.
24.	The voltage and time data are concatenated into a single array.
25.	This writes the time and voltage data to a spread sheet file. The data are transposed.

### **5.2.2 Test with Newtonian Material**

To check that voltage peaks were only present during the shearing of a material that was jamming, tests were performed with a Newtonian fluid. Glycerol was placed in the shear cell and the input voltage to the shear cell was varied (to alter the shear stress). The probe was placed half way across the gap and kept 3mm from the bottom of the shear cell.

With Newtonian systems that did not jam (such as glycerol), no intermittent forces that could knock the probe were measured. Instead, when the shear cell's motor was switched on, the probe simply displaced slightly from its initial position, where it stayed until the motor was switched off. When the motor was switched off, the probe returned to its initial position. The probe did not move sufficiently to hit the sensor and as a result, voltage peaks were not detected.

## 5.2.3 Steady Shear Experiments on Concentrated Colloidal Suspensions

The following section details the procedures for the various steady shear experiments that were performed with the force sensor technique on concentrated colloidal suspensions.

### 5.2.3.1 Effect of Volume Fraction

Various volume fractions (ranging from 0.54-0.61) of the concentrated colloidal suspensions ( $488\pm5$  nm radius) were sheared in the rotating inner cylinder shear cells. A shear cell with a 5mm gap and ~9mm fill height was used. The shear cell's inner cylinder had a 25mm diameter and the outer was 35mm.

In the first set of experiments, colloidal suspensions were sheared at the maximum voltage (10.8V) for 5 minutes in the shear cell. For each run, the probe was placed half way across the gap and kept 3mm from the bottom of the shear cell. This was to minimise interference from the shear cell's surfaces.

LabVIEW was used to obtain voltage versus time data from the piezo. MATLAB was then used to analyse the results to allow jamming trends to be identified. A minimum peak size of 0.03V was chosen to minimise the effect of noise. This cut-off value was necessary as it was found that the piezo sensor's output would often fluctuate between  $\pm 0.03$ V, even with the shear cell empty. This was thought to be an artefact of the set-up as attempts to eliminate it (e.g. using a different piezo) were unsuccessful. The effects of volume fraction on parameters such as peak magnitude and peak frequency were investigated.

The rotational rate (and therefore shear rate) was also measured at each volume fraction (using a tachometer). This allowed consistencies between the visual method and novel method to be checked in terms of the shear rate measured for a given applied shear stress. It also showed that the probe itself did not have an impact on the flow.

As detailed in [Chapter 4](#), the rotational rate quoted was an average, since when jamming occurred, the rotational rate was not constant. At a particular set of conditions, the rotational rate was measured at regular time intervals (every minute) and an average of the readings was determined. It was not possible to measure an instantaneous shear rate as the rotating cylinder had to complete a full revolution to

allow a rotational rate to be determined by the tachometer. During measurements, the rotational rate varied due to the jamming and unjamming of the suspensions. An average was therefore deemed as the most suitable way to present the shear rate. It was found that despite the rotational rate of the inner cylinder varying, measured averages appeared consistent throughout an experiment, typically varying by a maximum of 15%. This was within the error of repeat experiments.

### **5.2.3.2 Effect of Shear Stress**

The effect of different supplied voltages to the motor (and therefore different shear stresses) on jamming was also investigated. For this, samples ( $\Phi=0.54-0.61$ ) were sheared at various motor supply voltages (and therefore shear stresses). For example, a  $\phi=0.59$  sample was sheared at various voltages (4V, 5V, 6V, 8V and 10.8V) for 5 minutes in the 5mm gap shear cell. The output voltage-time data from the piezo were then analysed.

This also allowed comparisons with the visual onset of jamming and the onset of jamming with the force sensor to be made. These were then evaluated against the flow profiles detailed in 4.3.1.2.

### **5.2.3.3 Effect of System Geometry**

A procedure similar to the effect of volume fraction etc. experiments was performed, however, this time colloid samples were sheared in shear cells with different gap sizes between the inner and outer cylinders (2.5mm and 10mm), compared to the 5mm arrangement previously used. Different gaps were obtained by changing the diameter of the rotating inner cylinder.

### **5.2.3.4 Effect of Particle Size**

The effect of particle size was investigated by performing a range of experiments with  $287\pm4$  nm radius PMMA particles and comparing results to those with the  $488\pm5$  nm radius particles used previously. The behaviour of  $\Phi=0.54-0.61$  samples was investigated across a range of conditions (various supply voltages to the motor and with different gap sizes).

### **5.2.3.5 Effect of Closed System**

A close-fitting lid was designed for the shear cells to see how flow behaviour was affected when there was no open surface, since it was thought that confinement and expansion out of the open surface may have been a vital part of the mechanism causing the observed behaviour (see 4.3.1.1). This lid had the minimum clearance required to still allow the inner cylinder to rotate. The hole necessary for the probe to be inserted was chosen to be as small as possible, while still allowing the probe to move to strike the sensor.

Samples were placed in the 5mm gap shear cell and flow behaviour was observed at 10.8V as before. The rotational rate of the inner cylinder as a function of supplied voltage (0 to 10.8V), with the lid on, was obtained to allow comparisons with the open surface shear rate versus shear stress profiles.

To determine the impact of the lid on typical flow (i.e. flow without jamming), shear rate versus shear stress profiles for a  $\phi=0.55$  sample (a sample that did not show signs of jamming) were obtained with and without a lid. This allowed the effect of the lid on flow to be estimated.

### **5.2.3.6 Effect of Soft Walls**

Since confinement appeared important, experiments with soft-walled shear cells were performed. For this, a layer of neoprene foam was attached to the Perspex shear cell walls (the vertical walls of the cylinders). The shear cells were manufactured so that gaps and fluid fill heights with the foam present were the same as before.

Experiments were performed as before (sheared at 10.8V for 5 minutes), but now with the soft walled shear cells. Experiments with different volume fractions (0.55-0.61) and gap sizes (2.5mm, 5mm and 10mm) were carried out.

For all experiments, typically three to five repetitions were done. Error bars represent  $\pm$  one standard deviation. For example, if an average peak magnitude across a set of experiments was determined to be 0.21 V, 0.18 V and 0.20 V, an average of 0.20 V and standard deviation of 0.02 V was calculated. This was therefore quoted as 0.20  $\pm$ 0.02 V. The validity of this number of repetitions is discussed in 5.3.8.

## 5.3 Results and Discussion

### 5.3.1 Effect of Volume Fraction

#### 5.3.1.1 General Profiles

For volume fractions  $\geq 0.56$ , a series of voltage peaks in the piezo's output were seen across the 5 minute experiment durations. For volume fractions less than this, no peaks (or intermittent movement of the probe) were seen and the voltage remained constant at ~zero (Figure 5.9). This agreed with the visual experiments in [Chapter 4](#) where signs of jamming were only seen at  $\phi \geq 0.56$ .

The profiles obtained for each volume fraction differed. For example, with  $\phi=0.56$ , time gaps with no peaks were frequent and when peaks did occur, they had a large range of magnitude (Figure 5.10). At these lower volume fractions, jamming appeared to occur in bursts. After a time gap of no peaks, once one occurred, generally a lot occurred after, without long time gaps between them. At  $\phi=0.61$ , however, peaks were ~constantly present and they were generally of a similar magnitude (Figure 5.11).

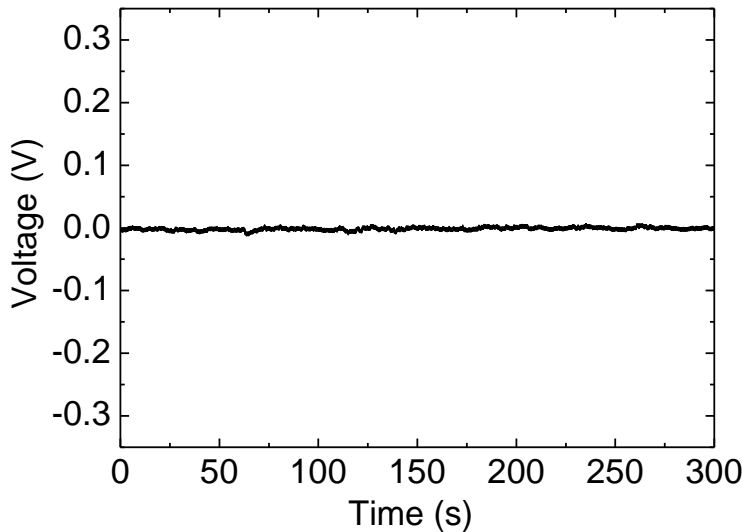


Figure 5.9- Example voltage-time profile from force sensor for  $\Phi=0.55$ . 5mm gap size and  $72.4\text{N/m}^2$  stress.

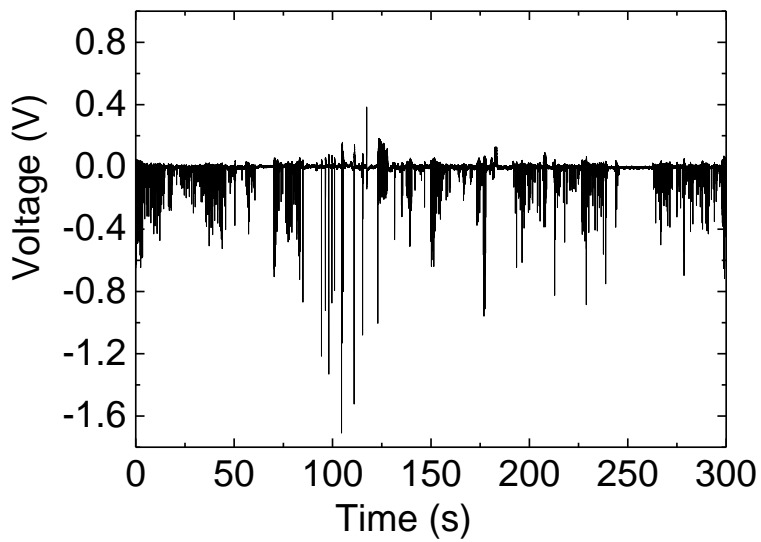


Figure 5.10- Example voltage-time profile from force sensor for  $\Phi=0.56$ . 5mm gap size and  $72.4\text{N/m}^2$  stress.

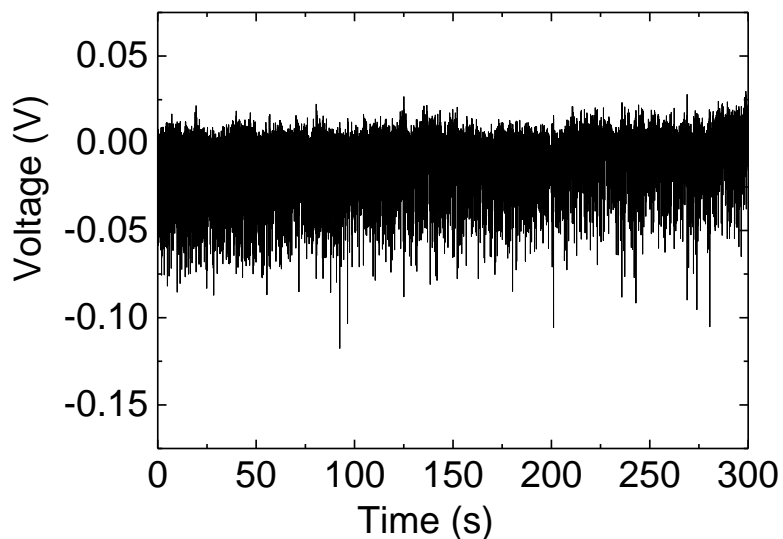
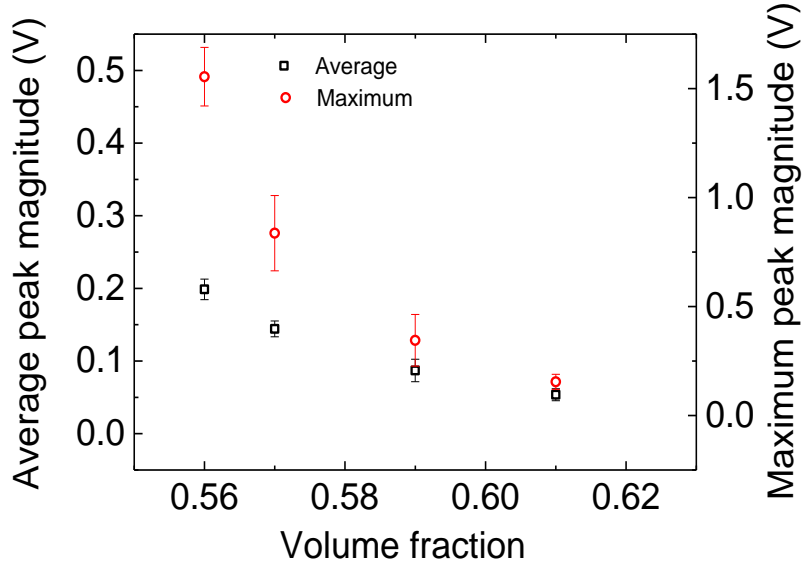


Figure 5.11- Example voltage-time profile from force sensor for  $\Phi=0.61$ . 5mm gap size and  $72.4\text{N/m}^2$  stress.

### 5.3.1.2 Peak Magnitude

The magnitude of a peak was taken to be analogous to the intensity of a jam- i.e. larger peaks corresponded to larger jams. It was found that as volume fraction increased, the average magnitude of the peaks decreased and the maximum peak magnitude decreased (Figure 5.12). This agrees with comparing Figure 5.10 and Figure 5.11.

By using the force calibration (detailed in 5.2.1.3), the maximum force associated with a jam was 0.4N. It was difficult to know whether this value was reasonable given the heterogeneity of fluctuating stresses in jamming systems [5, 6]. By accounting for the shear stress ( $72.4\text{N/m}^2$ ) and the area the stress was applied to from the shear cell geometry (cylinder circumference\*cylinder height), however, the applied force estimated from this was of the same order of magnitude as the maximum force measured from the force calibration (0.1N compared to 0.4N).



**Figure 5.12- Average and maximum peak magnitude variation with volume fraction. 5mm gap size and  $72.4\text{N/m}^2$  stress. Error bars show standard deviation of repetitions.**

The variation/ spread of peak magnitudes during an experiment decreased with increasing volume fraction, as could be seen visually when comparing Figure 5.10 and Figure 5.11. This suggested that jams were more consistent and homogeneous in more concentrated suspensions.

Histograms showing the distribution of peak magnitudes across the experiment time were produced. They showed that smaller peak events occurred significantly more often than larger peak events. The distributions of peak magnitudes showed exponential (decay) behaviour, with the distributions decaying more rapidly as volume fraction was increased (explaining the smaller variation in peak magnitude at higher volume fraction). Distributions and jamming probabilities are analysed and discussed in more detail in [Chapter 6](#).

Possible reasons for the reduction in peak magnitude and smaller spread of peaks measured with increasing volume fraction are discussed in 5.3.10.

### 5.3.1.3 Count and Time Gap between Jams

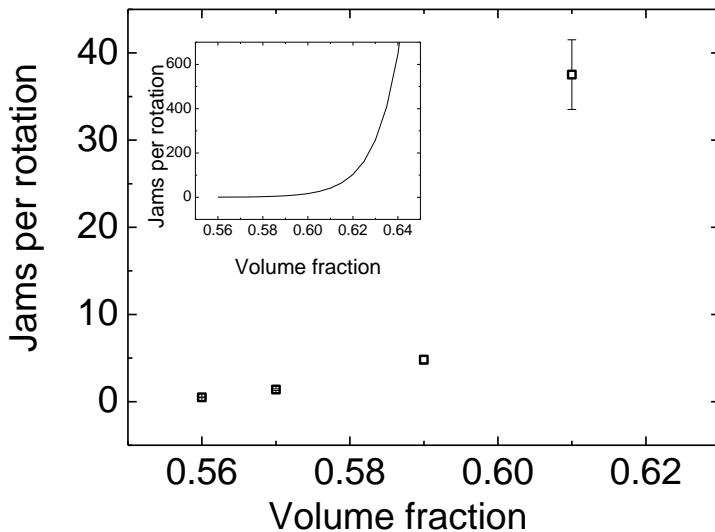


**Figure 5.13-** Jams per rotation of inner cylinder at various volume fractions. 5mm gap size and  $72.4\text{N/m}^2$  stress. Inset shows exponential fit to data showing a rapid increase as  $\Phi=0.64$  approached. Error bars show standard deviation of repetitions.

While there was no clear pattern between the number of jams in a fixed time and volume fraction, the number of jams per rotation of the inner cylinder (i.e. over a fixed strain) increased significantly with increasing volume fraction (Figure 5.13). The data showed an approximately exponential trend and as shown in Figure 5.13's inset, the number of jams per rotation increased rapidly as  $\Phi=0.64$ , the volume fraction corresponding to random close packing, was approached. This suggested that complete jamming would occur when this limit was approached.

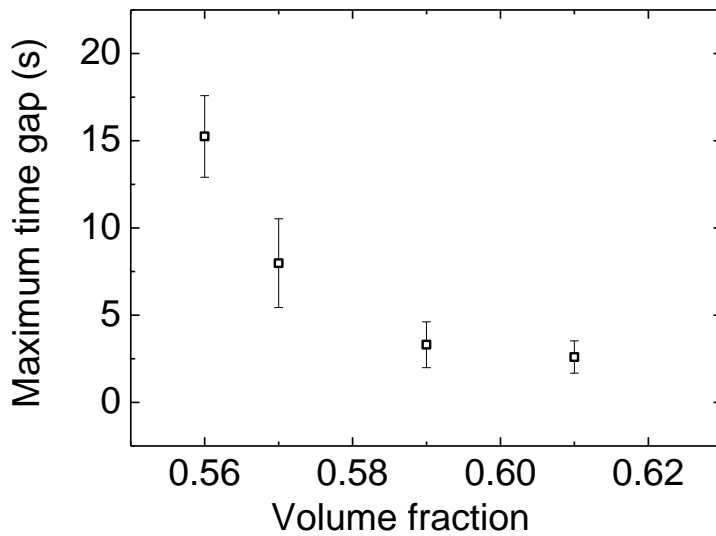


**Figure 5.14-** Maximum time gap between jams at various volume fractions. 5mm gap size and  $72.4\text{N/m}^2$  stress. Error bars show standard deviation of repetitions.

As the volume fraction increased, the maximum time gap between peaks decreased (Figure 5.14), in agreement with the earlier visual observations and Figure 5.10 and Figure 5.11.

The spread of time gaps between peaks generally decreased with increasing volume fraction. This suggested that time gaps were more consistent, with a smaller spread of times, at higher volume fractions.

Histograms showing the distribution of time gaps between peaks were produced. They showed that smaller time gap events occurred significantly more often than larger time gap events. Distributions and jamming probabilities are analysed and discussed in more detail in [Chapter 6](#).

Possible reasons for the increase in the number of jams per rotation of the inner cylinder and smaller spread of time gaps between jams with increasing volume fraction are discussed in 5.3.10.

### 5.3.1.4 Extent of Jamming

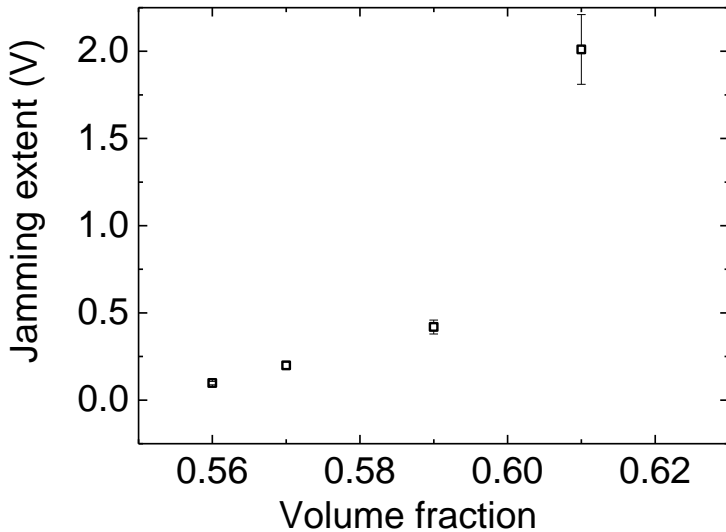


**Figure 5.15- Jamming extent at various volume fractions. 5mm gap size and 72.4N/m<sup>2</sup> stress. Error bars show standard deviation of repetitions.**

To account for the fact that the inner cylinder rotated more quickly at lower volume fractions (and so the material was sheared at a greater rate) due to the fixed shear stress and lower viscosity, a parameter based on the average peak magnitude and number of jams per rotation of the inner cylinder was calculated.

$$\text{Jamming extent} = \text{Average peak magnitude } [V] \times \text{Count per rotation} \quad \text{Equation 5.2}$$

This clearly showed that a greater extent of jamming occurred as volume fraction increased (Figure 5.15) and corresponded to a fixed strain of one rotation. The decrease in average peak magnitude with increasing volume fraction was not enough to ‘cancel out’ the increased number of jams per rotation with increasing volume fraction. Jamming therefore got ‘worse’ for higher volume fractions over a fixed strain.

The importance of strain on the extent of jamming is discussed in more detail in 5.3.4.

### 5.3.2 Effect of Shear Stress and the Link between Visual Observations, Flow Profiles and Novel Technique

The voltage supplied to the shear cell (and therefore the shear stress) had a significant impact on the voltage-time data from the force sensor (Figure 5.16). Peaks were only evident in the output when the shear stress reached a sufficient level. For example, when  $\Phi=0.59$ , peaks were only seen at shear stresses  $\geq 33.5\text{N/m}^2$ . This corresponded very closely to the shear stress required for the visual onset of dilatancy detailed in [Chapter 4](#). For example, at  $\Phi=0.59$ , visual dilatancy first became apparent at shear stresses  $\geq 33.5\text{N/m}^2$  and from the flow profiles in Figure 4.8, it was beyond this point that the flow profiles flattened and further increases in shear stress did not result in the shear rate increasing (a sign of strong shear thickening). This suggested that the intermittent forces were indeed related to jamming and dilatancy and matched up well with the visual signs of jamming.

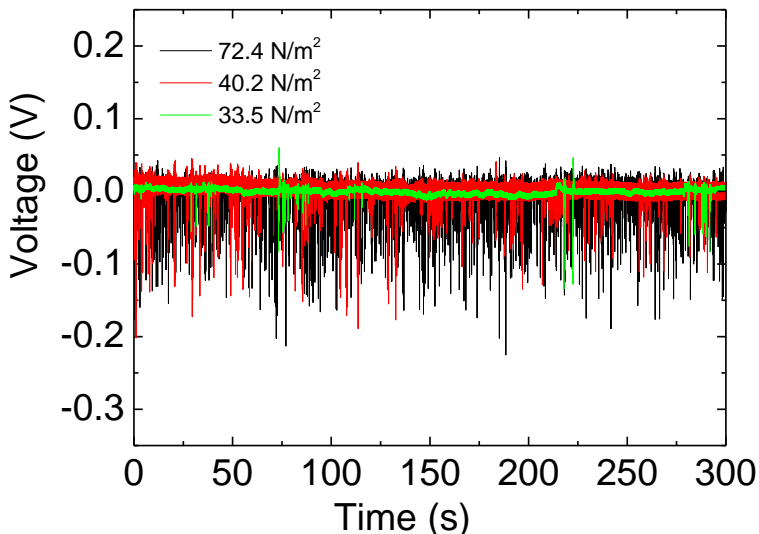
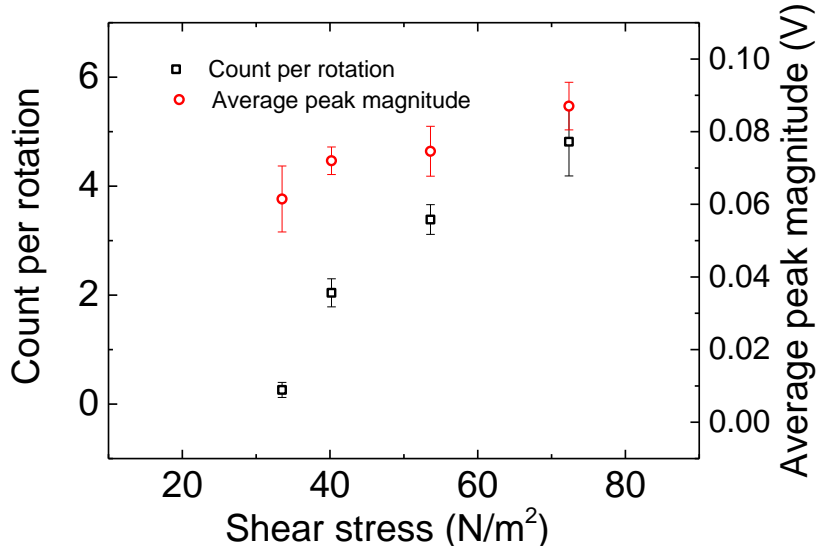


Figure 5.16- Example voltage-time profiles from force sensor for  $\Phi=0.59$  at various shear stresses. 5mm gap size.



**Figure 5.17- Variation of count and peak magnitude with shear stress for  $\phi=0.59$  sample. 5mm gap size. Error bars show standard deviation of repetitions.**

As the shear stress increased, the number of peaks per rotation of the inner cylinder increased for all volume fractions studied (Figure 5.17). The average peak magnitude did not change significantly, at most only slightly increasing with stress. This can also be seen in Figure 5.16 when comparing the voltage-time profiles from the force sensor at different shear stresses.

The larger count of peaks with increasing shear stress could explain why, beyond the onset shear stress/rate for peaks/visual dilatancy, increasing the shear stress did not result in the shear rate increasing, as shown in the flow profiles in 4.3.1.2.

An idea is that jamming, or more likely the dilatancy associated with it, may have been a means of energy dissipation. As the shear stress was increased, more energy must have been dissipated to prevent the shear rate from increasing. The additional energy supplied through increasing the shear stress may have been dissipated through dilatancy (e.g. dissipated through friction between particles as the system attempted to dilate and through the cracking and break-up that was seen), hence no increase in shear rate. This may explain why the number of peaks increased with increasing shear stress.

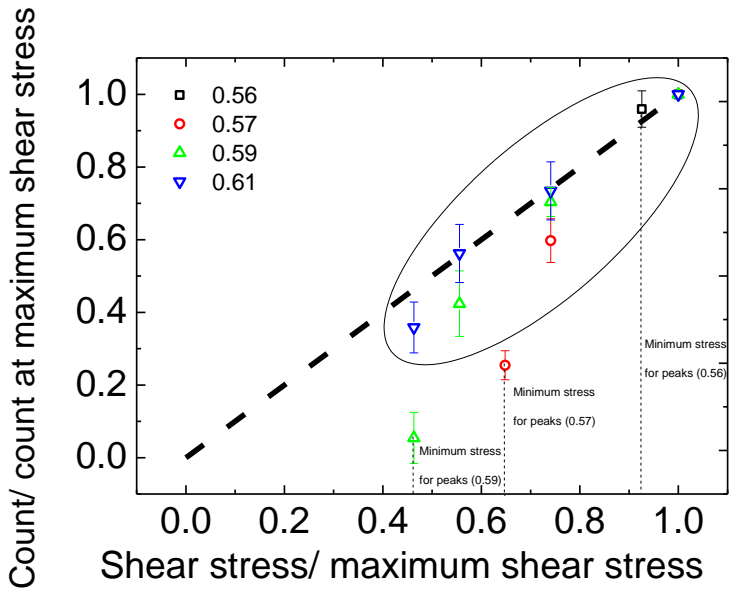


**Figure 5.18-** Normalised variation of jamming count in 5 minute experiment with shear stress for various volume fractions. Dashed line denotes  $y=x$ . Circled regions shows data that were close to  $y=x$  line. 5mm gap size. Error bars show standard deviation of repetitions.

At higher stress, the number of jams decreased close to proportionally to the decrease in the shear stress (circled region in Figure 5.18). For example, for  $\Phi=0.61$ , decreasing the shear stress by ~50% resulted in approximately half as many peaks. Near the critical shear stress from which jamming occurred, the number of jamming peaks dropped faster than the linear trend. This may have been due to the experiment operating very close to the boundary below which no jamming occurred.

Overall, these results suggested that the jamming peaks measured were part of some energy dissipation mechanism. Beyond the critical shear stress required for jamming, increasing the shear stress did not result in the shear rate increasing (as could be seen in the flow profiles) and this could be due to energy being dissipated through more extensive jamming and dilation. This has led to a better understanding of the flow profiles detailed in 4.3.1.2 and the idea of the jamming peaks being linked to some form of energy dissipation is discussed in more detail in 5.3.4 and 5.3.10.

### 5.3.3 Effect of System Geometry

Changing the gap size between the inner and outer cylinders appeared to have a significant impact on parameters such as the peak magnitude and count (Figure 5.19 and Figure 5.20). For example, with the 2.5mm gap arrangement there were approximately twice as many peaks in a given time compared to the 5mm set-up for a given volume fraction. The average peak magnitude was, however, approximately half that in the 5mm experiments. This suggested that with the smaller gap arrangement, there were more jams in a given time, but they were less intense. The converse was found for the larger 10mm gap arrangement: here fewer but stronger peaks were measured compared to the 5mm arrangement.

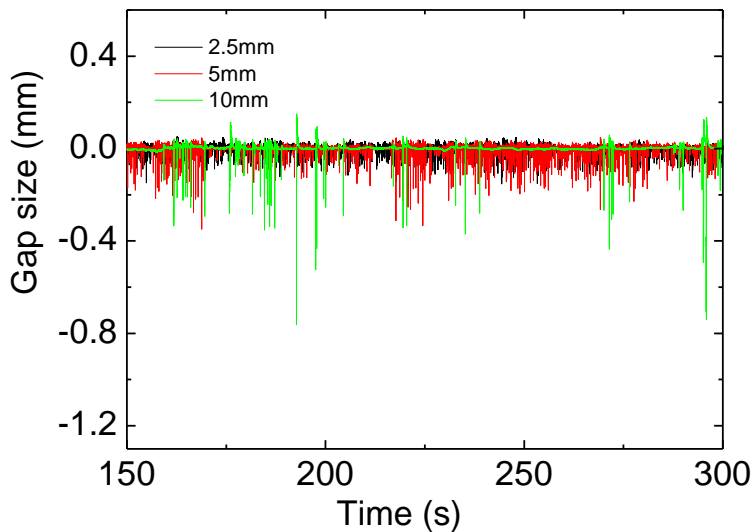
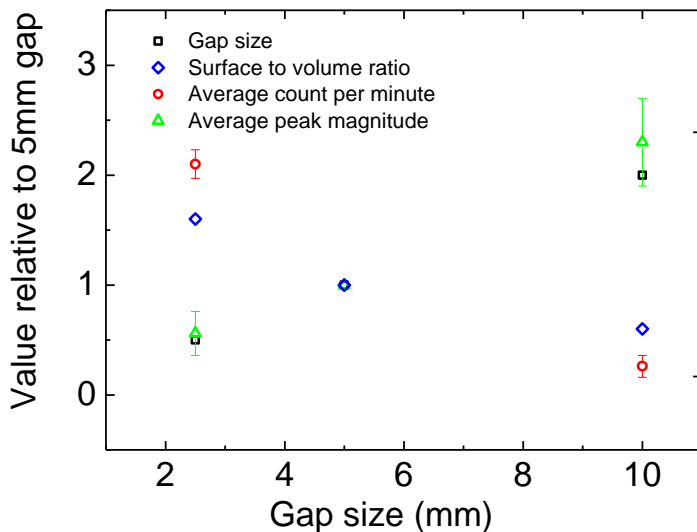


Figure 5.19- Example voltage-time profiles from force sensor for  $\Phi=0.59$  at various gap sizes. 72.4N/m<sup>2</sup> stress.



**Figure 5.20- Effect of gap size on peak magnitude and count. Average of results from  $\phi=0.56\text{-}0.61$  at  $72.4\text{N/m}^2$  stress. Error bars show standard deviation of repetitions.**

To gain a better insight into the geometries, the surface to volume ratio was calculated for the different set-ups since different gap sizes resulted in different volumes of suspension being used and different surface areas of the shear cell being in contact with the fluid. The surface used for the surface to volume ratio was the total area of the shear cell surface in contact with the suspension. The volume used was the volume of suspension that was required to fill the shear cells. The surface to volume ratio decreased with increasing gap size. From Figure 5.20, the decrease in count with increasing gap size appeared to follow the decrease in surface to volume ratio, while the increase in average peak magnitude with increasing gap size inversely followed this.

By considering just surface, rather than surface to volume ratio, no such trends were found. The surface area in contact with the suspension did not change substantially with the different gap sizes, with just a 15% maximum variation between the different gap set-ups. This meant that the volume of suspension may therefore have been important and this depended on the gap size. As shown in Figure 5.20, by considering the gap size, doubling the gap size resulted in peaks that were on average approximately twice as big, while their count halved.

It was therefore difficult to say whether it was the width of the gap or the surface to volume ratio that was important.

Possible reasons for the increase in the number of jams with smaller gap sizes and the smaller average size of peaks with smaller gap sizes are discussed in 5.3.10. The possible role of the surface to volume ratio is also discussed.

It is worth noting that for the 2.5mm arrangement, peaks were present but were too small to detect in the  $\phi=0.61$  sample. The probe could be seen moving, but its movement was not substantial enough to result in notable voltage peaks being measured. When a lower peak threshold was considered, it was too difficult to differentiate between peaks and noise.

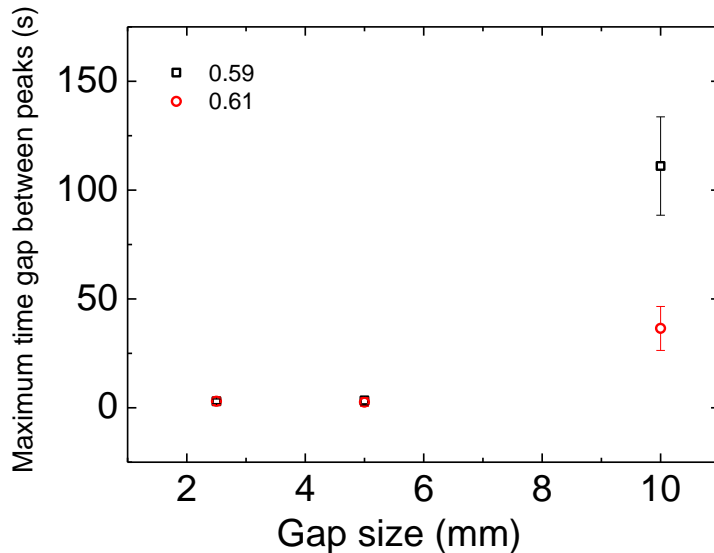


**Figure 5.21- Divergence of maximum time between peaks with increasing gap size for  $\phi=0.59$  and  $\phi=0.61$  at  $72.4\text{N/m}^2$  stress. Error bars show standard deviation of repetitions.**

With the 10mm arrangement, no peaks were detected in volume fractions less than 0.59 over the 5 minute experiments. This agreed with what was seen visually in [Chapter 4](#). Reasons for this may have been that jamming was occurring at too low a frequency for it to be observed over the experiment duration. For the  $\phi=0.59$  and  $\phi=0.61$  10mm gap shear cell experiments, the maximum time gap between peaks was notably higher compared to the 2.5mm and 5mm gap experiments, particularly for  $\phi=0.59$ , as shown in Figure 5.21. For example, at  $\phi=0.59$ , the maximum time gap increased from ~3s to almost 2 minutes when the gap size increased from 5mm to 10mm. It was therefore decided to run the 10mm gap experiments for a longer time at the volume fractions where jamming was not occurring over the 5 minute

experiment durations. 10 minute experiment runs still typically yielded no jamming peaks for  $\Phi=0.56$  and  $\Phi=0.57$ . Fewer than five jamming peaks were detected in two lots of  $\Phi=0.57$  experiments (out of three). None were ever detected in the  $\Phi=0.56$  experiments.

As mentioned in [Chapter 4](#), at a fixed stress and volume fraction, the shear rate remained approximately constant for the different gap sizes ( $\pm 15\%$ ) for the conditions studied. This suggested that the ‘average’ behaviour of the material remained the same with the different geometries and this idea is discussed in the next section.

### 5.3.4 Energy Dissipation per Unit Strain

Since the voltage peaks and visible dilation associated with them suggested some form of energy dissipation, the sum of peak magnitudes over each experiment (performed at the maximum motor voltage) was determined. As volume fraction increased, the sum of the peak magnitudes decreased (Figure 5.22); this was due to peak magnitude decreasing with increased volume fraction (Figure 5.12).

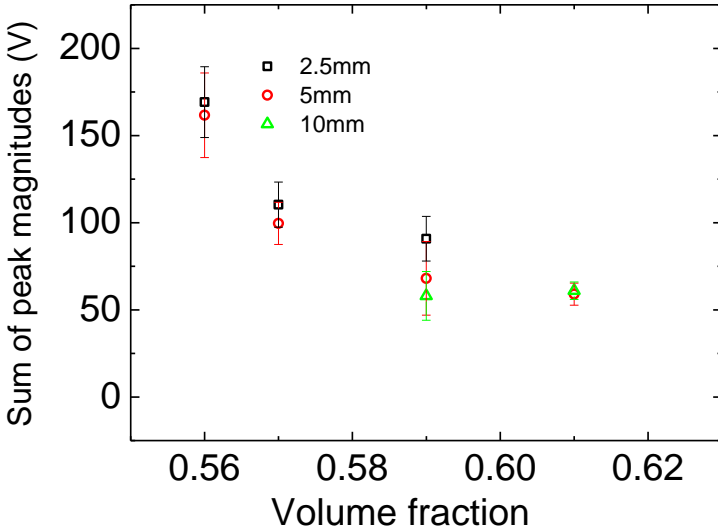
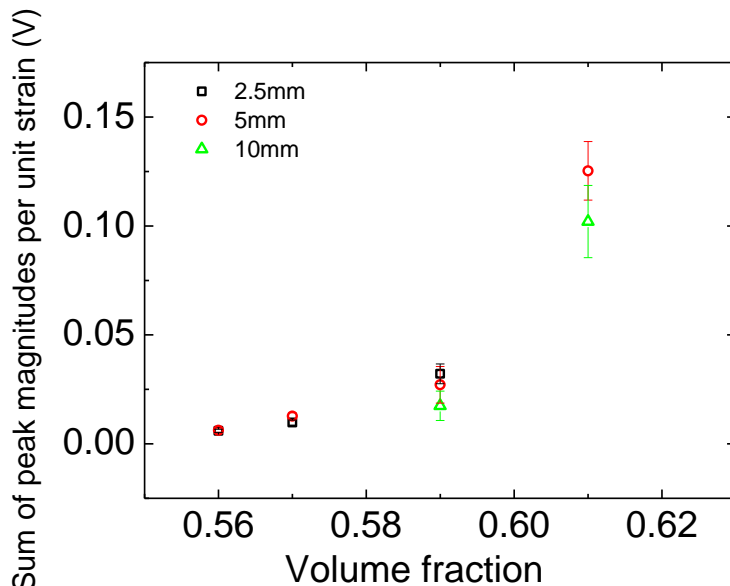


Figure 5.22- Sum of peak magnitudes over 5 minute experiments ( $72.4\text{N/m}^2$  stress) for various volume fractions and gap sizes. Error bars show standard deviation of repetitions.

The strain for the different experiments varied, however, due to different rotation rates and gap sizes.

$$\text{Strain} = \frac{\text{rotational rate} \times \text{experiment time} \times \pi \times d_{inner}}{\text{gap}} \quad \text{Equation 5.3}$$

As mentioned, the rotation rate of the inner cylinder decreased with increasing volume fraction (due to the fixed shear stress and greater viscosity). This resulted in a smaller strain over a given time. The sums of the peak magnitudes per unit strain were therefore determined to see if strain was important.



**Figure 5.23- Sum of peak magnitudes per unit strain for various volume fractions and gap sizes (for  $72.4\text{N/m}^2$  stress experiments). Error bars show standard deviation of repetitions.**

A significant increase in the sum of peak magnitudes per unit strain with increasing volume fraction was seen (Figure 5.23). This suggested that at higher volume fractions, the extent of jamming was more extreme for a fixed strain.

This trend was found for all gap sizes investigated, and the sum of peak magnitudes per unit strain for a particular volume fraction appeared similar for all gap sizes. The sum of peak magnitudes over the entire experiments was also similar for a particular volume fraction at different gap sizes (Figure 5.22). This was largely due to the actual strain achieved during the experiments being similar for all gap sizes at a particular volume fraction (due to the shear rates being similar at different gap sizes).

Results therefore suggested that strain is a very important factor in jamming, with energy dissipation through jams for a fixed strain increasing with increasing volume fraction. The total amount of energy dissipation per unit strain was approximately independent of gap size. This suggested that for a given energy input, a fixed amount per unit strain will be dissipated through jamming and dilation at a particular volume fraction, regardless of gap size.

This ‘similarity’ of the overall response at a fixed volume fraction and stress at different gap sizes was due to a larger gap resulting in fewer, but proportionally larger jams. This indicated the system’s overall behaviour was essentially

'independent' of gap size. The larger gap meant the behaviour was 'stretched' over time somehow but its 'total response' per unit strain is still the same.

In 5.3.2, results suggested that the applied shear stress was an important aspect in determining the extent of jamming at a particular volume fraction. Therefore a combination of the shear stress and strain likely influenced the extent of energy dissipation through jamming. In 5.3.2, the strains achieved in an experiment at a particular volume fraction were similar at all shear stresses where jamming was seen (since increasing the supplied voltage/shear stress did not result in an increase in the rotation rate of the inner cylinder). Despite similar strains, the count of jams was affected significantly by the applied shear stress. The strain and shear stress were therefore both important factors that influenced the extent of jamming.

This can be seen in Figure 5.24 where the sum of peak magnitudes per unit strain increased with increasing shear stress at a particular volume fraction. This was more significant at higher volume fractions, where a greater extent of jamming per unit strain occurred. High volume fractions at high shear stresses therefore resulted in the 'most jamming' per unit strain.

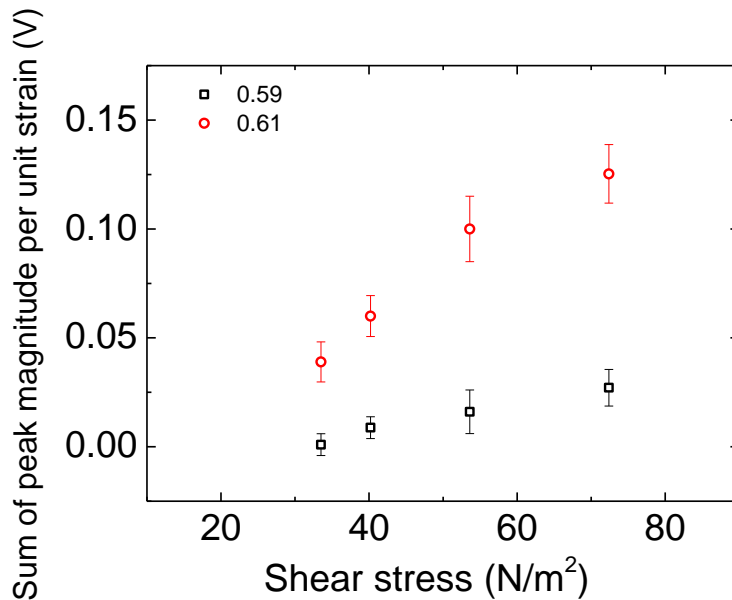


**Figure 5.24- Sum of peak magnitudes per unit strain for various shear stresses for  $\phi=0.59$  and  $\phi=0.61$  experiments. 5mm gap size. Error bars show standard deviation of repetitions.**

One possible picture is that the energy supplied to the motor was dissipated through a combination of viscosity due to shearing and jamming/dilation peaks. Beyond a particular input energy required to shear the material (and at or beyond the onset

stress where jamming occurred), additional supplied energy (from increasing the stress) was dissipated by further jamming/dilation. This increase involves more frequent jams rather than more ‘severe’ jams according to Figure 5.17 where the average peak magnitude does not change strongly with stress. This is discussed in 5.3.10.

### 5.3.5 Effect of Particle Size

As with the visual results obtained with smaller particles (see 4.3.1.7), when  $287\pm4$  nm radius particles (compared to  $488\pm5$  nm used previously) were used in the 5mm gap shear cell, no voltage peaks/ jamming was seen, even at the highest shear stresses and shear rates and with the highest volume fraction (Figure 5.25). This was then repeated in the 2.5mm gap shear cell (since previous results showed that a smaller gap increased the likelihood of jamming). Again, no jamming was seen in any of the conditions studied. This showed that particle size was an important factor in deciding whether or not jamming occurred for a particular set of conditions.

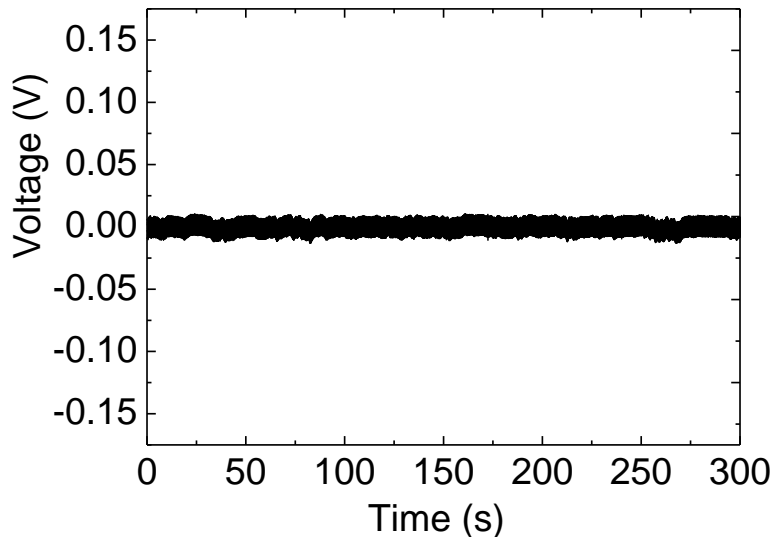


**Figure 5.25- Example voltage-time profile for smaller (287nm radius) particles at  $\Phi=0.61$ . 5mm gap size and  $72.4\text{N/m}^2$  stress.**

The importance of particle size in jamming may be related to the fact that particle size is important in shear thickening: the critical shear rate and shear stress required for shear thickening decrease with increasing particle size [6]. Studies have shown that the onset shear rate for shear thickening scales inversely with particle volume

(i.e. radius  $^{-3}$ ) [6]. Perhaps if higher shear stresses/rates were used experimentally, jamming would have been observed with the smaller particles.

Reasons for this particle size dependence are not yet fully understood, but it is thought that with smaller particles, interparticle interactions from various sources such as electrostatic interactions and Brownian motion are more significant than with larger particles and this can affect the onset stress for shear thickening. One effect mentioned in literature is that with small particles, there is a higher particle-liquid interfacial tension. This can result in an effective attraction between particles which results in a yield stress and this can hide shear thickening [7, 8].

From another perspective, smaller particles may have been more difficult to bridge across the gap of the shear cell (more of them would have been required), making jamming less likely. Less room would also be required for the material to volumetrically expand and dilate in order to flow. This would have resulted in less ‘pushing’ against frustrated boundaries, resulting in weaker confining stresses. Therefore if dilation was less extreme, the extent of jamming would likely have been greatly reduced, perhaps explaining why no sign of dilation/jamming was visible.

This work has shown the important influence particle size can have on jamming and again shows the strong links between the results seen visually and with the force sensor technique.

### 5.3.6 Effect of Closed System

Since the visual results (and literature) suggested that dilation was an important aspect of the DST/jamming mechanism, the effect of confinement was considered. Since visually dilation was seen at the open fluid-air interface (4.3.1.1), a close-fitting lid was designed for the shear cells to see how flow behaviour was affected when there was no open surface available for the material to dilate at (Figure 5.26).

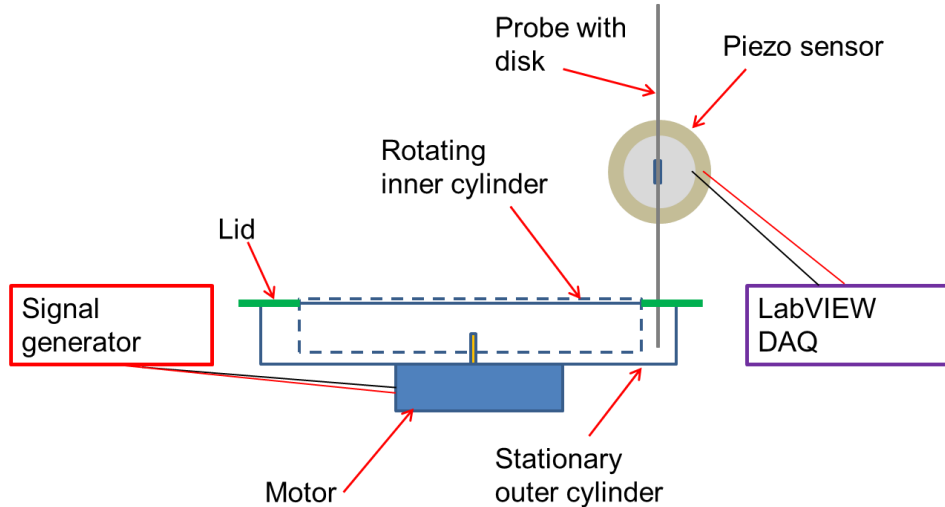
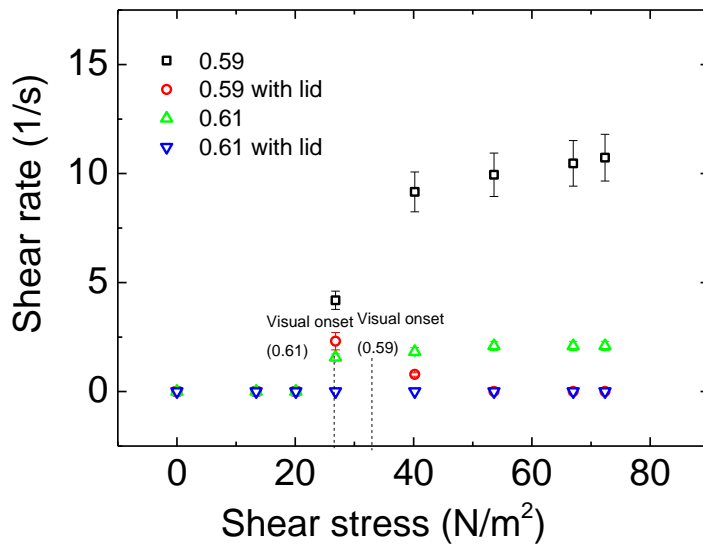


Figure 5.26- Force sensor set-up for closed system

For  $\phi=0.56-0.61$  at the maximum supplied voltage, when a lid was placed on top of the shear cell so that the fluid had no open surface, the material jammed completely, resulting in the inner cylinder's movement (and therefore the flow) ceasing. Prior to placing the lid on the shear cell, the material could be seen visibly dilating at the open air-liquid interface. With the lid on, the material was unable to do this and dilation was completely frustrated. Since unable to dilate, the sample was unable to flow hence complete jamming occurred. With the force sensor, no peaks were seen in the output, suggesting that the material was in a completely jammed state.

As detailed in [Chapter 2](#), these results are in agreement with the proposed idea that complete flow induced jamming occurs in systems that are simply unable to successfully dilate [9, 10]. As explained in [Chapter 2](#), discontinuous shear thickening and jamming can therefore essentially occur via the same mechanism, with the system set-up and confinement ultimately dictating whether discontinuous shear thickening or complete jamming occurs.

The shear rate versus shear stress flow profiles obtained with no open surface differed substantially from those with an open surface for the volume fractions investigated (Figure 5.27). With the lid present (i.e. no open surface), the measured shear rate was significantly lower than without and beyond a particular shear stress (corresponding to or slightly above that where visible dilatancy and peaks became apparent in the open system) the shear rate began to fall to zero as the systems jammed completely. For example, with a volume fraction of 0.59 at a stress of  $72.4\text{N/m}^2$ , a shear rate of  $\sim 11\text{s}^{-1}$  was measured without a lid present but this was reduced to  $0\text{s}^{-1}$  with a lid.



**Figure 5.27- Comparison of shear rate versus shear stress flow profiles for volume fractions showing jamming, with and without open surface (for  $\Phi=0.59$  and  $0.61$ ). 5mm gap size. Error bars show standard deviation of repetitions.**

In systems that did not show jamming behaviour (i.e.  $\phi=0.55$ ), the lid did not have a significant impact on the profiles (Figure 5.28); just slight reductions in the shear rate for a given shear stress were measured. This was likely due to an additional resistance to flow caused by the lid.

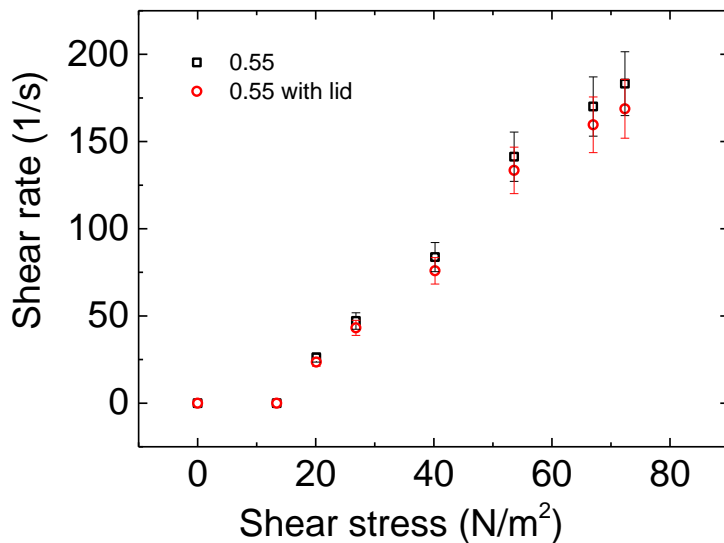


**Figure 5.28- Comparison of shear rate versus shear stress flow profiles for volume fraction that did not show jamming, with and without open surface. 5mm gap size. Error bars show standard deviation of repetitions.**

Overall, these results helped provide a greater understanding into the causes of jamming and showed that confinement is indeed an important part of the mechanism. The findings suggested that the visible dilation and peaks detected with the force sensor were part of the mechanism that enabled the material to continue flowing and not jam completely. To prevent complete jamming occurring, some form of volumetric compliance is necessary to allow the material to successfully dilate in order to flow.

### 5.3.7 Effect of Soft Walls

Since confinement appeared important, experiments with soft-walled shear cells were performed. For this, a layer of neoprene foam was attached to the Perspex shear cell walls (the vertical walls of the cylinders). The shear cells were manufactured so that gaps and fluid fill heights with the foam present were the same as before.

With soft walls, for a given applied voltage and volume fraction, the rotation rate of the inner cylinder was greater compared to the previous hard wall experiments (typically by 30-40%)- i.e. for a given shear stress, a greater shear rate was obtained. This suggested that with soft walls, the material appeared less viscous: jamming was perhaps less extreme.

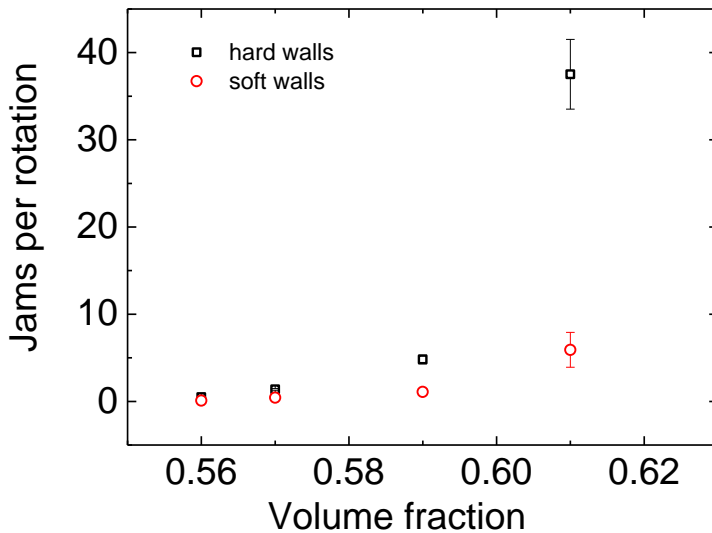
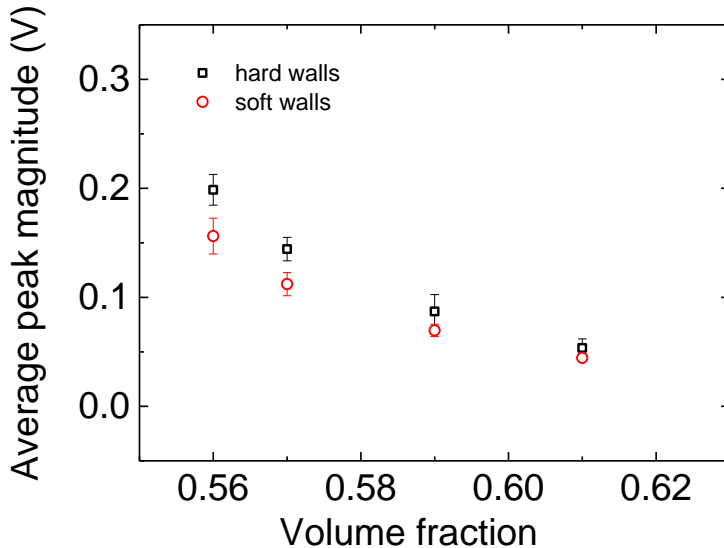


Figure 5.29- Jams per rotation of the inner cylinder comparison between soft and hard walls. 5mm gap size and 72.4N/m<sup>2</sup> stress. Error bars show standard deviation of repetitions.

It was also much more difficult to see visible dilatancy at the open surface, than previously with hard walls. With foam walls, it was more difficult to make optical observations since the foam was black and opaque, making the liquid appear darker. Dilatancy at the open surface did not appear to occur to nearly the same extent as before, with dilating regions that could be seen appearing smaller and less frequent than previously seen with hard walls.

A similar shear stress was required for peaks/visible dilatancy to be noticed compared to the hard wall experiments. Above this critical shear stress, with the

force sensor significantly fewer jams per rotation of the inner cylinder (i.e. over a fixed strain) were measured with soft walls for all conditions studied (Figure 5.29). The average peak magnitudes, however, were less affected but did reduce somewhat (Figure 5.30).



**Figure 5.30- Average peak magnitude comparison between soft and hard walls. 5mm gap size and  $72.4\text{N/m}^2$  stress. Error bars show standard deviation of repetitions.**

Fewer peaks may have been measured since soft walls are likely to have made it easier for particles to dilate: they could now dilate out of the open surface and against the soft walls. This would have made jamming less extreme, given the greater ease of dilation (due to less frustrated dilatancy). Although dilation was easier with soft walls, it was still confined to an extent- not all walls were soft (i.e. the horizontal cylinder bases were not covered), the walls were not entirely flexible and there was still confinement at the air-liquid interface. This confinement meant that jamming did still occur. Perhaps if the mixture had been surrounded by even more flexible walls, jamming would have been avoided altogether [8].

As gap size increased, the effect of the soft walls appeared less significant. For example, with the 2.5mm gap experiments, soft walls caused the count per rotation to decrease to ~20-30% of the hard wall equivalent, while with the 10mm gap, the count per rotation reduced to ~50-60% of the hard wall equivalent on average. This may have been due to the surface to volume ratio decreasing with increased gap size- the surface to volume ratio in the 2.5mm gap experiment was approximately twice that of the 10mm gap experiment. The surface used for the surface to volume

ratio was the total area of the soft shear cell surface in contact with the suspension. The volume used was the volume of suspension that was required to fill the shear cells

The energy dissipation per unit strain was similarly determined as done in 5.3.4 for the soft walled experiments (Figure 5.31). As with hard walls, an increase in the sum of peak magnitudes per unit strain with increasing volume fraction was seen. The change, however, was less extreme due to the significantly smaller number of peaks with the soft walls.

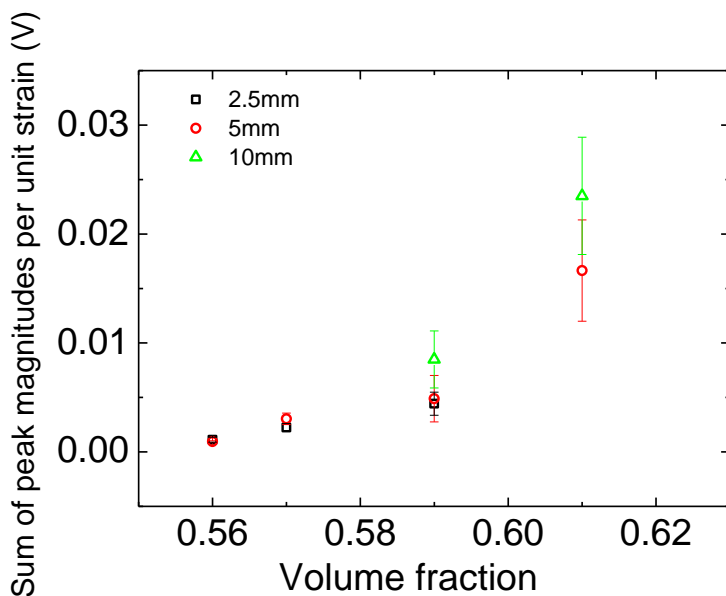


**Figure 5.31- Sum of peak magnitude per unit strain for various volume fractions and gap sizes (for 10.8V experiments) with soft walls. Error bars show standard deviation of repetitions.**

At a particular shear cell gap size, the sum of peak magnitudes per unit strain when using soft walls relative to hard walls was approximately constant when using different volume fractions.

Overall, this section of work and section 5.3.6 strongly suggested that confinement plays an important role in jamming. This agrees with recent literature on the area [7-10]. A consideration of system geometry and confinement could be used as a method of controlling jamming in the future.

### 5.3.8 Statistical Analysis of Precisions

*Carol Forsyth assisted with bootstrapping.*

Experiments were typically repeated between 3 and 5 times. To confirm that this was sufficient to say that trends were statistically significant, a bootstrapping procedure was performed on selected data.

Bootstrapping involved randomly resampling the experimental data for the set of conditions that were being investigated. Replacement was done so that a given data point could be re-selected.

Resampling was done by assigning a number to each piece of data/ each repetition for a particular set of conditions. A random number generator was then used to select which data points were to be used in the analysis.

Full and partial bootstraps were done. For full bootstraps, the number of resamples was equal to the number of repetitions for a particular set of conditions. For example, if three repetitions were done, three resamples were taken. For partial bootstraps, the number of resamples was varied from 1 to 3.

The resampled data were then plotted and the slope of the plot was calculated from a linear least squares fit (Equation 5.4). This procedure of resampling and calculating the slope of the data was repeated 200 times. The mean slope and standard deviation were then found.

$$m_j = \frac{\sum_{i=1}^N x_i y_i - \frac{1}{N} \sum_{i=1}^N x_i \sum_{i=1}^N y_i}{\sum_{i=1}^N x_i^2 - \frac{1}{N} (\sum_{i=1}^N x_i)^2} \quad \text{Equation 5.4}$$

Where:  $m_j$  is the linear least squares slope,  $j = 1, 2, \dots, M$ ,  $M$  is the number of times the procedure of resampling and calculating the slope was done (i.e. 200),  $N$  is the total number repetitions,  $i = 1, 2, \dots, N$ ,  $x_i$  is the x data (e.g. volume fraction) and  $y_i$  is its corresponding y data (e.g. peak magnitude).

Data for three repetitions of the experiments were analysed to check that three runs were sufficient. The following are example bootstraps that were performed.

### Average Peak Magnitude

For the variation of average peak magnitude with volume fraction, the relationship was assumed to be linear (see Figure 5.12). The bootstrapping procedure confirmed a clear trend (assuming the linear approximation was valid): increasing the volume fraction resulted in smaller peaks on average (Figure 5.32). A significant negative gradient was found and the standard deviation was low. The trend was therefore statistically significant.

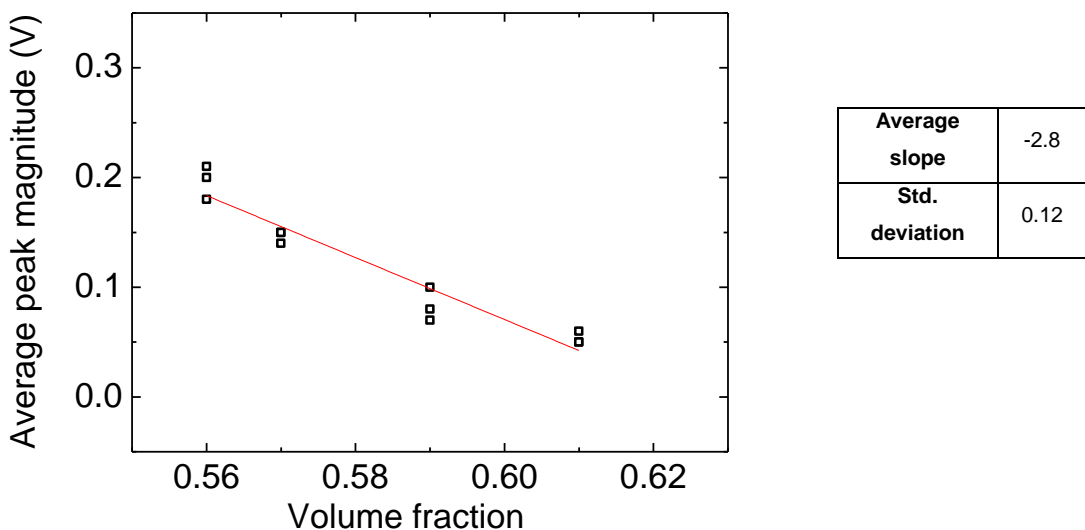


**Figure 5.32- Example bootstrap on full average peak magnitude data set**

The analysis showed that further repetitions would have had little impact on the slope, with their main effect being reducing the standard deviation. As mentioned, this was sufficiently low for three repetitions, therefore confirming that three repetitions sufficed and that statistically significant trends could be identified from them.

### Jams per Rotation of Inner Cylinder

For the variation of peaks per rotation of the inner cylinder with volume fraction, the relationship was not linear (Figure 5.13). The peaks per rotation values were logged ( $\ln$ ) and bootstrapping was performed on the logged values since this showed a linear trend. Again, a clear statistically significant trend was found- increasing the volume fraction resulted in an increase in the number of jams per rotation of the

inner cylinder (Figure 5.33). A significant positive gradient was found and the standard deviation on the linear fit was low.

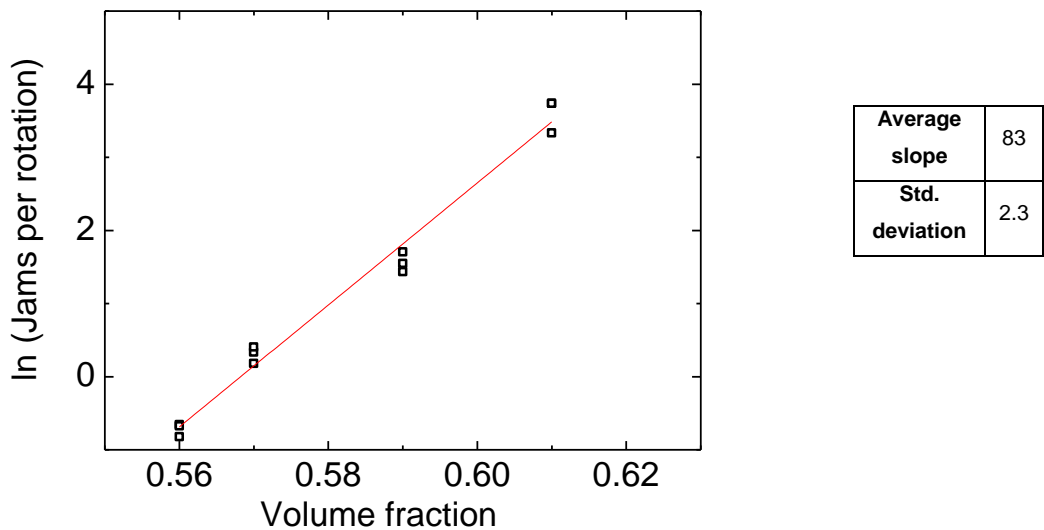


Figure 5.33- Example bootstrap on full jams per rotation of the inner cylinder data set

As with the average peak magnitude results, the analysis showed that further repetitions would have had little impact on the slope, with their main effect being reducing the standard deviation.

Overall, this bootstrapping method confirmed that three repetitions were sufficient for drawing statistically significant trends.

### 5.3.9 Mechanism Summary

Using the work done in [Chapter 4](#) and [Chapter 5](#) and relating it to the findings of [Chapter 2](#), it is now possible to propose a likely mechanism for discontinuous shear thickening and flow induced jamming that overcomes the flaws with the proposed mechanisms detailed in [Chapter 2](#). Based on the experimental findings and literature, it can be concluded that a likely mechanism involves a combination of both the hydrocluster formation mechanism and frustrated dilatancy.

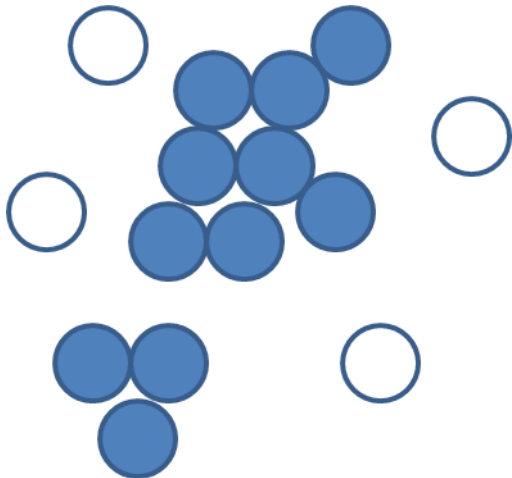


Figure 5.34- Example diagram of force transmitting hydroclusters

#### Hydrocluster Formation

This idea proposes that under shear, particles tend to be driven together into clusters (hydroclusters) that are local transient fluctuations in particle density that are more densely packed than the bulk (higher  $\phi$ ). These are held together through lubrication hydrodynamics at low volume fractions and stresses [8, 11]. At sufficiently high volume fractions and shears, these hydroclusters may be thought of more as frictional force transmitting hydroclusters, since particles are in very close contact and lubrication breaks down resulting in dissipative frictional contacts between particles (Figure 5.34) [8, 11].

The presence of hydroclusters could lead to continuous shear thickening due to their hydrodynamic impact: their presence results in increased dissipative hydrodynamic interactions, resulting in increased energy dissipation and therefore a higher viscosity [12].

It has been proposed that as concentration is increased, the effective volume of hydroclusters becomes larger and they may eventually span the system, causing discontinuous shear thickening and jamming [6, 8]. Experimental work and computer modelling has, however, shown that it is highly unlikely that these clusters spanning the system alone are enough to cause discontinuous shear thickening and flow induced jamming [8]. It is likely that friction and dilatancy now come into the mechanism [8].

### Frustrated Dilatancy

At certain volume fractions and beyond a critical shear rate, discontinuous shear thickening and jamming may occur. Force transmitting hydroclusters with dissipative frictional contacts (due to very close particle proximity and breakdown of lubrication) may span the system (e.g. across the gap in the shear cell) [13]. They must dilate to shear [8, 11, 14]. Dilatancy involves the volumetric increase/expansion of the material under shear. This allows concentrated systems to flow by effectively reducing the overall volume fraction, giving particles more room to move (Figure 5.35) [8].

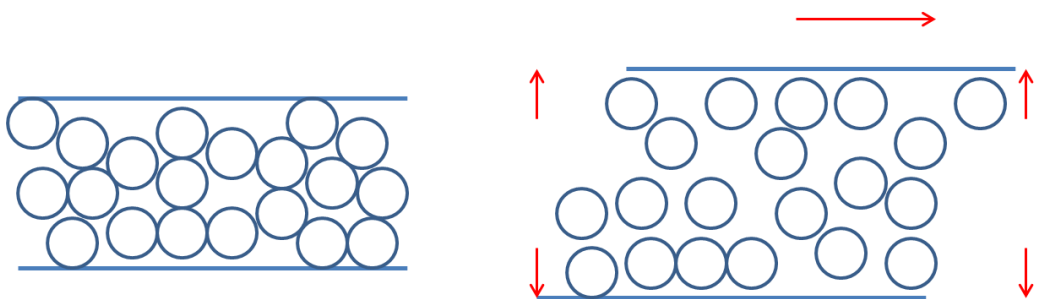


**Figure 5.35- Left:** material that is confined and therefore cannot dilate since dilation is completely frustrated

**Right:** material that is not confined (walls can expand) and can therefore dilate

Dilation alone, however, is not enough for discontinuous shear thickening and jamming, and as shown in the experiments (through studying the effects of soft walls and confinement) dilation must be frustrated/confined [7, 8]. Dilation was seen experimentally at the air-liquid interface (where there was a large confining capillary stress, frustrating dilatancy) and the work suggested that this visible dilation coincided with the onset of discontinuous shear thickening/jamming (as shown in the shear rate versus shear stress flow profiles and the detection of fluctuating stresses

with the force sensor). This strongly suggested that frustrated dilatancy was indeed a crucial part of the discontinuous shear thickening and jamming mechanism.

Dilation of the frictional force transmitting hydroclusters against a frustrated system boundary may therefore lead to the large fluctuations in stress and dramatic increases in viscosity associated with discontinuous shear thickening and jamming. When dilation is frustrated, shear results in normal stresses against the boundaries being measured that correspond to the material being pushed/ expanding against the boundary. Confinement provides equal and opposite restoring confining stresses (from Newton's 3<sup>rd</sup> law), and these can be transmitted along solid-solid frictional contacts between neighbouring particles that form part of a network of force chains or force transmitting clusters (i.e. the spanning frictional force transmitting hydroclusters) [6, 8, 15]. This allows the dramatic increases in shear stress with shear rate, that are associated with discontinuous shear thickening and jamming, to be achieved [7, 8].

In the shear cells, attempted expansion towards the solid system boundaries results in much higher confining stresses. Therefore, the material can dilate most successfully out of the open surface since it is here that additional volume can most readily be obtained (the confining capillary stress at the open surface is the weakest confining stress) [8].

This confining capillary stress which frustrates dilatancy (combined with the stronger confining effects of the solid boundaries and particle stiffness) can balance out interparticle and shear forces, resulting in regions resisting motion, i.e. jamming. If the weakest confining stress (i.e. the confining capillary stress at the air-liquid boundary) can be overcome, the jammed material fractures, as observed at the open surface of the shear cell [6, 16]. Flow is therefore able to continue, until the next 'jam' occurs.

### Discontinuous Shear Thickening and Jamming Relationship

As mentioned in [Chapter 2](#), discontinuous shear thickening and flow induced jamming are thought to be closely related [7, 9, 17-21]. The main difference is related to their flow rate. With flow induced jamming, when jammed, the material is fully arrested with no flow (i.e. a zero shear rate) [22]. With DST, however, the shear rate has a non-zero value when able to dilate [8, 9, 22]. It is possible that the fully

jammed (zero shear rate) state associated with flow induced jamming therefore simply occurs in DST systems that are unable to dilate [9].

If dilation is not possible at all (shear forces cannot overcome confining stresses from the boundaries), the material would undergo a complete jamming transition since the volume fraction could not be reduced (as shown in Figure 5.35 (left)) [10]. If a material is able to dilate, it may be sheared without completely jamming (as shown in Figure 5.35 (right)) [10]. This idea is similar to work which found that jamming can be viewed as the constant volume counterpart of dilatancy [9].

In the open shear cell experiments in [Chapter 4](#) and [Chapter 5](#), full flow induced jamming was not occurring since the material did not completely arrest. Discontinuous shear thickening (or ‘partial jamming’) was most likely occurring due to the confining stresses coupled with the fact that the system was able to dilate at the air-liquid interface (since the weakest confining stress could be overcome).

With the closed experiments (i.e. with the lid on), all confining boundaries were solid and these confining stresses were high enough to resist dilation. The sample was unable to dilate hence complete jamming occurred and flow ceased completely. Only if a stress greater than the confining stresses (in this case the solid boundaries or particle stiffness) was applied, could flow continue.

With soft walled shear cells (i.e. by reducing the confining stress of the walls), discontinuous shear thickening/jamming was less extreme than with hard walls. Soft walls make it easier for particles to dilate: they could now dilate out of the open surface and against the soft walls. It is worth noting that the confining stress from the soft walls used experimentally was estimated to be a similar magnitude to the confining stress at the air-liquid interface [7, 8].

Overall, these results are in agreement with the proposed idea that flow induced jamming occurs in systems that are simply unable to successfully dilate [9, 10]. DST and jamming therefore essentially occur via the same mechanism, with the system set-up and confinement ultimately dictating whether DST or complete jamming occurs.

### 5.3.10 Additional Considerations

There are still a number of considerations whose explanations are not yet fully known or understood in this work. This section will briefly discuss these main points and outline possible explanations that may be drawn from the findings.

#### What actually caused the fluctuating forces detected with the force sensor?

The actual cause of the fluctuating forces measured with the force sensor remains unclear, but there are a number of possibilities. Literature regarding fluctuating forces measured during DST and jamming often remains vague, saying that the fluctuating forces are caused by the building and destruction of clusters [5]. Others suggest the fluctuations are caused by the large normal stresses that are produced when the material attempts to dilate in order to flow [8, 23].

Other possible ideas from this work are as follows:

- The formation of clusters with a higher volume fraction/density than the bulk may have resulted in larger forces being applied to the probe as they struck the probe. Larger clusters, and clusters with higher volume fractions than the bulk, may have resulted in larger forces being measured.
- The formation or destruction of spanning frictional dilating clusters may have led to force fluctuations. As clusters formed and spanned the gap in the shear cell (i.e. the visible dilating regions), the flow slowed down. As the clusters broke up, the flow sped up. This change in fluid speed (and the rotating inner cylinder speed) implied accelerations and decelerations which may have resulted in fluctuating forces [24]. The collapse of jammed regions may also have led to fluctuating forces, as the solid regions reverted back to fluid like and flow continued.

It is worth noting that the ‘cluster formation and growth’ mechanisms are still not well understood. More microscopic measurements are necessary to fully understand why they form and what determines their growth. The results in this thesis tell us about conditions required for jamming and how to avoid it, but do not detail why the clusters form and how to control them. This is an area of future work.

## **Does dilatancy cause jamming or is it part of the mechanism to allow flow to continue when jammed?**

This work, in agreement with recent literature, suggests that it is frustrated dilatancy rather than just dilatancy that causes jamming [8]. It was only when frustrated dilatancy at the open surface of the shear cell began to become visible, that jamming peaks were detected and the rotation rate of the inner cylinder slowed down. When the sample began to crack open, gaining additional volume, and the region that was dilating was no longer frustrated (and was no longer visibly dilating across the gap at the open surface), the material began to flow as prior to the jam.

When system confinement was reduced by using soft walls, jamming appeared less extreme (fewer and weaker jams) since the sample could now dilate with less frustration at the soft walls. When confinement was increased by making a closed hard walled system, dilation was completely frustrated and complete jamming occurred.

When dilation is not frustrated, dilation is part of a mechanism to allow flow. Therefore dilation that is frustrated causes jamming and dilatancy itself is also a means to allow flow to continue.

## **What is the purpose of jamming?**

This work, in agreement with recent literature, suggested that jamming occurs when a material attempts to dilate in order to flow, but is unable to do so. The work also suggested that jamming, or more likely the dilation associated with it, may be a means of dissipating the energy that is supplied to make the material flow.

When jamming was occurring in the experiments, further increases in shear stress did not result in the shear rate increasing. The additional energy supplied through increasing the shear stress may have been dissipated through further dilatancy (e.g. dissipated through friction between particles as the system attempted to dilate and through the cracking and break-up that was seen when jammed regions broke up), hence no increase in shear rate.

In this picture the energy supplied to the shear cell's motor was dissipated through a combination of viscosity due to shearing and frictional/dilatancy losses associated with jamming peaks. Beyond a particular input energy required to shear the material (and at or beyond the onset stress where jamming occurred), additional supplied

energy (from increasing the shear stress) was dissipated by additional jamming/dilation, rather than increased viscous shear. This would explain why from the onset conditions for jamming, further increases in shear stress did not result in the shear rate increasing, but did result in an increased number of jams. Precisely how energy is dissipated in jamming/dilation events remains unclear.

**Why did average peak magnitudes decrease with increasing volume fraction and why was there a smaller spread of peak sizes with increasing volume fraction?**

The reason for smaller peaks (with a smaller spread of sizes) with increasing volume fraction is not clear, but may be explained as follows. It was possible that the intensity of a jam depended on the amount of material involved and the speed of fluid movement. At lower volume fractions, the rotation rate of the inner cylinder was greater at a given applied motor voltage (due to its lower viscosity), hence the material was moving more quickly. This may have partially accounted for the greater peak magnitudes recorded due to greater forces on the probe and therefore sensor. As an example, at a volume fraction of 0.56, the shear rate at  $72.4\text{N/m}^2$  was  $84\text{s}^{-1}$  and the average peak magnitude was  $0.2\text{V}$ . At a volume fraction of 0.61, the shear rate at  $72.4\text{N/m}^2$  was  $2\text{s}^{-1}$  and the average peak magnitude was  $0.05\text{V}$ . While larger rotation rates appeared to result in larger peak magnitudes, the results did not scale; for example, despite the shear rate reducing by  $\sim 40x$  by increasing the volume fraction from 0.56 to 0.61, the average peak magnitude did not decrease by  $40x$ . This suggested that more than just the rate of fluid movement was responsible for peak magnitudes.

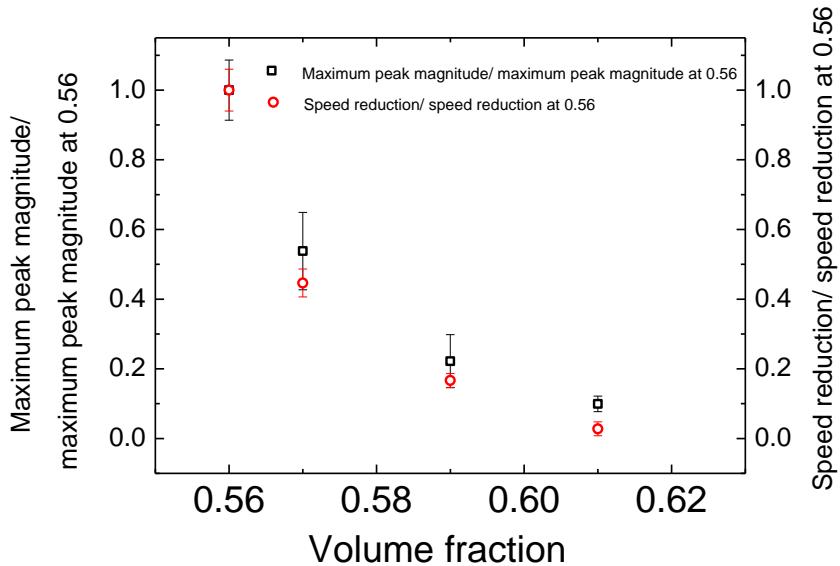


**Figure 5.36- Maximum peak magnitude variation with volume fraction comparison with velocity reduction during jamming (as deduced in [Chapter 4](#)). 5mm gap size and 72.4N/m<sup>2</sup> stress. Error bars show standard deviation of repetitions. Plot shows values relative to values measured at  $\Phi=0.56$  to allow simpler comparisons.**

As detailed in 4.3.1.5, the decrease in velocity of the material during jamming relative to when it was not jamming was more significant at lower volume fractions. Since the material was sheared at a greater rate for a given shear stress as volume fraction decreased, there was a greater range of decreased speeds the jammed material could go at when lower volume fractions were used. This may explain the larger spread of peaks. For example, a larger jam may result in a greater reduction in speed, hence a larger jamming peak. The extent of the reduction in velocity with volume fraction detailed in 4.3.1.5 scaled well with the dependence of maximum peak magnitude on volume fraction measured with the force sensor as shown in Figure 5.36. This suggested that the extent of speed reduction was likely related to the magnitude of peaks.

The voltage peak size/speed reduction observed may have depended on particle/cluster configurations and rearrangements. Since particles were further apart at a lower  $\Phi$ , many more rearrangements and configurations were possible. At higher volume fractions, particles were all closer together so rearrangements and configurations would have been more similar and homogeneous [25]. This likely contributed to smaller spreads of peak sizes at higher volume fractions, since jams are likely to have been similar to one another in terms of particle configurations.

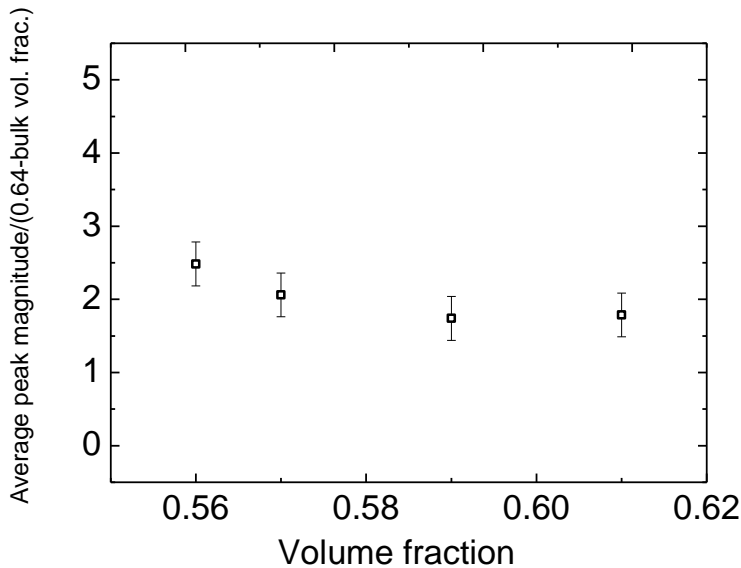


**Figure 5.37- Average peak magnitude scaled by  $(\phi_{RCP} - \phi_{bulk})$ . 5mm gap size and  $72.4\text{N/m}^2$  stress. Error bars show standard deviation of repetitions.**

The contrast between the jamming cluster volume fraction and the bulk volume fraction may have been important, assuming jamming clusters must be at some high volume fraction similar to close packing. Peaks may have appeared more extreme with lower volume fractions since there would have been a larger difference in volume fraction between the clusters and the bulk [14]. It is also possible that the intensity of a jam depended on the volume fraction of the clusters and, as mentioned, their arrangement. This may help explain the larger spread of peak magnitudes at lower volume fractions, since there was a larger range of volume fractions greater than the bulk volume fraction, and arrangements, that the clusters could take. Figure 5.37 shows the average peak magnitude scaled by the difference between  $\phi_{RCP}$  (i.e. 0.64, the maximum volume fraction a cluster could take) and  $\phi_{bulk}$ . This produced values that were close to constant for each volume fraction, suggesting that the difference between the bulk volume fraction and the maximum cluster volume fraction was approximately proportional to the average peak magnitude.

## **Why were there more jams per rotation of the inner cylinder as volume fraction increased?**

At higher volume fractions, more particles were present per unit volume and therefore they would have been closer together with less room to move and attempt to dilate. This combined with the fact that it is thought that as concentration is increased, the effective volume of hydroclusters becomes larger [6, 8] perhaps made the likelihood of particles bridging across the gap and jamming greater for a fixed strain at higher volume fractions [12]. The time for one rotation increased with increasing volume fraction since the rotational rate was lower. This may also have been important since the larger time may have resulted in a greater likelihood of a jam occurring within the time period of one rotation of the inner cylinder. The importance of strain on the extent of jamming was discussed in more detail in 5.3.4.

Jamming distributions and probabilities are discussed in [Chapter 6](#).

## **Why did increasing the shear cell gap size result in fewer but larger jams?**

More peaks may have occurred with a smaller gap since it was easier for force transmitting clusters to bridge across the gap, causing jamming. The smaller gap meant that less material was required to cause a jam; this may explain why jams were weaker but more frequent.

The surface to volume ratio was affected by gap size and this may have been important as mentioned in 5.3.3. The surface to volume ratio decreased with increasing gap size. Surfaces/boundaries and the confining stresses they provide are very important in dilation as mentioned [7, 8, 10, 26]. Therefore if dilation is related to jamming, the larger surface to volume ratio with decreasing gap size may have led to more jams since frustrated dilatancy against the solid walls would have been more apparent. These factors may have made the probability of a jam occurring greater.

The area of the open surface decreased with decreasing gap size. This was the weakest confining stress as it was here that dilation/fracturing was seen. This may have resulted in weaker peaks being detected due to the smaller area being involved in this frustrated dilatancy.

### **5.3.11 Wider Applications**

From the trends identified, it is clear that volume fraction, applied stress and system geometry are important factors in controlling jamming. By ensuring flow volume fractions are kept below those where jamming is possible, the likelihood of jamming occurring could be minimised. If operating at volume fractions where jamming could occur, the likelihood of jamming could be reduced by lowering the applied stress (e.g. a lower flow rate). Reducing the particle size or using a wider system geometry could also be effective (e.g. wider openings). The possibility of considering confinement and allowing the flow geometries to expand, for example by making them flexible, is also a possible means to reduce jamming problems. Particle deformability is also worth considering.

## 5.4 Conclusions

A novel jamming detection technique was designed and it was able to overcome the shortcomings of the visual investigations detailed in [Chapter 4](#). The method involved designing equipment to measure intermittent forces in the samples that were undergoing shear, that were only present when jamming occurs. This force sensor technique allowed a thorough investigation into jamming trends and its findings could be linked to the results seen visually.

As with the visual results, concentration appeared very important. With the force sensor, a series of peaks in the output were detected only at  $\phi \geq 0.56$ . A peak was taken as analogous to a jam and the presence of peaks corresponded to the visual onset of dilation.

Further investigations of voltage peaks from the piezo's output were made to allow jamming trends to be identified. These included studies of the frequency and size of peaks, as well as the time gaps between them. The effect of system geometry and the applied shear stress were also investigated. System confinement appeared important and could be used to influence the extent of jamming and discontinuous shear thickening. This analysis resulted in an improved understanding of conditions where jamming occurs and how it may be controlled and prevented. This could ultimately lead to a better understanding of complex flow systems and lead to more efficient processes.

Based on the experimental findings, a mechanism for discontinuous shear thickening and flow induced jamming was proposed that involves a combination of force transmitting hydrocluster formation and frustrated dilatancy.

The data obtained from the force sensor (voltage-time data from the piezo) is subsequently used in [Chapter 6](#) where a more thorough analysis of jamming peak distributions and probabilities is detailed across the conditions investigated in this chapter. The findings of this chapter are also referred to in [Chapter 7](#), where the results are compared to those found using a commercial rheometer.

d	Diameter
RPM	Rotations per minute
t	Time
V	Initial voltage
v	Current voltage
$\Phi$	Volume fraction
$\tau$	Time constant

1. Physik-Instrumente, *Fundamentals of Piezomechanics*. 2006.
2. Karki, J., *Signal Conditioning Piezoelectric Sensors*. 2000: Texas Instruments.
3. Change, D., *Introduction to Piezoelectric Sensors*. 2008.
4. Travis, J. and J. Kring, *Labview for Everyone: Graphical Programming Made Easy and Fun*. 2006: Prentice Hall.
5. Lootens, D., H. Van Damme, and P. Hebraud, *Giant stress fluctuations at the jamming transition*. Physical Review Letters, 2003. **90**(17).
6. Mewis, J. and N. Wagner, *Colloidal Suspension Rheology*. 2012: Cambridge University Press.
7. Brown, E. and H.M. Jaeger, *The role of dilation and confining stresses in shear thickening of dense suspensions*. Journal of Rheology, 2012. **56**(4): p. 875-923.
8. Brown, E. and H. Jaeger, *Shear thickening in concentrated suspensions: phenomenology, mechanisms, and relations to jamming*. Reports on Progress in Physics, 2013. **77**(4): p. 046602.
9. Cates, M.E., et al., *Jamming, force chains, and fragile matter*. Physical Review Letters, 1998. **81**(9): p. 1841-1844.
10. Fall, A., et al., *Shear thickening of cornstarch suspensions*. Journal of Rheology, 2012. **56**(3): p. 575-591.
11. Seto, R., et al., *Discontinuous Shear Thickening of Frictional Hard-Sphere Suspensions*. Physical Review Letters, 2013. **111**(21): p. 5.
12. Wagner, N.J. and J.F. Brady, *Shear thickening in colloidal dispersions*. Physics Today, 2009. **62**(10): p. 27-32.
13. Wyart, M. and M.E. Cates, *Discontinuous Shear Thickening without Inertia in Dense Non-Brownian Suspensions*. Physical Review Letters, 2014. **112**(9).
14. O'Brien, V.T. and M.E. Mackay, *Stress components and shear thickening of concentrated hard sphere suspensions*. Langmuir, 2000. **16**(21): p. 7931-7938.
15. Weeks, E., *Soft Jammed Materials*. 2007, Tokohu University Press.
16. Smith, M.I., et al., *Dilatancy in the flow and fracture of stretched colloidal suspensions*. Nature Communications, 2010. **1**: p. 5.
17. Haw, M.D., *Jamming, two-fluid behavior, and "self-filtration" in concentrated particulate suspensions*. Physical Review Letters, 2004. **92**(18): p. 185506.
18. Campbell, A.I. and M.D. Haw, *Jamming and unjamming of concentrated colloidal dispersions in channel flows*. Soft Matter, 2010. **6**(19): p. 4688-4693.
19. Hebraud, P. and D. Lootens, *Concentrated suspensions under flow: Shear-thickening and jamming*. Modern Physics Letters B, 2005. **19**(13-14): p. 613-624.
20. Brown, E. and H.M. Jaeger, *Dynamic Jamming Point for Shear Thickening Suspensions*. Physical Review Letters, 2009. **103**(8): p. 4.
21. Bertrand, E., J. Bibette, and V. Schmitt, *From shear thickening to shear-induced jamming*. Physical Review E, 2002. **66**(6): p. 3.

22. Cates, M.E., M.D. Haw, and C.B. Holmes, *Dilatancy, jamming, and the physics of granulation*. Journal of Physics-Condensed Matter, 2005. **17**(24): p. S2517-S2531.
23. Hebraud, P., *Normal and tangential stress fluctuations during jamming*. Rheologica Acta, 2009. **48**(8): p. 845-853.
24. Larsen, R.J., et al., *Fluctuations in flow produced by competition between apparent wall slip and dilatancy*. Rheologica Acta, 2014. **53**(4): p. 333-347.
25. Weeks, E., *Flow of Amorphous Solids Modeled with Emulsion Droplets*, in *AIChE Annual Meeting*. 2014: Atlanta.
26. Fall, A., et al., *Shear thickening of cornstarch suspensions as a reentrant jamming transition*. Physical Review Letters, 2008. **100**(1): p. 018301.

# 6. Jamming Peak Distributions

## This section will cover:

- A further analysis of the data obtained from the force sensor used in Chapter 5, where intermittent forces in the sample that were only present when jamming occurred were measured.
  - An analysis of the distributions of jamming peak magnitudes.
  - An analysis of the distributions of time gaps between jamming peaks.



## 6.1 Summary

The voltage/time data from the jamming detection method developed and used in [Chapter 5](#) was analysed further. In [Chapter 5](#), voltage peaks were detected when the material jammed. In this chapter, from this voltage data from [Chapter 5](#), jamming distributions and jamming probabilities were analysed and discussed. Findings were related to literature on bottleneck flows.

An analysis of the magnitudes of jamming peaks and the time gap between jamming peaks was done. Histograms and cumulative distributions were produced and analysed to see if the data followed particular distributions. This resulted in a greater understanding of the experimental results in [Chapter 4](#) and [Chapter 5](#). It also allowed similarities between the experimental system and findings in literature, largely related to granular media, to be found.

By analysing the distributions of jamming peak magnitudes at different volume fractions, it was found that smaller peak events occurred significantly more often than larger peak events for all volume fractions considered. All histogram distributions of peak magnitudes at different volume fractions showed approximate exponential behaviour. Analysing the distributions of the time gap between peaks found that smaller time gap events occurred significantly more often than larger gap events for all volume fractions considered. The histogram distributions of the time gap between peaks at different volume fractions did not show a clear single distribution and appeared to transition from approximate power law behaviour to approximate exponential behaviour as volume fraction was increased.

The effects of shear stress, system geometry and confinement on the distributions were also investigated. This allowed a deeper understanding of the results in [Chapter 5](#).

To ensure the reliability of these results, a significant number of repetitions would be necessary. It was difficult to draw conclusive trends from the data, given that the fits to the distributions relied heavily on data with low counts. The trends identified did, however, appear consistent for the data that were obtained.

## 6.2 Analysis of Peak Magnitude Distributions- Effect of Volume Fraction

As detailed briefly in [Chapter 5](#), histograms showing the distribution of peak magnitudes were produced at different volume fractions. They showed that smaller peak events occurred significantly more often than larger peak events for all volume fractions considered (Figure 6.1 and Figure 6.2).

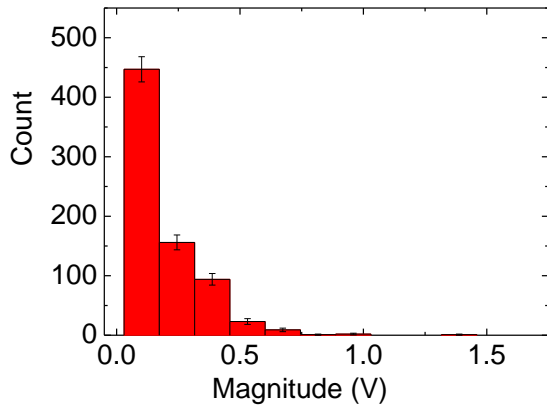


Figure 6.1- Peak magnitude histogram example for  $\phi=0.56$  (count in 5 minutes). 5mm shear cell gap size and  $72.4\text{N/m}^2$  stress. Error bars are the square root of the bin count. The minimum peak magnitude was  $0.03\text{V}$ . This was due to the cut-off value chosen due to noise, as detailed in [Chapter 5](#).

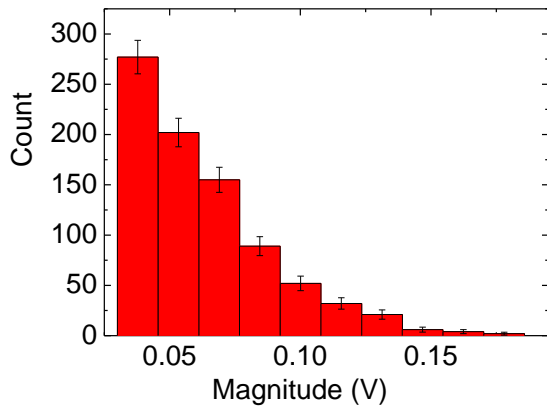


Figure 6.2- Peak magnitude histogram example for  $\phi=0.61$  (count in 5 minutes). 5mm shear cell gap size and  $72.4\text{N/m}^2$  stress. Error bars are the square root of the bin count. The minimum peak magnitude was  $0.03\text{V}$ . This was due to the cut-off value chosen due to noise, as detailed in [Chapter 5](#).

Histograms at different volume fractions were then normalised by dividing the count by the bin width. This meant that the area of a bin rectangle corresponded to the

count in that bin. These could be further adjusted by dividing by the total count ((count/total count)/bin width). In this case, the area of a bin rectangle corresponded to the probability of being in that bin and the areas summed to equal 1.

Histograms were then analysed in more detail to see whether distributions showed a particular behaviour, for example power law or exponential.

Exponential behaviour:

With exponential behaviour, the data takes the form:

$$y = ca^{-bx} \quad \text{Equation 6.1}$$

Using the natural exponential function:

$$y = ae^{-bx} \quad \text{Equation 6.2}$$

$$\ln(y) = \ln(a) - bx \quad \text{Equation 6.3}$$

This appears linear on a log-linear plot.

Power law behaviour:

With power law behaviour, the data takes the form

$$y = ax^{-b} \quad \text{Equation 6.4}$$

$$\log(y) = \log(a) - b \log(x) \quad \text{Equation 6.5}$$

This appears linear on a log-log plot.

For all volume fractions studied, the histogram distributions of peak magnitudes showed approximately exponential behaviour and appeared approximately linear on a log-linear plot (Figure 6.3).

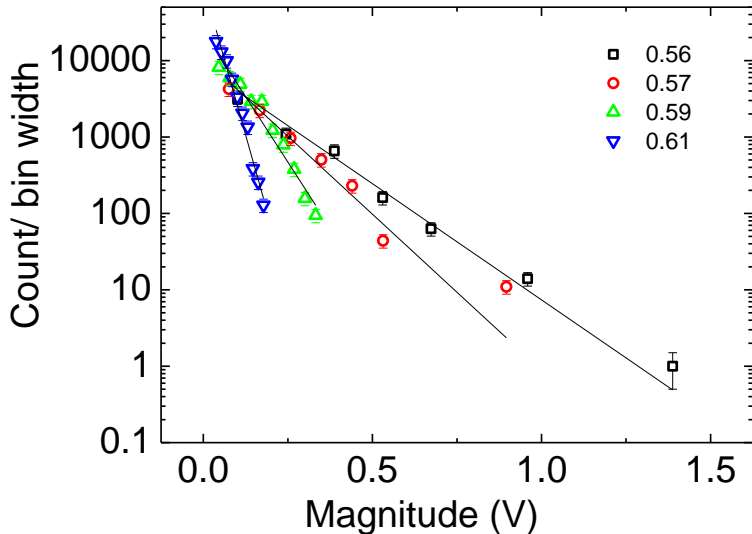


**Figure 6.3-** Plot of example normalised peak magnitude histogram data for various volume fractions on a log-linear plot. Exponential behaviour appears linear on a log-linear plot. 5mm shear cell gap size and  $72.4\text{N/m}^2$  stress. Data from 5 minute experiments.

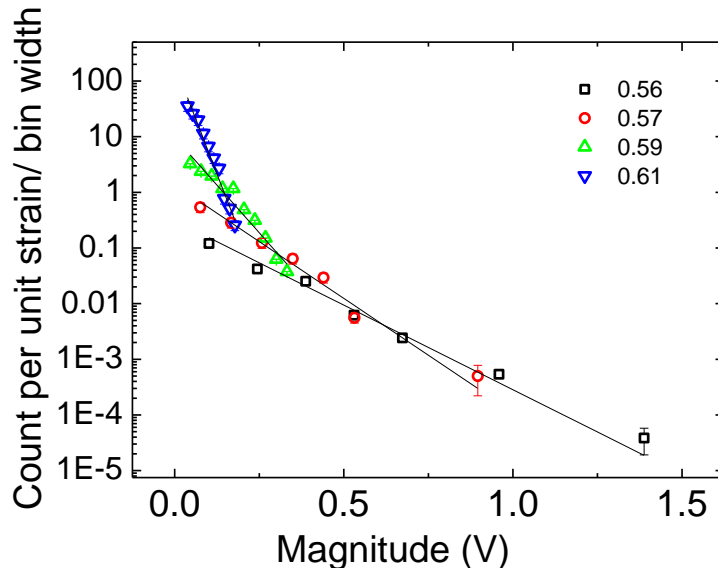


**Figure 6.4-** Plot of example normalised peak magnitude count per unit strain histogram data for various volume fractions on a log-linear plot. 5mm shear cell gap size and  $72.4\text{N/m}^2$  stress. Data from 5 minute experiments were normalised by the total strain from the corresponding experiment.

Figure 6.4 shows the data from Figure 6.3 normalised by the total strain for each experiment (since this varied with volume fraction). This had the effect of showing the greater count of jams per unit strain as volume fraction was increased, particularly at lower peak magnitudes.

From exponential fits (Equation 6.2) to the histogram data in Figure 6.3, it was found that the parameters ‘a’ and ‘b’ both increased with increasing volume fraction (Figure 6.5). This suggested that more small peaks and fewer large magnitude peaks occurred, with the count falling more rapidly as magnitude increased, as volume fraction increased. This agreed with the findings of [Chapter 5](#) where a narrower spread of peak magnitudes was obtained at higher volume fractions.

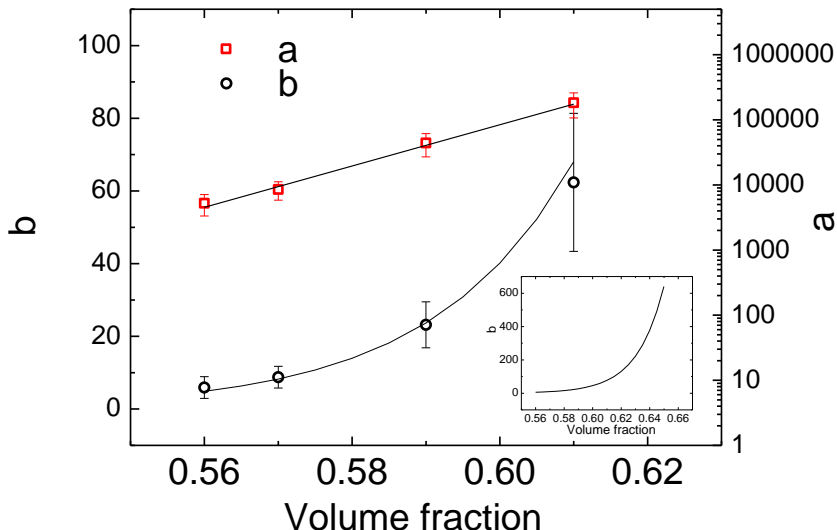


**Figure 6.5-** Variation of parameters from exponential fits to normalised peak magnitude histograms with volume fraction. Error bars show standard deviation of repetitions. 5mm shear cell gap size and 72.4N/m<sup>2</sup> stress. Inset shows exponential fit to ‘b’ data showing a rapid increase in b as  $\Phi=0.64$  approached.

As  $\Phi=0.64$ , the volume fraction corresponding to random close packing, was approached, parameter ‘b’ increased rapidly, as shown in the inset of Figure 6.5. From the exponential function fitted to the histograms-  $y = ae^{-bx}$  where y is the bin count/bin width and x is the peak magnitude- the rapid increase of ‘b’ suggested that as  $\Phi=0.64$  was approached, the spread of jamming peaks would reduce significantly and the count would fall sharply as peak magnitude increased. Using expected parameters for ‘a’ and ‘b’ at  $\Phi=0.64$ , this suggested that no measurable (and differentiable from noise) jamming peaks would be detected at this volume

fraction. A very large number of very small magnitude peaks would be occurring at  $\Phi=0.64$ , however, these would be indistinguishable from noise. This suggested that as random close packing was approached, the material would be in a completely jammed state with no measureable force fluctuations and also a vanishing shear rate.

### Variability and Precision of Fits

The error bars shown in Figure 6.5 show the standard deviation of repetitions. The variation between experimental runs was highest at  $\phi=0.61$ , the highest volume fraction investigated. This was likely due to all peaks in those conditions being small, and it therefore being more difficult to differentiate notably between peak sizes, making ‘binning’ more difficult. It is worth noting that the fits (and therefore ‘a’ and ‘b’) depended on the histogram data points chosen. Excluding a point, for example, often resulted in a very different fit but still showed low residuals. The low residuals suggested that the data trends, for example exponential behaviour, were at least reliable. The actual parameter values from the fits were less reliable. The general trends were, however, consistent.

### Cumulative Distributions

Cumulative distributions were produced to look at the probabilities of a peak magnitude being less than or equal to a particular value at different volume fractions (Figure 6.6). Peak magnitudes were arranged in order from lowest to highest and numbered sequentially ( $i=1,2,3\dots N$ ). The probability of the peak being less than or equal to a particular value was therefore:

$$P(x \leq X) = \frac{i}{N} \quad \text{Equation 6.6}$$

Here  $i$  is the sequential number of the peak when peak magnitudes were arranged in order from lowest to highest and  $N$  is the total number of peaks.

Cumulative distributions showed a sharp increase in the probability of a peak magnitude being less than or equal to a particular magnitude at low peak magnitudes, as was expected from the histograms. The sharpness of this increase in probability increased as volume fraction increased. This meant that at higher volume fractions, it was more probable to find a low magnitude peak (e.g.  $\leq 0.2V$ ) than at low volume fractions. At low volume fractions, the probability of

encountering a high magnitude peak (e.g. >0.2V) was greater than at higher volume fractions.

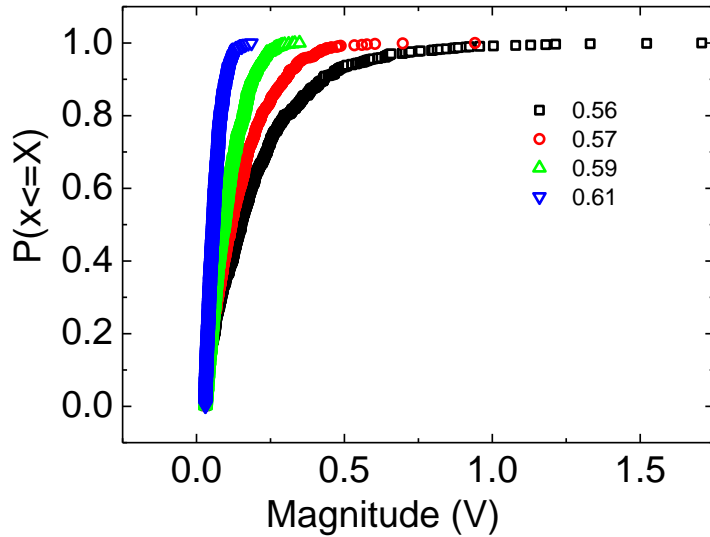


**Figure 6.6- Example cumulative distributions of peak magnitudes for various volume fractions. 5mm shear cell gap size and 72.4N/m<sup>2</sup> stress. Data from 5 minute experiments.**

The cumulative distributions showed exponential behaviour taking the form:

$$P(X \leq X) = 1 - e^{-\lambda X} \quad \text{Equation 6.7}$$

This exponential behaviour is shown more clearly in Figure 6.8 where the distributions are re-plotted on a log-linear plot, showing approximately linear behaviour. As volume fraction increased, the rate parameter,  $\lambda$ , increased. The fact that the peak magnitude data conformed to an exponential cumulative distribution function suggested that the jamming events occurred continuously with a well-defined average magnitude over time [1].

For an exponential cumulative distribution, the expected mean value is given by:

$$\bar{x} = \frac{1}{\lambda} \quad \text{Equation 6.8}$$

This was calculated for the cumulative distribution functions and compared to the average peak magnitudes obtained in [Chapter 5](#) (where the peak magnitudes in an experiment were simply summed and divided by the total number). These were found to compare well, suggesting that the simple average used in [Chapter 5](#) was sufficient to describe the peak magnitude data (Figure 6.7).

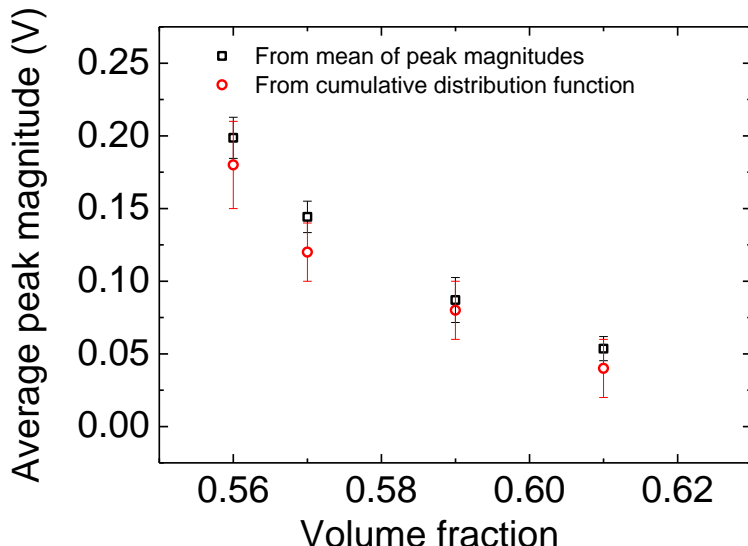


**Figure 6.7-** Average peak magnitude variation with volume fraction from mean of peak magnitudes in **Chapter 5** and from cumulative distribution functions for comparison. 5mm shear cell gap size and  $72.4\text{N/m}^2$  stress. Error bars show standard deviation of repetitions.

To allow better comparisons to the histogram distributions, the cumulative distributions were re-plotted as:

$$P(x \geq X) = 1 - \frac{i-1}{N} \quad \text{Equation 6.9}$$

Here  $i$  is the sequential number of the peak when peak magnitudes were arranged in order from lowest to highest and  $N$  is the total number of peaks.

The distributions were approximately linear on a log-linear plot, suggesting exponential behaviour, as had been deduced with the histograms (Figure 6.8). Large peak magnitudes appeared to fit the trend less well than smaller peaks. This was perhaps due to larger peaks being more likely to generate other large peaks so the number of large peaks was higher than it would have been for completely independent events. Since the larger peaks typically had very small counts, their data were perhaps less reliable.

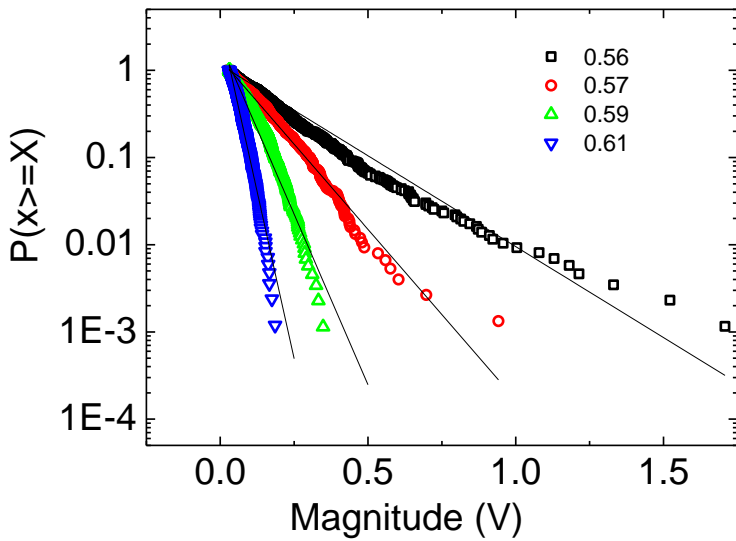


**Figure 6.8- Example cumulative distributions of peak magnitudes for various volume fractions plotted on a log-linear plot. 5mm shear cell gap size and 72.4N/m<sup>2</sup> stress. Data from 5 minute experiments.**

The idea of fluctuating forces in a material that is undergoing discontinuous shear thickening or flow induced jamming showing a decreasing exponential type distribution of force magnitudes has been reported in literature, with work largely covering granular materials undergoing flow [2-8]. For example, theoretically a distribution of force fluctuations that decreased exponentially with force amplitude in a granular system was found where the fluctuations were thought to be due to the build-up and destruction of particle clusters [2]. A study shearing granular materials in a Couette geometry showed a similar distribution of fluctuating forces, as did a study of granular materials being sheared in a rotating piston geometry (with similarities to a parallel plate rheometer geometry) [4, 8]. The work suggests that jammed packings are characterised by a force distribution that decays exponentially [4]. More details on the exponential distribution of jamming peak magnitudes are given in 6.4 where the results from analysing time gaps between peaks and jamming peak magnitudes are related to findings from bottleneck flows in literature.

Cumulative distributions were likely a more reliable way to present the data from the force sensor compared to histograms. Histograms depended on bin sizes and were easily influenced by extreme points with low counts. Cumulative distributions did not rely on these and produced more consistent results. They were also more

transparent since all data points were shown. They do, however, lack the quantitative information (e.g. in terms of ‘count’) histograms can provide. For the remainder of this chapter, a combination of histograms and cumulative distributions are used.

A point worth making (especially given Figure 6.7) is that the analysis has shown there is a well-defined average jamming peak magnitude. This is expected for an exponential or Poisson distribution (independent events with a constant average magnitude over time). This would not be expected for a power law distribution.

## 6.3 Analysis of Time Gap between Peaks Distributions- Effect of Volume Fraction

As detailed briefly in [Chapter 5](#), histograms showing the distribution of time gaps between peaks were produced for different volume fractions. They showed that smaller time gap events occurred significantly more often than larger gap events for all volume fractions considered (Figure 6.9 and Figure 6.10).

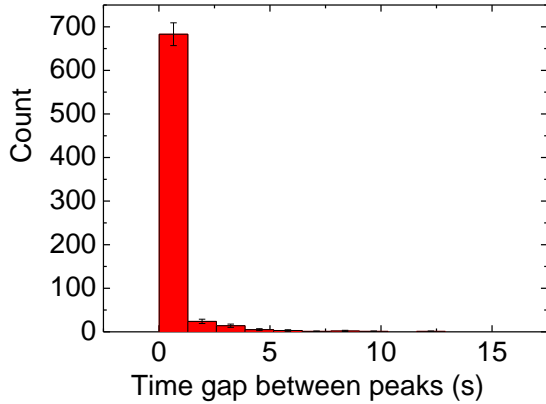


Figure 6.9- Time gap between peaks histogram example for  $\phi=0.56$  (count in 5 minutes). 5mm shear cell gap size and  $72.4\text{N/m}^2$  stress. Error bars are the square root of the bin count.

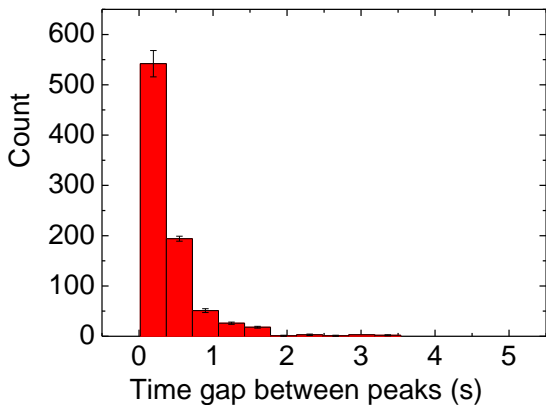
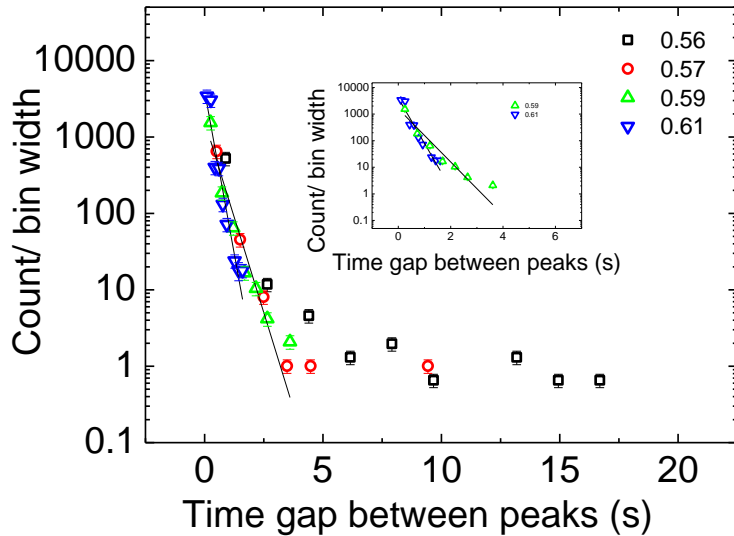
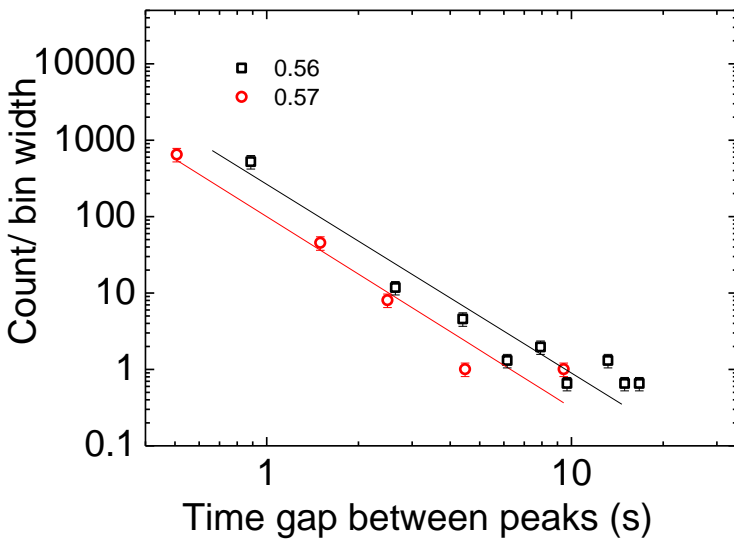


Figure 6.10- Time gap between peaks histogram example for  $\phi=0.61$  (count in 5 minutes). 5mm shear cell gap size and  $72.4\text{N/m}^2$  stress. Error bars are the square root of the bin count.

The histogram distributions of the time gap between peaks did not show a clear single distribution and appeared to transition from approximate power law behaviour to exponential behaviour as volume fraction was increased.



**Figure 6.11-** Plot of example normalised histogram data for various volume fractions on a log-linear plot.  $\Phi=0.59$  and  $\Phi=0.61$  appear approximately linear on the log-linear plot, suggesting exponential behaviour (as can be seen more clearly in the inset). 5mm shear cell gap size and  $72.4\text{N/m}^2$  stress. Data from 5 minute experiments.



**Figure 6.12-** Plot of example normalised histogram data for  $\Phi=0.56$  and  $\Phi=0.57$  on a log-log plot. Power law behaviour appears linear on a log-log plot. 5mm shear cell gap size and  $72.4\text{N/m}^2$  stress. Data from 5 minute experiments. Slopes (and therefore power law exponents) were typically in the region of 1.5-2.5.

For example, at  $\Phi=0.59$  and  $\Phi=0.61$ , all repetitions showed approximately exponential behaviour. This can be seen in Figure 6.11 where example histogram plots for  $\Phi=0.59$  and  $\Phi=0.61$  appeared approximately linear on a log-linear plot.

$\Phi=0.56$  and  $\Phi=0.57$  histograms did not appear linear on a log-linear plot. They did, however, appear approximately linear on a log-log plot for all repetitions (as seen for example plots in Figure 6.12). This suggested that power law behaviour was prevalent for the time gap between peaks distributions for  $\Phi=0.56$  and  $\Phi=0.57$ . Power law behaviour was found here due to the ‘heavy tail’ of the distributions; a small number of large time gap events were found at these volume fractions. These were not found at higher  $\Phi$  when exponential behaviour was seen.

To ensure the reliability of these distributions, additional repetitions would be necessary. It is difficult to draw conclusive trends from the data, given that the fits to the distributions rely heavily on data with low counts. For example, large time gaps (e.g. over 5s) typically just had 1 or 2 counts in an experiment, but had a notable impact on the fits. The fits did, however, consistently show power law behaviour when large time gaps were present and whether exponential or power law behaviour was detected was consistent through repetitions. It is worth noting that this is the nature of power law behaviour- it is found when a small number of ‘large’ events occur and this is a reason why power law behaviour is difficult to prove unless very large datasets are available.

## Cumulative Distributions

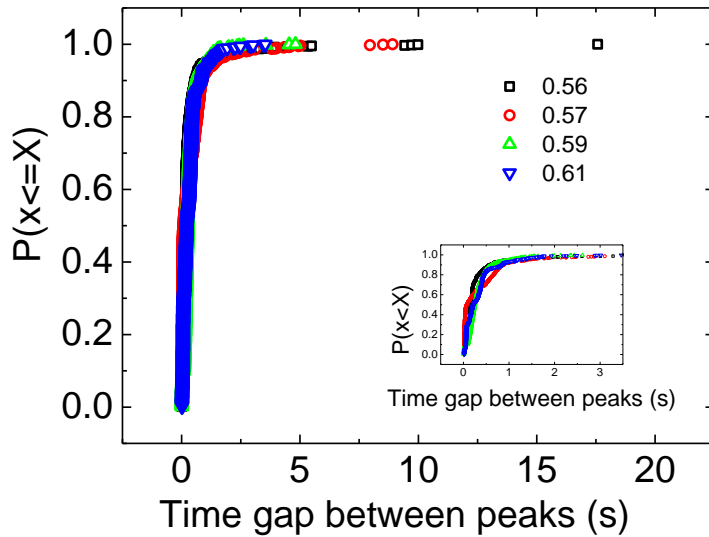


**Figure 6.13-** Example cumulative distributions of time gap between peaks for various volume fractions. 5mm shear cell gap size and  $72.4\text{N/m}^2$  stress. Data from 5 minute experiments. Inset shows plots over shorter x-axis range.

Cumulative distributions were produced to look at the probability of a time gap between jamming peaks being less than, or equal to, a particular value at different volume fractions (Figure 6.13). These showed a sharp increase in the probability of a time gap between peaks being less than or equal to a particular time at low time gaps between peaks, as was expected from the histograms. All distributions showed that the majority of jams (~80%) had a time gap of 0.8s or less from the previous peak.

There was not as notable a difference between the cumulative distributions at different volume fractions, as had been the case with the peak magnitude cumulative distributions. As shown in Figure 6.13's inset, the sharpness of the increase in probability at low time gaps between peaks did not vary significantly as the volume fraction increased. The main difference was that as volume fraction decreased, there was a greater probability (while still very low) that a larger time gap between jamming peaks would be measured, compared to higher volume fractions where there were not generally larger time gaps between peaks (e.g. >5s).

To allow better comparisons to the histogram distributions, the cumulative distributions were re-plotted as before to show  $P(x \geq X)$ . Power law or exponential

behaviour was not particularly convincing for any, but as a ‘best fit’, the distributions for  $\Phi=0.59$  and  $\Phi=0.61$  were approximately linear on a log-linear plot, suggesting exponential behaviour, as had been deduced with the histograms (Figure 6.14).  $\Phi=0.56$  and  $\Phi=0.57$  did not appear approximately linear on a log-linear plot. When plotted on a log-log plot they showed power-law behaviour in the tails, suggesting power law behaviour (Figure 6.15).

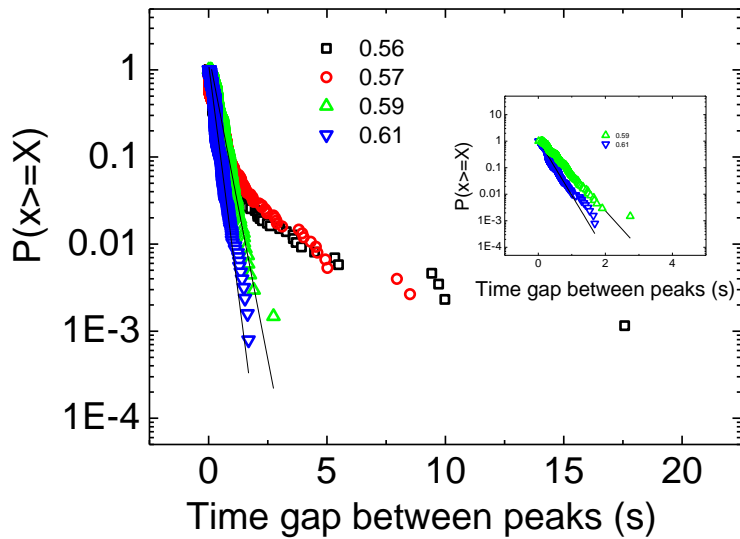


**Figure 6.14-** Example cumulative distributions of time gap between peaks for various volume fractions on a log-linear plot. 5mm shear cell gap size and 72.4N/m<sup>2</sup> stress. Data from 5 minute experiments. Inset shows  $\Phi=0.59$  and  $\Phi=0.61$  plots over shorter x-axis range.

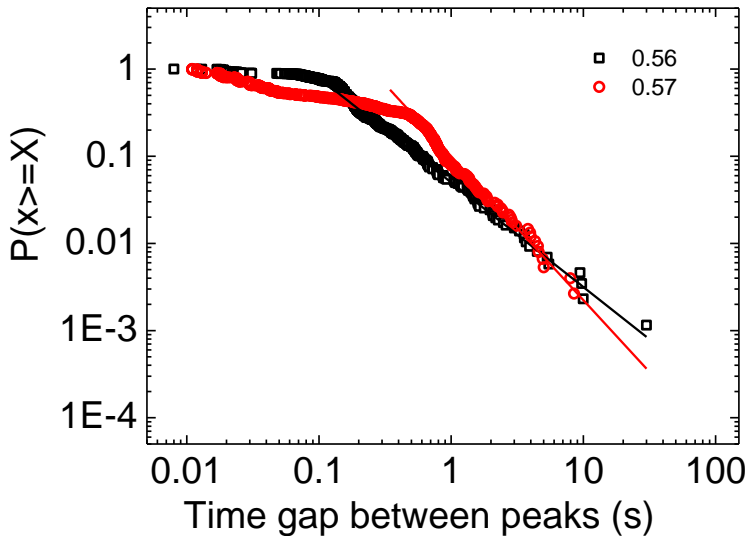


**Figure 6.15-** Example cumulative distributions of time gap between peaks for  $\Phi=0.56$  and  $\Phi=0.57$  on a log-log plot to show power law tails. 5mm shear cell gap size and  $72.4\text{N/m}^2$  stress. Data from 5 minute experiments. Slopes were typically in the region of 1.5-2.5.

It was noticed that when plotted on a log-log plot, all the time gap cumulative distributions showed a kink in the data at times between  $\sim 0.01\text{s}$  and  $\sim 1\text{s}$ . Reasons for this are not clear, but since it was consistent for all data, it was likely an artefact of the system. Another possibility was that it was in some way related to the shear rate. For the experiments, the shear rate varied from  $\sim 10\text{s}^{-1}$  to  $\sim 100\text{s}^{-1}$ . The inverse of this corresponded approximately to the time regions where there was a kink in the data. There was no consistent trend of where the kink was found in the  $0.01\text{s}$  and  $1\text{s}$  region across repetitions and different conditions. Its position did not vary consistently with volume fraction (and different volume fractions were associated with different shear rates).

## 6.4 Relevance to Literature

The nature of the distributions described above, and their possible transitions with volume fraction, is not well understood, but may be related to the flow of material through bottlenecks, such as the flow of granular materials through hoppers or the movement of material through a constriction.

A difficulty relating the work done here to the studies on bottleneck flow found in literature is that with this work, an individual jam only lasts a very short time, whereas with bottleneck flow, such as the flow from hoppers, jammed states are much less instantaneous. There can be a significant amount of time when there is no flow and the material is 'jammed'.

With studies on bottleneck flow, such as flow from hoppers, the time between bursts of flow was measured whereas with this work, the time gap between jamming peaks was measured. Similarities in distributions when comparing these were found as outlined subsequently. This suggested that the time gaps between jams measured with the force sensor data may have been related to the time gaps between flow bursts occurring with bottleneck flows.

The sizes of the bursts of flow (e.g. the number of particles in a burst) with bottleneck flow also show similar distributions to the magnitudes of the jams measured with the force sensor, as outlined below. In other words, for relating the work with the force sensor to the bottleneck flow distributions in literature, a jamming peak measured with the force sensor is treated as similar to a burst of flow occurring with the bottleneck flow. The time gap between jamming peaks and the time gap between bursts of flow are therefore treated as comparable. Jamming peak magnitudes and the sizes of bursts of flow are also treated as comparable. The reasonability of these assumptions is discussed towards the end of this section.

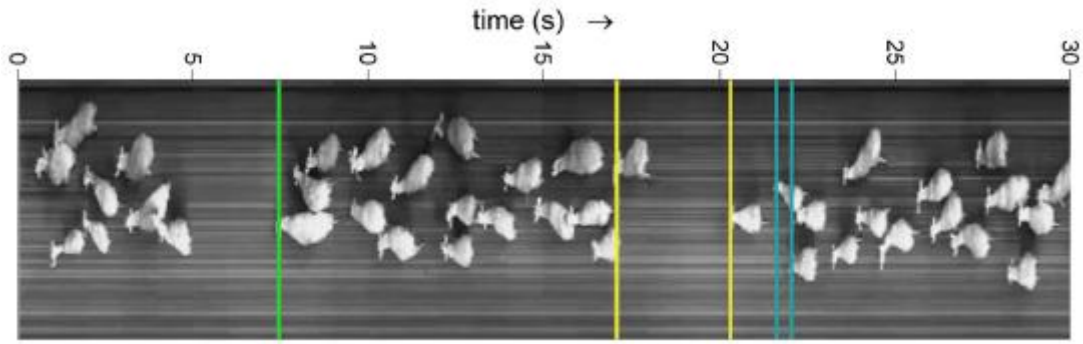


**Figure 6.16- Spatio-temporal diagram of sheep passing through a gate. Green line shows gate, two yellow lines show example of 'long' time between bursts of sheep flow and two blue lines show example of 'short' time between bursts of sheep flow [9].**

A significant amount of work has been done looking at the clogging and jamming of the flow of materials through bottlenecks, with results showing qualitatively similar trends to the findings of the force sensor work [9-11]. The studies are diverse, ranging from the flow of sheep through a gate to get food (Figure 6.16), to the passage of pedestrians through a small door, to traffic jams, to the flow out of grain silos and hoppers, to the flow of colloidal suspensions passing through a constriction [9, 11-13]. Studies show similar trends, suggesting some form of universality.

The sizes of flow bursts (in terms of number of individuals in a burst) have been found to display exponential distributions both experimentally and theoretically [5, 9, 14-20]. This is perhaps analogous to the exponential distribution of jamming peak magnitudes seen with the force sensor measurements. The time gaps between bursts of flow typically shows power law behaviour, which was perhaps analogous to power law behaviour found with the  $\Phi=0.56$  and  $\Phi=0.57$  volume fraction experiments [5, 9, 11, 12, 21-23]. Power law behaviour of time gap distributions was also found for other experimental conditions using the force sensor, as subsequently detailed, such as for lower applied stresses and larger gaps between the cylinders in the shear cell geometries.

The work also highlights the importance of system geometry and the effects it can have [10]. Studies have found that with larger silo orifices, the probability of clogging/jamming decreases. The work also found that a critical orifice size exists, above which jamming can no longer occur [10, 14]. This may have relevance to the work done in [Chapter 4](#) and [Chapter 5](#) where fewer jams were found to occur as the gap size between the cylinders increased. Studies have also shown that placing an

obstacle in the path of the flow can greatly reduce the probability of the flow jamming. The probability of a jam occurring can be reduced by up to 100 times with an obstacle present [20]. This is thought to be due to the obstacle causing a decrease in particle velocity and pressure [9, 20].

Distribution transitions in the flow behaviour of particles through a hopper have been reported [24]. For example, with granular hopper flows, a transition in the distribution of the time between bursts of flow was reported. When flow was ~continuous without large gaps between bursts of flow, exponential behaviour was seen. When the flow was not continuous, with significant start stop behaviour with large gaps between bursts of flow, power law behaviour was seen [5, 24]. The transition in behaviour (from exponential to power law) was measured when the particle velocity was decreased [24].

The start stop behaviour seen in the hopper may be related to the larger spread of time gaps between peaks seen with lower volume fractions in the experiments: at  $\Phi=0.56$  and  $\Phi=0.57$  power law behaviour was seen due to a number of large time gaps between jamming peaks events being found. At the higher volume fractions ( $\Phi=0.59$  and  $\Phi=0.61$ ), there was a much smaller spread of the time gaps between jams, so jams were much more continuous. Here exponential behaviour was seen and this was perhaps related to the exponential behaviour found in ~continuous hopper flow, where the flow was much more homogeneous. Volume fraction has also been shown to be important in determining jamming distributions measured, with lower volume fractions showing power law behaviour [22].

Treating the occurrence of a jamming peak measured with the force sensor as similar to the occurrence of a burst of flow in bottleneck flow resulted in similar trends being found as highlighted above. Treating a jamming peak as related to a burst of flow occurring may be reasonable. Since the experimental results suggested that jamming was related to dilation and was caused by the material attempting to flow, the fact that the bottlenecks transitioned from not flowing to flowing suggests that some form of dilation must occur at the onset of flow. As detailed in [Chapter 5](#), one of the possible causes of the fluctuating force peaks is jammed regions collapsing and breaking up, allowing flow to continue. This is perhaps analogous to what happens in a silo, for example, allowing flow to continue.

It is worth noting that when power law behaviour was detected in the force sensor experiments, the exponent, 'b', from the histograms was typically in the region of 1.5-2.5 (Figure 6.31). According to literature where power law tails were detected in the time gaps between bursts of flow distributions, an exponent  $> 2$  suggests the flow is in an 'unclogged' state. An exponent  $\leq 2$  suggests the flow is in a 'clogged' state. It is interesting that the power law exponents determined in this work were close to this transitional region and were at least of a similar size to those reported for 'clogged' states in literature (which in some cases were for very different systems, such as pedestrian flow and silo flow) [9]. Other work has found that the power law exponent is typically in the region of 1.5-3 for flowing granular media showing jamming behaviour [5].

The similarity between the behaviour of the colloidal suspensions investigated here and the granular studies, suggests a link between the behaviour of concentrated colloidal suspensions under flow and granular materials. This is in agreement with the work done in [Chapter 7](#) and [Chapter 8](#) of this thesis. It is worth noting that in a hopper, the stress is fixed since it is imposed by gravity (at least in the absence of obstacles). In the shear cell, however, the stress is variable. The effect of stress on the distributions is discussed in the next section.

## 6.5 Effect of Shear Stress on Distributions

As detailed in [Chapter 5](#), the voltage supplied to the shear cell (and therefore the shear stress) had a significant impact on the voltage-time data from the force sensor. As the shear stress increased, the number of peaks per rotation of the inner cylinder increased for all volume fractions studied. The average peak magnitude did not change significantly.

The distributions of these data were therefore considered to see how shear stress affected them. It is worth noting that at the different shear stresses considered, the shear rate (and therefore strain) stayed approximately constant for a particular volume fraction due to shear thickening. This was discussed in [Chapter 4](#) and [Chapter 5](#).

Data is typically shown for  $\Phi=0.59$  and  $\Phi=0.61$  since they showed jamming behaviour across a wide range of stresses.  $\Phi=0.56$  and  $\Phi=0.57$  only showed jamming behaviour over a very narrow range of shear stresses and were less useful for showing the effects of stress.

### Peak Magnitude

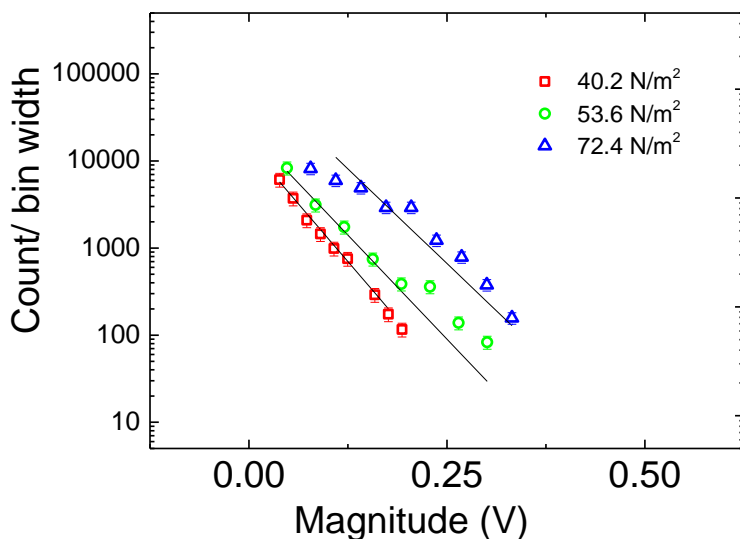


**Figure 6.17-** Plot of example normalised peak magnitude histogram data for various shear stresses on a log-linear plot. 5mm shear cell gap size and  $\Phi=0.59$ . Data from 5 minute experiments. Shear rate was constant at the different stresses due to thickening.

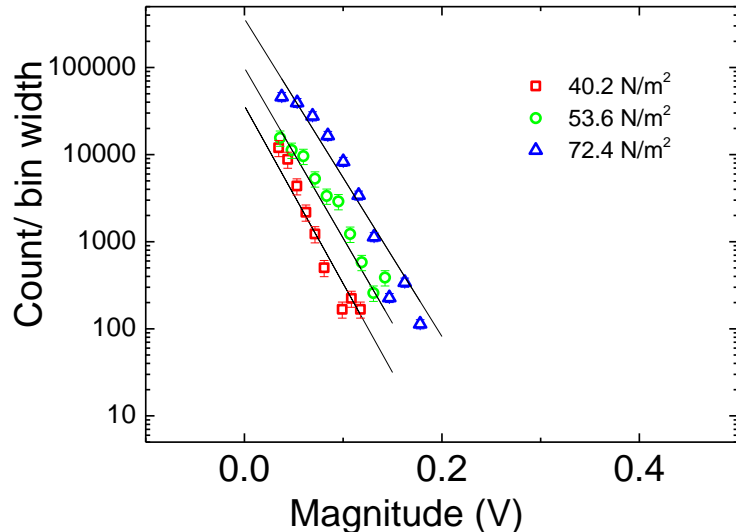


Figure 6.18- Plot of example normalised peak magnitude histogram data for various shear stresses on a log-linear plot. 5mm shear cell gap size and  $\Phi=0.61$ . Data from 5 minute experiments. Shear rate was constant at the different stresses due to thickening.

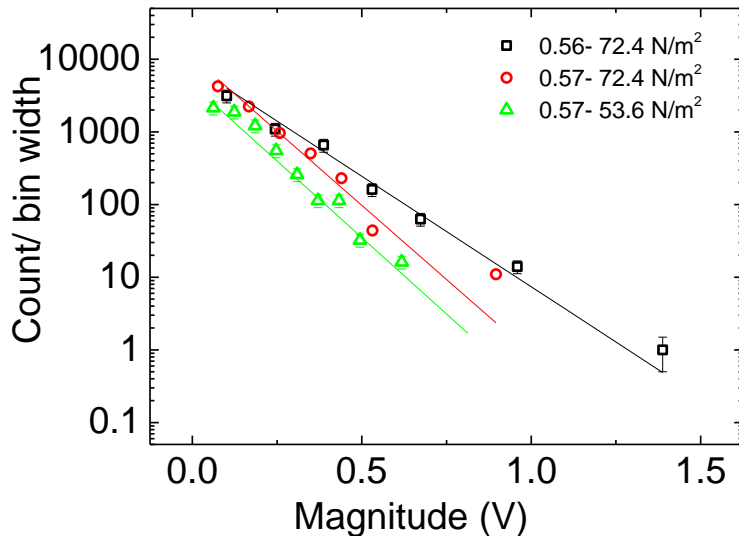


Figure 6.19- Plot of example normalised peak magnitude histogram data for various shear stresses on a log-linear plot. 5mm shear cell gap size and  $\Phi=0.56$  and  $\Phi=0.57$ . Data from 5 minute experiments. Shear rate was constant at the different stresses due to thickening. Only one set of data is shown for  $\Phi=0.56$  and two for  $\Phi=0.57$  since, as mentioned, they only showed jamming behaviour over a narrow range of shear stresses.

Approximate exponential distributions (with the form  $y = ae^{-bx}$ ) of jamming peak magnitudes were found for all volume fractions at the various applied shear stresses investigated, where there were a sufficient number of peaks measured in the experimental time for adequate data to form histograms (Figure 6.17, Figure 6.18 and Figure 6.19).

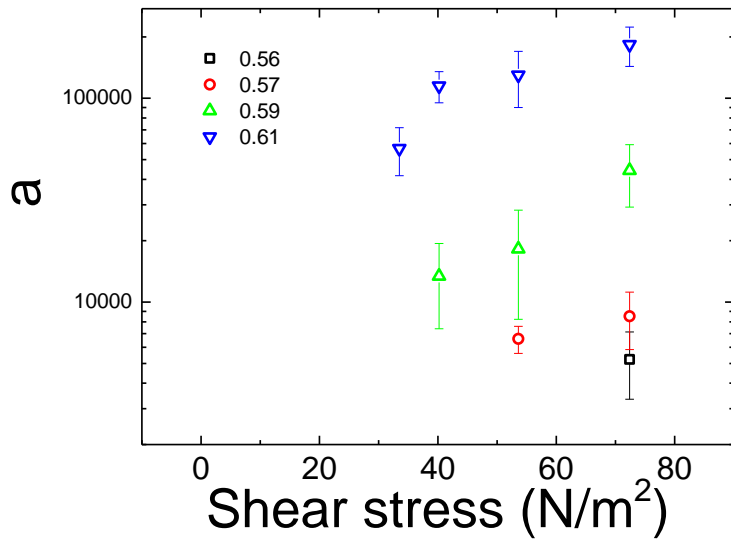


Figure 6.20- Variation of 'a' parameter from exponential fits to normalised peak magnitude histograms with shear stress. Error bars show standard deviation of repetitions. 5mm shear cell gap size. Only one data point is shown for  $\Phi=0.56$  and two for  $\Phi=0.57$  since, as mentioned, they only showed jamming behaviour over a narrow range of shear stresses.

At a particular volume fraction, the exponential fits to the distributions varied with shear stress. The decay rate parameter 'b' did not vary significantly with shear stress but the parameter 'a' decreased as the shear stress decreased (Figure 6.20 and Figure 6.21). The parameter 'b' not varying significantly is consistent with the fact that the average peak magnitudes did not vary significantly with applied stress. The decrease in 'a' with decreasing shear stress indicates that the total number of jamming peaks decreased as the shear stress decreased.

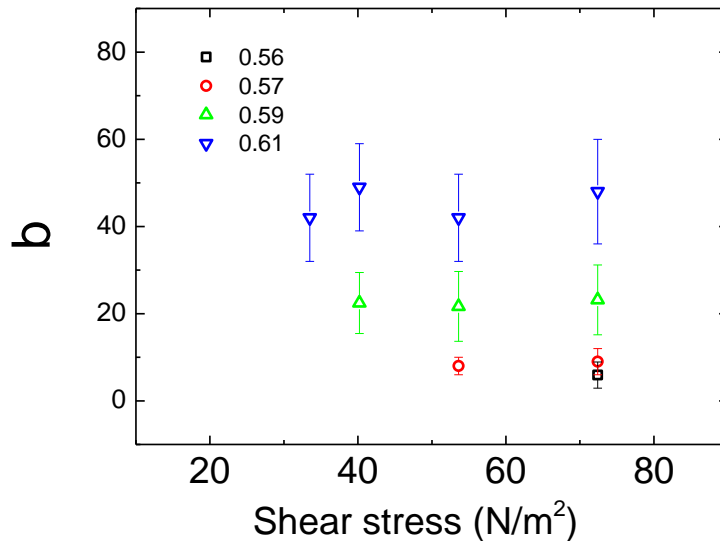


Figure 6.21- Variation of ‘b’ parameter from exponential fits to normalised peak magnitude histograms with shear stress. Error bars show standard deviation of repetitions. 5mm shear cell gap size. Only one data point is shown for  $\Phi=0.56$  and two for  $\Phi=0.57$  since, as mentioned, they only showed jamming behaviour over a narrow range of shear stresses.

The data was then plotted as cumulative distributions as before. Cumulative distributions at the different shear stresses were similar at a particular volume fraction, showing approximate exponential behaviour (Figure 6.22, Figure 6.23, Figure 6.24 and Figure 6.25). The expected values of the mean peak magnitudes from the distributions compared well to the average peak magnitude calculated in Chapter 5 (Figure 6.26). Distributions were likely similar since the average peak magnitudes did not vary significantly at different shear stresses. These trends were found for all volume fractions considered.

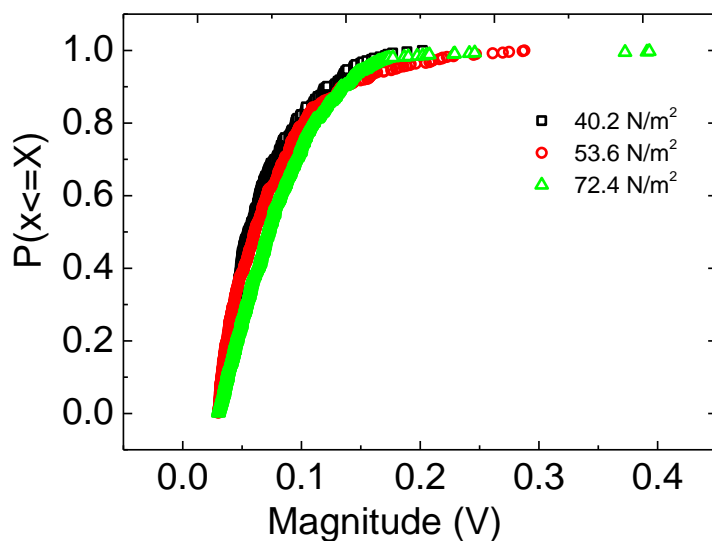


Figure 6.22- Example cumulative distributions of peak magnitudes for various shear stresses. 5mm shear cell gap size and  $\Phi=0.59$ . Data from 5 minute experiments.

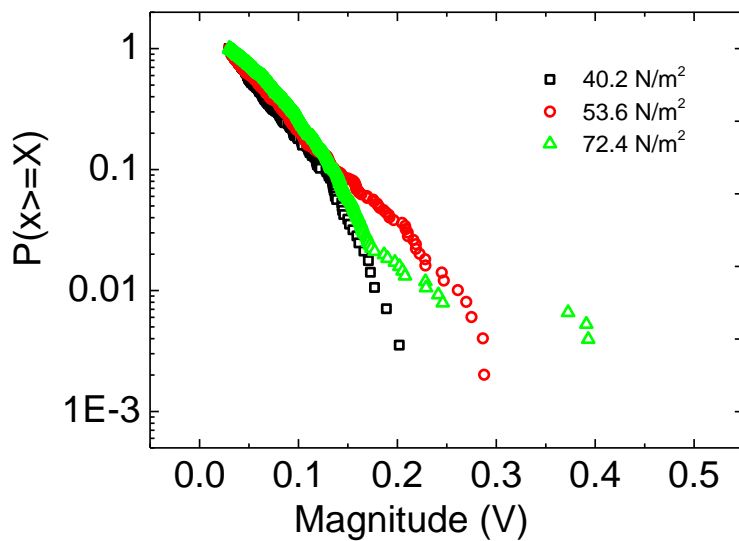
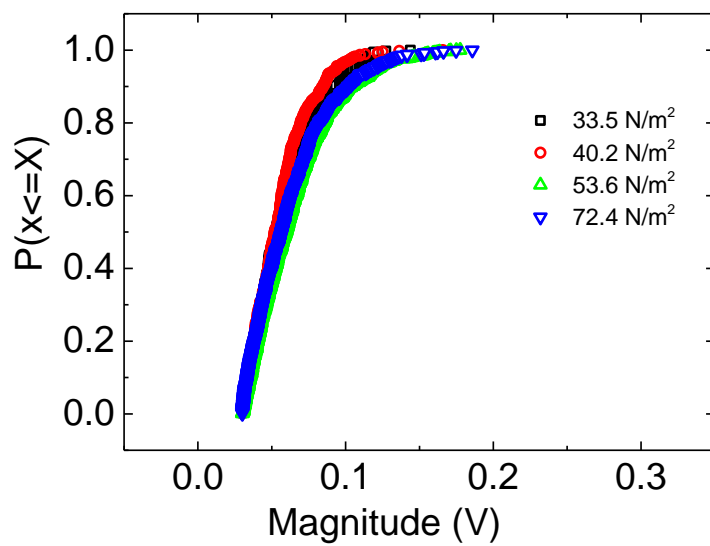
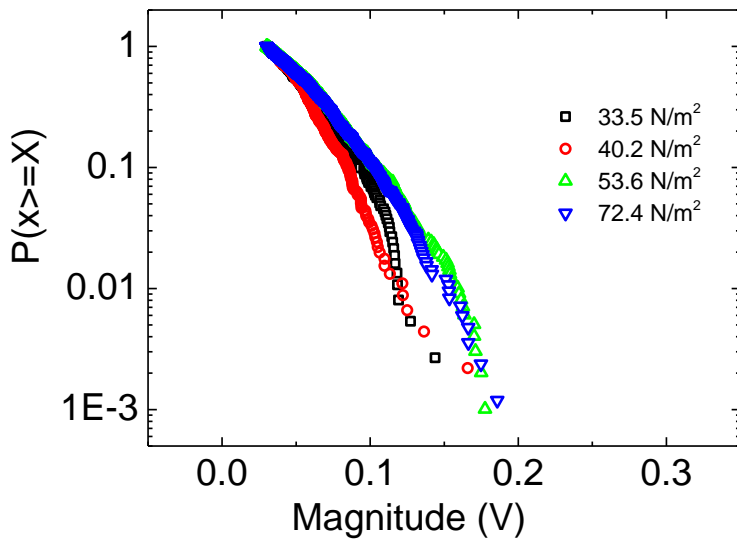


Figure 6.23- Example cumulative distributions of peak magnitudes for various shear stresses on a log-linear plot. 5mm shear cell gap size and  $\Phi=0.59$ . Data from 5 minute experiments.



**Figure 6.24-** Example cumulative distributions of peak magnitudes for various shear stresses. 5mm shear cell gap size and  $\Phi=0.61$ . Data from 5 minute experiments.



**Figure 6.25-** Example cumulative distributions of peak magnitudes for various shear stresses on a log-linear plot. 5mm shear cell gap size and  $\Phi=0.61$ . Data from 5 minute experiments.

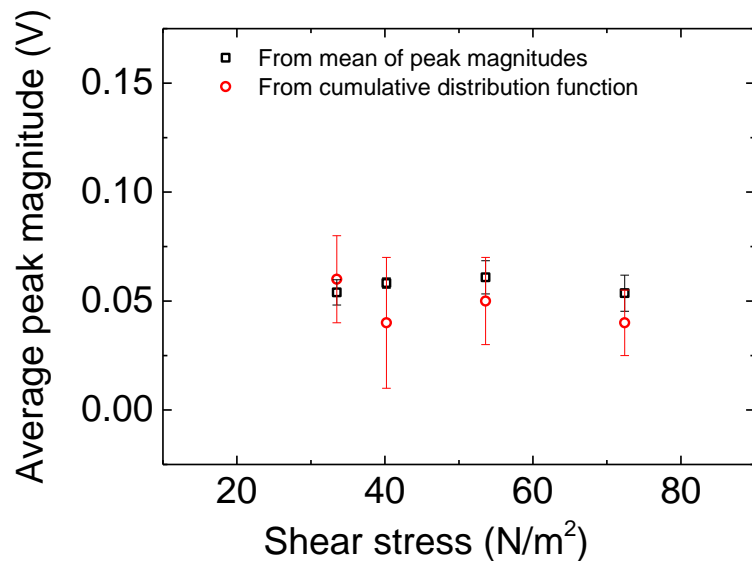
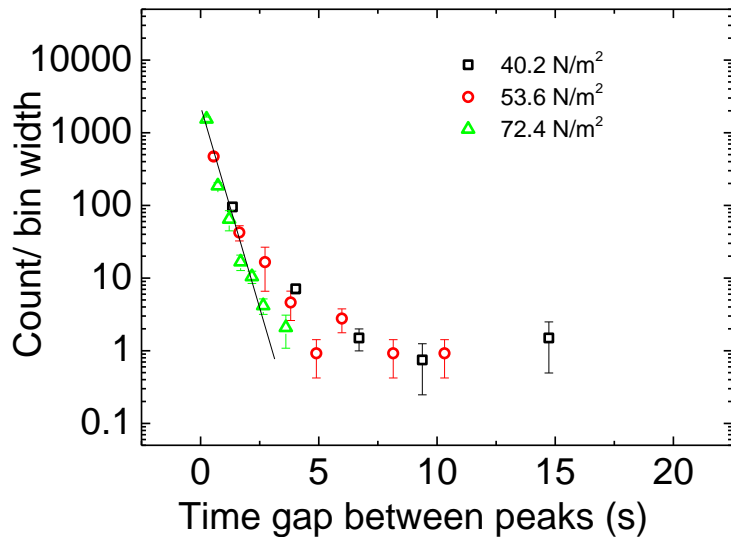


Figure 6.26- Average peak magnitude variation with shear stress from mean of peak magnitudes in [Chapter 5](#) and from cumulative distribution functions for comparison. 5mm shear cell gap size and  $\Phi=0.61$ . Error bars show standard deviation of repetitions.

### Time Gap between Peaks

Decreasing the shear stress had a notable impact on the time gap between peaks distributions. At the maximum shear stress ( $72.4\text{N/m}^2$ ),  $\Phi=0.59$  and  $\Phi=0.61$  appeared to show approximate exponential distributions, while  $\Phi=0.56$  and  $\Phi=0.57$  showed approximate power law behaviour, as detailed in 6.3.

As the shear stress decreased, however, the  $\Phi=0.59$  and  $\Phi=0.61$  distributions transitioned from approximately exponential to approximately power law behaviour (Figure 6.27, Figure 6.28, Figure 6.29 and Figure 6.30). Reduced stress results in a decreased number of jams and the appearance of a small number of large time gap events. This resulted in ‘heavy tails’ on the distributions, leading to approximate power law behaviour being detected. Power law behaviour was found for  $\Phi=0.56$  and  $\Phi=0.57$  samples at all shear stresses investigated.



**Figure 6.27-** Plot of example normalised histogram data for various shear stresses on a log-linear plot. Only  $72.4\text{N/m}^2$  appears approximately linear, suggesting exponential behaviour. 5mm shear cell gap size and  $\Phi=0.59$ . Data from 5 minute experiments.

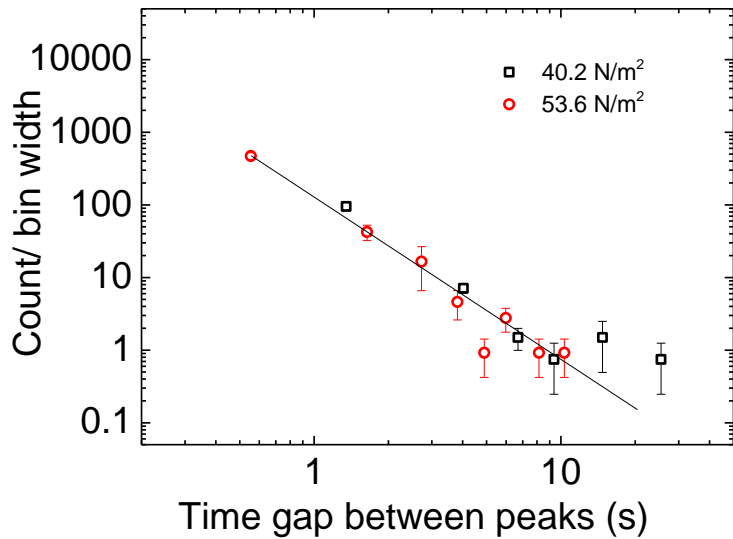


Figure 6.28- Plot of example normalised histogram data for various shear stresses on a log-log plot. Plots appear approximately linear, suggesting power law behaviour. 5mm shear cell gap size and  $\Phi=0.59$ . Data from 5 minute experiments. The line shows a power law with an exponent of  $\sim 2$  and demonstrates that there is little measurable effect of stress on the exponent.

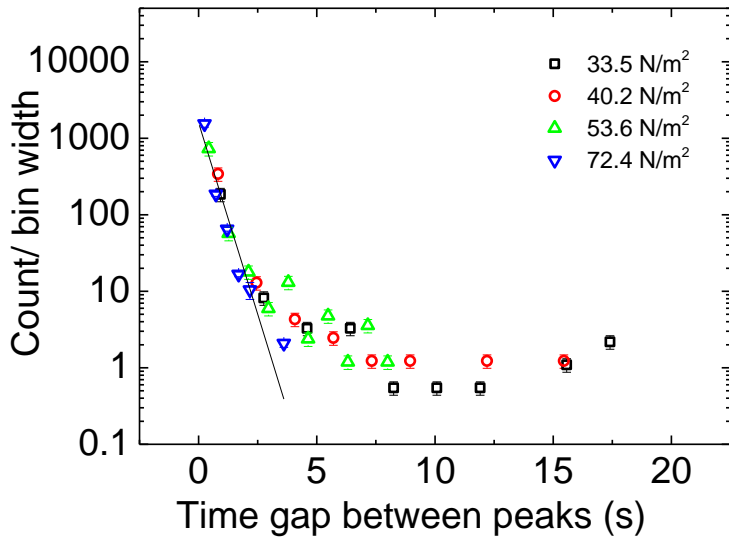
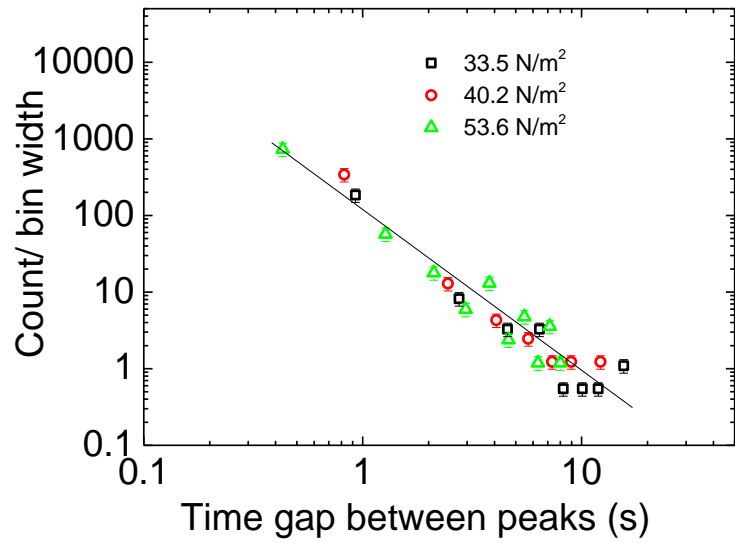


Figure 6.29- Plot of example normalised histogram data for various shear stresses on a log-linear plot. Only  $72.4\text{N/m}^2$  appears approximately linear, suggesting exponential behaviour. 5mm shear cell gap size and  $\Phi=0.61$ . Data from 5 minute experiments.



**Figure 6.30-** Plot of example normalised histogram data for various shear stresses on a log-log plot. Plots appear approximately linear, suggesting power law behaviour. 5mm shear cell gap size and  $\Phi=0.61$ . Data from 5 minute experiments. The line shows a power law with an exponent of  $\sim 2.2$  and demonstrates that there is little measurable effect of stress on the exponent.

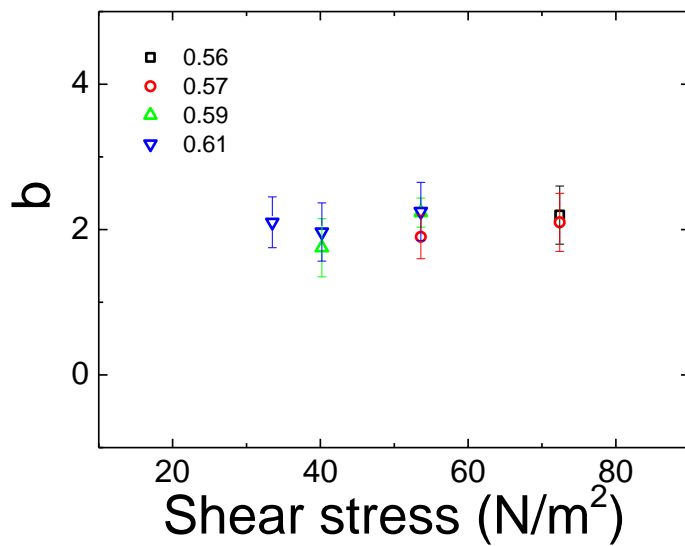
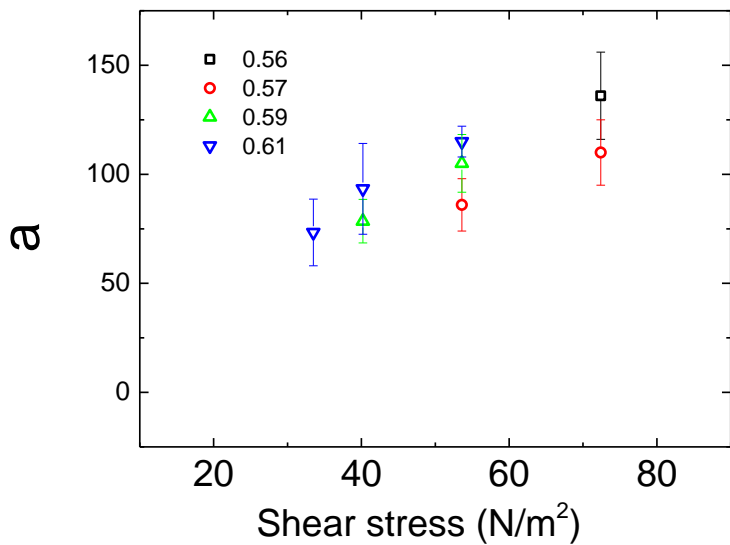


Figure 6.31- Variation of 'b' parameter from power law fits to normalised time gap histograms with shear stress. Error bars show standard deviation of repetitions. 5mm shear cell gap size. Only one data point is shown for  $\Phi=0.56$  and two for  $\Phi=0.57$  since, as mentioned, they only showed jamming behaviour over a narrow range of shear stresses.

From the power law function fitted to the histograms-  $y = ax^{-b}$  where  $y$  is the count/bin width and  $x$  is the time gap between peaks- it was noticed that in all cases where power law behaviour was detected, the power law exponent,  $b$ , remained approximately constant and was independent of volume fraction and shear stress (Figure 6.31).

The pre-factor parameter 'a' decreased as the stress decreased, i.e. there was a decreased total number of jams detected as stress decreased (Figure 6.32). It is worth noting again that the fit parameters, 'a' in particular, depended greatly on the data points chosen for the fits and on small count events (i.e. the small number of 'large time gap' events).



**Figure 6.32-** Variation of ‘a’ parameter from power law fits to normalised time gap histograms with shear stress. Error bars show standard deviation of repetitions. 5mm shear cell gap size. Only one data point is shown for  $\Phi=0.56$  and two for  $\Phi=0.57$  since, as mentioned, they only showed jamming behaviour over a narrow range of shear stresses.

Cumulative distributions were plotted as before (Figure 6.33, Figure 6.34, Figure 6.35 and Figure 6.36). All cumulative distributions at the different shear stresses were similar at the start of the plots but began to differ slightly at probabilities  $>\sim 0.8$ . The main difference was that at higher stresses, the cumulative probability approached one and levelled off more rapidly, indicating that fewer long time gap events occurred as the shear stress was increased. This is consistent with the emergence of approximate power law behaviour as stress decreases.

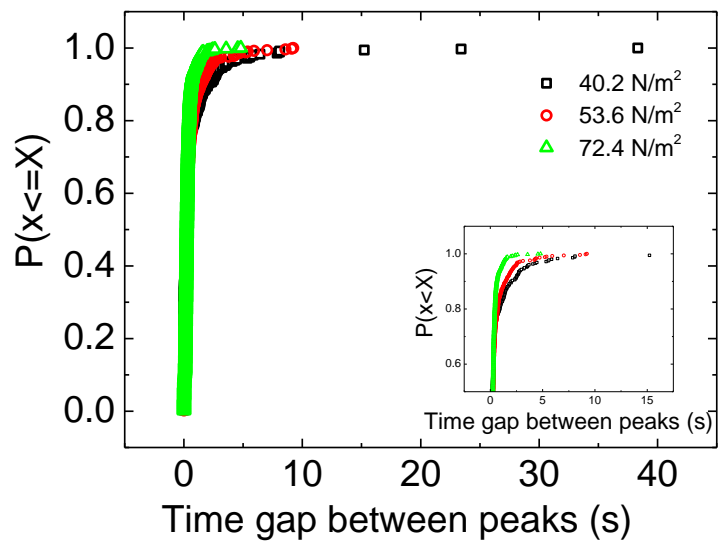


Figure 6.33- Example cumulative distributions of time gap between peaks for various shear stresses. 5mm shear cell gap size and  $\Phi=0.59$ . Inset shows plots over shorter y-axis range.

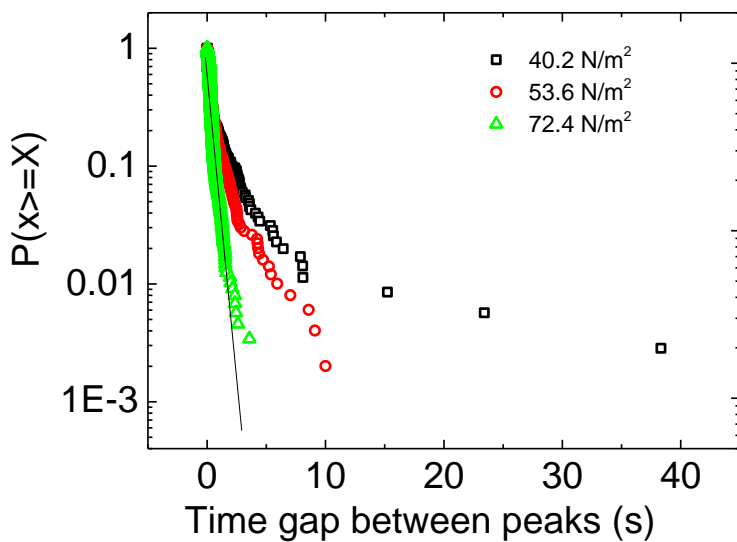
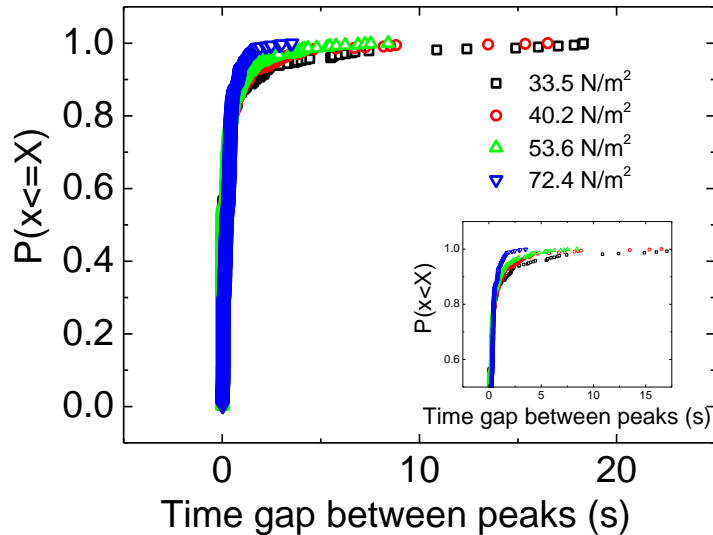
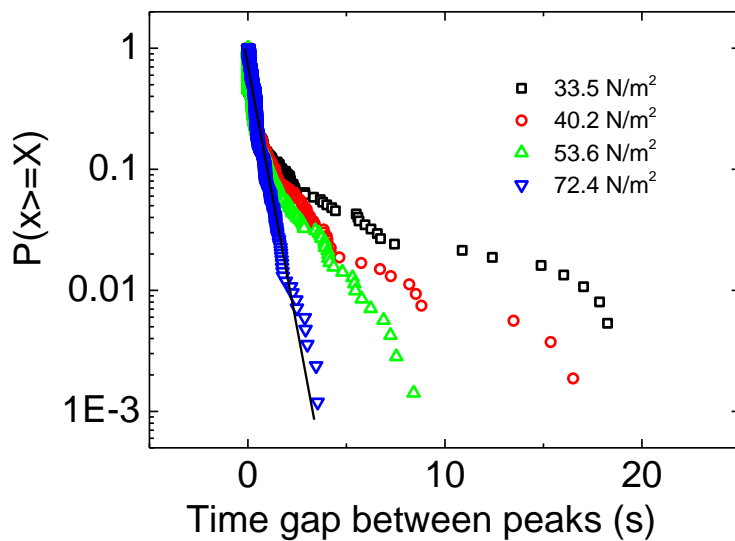


Figure 6.34- Example cumulative distributions of time gap between peaks for various shear stresses on a log-linear plot. 5mm shear cell gap size and  $\Phi=0.59$ .



**Figure 6.35-** Example cumulative distributions of time gap between peaks for various shear stresses. 5mm shear cell gap size and  $\Phi=0.61$ . Inset shows plots over shorter y-axis range.



**Figure 6.36-** Example cumulative distributions of time gap between peaks for various shear stresses on a log-linear plot. 5mm shear cell gap size and  $\Phi=0.61$ .

## 6.6 Effect of System Geometry on Distributions

As detailed in [Chapter 5](#), the shear cell geometry had a significant impact on the voltage-time data from the force sensor. As the gap size between the rotating and stationary cylinder increased, the number of peaks per rotation of the inner cylinder decreased and the average peak magnitude increased for all volume fractions studied. The distributions of these data were therefore considered.

It is worth noting that at a particular volume fraction, the shear rate (and strain rate) did not vary significantly with the different gap sizes. Since the stress and viscosity were fixed, the shear rate remained approximately constant.

### Peak Magnitude

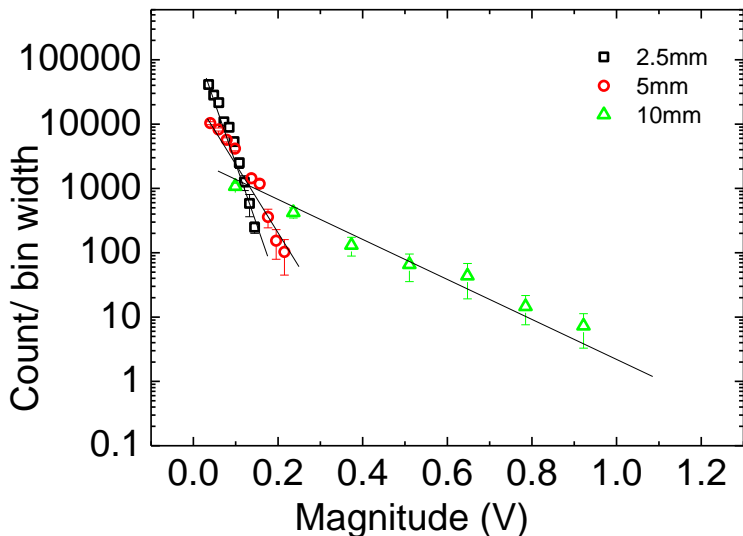


**Figure 6.37-** Plot of example normalised peak magnitude histogram data for various shear cell gap sizes on a log-linear plot.  $\Phi=0.59$  and  $72.4\text{N/m}^2$  stress. Data from 5 minute experiments.

Approximate exponential behaviour was found for all volume fractions in all geometries (Figure 6.37 and Figure 6.38). As the gap size between the cylinders increased, the decay rate decreased due to larger peaks on average (Figure 6.39). This can be seen by the decreased slope of the plots with increasing gap size from the histogram examples in Figure 6.37 and Figure 6.38.

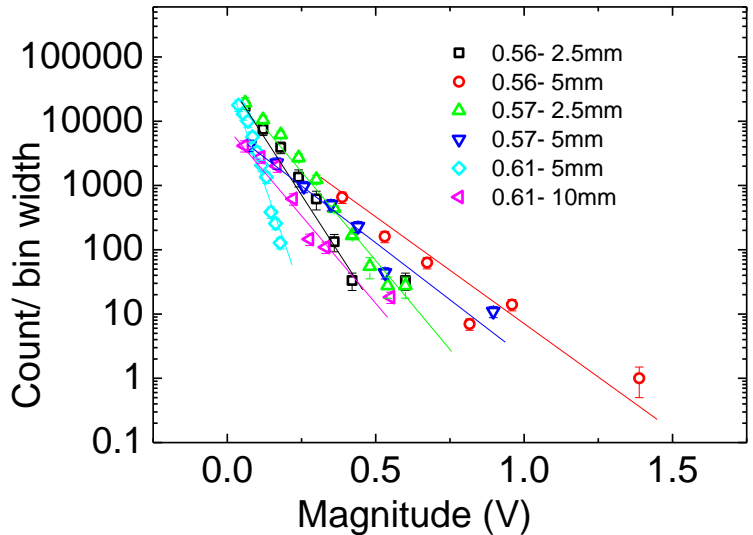


Figure 6.38- Plot of example normalised peak magnitude histogram data for various shear cell gap sizes on a log-linear plot.  $\Phi=0.56$ ,  $\Phi=0.57$  and  $\Phi=0.61$ .  $72.4\text{N/m}^2$  stress. Data from 5 minute experiments.

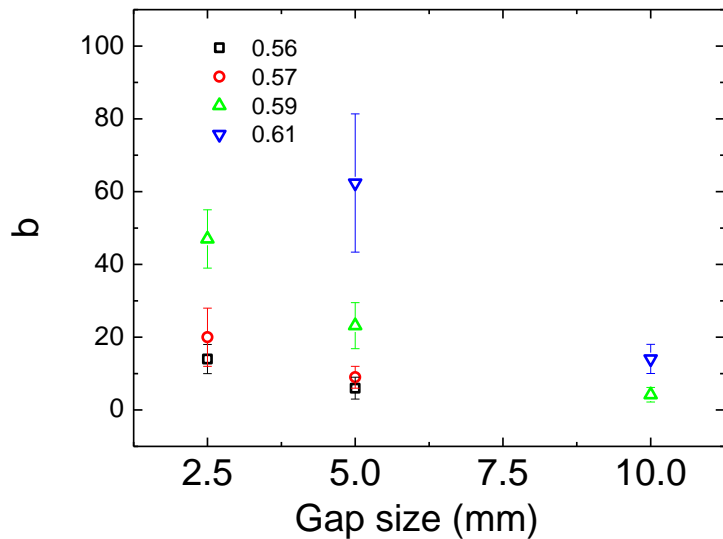
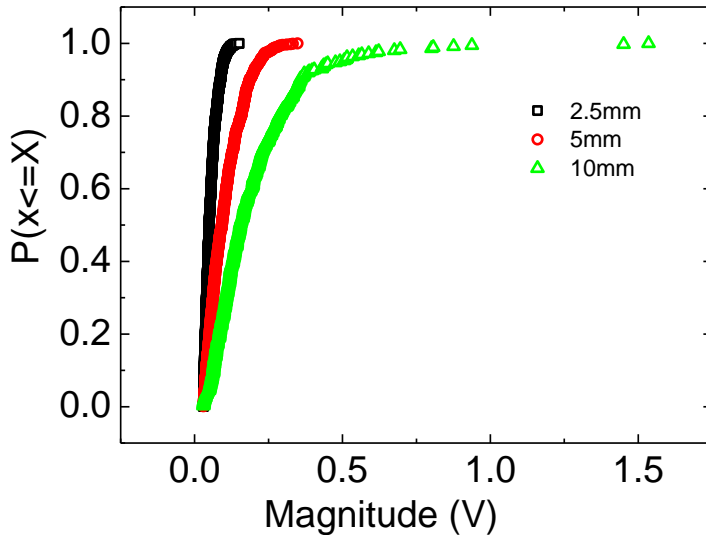


Figure 6.39- Variation of 'b' decay rate parameter from exponential fits to normalised peak magnitude histograms with shear cell gap size. Error bars show standard deviation of repetitions.  $72.4\text{N/m}^2$  stress. As detailed in [Chapter 5](#), no peaks were detected with the 10mm gap geometry using  $\Phi=0.56$  and  $\Phi=0.57$  in the 5 minute experiments. Peaks were detected with  $\Phi=0.61$  in the 2.5mm geometry but peaks were too small to reliably measure.

Cumulative distributions were produced, as before (Figure 6.40 and Figure 6.41). Reasonable exponential behaviour was found and the decay constant decreased as gap size increased, due to the larger peak magnitudes found with larger gaps. The expected values of the mean peak magnitudes calculated from the cumulative distributions compared well to the average peak magnitude calculated in [Chapter 5](#) (Figure 6.42).

An example for  $\Phi=0.59$  is shown since it had most data, allowing trends to be identified more clearly. Similar trends were, however, found for all volume fractions.



**Figure 6.40-** Example cumulative distributions of peak magnitudes for various shear cell gap sizes.  $\Phi=0.59$  and  $72.4\text{N/m}^2$  stress. Data from 5 minute experiments.

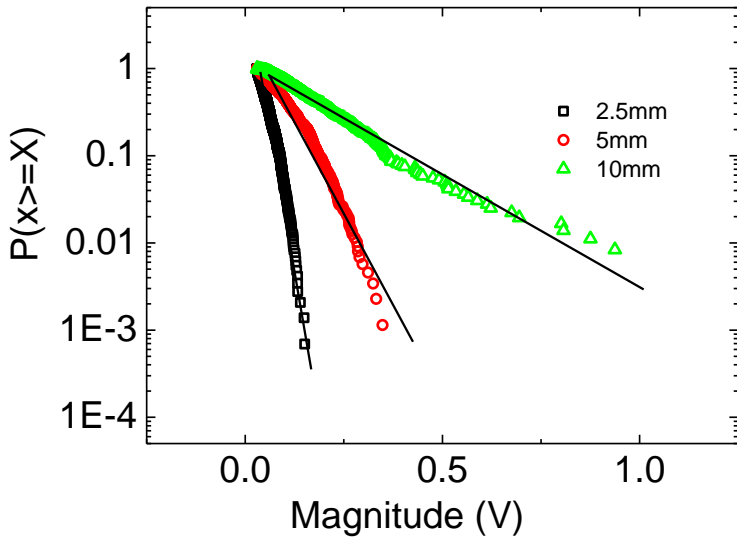


Figure 6.41- Example cumulative distributions of peak magnitudes for various shear cell gap sizes on a log-linear plot.  $\Phi=0.59$  and  $72.4\text{N/m}^2$  stress. Data from 5 minute experiments.

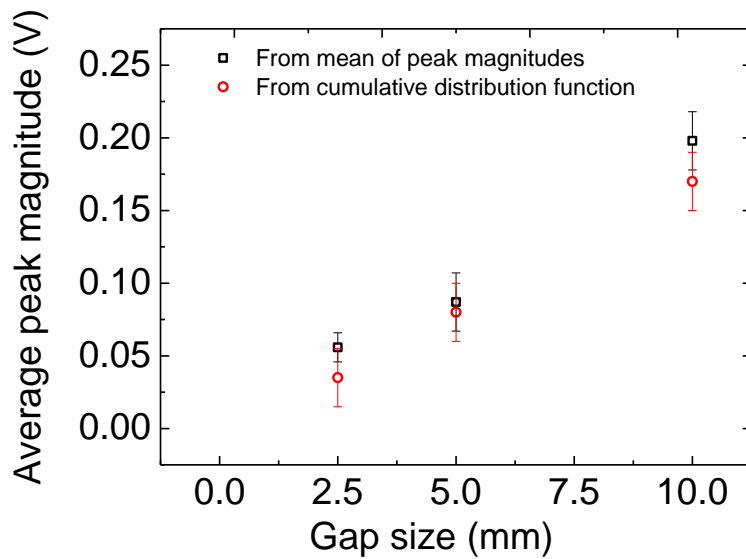


Figure 6.42- Average peak magnitude variation with shear cell gap size from mean of peak magnitudes in Chapter 5 and from cumulative distribution functions for comparison.  $\Phi=0.59$  and  $72.4\text{N/m}^2$  stress. Error bars show standard deviation of repetitions.

### Time Gap between Peaks

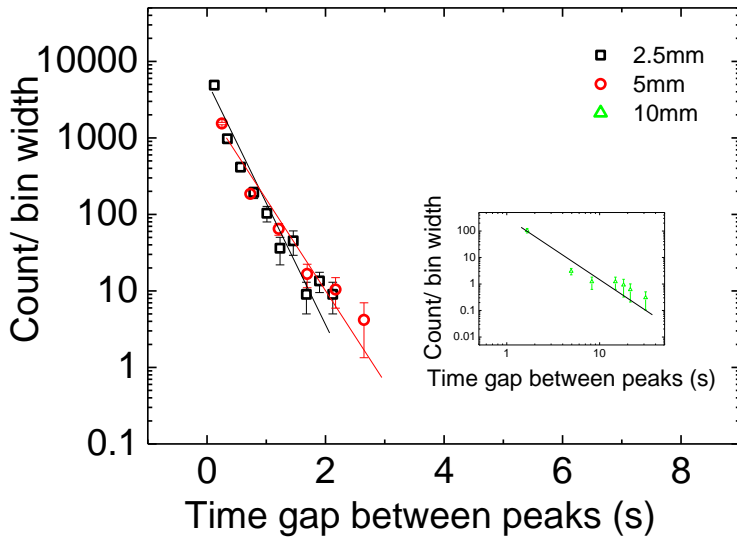


Figure 6.43- Plot of example normalised histogram data for various shear cell gap sizes on a log-linear plot.  $\Phi=0.59$  and  $72.4\text{N/m}^2$  stress. 2.5mm and 5mm gap sizes appear approximately linear, suggesting exponential behaviour. Inset shows 10mm gap size on log-log plot. Plot appears approximately linear, suggesting power law behaviour. Data from 5 minute experiments.

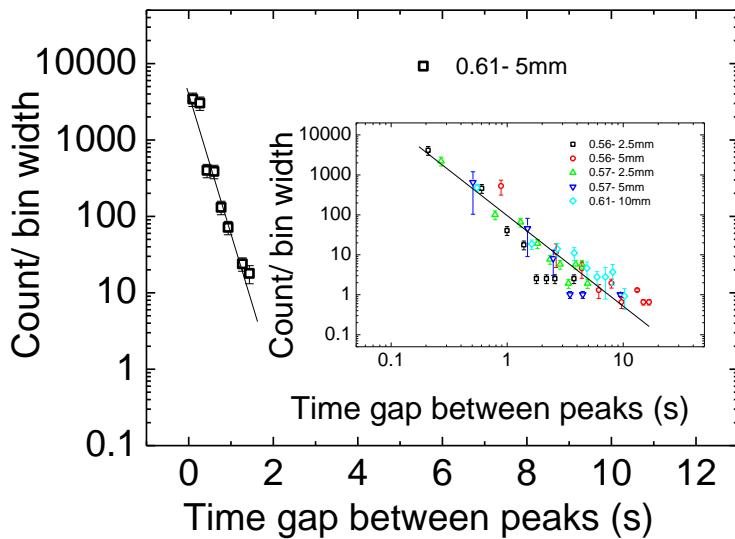


Figure 6.44- Plot of example normalised histogram data for various shear cell gap sizes on a log-linear plot (to show exponential behaviour) and log-log plot (to show power law behaviour).  $\Phi=0.56$ ,  $\Phi=0.57$  and  $\Phi=0.61$ .  $72.4\text{N/m}^2$  stress.

For  $\Phi=0.59$  and  $\Phi=0.61$ , approximate exponential time gap distributions were found for the 2.5mm and 5mm geometries (Figure 6.43 and Figure 6.44). Increasing the gap size to 10mm resulted in approximate power law distributions being found. A small number of large time gap events occurred with the 10mm geometry. For  $\Phi=0.56$  and  $\Phi=0.57$ , approximate power law distributions were found for all geometries investigated (Figure 6.44).

Similarly to the effect of reducing the stress in the high  $\Phi$  cases, increasing the geometry size enables the emergence of power law behaviour in the time gap statistics. The overall frequency of peaks decreases and large time gaps emerge.

Cumulative distributions were plotted as before (Figure 6.45 and Figure 6.46). All cumulative distributions with the different geometries were similar at low time gaps/probabilities but began to differ at probabilities  $>\sim 0.8$ . The main difference was that the 2.5mm and 5mm gap experiments approached one and levelled off more rapidly than the 10mm gap experiments. Fewer long time gap events occurred with the smaller gap sizes.

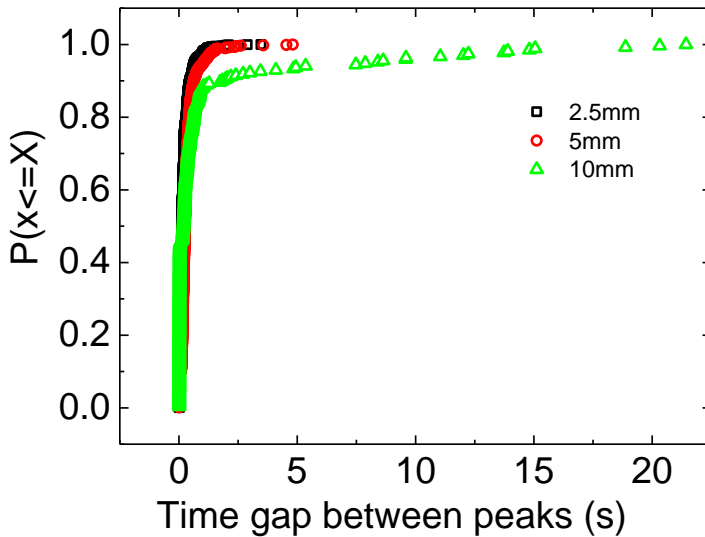
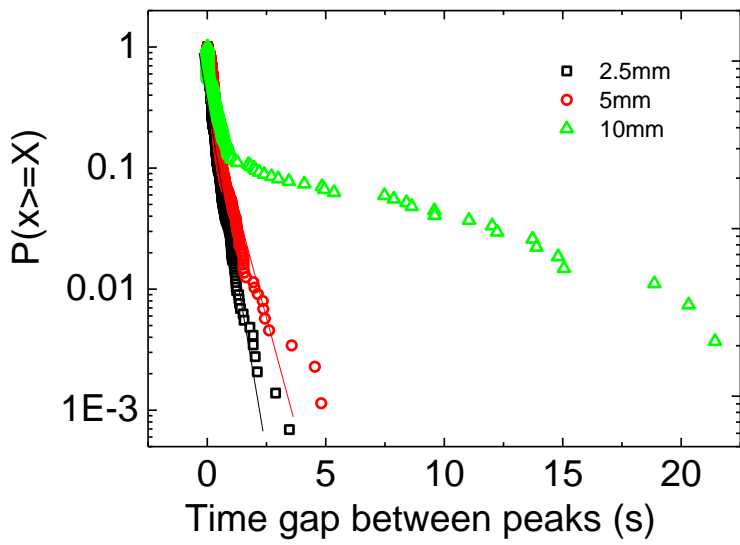


Figure 6.45- Example cumulative distributions of time gap between peaks for various shear cell gap sizes.  $\Phi=0.59$  and  $72.4\text{N/m}^2$  stress. Data from 5 minute experiments.



**Figure 6.46-** Example cumulative distributions of time gap between peaks for various shear cell gap sizes on a log-linear plot.  $\Phi=0.59$  and  $72.4\text{N/m}^2$  stress. Data from 5 minute experiments.

## 6.7 Effect of System Confinement (Soft Walls) on Distributions

The effect of system confinement on distributions was briefly considered by analysing the data obtained from the force sensor when soft walls were used and comparing to when hard walls were used. As a reminder, soft-walled shear cells were produced by attaching a layer of neoprene foam to the Perspex shear cell walls (the vertical walls of the cylinders). The shear cells were manufactured so that gaps and fluid fill heights with the foam present were the same as before.

### Peak Magnitude

Approximate exponential behaviour was found for soft and hard wall peak magnitude histogram distributions (Figure 6.47 and Figure 6.48). Cumulative distributions were plotted and sharper decays were found with soft walls (Figure 6.49, Figure 6.50, Figure 6.51 and Figure 6.52). As explained in [Chapter 5](#), there was a reduction in average peak magnitude with soft walls. This can also be seen by the increased slope of the plots with soft walls from the histogram examples in Figure 6.47 and Figure 6.48.

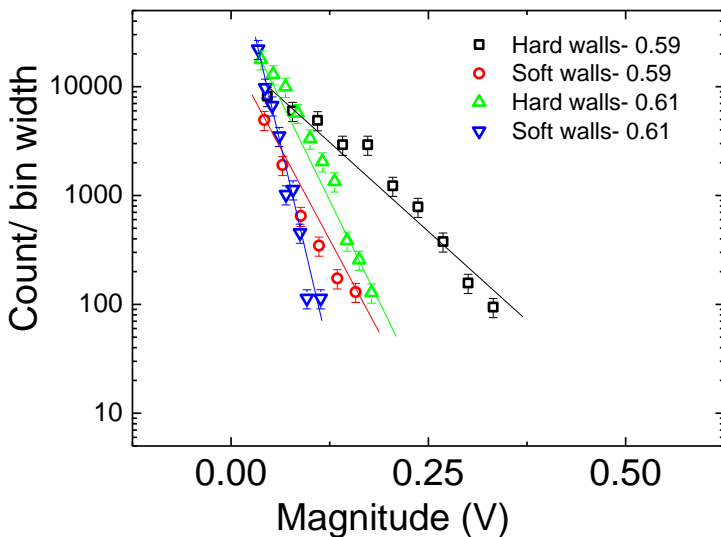


Figure 6.47- Plot of example normalised peak magnitude histogram data for hard walls and soft walls on a log-linear plot.  $\Phi=0.59$  and  $\Phi=0.61$ .  $72.4\text{N/m}^2$  stress. Data from 5 minute experiments.

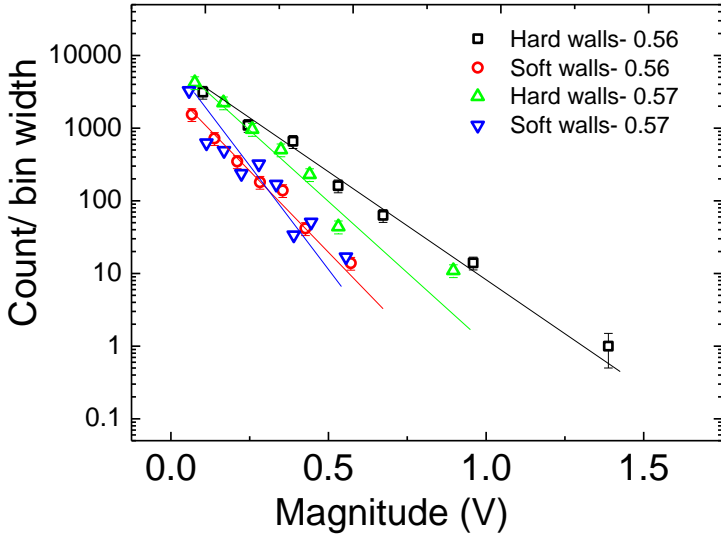


Figure 6.48- Plot of example normalised peak magnitude histogram data for hard walls and soft walls on a log-linear plot.  $\Phi=0.56$  and  $\Phi=0.57$ .  $72.4\text{N/m}^2$  stress. Data from 5 minute experiments

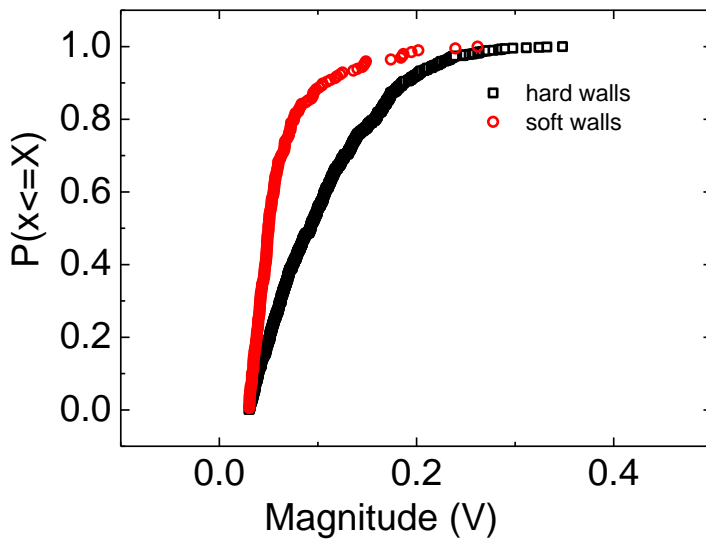
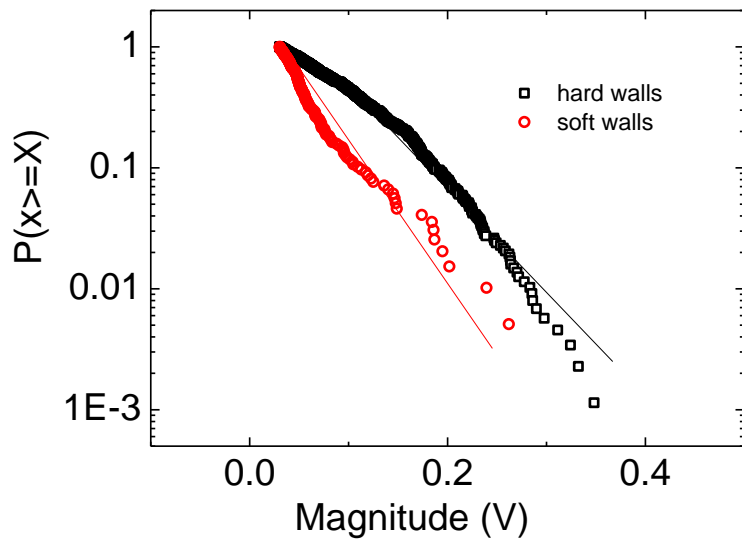
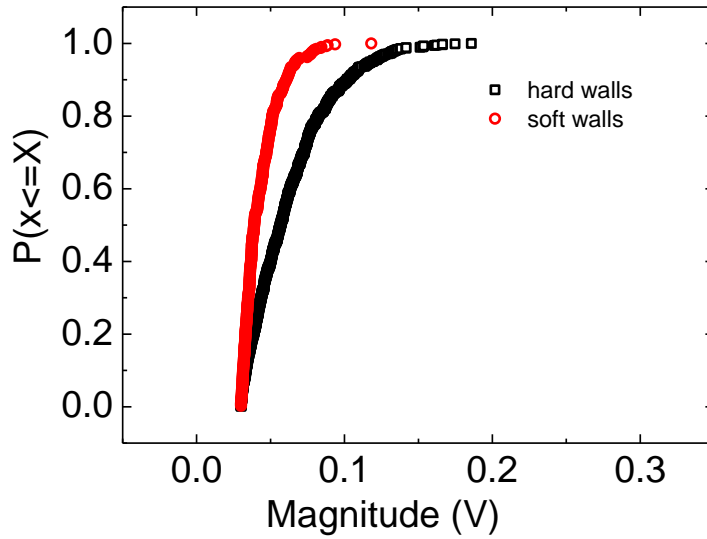


Figure 6.49- Example cumulative distributions of peak magnitudes for soft and hard walls.  $\Phi=0.59$ , 5mm shear cell gap size and  $72.4\text{N/m}^2$  stress. Data from 5 minute experiments.



**Figure 6.50-** Example cumulative distributions of peak magnitudes for soft and hard walls on log-linear plot.  $\Phi=0.59$ , 5mm shear cell gap size and  $72.4\text{N/m}^2$  stress. Data from 5 minute experiments.



**Figure 6.51-** Example cumulative distributions of peak magnitudes for soft and hard walls.  $\Phi=0.61$ , 5mm shear cell gap size and  $72.4\text{N/m}^2$  stress. Data from 5 minute experiments.

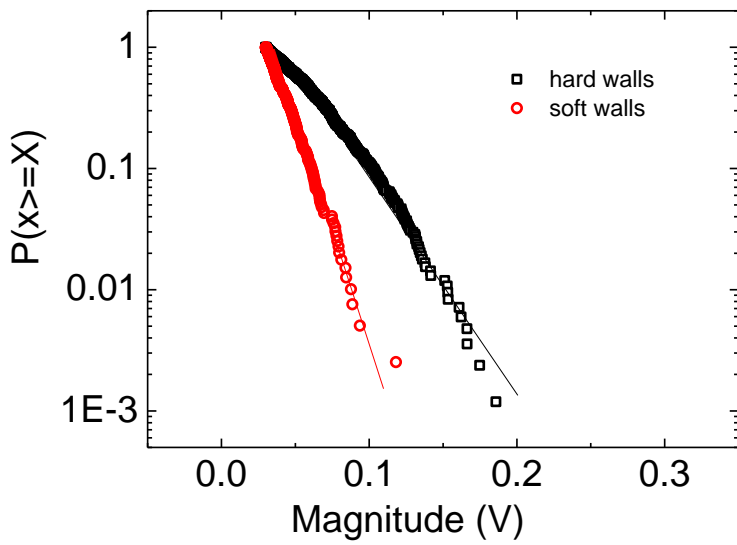


Figure 6.52- Example cumulative distributions of peak magnitudes for soft and hard walls on log-linear plot.  $\Phi=0.61$ , 5mm shear cell gap size and  $72.4\text{N/m}^2$  stress. Data from 5 minute experiments.

### Time Gap between Peaks

Soft walls resulted in time gap histogram distributions that were previously approximately exponential with hard walls transitioning to show approximate power law behaviour. For example, with hard walls, a 5mm gap geometry and 72.4 N/m<sup>2</sup> stress with 0.59 and 0.61 volume fractions, approximate exponential distributions were found. The same arrangement but with soft walls resulted in approximate power law distributions being found (Figure 6.53). This was due to a small number of large time gap events occurring with soft walls.

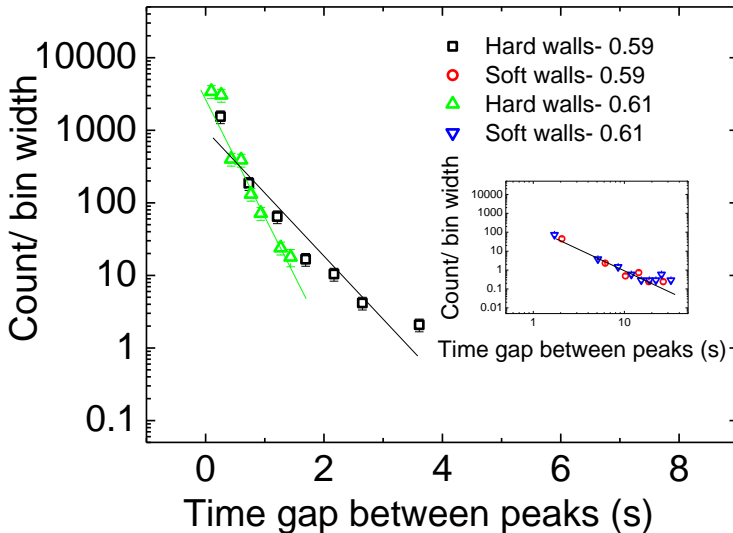


Figure 6.53- Plot of example normalised histogram data for soft wall arrangement and hard wall arrangement on a log-linear plot and log-log plot (inset).  $\Phi=0.59$  and  $\Phi=0.61$ , 5mm shear cell gap size and 72.4N/m<sup>2</sup> stress. Data from 5 minute experiments.

Cumulative distributions were plotted (Figure 6.54 and Figure 6.56). Cumulative distributions with soft walls and hard walls were similar at the start of the plots but began to differ at probabilities  $\sim 0.9$ . The main difference was that hard wall experiments approached one and levelled off more rapidly than the soft wall experiments. This was due to more long time gap events occurring with the soft wall arrangement.

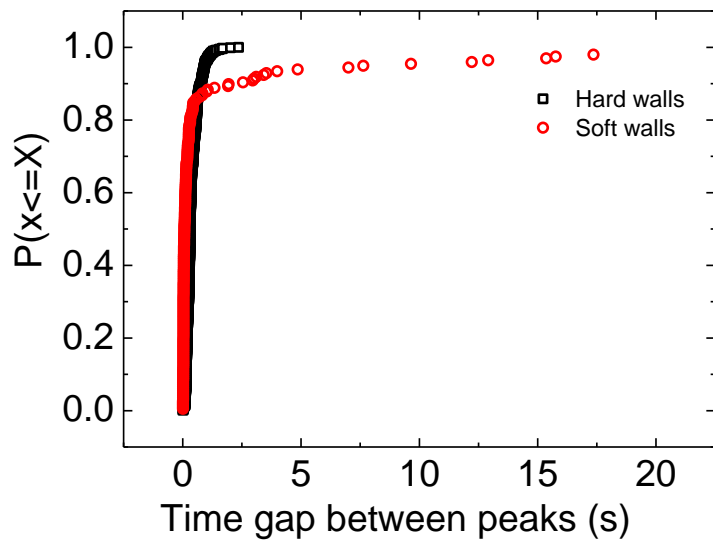


Figure 6.54- Example cumulative distributions of time gap between peaks for soft and hard walls.  $\Phi=0.59$ , 5mm shear cell gap size and  $72.4\text{N/m}^2$  stress. Data from 5 minute experiments.

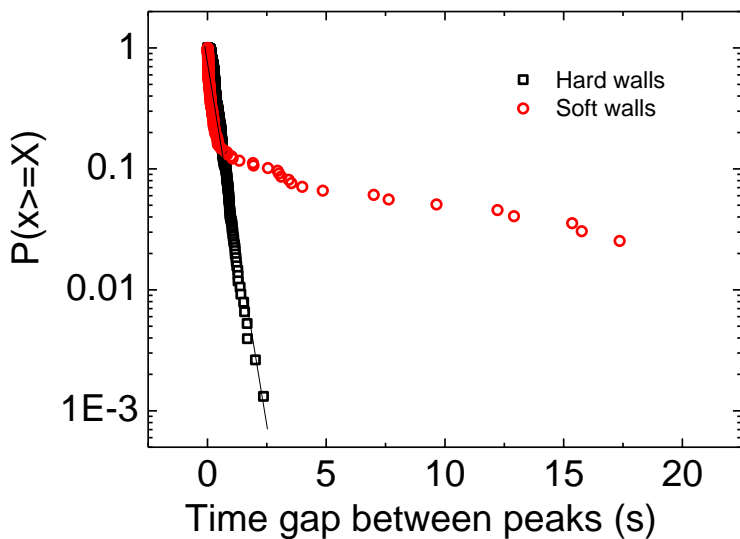


Figure 6.55- Example cumulative distributions of time gap between peaks for soft and hard walls on a log-linear plot.  $\Phi=0.59$ , 5mm shear cell gap size and  $72.4\text{N/m}^2$  stress. Data from 5 minute experiments.

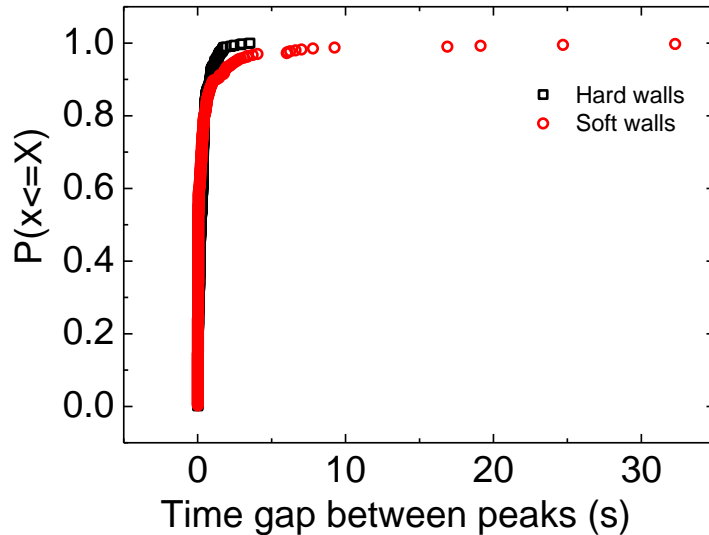


Figure 6.56- Example cumulative distributions of time gap between peaks for soft and hard walls.  $\Phi=0.61$ , 5mm shear cell gap size and  $72.4\text{N/m}^2$  stress. Data from 5 minute experiments.

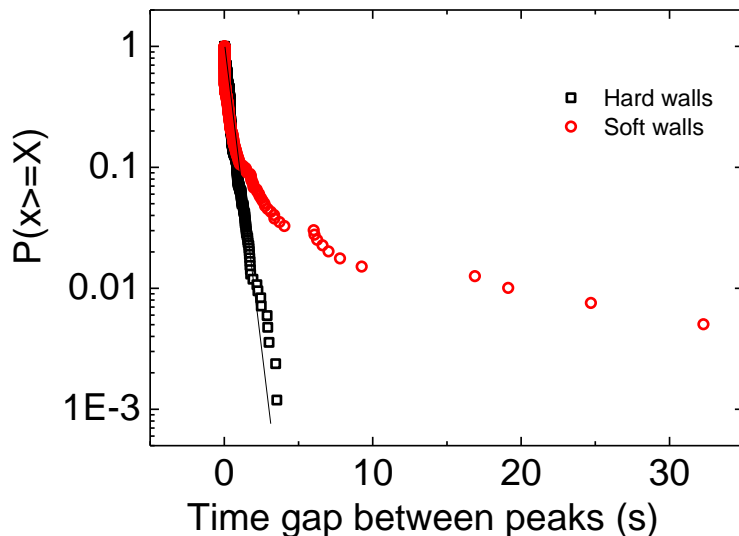


Figure 6.57- Example cumulative distributions of time gap between peaks for soft and hard walls on a log-linear plot.  $\Phi=0.61$ , 5mm shear cell gap size and  $72.4\text{N/m}^2$  stress. Data from 5 minute experiments.

## 6.8 Consideration of Observation Time

For all previous analyses, data from the full experimental observation time (5 minutes) were considered. It was decided to split the data into smaller time intervals to see if similar trends were found in each time interval. This was to investigate the effect of experiment time on the statistics.

### Peak Magnitude

The data in 6.2 (the effect of volume fraction on peak magnitude distributions) were analysed. Similar trends were found for each of the smaller time intervals and these compared very well to the full time interval trends. For example, the first 2.5 minutes of peak magnitude distribution data was similar to the latter 2.5 minutes of data, as shown in the example cumulative distributions in Figure 6.58 and Figure 6.59.

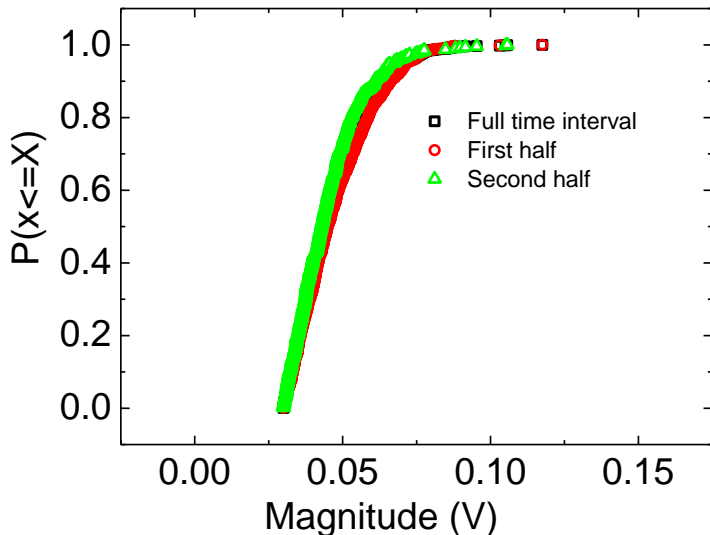


**Figure 6.58- Example cumulative distributions of peak magnitudes across different time intervals of experimental data. Full time interval represents all data collected in 5 minute experiment. First half represents first 2.5 minutes of data and second half represents final 2.5 minutes of data.  $\Phi=0.61$ , 5mm shear cell gap size and  $72.4\text{N/m}^2$  stress.**

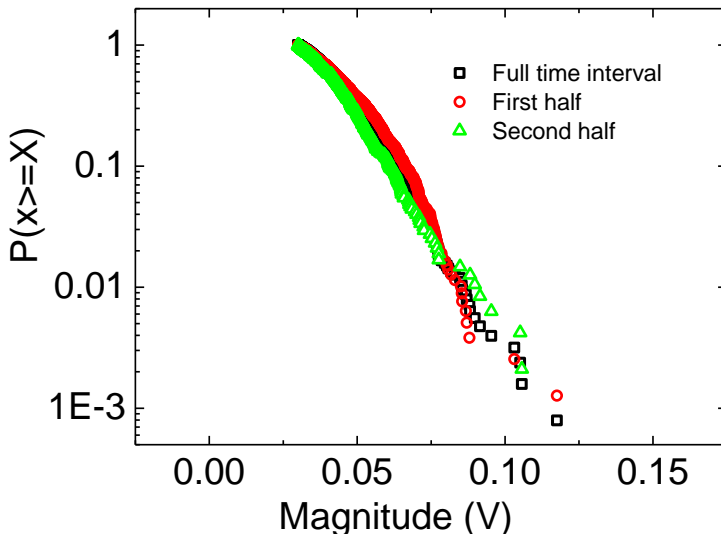


**Figure 6.59-** Example cumulative distributions of peak magnitudes across different time intervals of experimental data on a log-linear plot. Full time interval represents all data collected in 5 minute experiment. First half represents first 2.5 minutes of data and second half represents final 2.5 minutes of data.  $\Phi=0.61$ , 5mm shear cell gap size and  $72.4\text{N/m}^2$  stress.

#### Time Gap between Peaks

The data in 6.3 were analysed, and again, similar trends were generally found over the different time intervals. More notable differences between different time intervals of data were seen when time gaps were not spread ~evenly throughout the data. The distributions differed slightly due to, for example, a large time gap event occurring in one half of the data and not the other. For the cumulative distributions, this meant that for one half of the data, there was a greater probability (while still very low) that a larger time gap between peaks would be measured, compared to the other half where a large time gap may not have been found. Due to the probability of large time gap events being low overall, the difference in the cumulative distributions was not significant and they appeared very similar for the different time intervals (Figure 6.60 and Figure 6.61). Figure 6.62 and Figure 6.63 show cumulative distributions for an example where there were more long time gap events occurring compared to Figure 6.60. Despite this, cumulative distributions still appeared similar for the different time intervals. This was due to the frequency of long time gap events still being low overall.

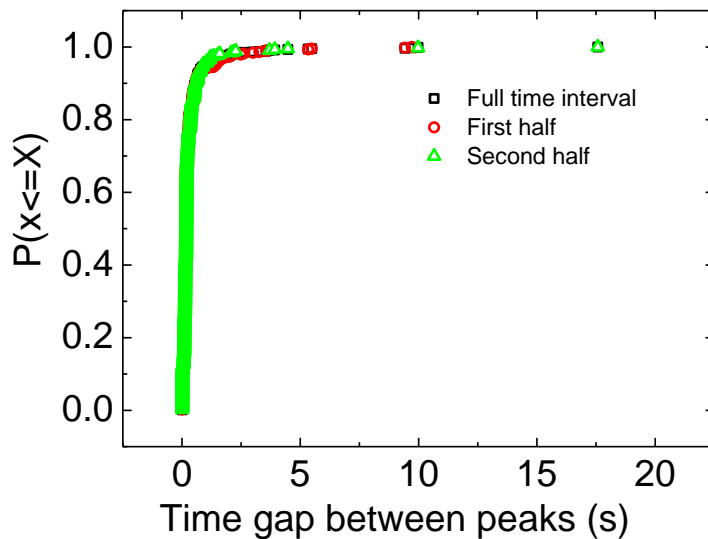


**Figure 6.60-** Example cumulative distributions of time gaps between peaks across different time intervals of experimental data. Full time interval represents all data collected in 5 minute experiment. First half represents first 2.5 minutes of data and second half represents final 2.5 minutes of data.  $\Phi=0.56$ , 5mm shear cell gap size and  $72.4\text{N/m}^2$  stress.

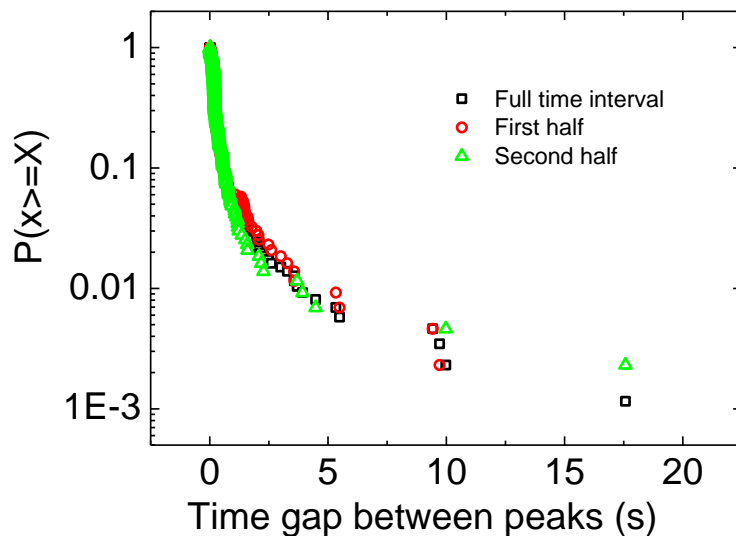


**Figure 6.61-** Example cumulative distributions of time gaps between peaks across different time intervals of experimental data on a log-linear plot. Full time interval represents all data collected in 5 minute experiment. First half represents first 2.5 minutes of data and second half represents final 2.5 minutes of data.  $\Phi=0.56$ , 5mm shear cell gap size and  $72.4\text{N/m}^2$  stress.

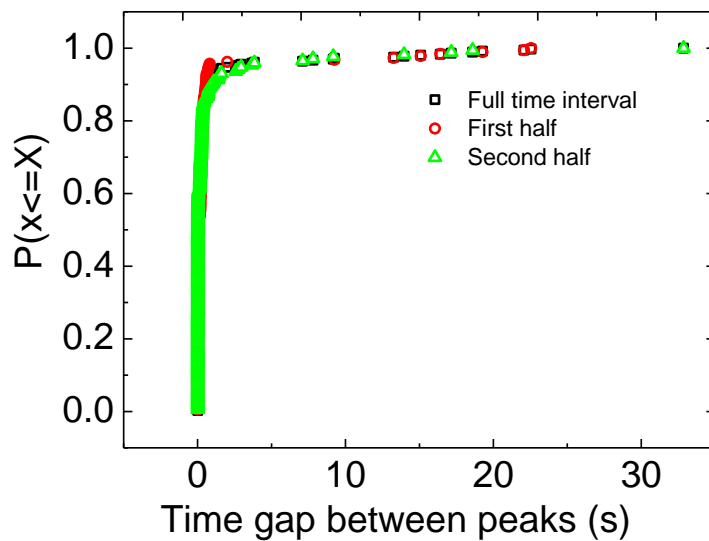


**Figure 6.62-** Example cumulative distributions of time gaps between peaks across different time intervals of experimental data. Full time interval represents all data collected in 5 minute experiment. First half represents first 2.5 minutes of data and second half represents final 2.5 minutes of data.  $\Phi=0.59$ , 10mm shear cell gap size and  $72.4\text{N/m}^2$  stress.

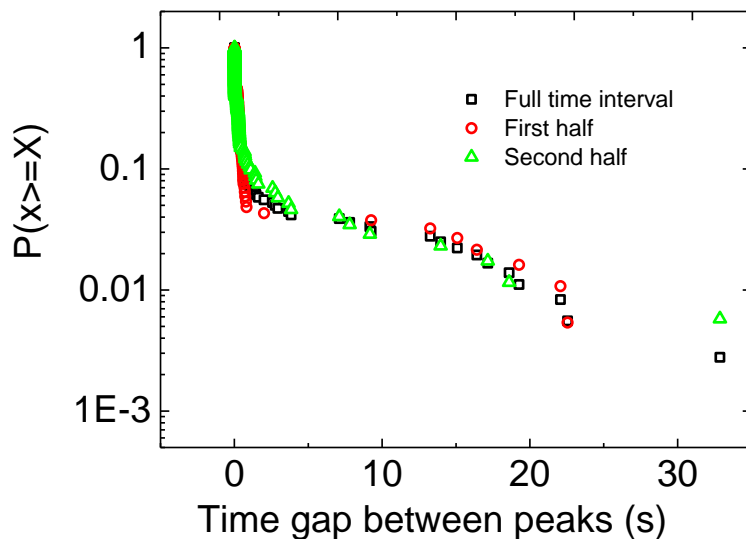


**Figure 6.63-** Example cumulative distributions of time gaps between peaks across different time intervals of experimental data on a log-linear plot. Full time interval represents all data collected in 5 minute experiment. First half represents first 2.5 minutes of data and second half represents final 2.5 minutes of data.  $\Phi=0.59$ , 10mm shear cell gap size and  $72.4\text{N/m}^2$  stress.

## 6.9 Overall Observations

To summarise, jamming peak magnitude histogram distributions appeared approximately exponential for all conditions studied, such as at different volume fractions, shear stresses and system geometries. The exponential peak magnitude distributions showed that for a particular set of conditions, there is a well-defined average jamming peak magnitude.

The histogram distributions of the time gap between peaks did not show a clear single distribution. When jams were very consistent, without large time gaps between them, approximate exponential behaviour was found. When large time gaps started to occur, and jams occurred less consistently, this behaviour transitioned to approximate power law behaviour. This therefore suggested that when jamming conditions are less favourable, whether through a lower concentration, lower shear stress, larger shear cell gap size or with less confinement, it is more likely that a power law distribution of time gaps between peaks will be found due to the emergence of long time gap events. Under these conditions, jamming is less ‘predictable’. There therefore appears to be a transition from predictable exponential behaviour of jams at very favourable jamming conditions, to less predictable power law behaviour at less favourable jamming conditions. At even less favourable jamming conditions, jamming will not occur at all.

Cumulative distributions were likely a more reliable way to present the data from the force sensor compared to histograms (particularly when power law behaviour was found). Histograms depended on bin sizes and were easily influenced by extreme points with low counts. Cumulative distributions did not rely on these and produced more consistent results. They were also more transparent since all data points contribute to the plot and no ‘arbitrary’ decision about which bin size to use was required. Cumulative distributions do, however, lack the quantitative information (e.g. in terms of ‘count’) histograms can provide and so both were useful methods for analysing the data.

## 6.10 Conclusions

By analysing the voltage/time data from the jamming detection method developed and used in [Chapter 5](#), jamming distributions and probabilities were investigated and the findings were related to literature on bottleneck flows.

Analysing the distributions of jamming peak magnitudes found that smaller peak events occurred significantly more often than larger peak events for all experiments considered. All histogram distributions of peak magnitudes showed approximate exponential behaviour.

Analysing the distributions of the time gap between peaks found that smaller time gap events occurred significantly more often than larger gap events for all experiments considered. The histogram distributions of the time gap between peaks did not show a clear single distribution and appeared to transition from approximate power law behaviour to approximate exponential behaviour depending on conditions (e.g. as volume fraction was increased).

The effects of shear stress, system geometry and confinement on the distributions were investigated. This allowed a deeper understanding of the results in [Chapter 5](#). All histogram distributions of peak magnitudes showed approximate exponential behaviour under the different conditions. The histogram distributions of the time gap between peaks did not show a clear single distribution. Reducing the shear stress, increasing the shear cell gap size or reducing confinement could result in distributions transitioning from exponential to power law.

To summarise, jamming peak magnitude histogram distributions appeared approximately exponential for all conditions studied. This indicates a ‘constant’ average peak magnitude for a particular set of conditions that is well defined. The histogram distributions of the time gap between peaks did not show a clear single distribution. When jams were very consistent, without large time gaps between them, approximate exponential behaviour was found. When large time gaps started to occur, and jams occurred less consistently, this behaviour transitioned to approximate power law behaviour.

The results showed similarities to studies on bottleneck flows (such as the flow of granular materials out of a hopper) in literature. For example, the distributions of the sizes of bursts of flow occurring in bottleneck flows (in terms of number of particles)

typically show exponential behaviour and this was perhaps analogous to the approximately exponential distributions of jamming peak magnitudes found with the experiments. The time gaps between bursts of flow in bottleneck flows also typically show power law distributions (and transitions from exponential to power law behaviour have been reported).

To ensure the reliability of these results, a significant number of repetitions would be necessary. It was difficult to draw conclusive quantitative measures from the data (such as power law exponents), given that the fits to the distributions relied heavily on data with low counts, particularly in the case of power law behaviour. The trends identified did, however, appear consistent for the data that were obtained.

1. Montgomery, C., *Applied Statistics and Probability for Engineers*. 4th ed. 2006: Wiley.
2. Coppersmith, S.N., et al., *Model for force fluctuations in bead packs*. Physical Review E, 1996. **53**(5): p. 4673-4685.
3. Lootens, D., H. Van Damme, and P. Hebraud, *Giant stress fluctuations at the jamming transition*. Physical Review Letters, 2003. **90**(17).
4. Corwin, E.I., H.M. Jaeger, and S.R. Nagel, *Structural signature of jamming in granular media*. Nature, 2005. **435**(7045): p. 1075-1078.
5. Longhi, E., N. Easwar, and N. Menon, *Large force fluctuations in a flowing granular medium*. Physical Review Letters, 2002. **89**(4).
6. Bi, D. and B. Chakraborty, *Stress fluctuations in shear jammed granular materials*. 2012, Brandeis University.
7. Hebraud, P., *Normal and tangential stress fluctuations during jamming*. Rheologica Acta, 2009. **48**(8): p. 845-853.
8. Miller, B., C. Ohern, and R.P. Behringer, *Stress fluctuations for continuously sheared granular materials*. Physical Review Letters, 1996. **77**(15): p. 3110-3113.
9. Zuriguel, I., et al., *Clogging transition of many-particle systems flowing through bottlenecks*. Scientific Reports, 2014. **4**: p. 8.
10. Zuriguel, I., et al., *Jamming during the discharge of granular matter from a silo*. Physical Review E, 2005. **71**(5): p. 9.
11. Zuriguel, I., *Clogging of granular materials in bottlenecks*. Papers in Physics, 2014. **6**(060014).
12. Nagel, K. and M. Paczuski, *Emergent Traffic Jams*. Physical Review E, 1995. **51**(4): p. 2909-2918.
13. Garcimartin, A., et al., *Flow and clogging of a sheep herd passing through a bottleneck*. Physical Review E, 2015. **91**(022808): p. 1-7.
14. Garcimartin, A., et al., *Flow and Jamming of Granular Matter Through an Orifice*. Traffic and Granular Flow '07, 2009: p. 471-486.
15. Zuriguel, I., et al., *Jamming during the discharge of grains from a silo described as a percolating transition*. Physical Review E, 2003. **68**(3): p. 4.
16. Lafond, P.G., et al., *Orifice jamming of fluid-driven granular flow*. Physical Review E, 2013. **87**(4): p. 8.
17. Helbing, D., et al., *Analytical approach to continuous and intermittent bottleneck flows*. Physical Review Letters, 2006. **97**(16): p. 4.
18. Masuda, T., K. Nishinari, and A. Schadschneider, *Critical Bottleneck Size for Jamless Particle Flows in Two Dimensions*. Physical Review Letters, 2014. **112**(13): p. 5.
19. Janda, A., et al., *Jamming and critical outlet size in the discharge of a two-dimensional silo*. Epl, 2008. **84**(4).
20. Zuriguel, I., et al., *Silo Clogging Reduction by the Presence of an Obstacle*. Physical Review Letters, 2011. **107**(27): p. 5.
21. Janda, A., et al., *Unjamming a granular hopper by vibration*. Epl, 2009. **87**(2).
22. Pastore, R., M.P. Ciamarra, and A. Coniglio, *'Flow and jam' of frictional athermal systems under shear stress*. Philosophical Magazine, 2011. **91**(13-15): p. 2006-2013.
23. Saloma, C., et al., *Self-organized queuing and scale-free behavior in real escape panic*. Proceedings of the National Academy of Sciences of the United States of America, 2003. **100**(21): p. 11947-11952.
24. Weeks, E., *Flow of Amorphous Solids Modeled with Emulsion Droplets*, in *AIChE Annual Meeting*. 2014: Atlanta.

# 7. Further Material Studies: Light Scattering and Rheometry

## This section will cover:

- The theory and experimental procedures for performing dynamic light scattering on the colloidal suspensions used in **Chapter 4** and **Chapter 5**.
  - The results obtained from performing dynamic light scattering on the colloidal suspensions.
  - The theory and experimental procedures for performing rheometry on the colloidal suspensions used in **Chapter 4** and **Chapter 5** and the cornflour suspensions used in **Chapter 8**.
  - The results obtained from performing rheometry on the colloidal suspensions and cornflour suspensions.
  - The theory and experimental procedures used to investigate ordering under shear of the colloidal suspensions used in **Chapter 4** and **Chapter 5**.
  - The results obtained from investigating the ordering of the colloidal suspensions under shear.



## 7.1 Summary

Commercial instruments were used to further investigate the properties of the colloidal suspensions used in Chapter 4 and Chapter 5 and the cornflour suspensions used in Chapter 8.

Dynamic light scattering (DLS) was performed on the supplied colloids to check particle size and polydispersity. It was also used to obtain preliminary information about the dynamics of the concentrated colloidal suspensions. This was to see if the results obtained using the bespoke shear cells and force sensor technique could be linked to the dynamic behaviour of the particles at high volume fractions.

Rheometry (using a parallel plate rheometer) was performed on the concentrated colloidal suspensions. This was to see if the results obtained using the shear cells and force sensor technique could be linked to basic sample rheology as measured in a standard commercial instrument. Rheometry was also performed on the cornflour suspensions that are used in Chapter 8.

It was hoped that the use of the commercial instruments would lead to a better understanding of the systems, or at least help confirm some of the trends obtained from the more novel techniques used.

Dynamic light scattering confirmed particle sizes and showed that the colloids were highly monodisperse. DLS showed that colloidal suspensions at the volume fractions that showed jamming behaviour in Chapter 4 and Chapter 5 ( $\Phi \geq 0.56$ ) had significantly slower dynamics than those that did not show jamming behaviour. This suggested that at the volume fractions that showed jamming behaviour, jamming behaviour in response to an applied stress can be linked to particle dynamics in the absence of a flow.

Rheometry showed many trends that agreed with the work done with the concentrated colloidal suspensions in the shear cells in Chapter 4 and Chapter 5. For example, with the rheometer, discontinuous shear thickening was only seen at  $\Phi \geq 0.56$ , in agreement with the volume fractions where visible dilatancy and jamming peaks were observed using the shear cells in Chapter 4 and Chapter 5. This suggested the means of detecting jamming in Chapter 4 and Chapter 5 (whether visual or with the force sensor technique) were reasonable. When DST occurred, granules and opaque material, very similar to that seen when the material dilated in

the shear cells, were seen. Another similarity to the shear cell experiment results was that as volume fraction increased, the shear rate required for the onset of discontinuous shear thickening decreased. The critical shear rates obtained from the rheometer were of a similar magnitude to those measured using the shear cells for the onset shear rates required for jamming.

The rheometry work on the cornflour suspensions showed similar trends to those in [Chapter 8](#) where the effects of pipe flow on concentrated suspensions were investigated. It was only at mass fractions  $\geq 0.5$  that discontinuous shear thickening was seen using the rheometer, in agreement with the mass fractions required for jamming with the pipe flow geometry in [Chapter 8](#). This suggested that the means of detecting jamming used in [Chapter 8](#) was reasonable. In agreement with the colloidal experiments, as mass/volume fraction increased, the shear rate required for the onset of DST decreased. This showed similarities between the behaviour of concentrated colloidal and granular materials under flow, agreeing with the findings of [Chapter 6](#) and [Chapter 8](#).

While the geometries of the shear cells, rheometer (parallel plate) and pipe flow set-ups differed, the behaviour of the materials under shear remained ~constant (for example in terms of onset concentrations and shear rates for jamming/DST). This showed that the behaviour observed is not something 'special' to one type of flow.

A light scattering technique was performed on the colloidal suspensions used in [Chapter 4](#) and [Chapter 5](#) to see if the particles were ordering under shear. For this, laser light was passed through a sample and its scattering pattern before and after shear was compared. Results suggested that the colloidal suspensions were not strongly ordering under shear.

Overall, this chapter resulted in a greater understanding of the behaviour of the materials used in the thesis and supported the work done in other chapters. The work suggested robustness of the more novel methods used, with strong similarities between the results from the novel equipment and commercial instruments being found.

## 7.2 Dynamic Light Scattering

*Dynamic light scattering work was done with Carol Forsyth, who assisted with the theory and experiments.*

Dynamic light scattering (DLS) was performed on the supplied colloids to check particle size and polydispersity. It was also used to obtain information about the dynamics of the concentrated colloidal suspensions that were used in [Chapter 4](#) and [Chapter 5](#).

### 7.2.1 Light Scattering Theory

#### 7.2.1.1 Light Scattering Background

Light that reaches our eyes is rarely observed directly from its source. Most of it reaches the eyes indirectly, for example as scattered light. This is what gives objects their colour. For example, the sky looks blue since blue light is scattered more than the other colours [1].

Light scattering can be defined as the change in intensity and direction of a beam of incident light when it hits an object [1]. The oscillating electric field from the light interacts with matter and when this field interacts with electrons in the material, it can induce oscillatory electric dipole moments. These oscillating dipole moments form sources of radiation i.e. the scattered light [2-4].

The arrangement of the atoms and molecules in the material the light passes through dictates the nature of the scattered light that is observed [1, 2]. For example, if light passes through a perfectly homogeneous, isotropic material, no scattered light is detected [1]. If the light passes through a suspension of particles where the particles are randomly arranged and subject to fluctuations, scattering is observed due to the inhomogeneities (such as density fluctuations and refractive index differences between the particles and fluid) [1, 2]. The intensity of scattered light in any particular direction relative to the incident light will depend on the arrangement of the particles at any given moment, a fact which is used in light scattering measurements to reveal the structure and dynamics of the suspension.

### 7.2.1.2 Light Scattering Set-Up

A typical light scattering setup is shown in Figure 7.1. An incident laser light beam is passed through the sample. Some of this incident light is scattered due to inhomogeneities in the sample and this scattered light is measured by a detector at an angle,  $\theta$ . Laser light is used since it is collimated and monochromatic. This means the waves travel parallel to each other and all have the same wavelength. Laser light is also coherent meaning that all light is in phase.

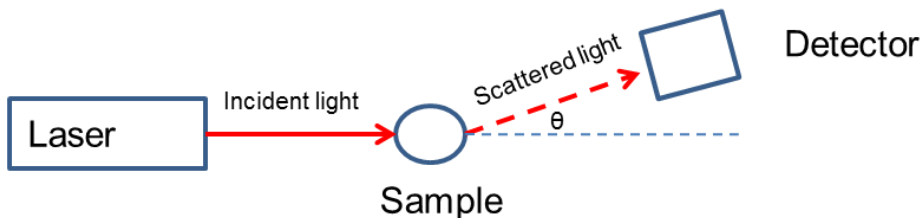


Figure 7.1- Example light scattering set-up

Light scattering experiments can be classified as static or dynamic. The differences between these were mentioned briefly in [Chapter 1](#).

### 7.2.1.3 Dynamic Light Scattering

Dynamic light scattering involves measuring temporal variations of intensity of scattered light (Figure 7.2). It is based on the random Brownian motion of particles in solution. It allows time-dependent information to be obtained, such as properties based on particle motion, including diffusion coefficients [2, 5].

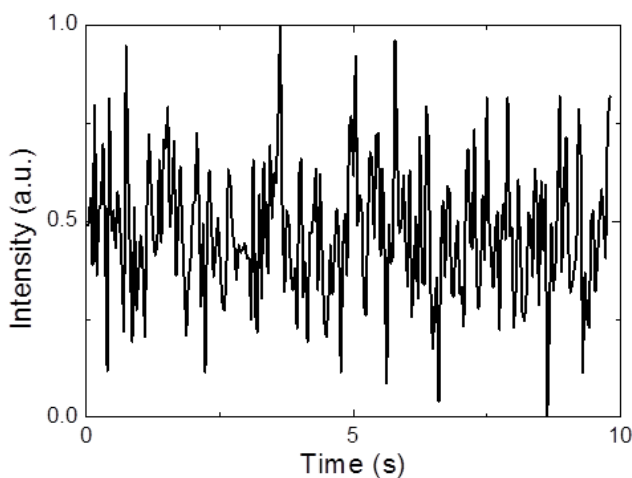


Figure 7.2- Example plot showing fluctuating intensity with time

DLS theory is based on the electric field of the scattered light (E). This is related to the intensity which can easily be measured.

$$I = |E|^2 \quad \text{Equation 7.1}$$

Here I is the intensity and E is the electric field of the scattered light.

As mentioned, the intensity of scattered light fluctuates with time due to particle movement. The intensity measurements can be converted to autocorrelation functions and from these, usable information can be deduced [5].

### Autocorrelation Functions and Monodisperse Systems

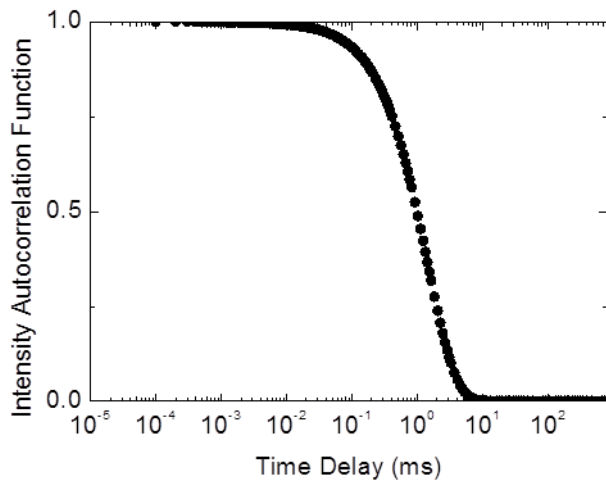


Figure 7.3- Example normalised autocorrelation function

The intensity autocorrelation function ( $G_2(\tau)$ ) can be defined as:

$$G_2(\tau) = \langle I(t)I(t + \tau) \rangle \quad \text{Equation 7.2}$$

Here t is the time and  $\tau$  is a delay time.

The normalised intensity autocorrelation function ( $g_2(\tau)$ ) can be defined as:

$$g_2(\tau) = \frac{G_2(\tau)}{\langle I(t)^2 \rangle} = \frac{\langle I(t)I(t+\tau) \rangle}{\langle I(t)^2 \rangle} \quad \text{Equation 7.3}$$

The intensity autocorrelation function compares a signal with a delayed version of itself. An example normalised intensity autocorrelation function is shown in Figure 7.3. It shows that for short delay times, the intensities of scattering from the particles are highly correlated. After longer delays, however, intensities are no longer

correlated. This is due to the movement of the particles [5, 6]. At short delays, there has been little movement to destroy correlation, while after longer delays, increased movement has reduced the correlation.

The normalised intensity autocorrelation function ( $g_2(\tau)$ ) can be used to get a normalised electric field autocorrelation function ( $g_1(\tau)$ ). This comes from a Siegert relation [5, 6].

$$g_2(\tau) = 1 + |g_1(\tau)|^2 \quad \text{Equation 7.4}$$

Hence:

$$g_1(\tau) = \sqrt{g_2(\tau) - 1} \quad \text{Equation 7.5}$$

For a monodisperse sample where the particles undergo normal free diffusion, the normalised electric field autocorrelation function decays as a single exponential with the delay time.

$$g_1(\tau) = e^{-\tau\Gamma} \quad \text{Equation 7.6}$$

Here  $\Gamma$  is the decay rate of the correlation function.

Taking the natural logarithm of both sides:

$$\ln(g_1(\tau)) = -\tau\Gamma \quad \text{Equation 7.7}$$

Plotting  $\ln(g_1(\tau))$  versus  $\tau$  therefore produces a straight line with a slope equal to the decay rate.

This method of obtaining the decay rate applies only to truly monodisperse systems. In practice, most systems contain small amounts of polydispersity and these do not follow the straight line relationship so closely. Therefore a cumulant analysis is typically performed [6, 7]. With a polydisperse sample, differently sized particles show different decays (smaller particles decay more rapidly as outlined below) so the overall decay becomes a mixture of multiple decays.

## Cumulant Analysis

A cumulant analysis involves fitting a polynomial to  $\ln(g_1(\tau))$ , rather than a straight line.

$$\ln(g_1(\tau)) = a + b\tau + c\tau^2 + d\tau^3 \quad \text{Equation 7.8}$$

Here a, b, c and d are coefficients from the polynomial fit.

This 3<sup>rd</sup> order fit is sufficient. Higher order fits are unwarranted due to lack of precision in the data and can lead to other parameters being less precisely deduced [6].

The coefficient of the first cumulant represents the decay rate:

$$|b| \approx \Gamma \quad \text{Equation 7.9}$$

The decay rate is an average decay rate of the particles in the solution and it can be related to the average diffusion coefficient (D). This is through the scattering vector (q).

$$\Gamma = Dq^2 \quad \text{Equation 7.10}$$

The scattering vector is the difference in magnitude of the incident and scattered light vectors and can be derived through trigonometry.

$$q = \frac{4\pi n}{\lambda} \sin\left(\frac{\theta}{2}\right) \quad \text{Equation 7.11}$$

Here  $\lambda$  is the wavelength of laser light used in a vacuum, n is the refractive index of the dispersion medium and  $\theta$  is the angle between the incident and scattered light (Figure 7.1).

With the diffusion coefficient known, the Stokes-Einstein equation can now be used to deduce the average hydrodynamic radius of the particles. Details of this were given in [Chapter 1](#).

$$R_h = \frac{k_B T}{6\pi\eta D} \quad \text{Equation 7.12}$$

Here D is the diffusion coefficient,  $k_B$  is the Boltzmann Constant, T is the absolute temperature,  $\eta$  is the solvent viscosity and  $R_h$  is the hydrodynamic radius.

The Stokes-Einstein equation is based on assumptions such as single, non-interacting spheres in a viscous liquid. The hydrodynamic radius represents the radius of a hard sphere diffusing at the same rate as the particle.

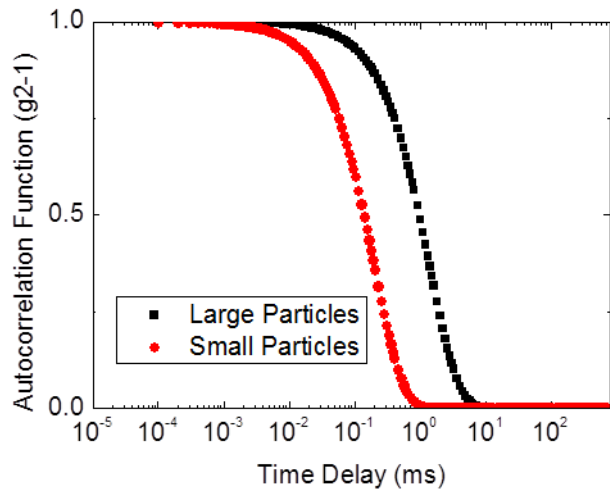


**Figure 7.4- Autocorrelation functions showing differences between large and smaller particles**

Small particles have larger diffusion coefficients than larger particles. Therefore, they are associated with larger decay rates, as shown in Figure 7.4, where the function decays more rapidly with the smaller particles.

## **7.2.2 Experimental Procedures**

Dynamic light scattering was performed on the colloid particles when dilute and in the concentrated suspensions used in [Chapter 4](#) and [Chapter 5](#).

### **7.2.2.1 DLS of Colloid Particles**

Dynamic light scattering was performed on the supplied colloids (PMMA in decalin) to check the particle size and deduce information about polydispersity. Measurements took place at 90° (ALV/CG3 Compact Goniometer, ALV/LSE 5004 Electronic System and 50 mW He-Ne laser ( $\lambda=632$  nm)). Samples were sufficiently diluted by decalin so that multiple scattering would not be an issue.

### **7.2.2.2 DLS of Concentrated Suspensions**

Dynamic light scattering was performed on samples of the concentrated suspensions (used in [Chapter 4](#) and [Chapter 5](#)) with volume fractions ranging from  $\Phi=0.55-0.61$  to see how dynamics differed in the stationary suspensions. Samples were index matched to prevent multiple scattering. Measurements took place at 90° (ALV/CG3 Compact Goniometer, ALV/LSE 5004 Electronic System and 50 mW He-Ne laser ( $\lambda=632$  nm)). Samples used for DLS were taken from the same mixtures that were used for the rotating cylinder shear cell experiments in [Chapter 5](#). This ensured volume fraction consistencies. Decay rates were obtained as explained in 7.2.1.3.

**For all experiments, typically three repetitions were done. Error bars represent  $\pm$  one standard deviation.**

## 7.2.3 Results and Discussion

### 7.2.3.1 DLS of Colloid Particles

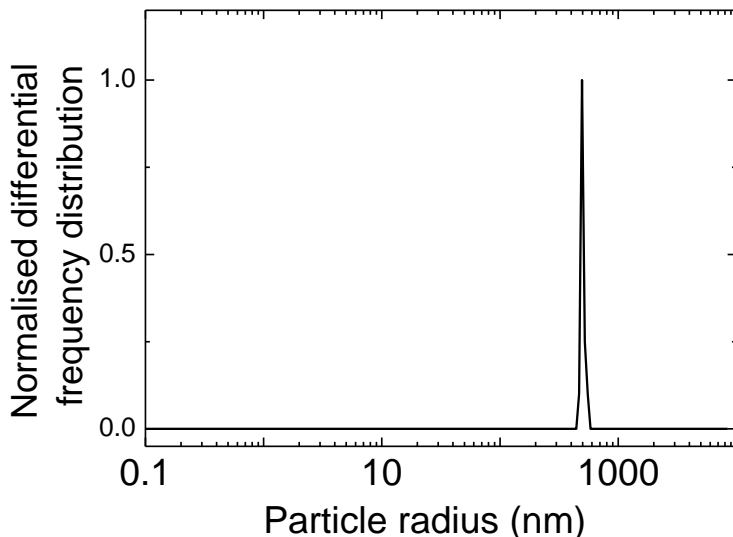


Figure 7.5- Particle size distribution of colloid particles used in experiments, obtained from DLS.

DLS confirmed that the particles used in the experiments had a radius of ~500nm ( $488 \pm 5$  nm). Their polydispersity was also analysed and it confirmed that the samples were highly monodisperse.

From the autocorrelation function, a polydispersity index and particle size distribution was obtained (Figure 7.5). The particle size distribution was obtained from a CONTIN analysis. This was built into the ALV software used with the instrument. Further details of the theory behind a CONTIN analysis can be found in work by Provencher [8]. The particle size distribution was used to determine the polydispersity.

In literature, there are different definitions of polydispersity. In many cases, the polydispersity is defined as the width of the particle size distribution (full width at half maximum height) [9]. The percentage polydispersity is defined as the polydispersity divided by the mean particle size [9, 10].

$$\% \text{ polydispersity} = \frac{FWHM}{\text{mean particle size}} \times 100 \% \quad \text{Equation 7.13}$$

In other sources, the polydispersity is defined as the standard deviation of the size distribution. The percentage polydispersity is then defined as the polydispersity divided by the mean particle size [11, 12].

$$\% \text{ polydispersity} = \frac{\text{std.deviation of sizes}}{\text{mean particle size}} \times 100 \% \quad \text{Equation 7.14}$$

Both methods suggested the polydispersity of the colloids was very low and that the particles were highly monodisperse (Figure 7.5). Using the polydispersity definition based on standard deviation, the experimental colloids had a  $4\pm2\%$  polydispersity.

The polydispersity index (Pdl) was calculated from the cumulant analysis (Equation 7.8) [13].

$$PdI = \frac{2c}{b^2} \quad \text{Equation 7.15}$$

Here b and c are coefficients obtained from the polynomial fit.

From this, the polydispersity index was just  $0.04\pm0.02$ ; this suggested a highly monodisperse sample [10].

### 7.2.3.2 DLS of Concentrated Suspensions

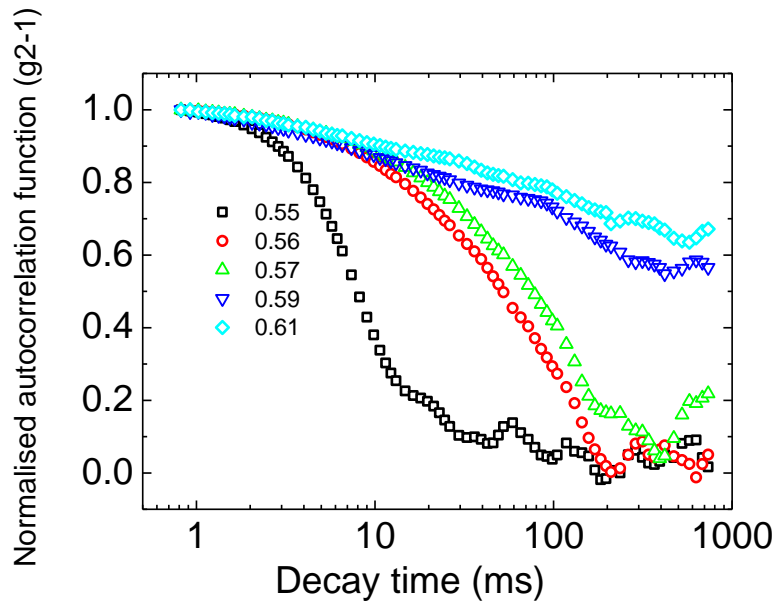


Figure 7.6- Example autocorrelation functions for various volume fractions of concentrated suspensions

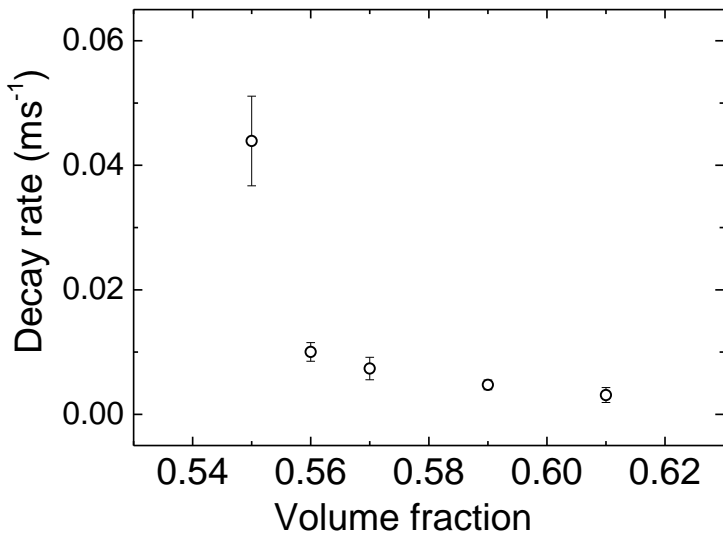


Figure 7.7- Decay rates from autocorrelation functions for various volume fractions of concentrated colloidal suspensions. Error bars show standard deviation of repetitions.

Dynamic light scattering showed that volume fractions where jamming occurred in [Chapter 4](#) and [Chapter 5](#) had significantly slower decay rates than volume fractions where jamming did not occur ( $\phi < 0.56$ ) (Figure 7.6 and Figure 7.7). The functions for

$\phi=0.59$  and  $\phi=0.61$  did not decay to the baseline. According to literature, this suggests glassy behaviour and is typically found in samples at and above the glass transition (see [Chapter 1](#) and [Chapter 2](#)) [14, 15]. At and above the glass transition, particles are ‘arrested’ by cages of neighbours and therefore only move very slowly at high concentrations. This explains why the apparent correlation never completely disappears. Results therefore suggested that in the suspensions that jammed in the rotating cylinder shear cell geometry, particle dynamics were significantly slower.

The DLS results, in accordance with the rheometry results detailed in 7.3, suggested that suspensions with a volume fraction greater than 0.55 behaved very differently from lower volume fractions- both sheared and unsheared- as was found in [Chapter 4](#) and [Chapter 5](#). The critical volume fraction found with DLS (and rheometry) matched the volume fraction where dilation became visible and jamming peaks became apparent with the force sensor in [Chapter 4](#) and [Chapter 5](#).

It is worth noting that the DLS results are just ‘preliminary’ results. Dynamic light scattering at high concentrations really requires more complicated methods since samples become non-ergodic [16].

## 7.3 Rheometry

*Rheometry work was done with Carol Forsyth and Sandy Hope.*

Rheometry (using a parallel plate rheometer) was performed on the concentrated colloidal suspensions used in [Chapter 4](#) and [Chapter 5](#) and on the cornflour suspensions that are used in [Chapter 8](#). It was hoped that the use of a commercial rheometer would lead to a better understanding of the systems, or at least help confirm some of the trends obtained from the more novel techniques used.

### 7.3.1 Rheometry Background and Theory

#### 7.3.1.1 Rheometry Background

Rheometers are instruments designed to measure the rheological properties of materials. An aim of rheometry is to determine relationships between material flow and an applied stress [17-19].

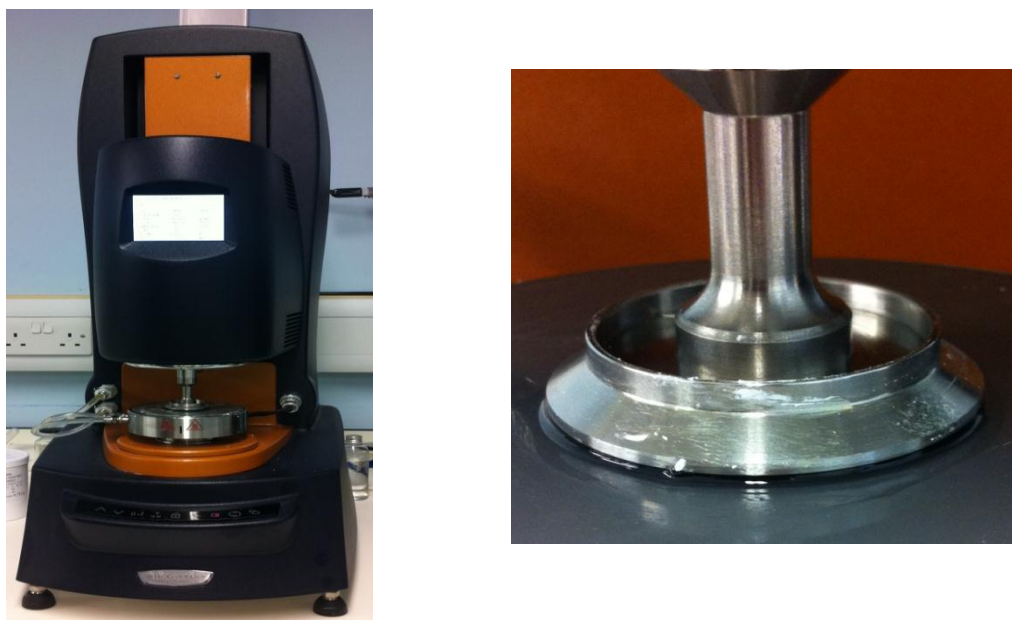


**Figure 7.8-** Rotational rheometer (TA Discovery HR-2) used for experiments (left) and its parallel plate geometry (right)

Rheometers can be divided into two main categories: rotational or shear rheometers and extensional rheometers. Rotational rheometers control the applied shear stress or shear rate, while extensional rheometers control the extensional stress or extensional strain [18].

The most common type of rheometer used is the rotational rheometer. They typically have two main modes of operation- controlled rate or controlled stress. With controlled rate operation, the desired shear rate is defined by the user and the resultant shear stress required to achieve this is measured. With controlled stress operation, the desired applied shear stress is set by the user and the resultant shear rate is measured [19]. Controlled rate rheometers are most common, however, flow curve data from both types are typically plotted in a similar manner (shear stress versus shear rate or viscosity versus shear rate) to allow simpler comparisons [19]. Some modern rheometers come with the option to work in both operation modes [19].

Various rotational rheometer geometries exist. Simple geometries are those where the shear rate remains constant across the geometry [17]. Examples of these include narrow-gap concentric cylinder geometries (similar to the shear cells used in [Chapter 4](#) and [Chapter 5](#)) and certain cone and plate geometries [17].

More complex geometries are those where the shear rate is not constant across the geometry. These include wide-gap concentric cylinder geometries and parallel plate geometries (as used in this section and shown in Figure 7.8). Because of the non-constant shear rate, an intermediate calculation step is necessary to obtain an overall viscosity for the fluid at a particular shear stress/rate, as outlined in 7.3.1.2.

### 7.3.1.2 Parallel Plate Rheometer Theory

A plate-plate/ parallel plate geometry was used for the rheometry work done in this chapter (Figure 7.9). Advantages of this geometry include that the gap can be easily adjusted for different samples, low sample volumes are required and that it is easy to establish a uniform temperature profile. Disadvantages include that the shear rate is not constant across the geometry (as mentioned in 7.3.1.1) and that solvent evaporation at the edges may occur [18].

An outline of the main theory behind the geometry is given below.

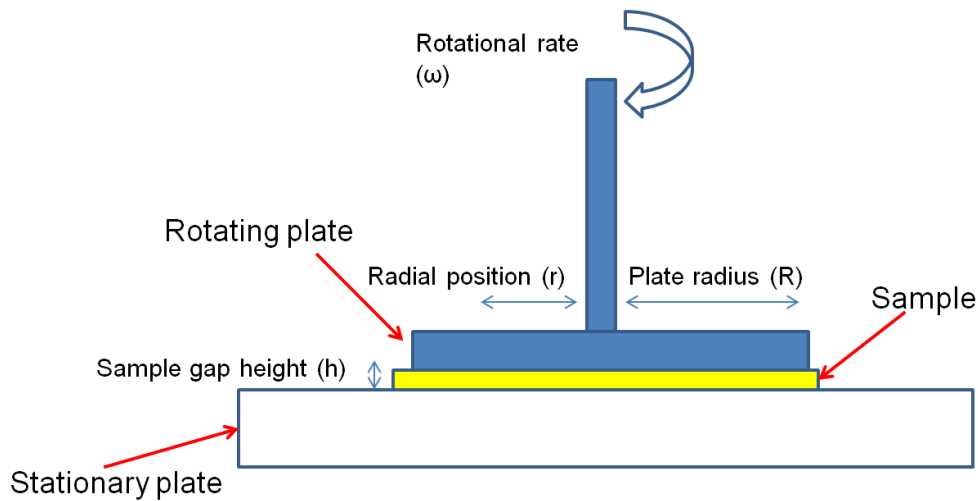


**Figure 7.9- Parallel plate geometry**

As mentioned, with a parallel plate set-up, the shear rate is not constant across the geometry. The shear rate ( $\dot{\gamma}$ ) as a function of radial position can be written as [17, 20, 21]:

$$\dot{\gamma}(r) = \frac{v(r)}{h} = \frac{\omega r}{h} = \frac{2\pi N r}{h} \quad \text{Equation 7.16}$$

Here  $v(r)$  is the rotational velocity,  $h$  is the sample gap height,  $\omega$  is the angular rotational rate,  $N$  is the rotational rate and  $r$  is the radial position.

The shear rate therefore varies from zero at the centre to a maximum ( $\dot{\gamma}_R$ ) at the outer radius ( $r=R$ ) [17]:

$$\dot{\gamma}_R = \frac{\omega R}{h} \quad \text{Equation 7.17}$$

The shear rate at a given radial distance is assumed to be independent of its height within the gap [22].

The applied torque ( $T$ ) is given by [22]:

$$T = \int_0^A \text{stress}(\tau) \times \text{radial distance}(r) \times dA (2\pi r dr) \quad \text{Equation 7.18}$$

Here  $dA$  is the incremental increase in area.

This gives:

$$T = 2\pi \int_0^R \tau r^2 dr \quad \text{Equation 7.19}$$

Since  $\tau = \eta\dot{\gamma}$ , the expression for the shear rate as a function of radial position can be substituted into Equation 7.19.

$$T = \frac{2\pi\eta\omega}{h} \int_0^R r^3 dr \quad \text{Equation 7.20}$$

Integrating gives:

$$T = \frac{\pi\eta\omega R^4}{2h} \quad \text{Equation 7.21}$$

Rearranging this for viscosity gives [20]:

$$\eta = \frac{2Th}{\pi\omega R^4} \quad \text{Equation 7.22}$$

This can be multiplied by the maximum shear rate to get the shear stress at the outer radius [23]:

$$\tau = \frac{2T}{\pi R^3} \quad \text{Equation 7.23}$$

The above theory is valid for Newtonian materials, where the viscosity remains constant. For non-Newtonian materials, corrections must be applied. These corrections generally involve assumptions such as that at any particular shear rate, the local shear stress versus shear rate relationship can be described by power-law behaviour. Here the slope of  $\ln$  (shear stress) versus  $\ln$  (shear rate) equals the power law index,  $n$  (see [Chapter 2](#)) [17].

For a non-Newtonian material, the following can be applied [21, 23]:

$$\tau = \frac{T}{2\pi R^3} \left[ 3 + \frac{d \ln T}{d \ln \omega} \right] \quad \text{Equation 7.24}$$

For a Newtonian material,  $\frac{d \ln T}{d \ln \omega}$  equals one, so the equation reduces to Equation 7.23.

The theory behind this can be found elsewhere [22, 24].

Typically the shear rate referenced by the rheometer is the shear rate at the outer radius (i.e. the maximum) [17].

### 7.3.2 Experimental Procedures

Rheometry was performed on the concentrated colloidal suspensions ([Chapter 4](#) and [Chapter 5](#)) and the cornflour-water suspensions ([Chapter 8](#)).

#### 7.3.2.1 Rheometer

The rheometer used (TA Discovery HR-2) was a rate controlled rotational rheometer. A parallel plate geometry was used and the plate had a 40mm diameter.

Continuous shear ramps were performed on samples. With these, the shear rate was increased linearly between a specified initial shear rate and final shear rate over a set time period. If the torque that was required to achieve the target shear rate at a given point was too high for the motor to achieve (for example due to a significant increase in sample viscosity) then the shear rate would fall below its target value. The rheometer would then continue trying to meet the target shear rate at subsequent points in time. It is worth noting that the rheometer was rate controlled whereas the shear cells used in [Chapter 4](#) and [Chapter 5](#) were stress controlled.

The gap distance between the top plate and base plate was 1000 $\mu\text{m}$  for the concentrated colloidal suspension samples and 800 $\mu\text{m}$  for the cornflour suspensions. The reason for the smaller gap with the cornflour suspensions was that the samples spread out significantly more than the colloidal suspensions, making it difficult for their depth to reach 1000 $\mu\text{m}$ , and therefore wet the top plate.

### **7.3.2.2 Rheology of Concentrated Colloidal Suspensions**

Colloidal suspensions with volume fractions used in the shear cell experiments in [Chapter 4](#) and [Chapter 5](#) ( $\Phi=0.55-0.61$ ) were analysed using the rheometer. Samples were taken from the same mixtures that were used for the rotating cylinder shear cell experiments in [Chapter 5](#). This ensured volume fraction consistencies.

A continuous shear ramp (typically between  $0.1-1000\text{s}^{-1}$ ) was performed. The shear rate increased in increments of  $\sim 3\text{s}^{-1}$  every second. This allowed shear stress versus shear rate data to be obtained, allowing sample viscosities to be measured as a function of shear rate.

### **7.3.2.3 Rheology of Concentrated Cornflour-Water Suspensions**

A similar procedure was performed for cornflour-water suspensions, with mass fractions used in the pipe flow experiments in [Chapter 8](#) being analysed ( $x=0.48-0.56$ ). A continuous shear ramp (typically between  $0.1-1000\text{s}^{-1}$ ) was performed. Details regarding sample preparation are given in [Chapter 8](#).

[For all experiments, typically three repetitions were done. Error bars represent  \$\pm\$  one standard deviation.](#)

### 7.3.3 Results and Discussion

#### 7.3.3.1 Rheology of Concentrated Colloidal Suspensions

The concentrated colloidal suspension measurements made using the rheometer showed similar trends to the rotating cylinder shear cell experiments in [Chapter 4](#) and [Chapter 5](#). Discontinuous shear thickening was only seen at volume fractions greater than 0.55 over the shear rates considered using the rheometer, and it was only at volume fractions beyond 0.55 that visible dilatancy and jamming peaks were observed using the shear cells in [Chapter 4](#) and [Chapter 5](#). This suggested the means of detecting jamming in [Chapter 4](#) and [Chapter 5](#) (whether visual or with the force sensor technique) were reasonable and jamming appeared closely related to discontinuous shear thickening. With the rheometer measurements, DST was seen as a significant jump in the shear stress (and therefore viscosity) with increasing shear rate (Figure 7.10 and Figure 7.11).

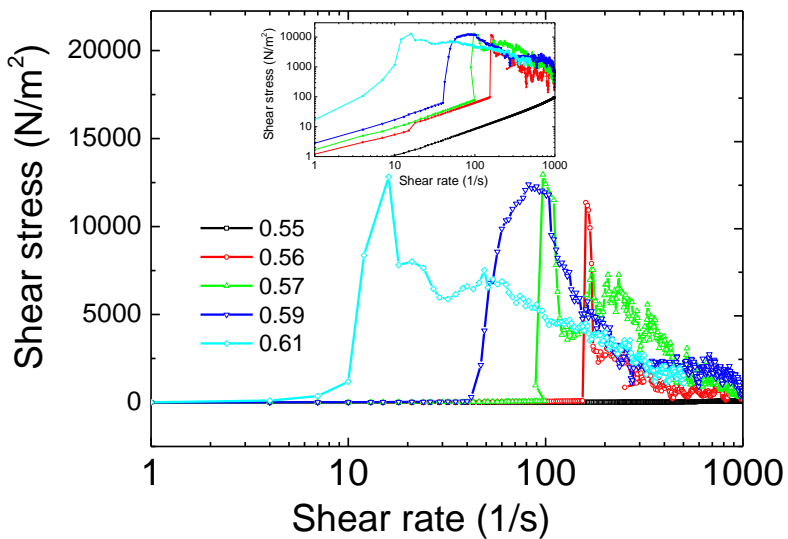


**Figure 7.10-** Example shear stress versus shear rate rheometer profiles for various colloid volume fractions. Inset shows data on log-log plot.

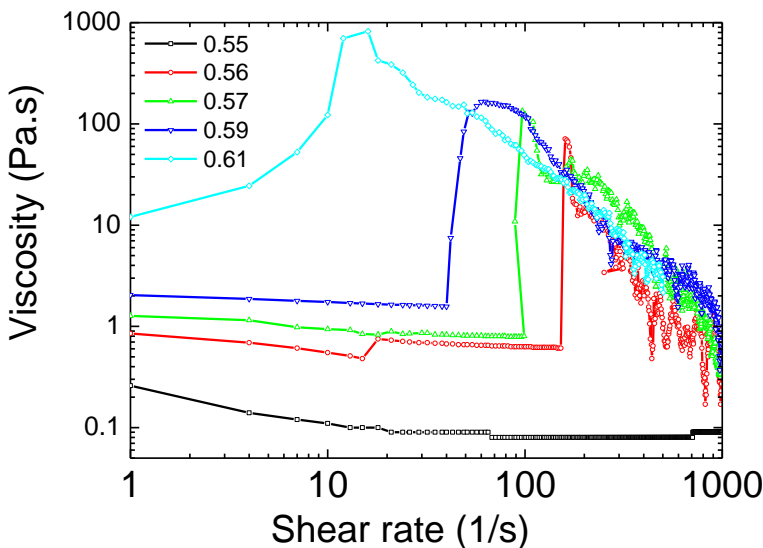


**Figure 7.11- Example viscosity versus shear rate rheometer profiles for various colloid volume fractions**

Once DST occurred, the material began to get thrown out radially or slide out from between the rheometer's plates. This explained why the shear stresses and viscosities began to decrease after their peaks; recorded shear stresses and viscosities decreased due to the fact that there was less material being sheared. At this point, granules and opaque material, very similar to that seen when the material dilated and jammed in the shear cells, were seen (Figure 7.12).



**Figure 7.12- Material ejected from rheometer during DST (left) and granules and opaque material seen (right)**

Another similarity to the shear cell experiments in [Chapter 4](#) and [Chapter 5](#) was that as volume fraction increased, the shear rate required for the onset of DST (or jamming) decreased (Figure 7.13). For example, when  $\Phi=0.61$ , DST was seen at a shear rate of  $\sim 6\text{s}^{-1}$ , while at  $\Phi=0.56$  a shear rate of  $\sim 150\text{s}^{-1}$  was necessary. The critical shear rate required for DST decreasing with increased volume fraction was expected [21, 25].

While the particular critical shear rates found using the rheometer differed from the critical shear rates found for jamming in the shear cell experiments in [Chapter 4](#) and [Chapter 5](#), they were similar in magnitude and showed a similar trend (Figure 7.13). Given that the rheometer was a different geometry and was a high-precision, expensive instrument, the shear cell results compared well. The shear rates reported for the rheometer were the maximum shear rates across the geometry (i.e. at the edge of the plate) whereas the shear rate reported for the shear cells was the average across the gap between the cylinders. This might help explain why the critical shear rates measured with the rheometer were higher.

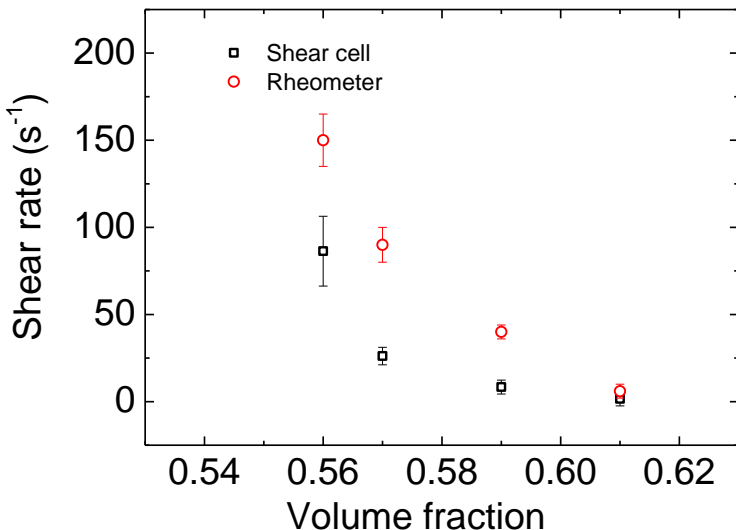


**Figure 7.13- Critical shear rate required for onset of DST for various volume fractions (for rheometer and shear cell). Error bars show standard deviation of repetitions.**

The shear stress required for the onset of DST decreased as volume fraction increased, as was similarly found in the shear cell experiments (Figure 7.14). Again, although values differed from the shear cell experiments, the magnitudes and trends were similar. While the shear stress required for DST decreased with increasing volume fraction, the shear stresses were still of a similar magnitude and could be viewed as approximately constant when considering the dramatic change in stress that occurred during DST [26, 27]. Critical shear stresses were all below  $100\text{N/m}^2$ , while during DST the shear stress increased to over  $10,000\text{N/m}^2$ . Literature contains conflicting results on the variation of the critical shear stress for the onset of DST with volume fraction. While the majority of work agrees that the critical shear rate decreases with increased volume fraction, some work has found that the critical shear stress remains approximately constant with increasing volume fraction, while others have found that it decreases [21, 25, 28]. The critical shear stress is thought to be the minimum shear stress that exceeds all local stress barriers that are responsible for preventing relative shear between particles [28].

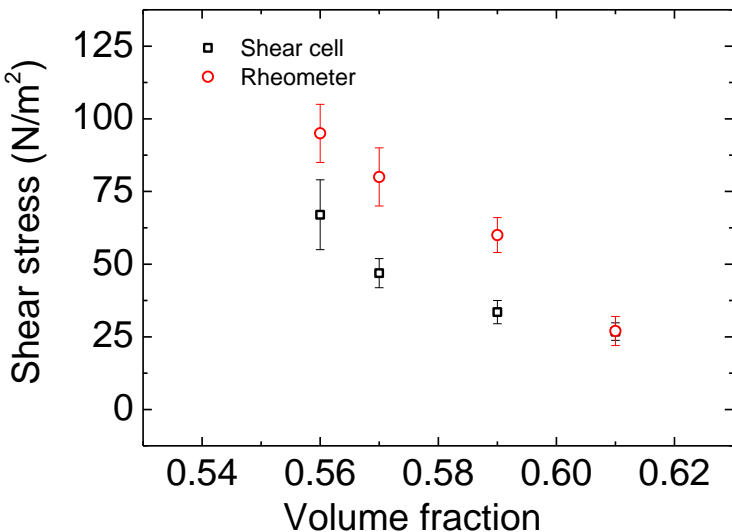


**Figure 7.14- Shear stress at onset of DST for various volume fractions (for rheometer and shear cell).** Error bars show standard deviation of repetitions.

A similar maximum peak in shear stress was found for all volume fractions that showed DST (Figure 7.10). This was typically  $10,000\text{-}13,000\text{N/m}^2$ . This suggested that the jammed material was similar for all volume fractions, in terms of how much stress it could be subjected to by the rheometer before fracturing and being thrown out. From literature (see [Chapter 2](#)), the weakest confining stress is thought to limit the maximum shear stress the material can withstand during DST [26, 28]. The weakest confining stress is typically the confining capillary stress (at the edge of the sample in the case of the parallel plate rheometer). As detailed in [Chapter 2](#), for a dilating material with particles protruding from the interface, this confining stress can be defined as the surface tension divided by the particle diameter [21, 28]. For the  $\sim 500\text{nm}$  radius particles used in the experiments and using the surface tension of the decalin and tetralin solvents (32 mN/m for the solvent mixture based on relative volumes [29]), this confining capillary stress was estimated to be in the region of  $30,000\text{ N/m}^2$  which was a similar magnitude to that found using the rheometer. This suggested that frustrated dilation at the suspension-air interface was indeed a fundamental part of the jamming mechanism in the shear cells used in [Chapter 4](#) and [Chapter 5](#), as detailed in 5.3.9.

When DST occurred, large normal stress fluctuations were measured (Figure 7.15). These were found to correlate with changes in the shear stress (Figure 7.16). These

stress fluctuations and normal and shear stress couplings have been shown to accompany DST in literature, with direct proportionality often being evident [26, 28, 30-32]. For particles to shear past each other, dilation is necessary and this causes fluctuations in the normal stress [28]. The fluctuating stresses were possibly related to the fluctuating forces measured with the force sensor technique in [Chapter 5](#). This, however, is not clear since with the rheometer, fluctuating stresses were measured as the shear rate was increased while with the shear cell, these fluctuations were found to occur over time at a constant stress.

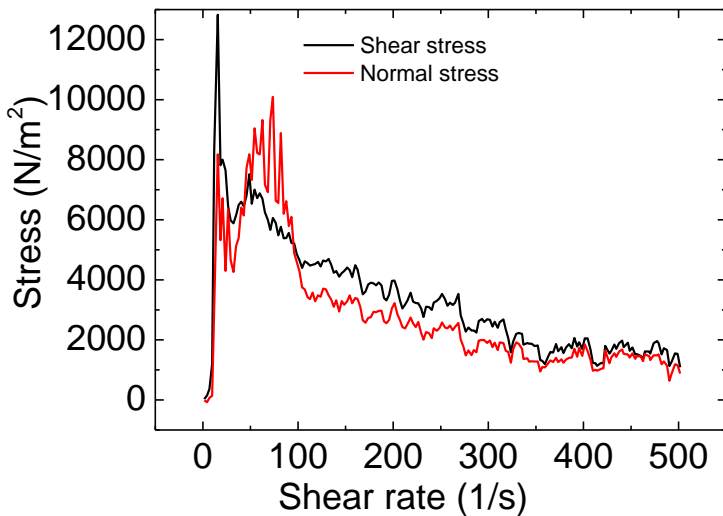


Figure 7.15- Example fluctuating normal and shear stresses during DST ( $\Phi=0.61$  sample)

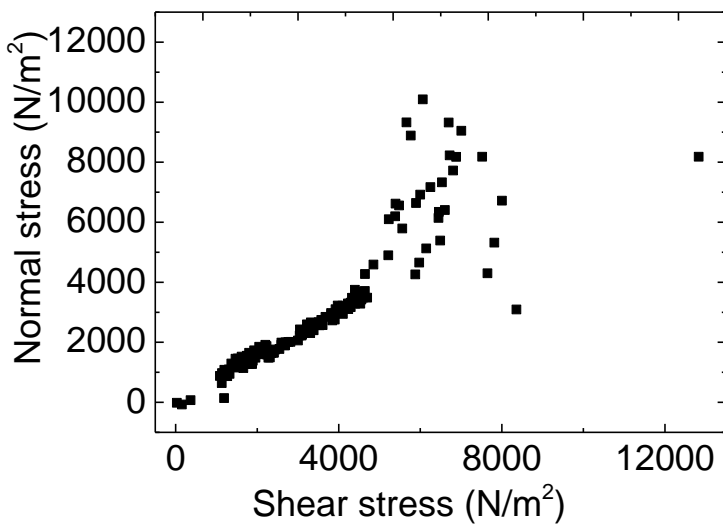
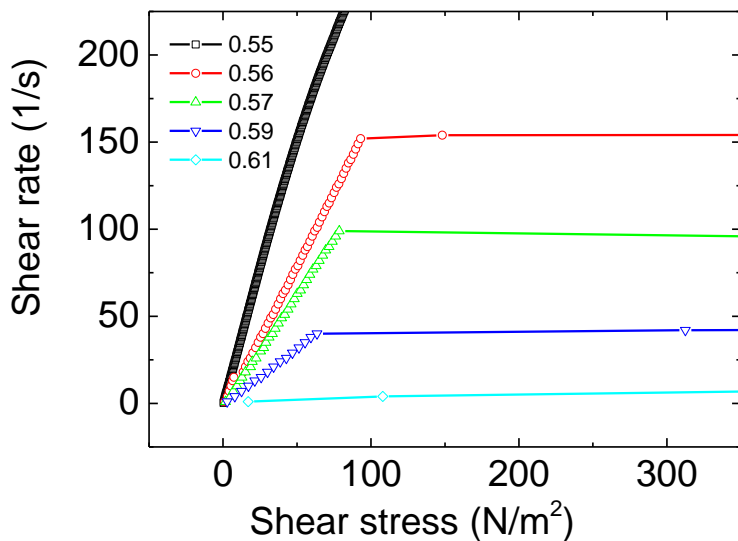


Figure 7.16- Example coupling of shear and normal stresses for sample undergoing DST ( $\Phi=0.61$ )

To further compare the performance of the commercial rheometer and shear cells used in [Chapter 4](#) and [Chapter 5](#), Figure 7.10 was replotted to show the same axes as the flow profiles that were produced in 4.3.1.2. The plots (Figure 7.17) showed similar trends; beyond a particular stress, increasing the shear stress further did not result in the material flowing more quickly (i.e. an increased shear rate). These results again suggested that the results obtained using the shear cells matched well with the results from the commercial rheometer. Considering the economic comparison of the shear cells and the commercial rheometer, the shear cells could be used to provide cheap and simple rheometry estimates in a lab where an expensive rheometer is not available. This is discussed in more detail in 7.3.3.3.



**Figure 7.17-** Example shear rate versus shear stress flow profiles from rheometer for various volume fractions. See Figure 4.8 for comparison.

### 7.3.3.2 Rheology of Concentrated Cornflour-Water Suspensions

The rheometry measurements for concentrated cornflour-water suspensions showed similar trends to the shear cell colloidal suspension experiments and the pipe cornflour-water experiments in [Chapter 8](#). Discontinuous shear thickening was only seen at mass fractions of 0.5 and above across the shear rates investigated. This was in agreement with the pipe flow experiments in [Chapter 8](#), where evidence of strong shear thickening and jamming was only seen at mass fractions  $\geq 0.5$ . This suggested that the means of detecting jamming used in [Chapter 8](#) was reasonable and that jamming is not very dependent on geometry but mostly depends on sample concentration. As with the concentrated colloidal suspensions, with the rheometer measurements, DST was seen as a significant jump in the shear stress (and therefore viscosity) with increasing shear rate (Figure 7.18 and Figure 7.19). The idea of a critical mass/volume fraction was in agreement with what was found for the concentrated colloidal suspensions, suggesting a similarity between the colloidal and granular systems under shear.

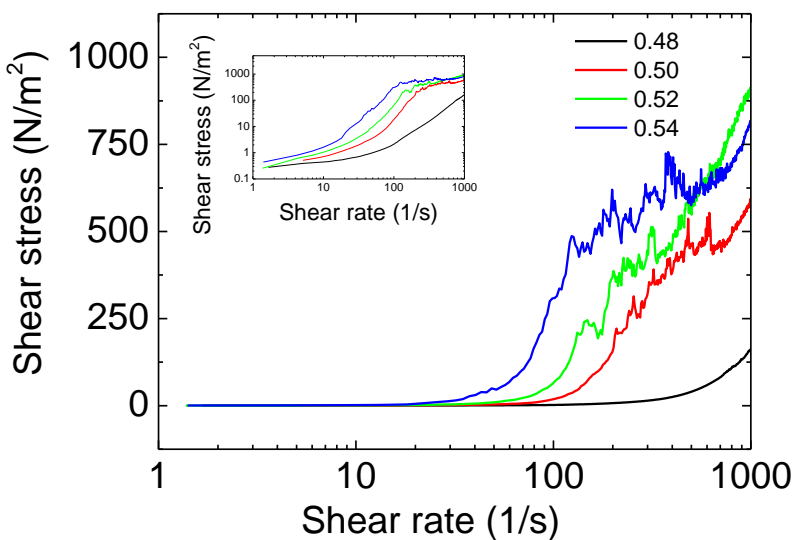
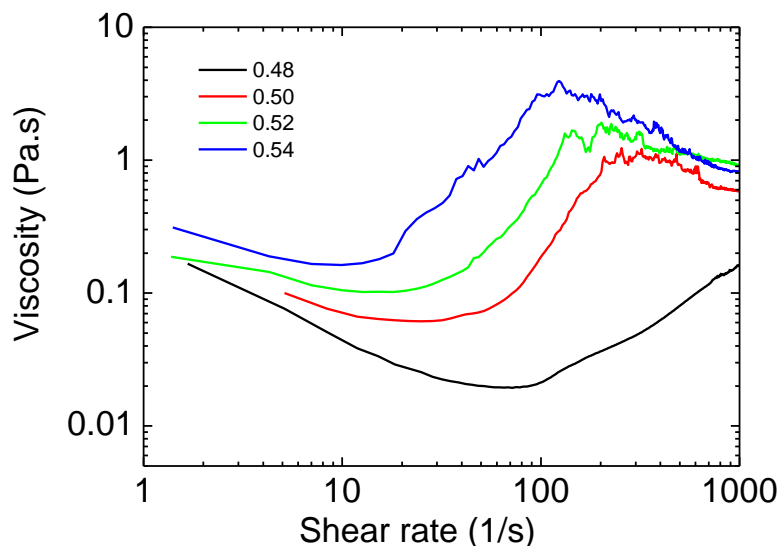


Figure 7.18- Example shear stress versus shear rate rheometer profiles for various cornflour mass fractions. Inset shows data on log-log plot.



**Figure 7.19- Example viscosity versus shear rate rheometer profiles for various cornflour mass fractions**

At mass fractions  $>0.54$  very erratic profiles were seen, with very large stress fluctuations. Here the maximum stress and torque that could be applied by the rheometer was reached- the material was in such a viscous, jammed state that the rheometer was unable to handle it. Under these conditions, the ejection of jammed cornflour granules from the gap occurred as shown in Figure 7.20. These appeared drier than the bulk sample.



**Figure 7.20- Material ejected from rheometer during DST at mass fractions  $>0.54$ , showing granules**

From Figure 7.19, it can be seen that shear thinning occurred at lower shear rates, particularly with lower mass fraction suspensions. This was expected from literature and is thought to be due to particles aligning into planes that can slide over each other [26, 27, 33].

The DST observed during the continuous shear of cornflour suspensions did, however, differ from that observed with the concentrated colloidal suspensions. From Figure 7.18, the shear stresses did not decrease significantly after the DST peaks, as occurred with the colloidal suspensions, as shown in Figure 7.10. This was because with the cornflour suspensions at lower mass fractions, the samples were not ejected from the gap and no granules were seen, as had been the case with the colloids. As mentioned, it was only at mass fractions  $>0.54$  that the ejection of jammed cornflour granules occurred.

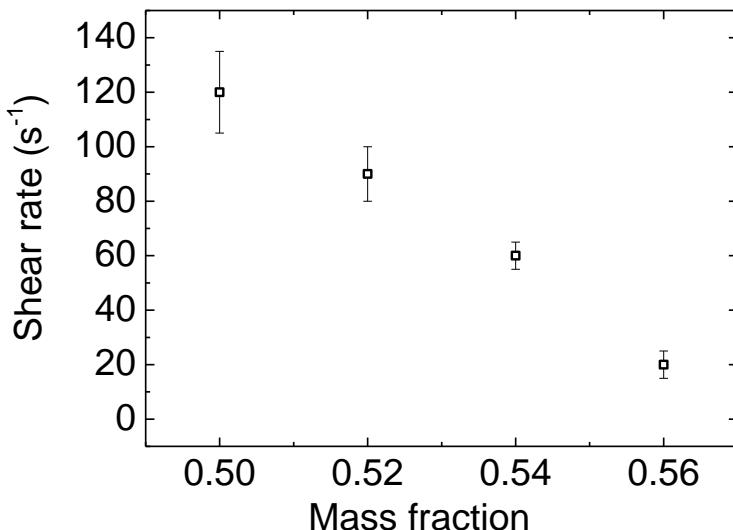


**Figure 7.21- Critical shear rate required for onset of DST for various cornflour mass fractions.**  
Error bars show standard deviation of repetitions.

As mass fraction was increased, the shear rate required for the onset of DST decreased (Figure 7.21). This was similar to what was found for the colloid experiments. The shear stress at the onset of DST appeared ~constant for all mass fractions, in agreement with literature [27, 28, 33].

A similar magnitude in shear stress at the end of the DST regime was found for all mass fractions that showed DST (Figure 7.18). This was typically  $700\text{-}1000\text{ N/m}^2$ . This suggested that the jammed material was similar for all mass fractions, in terms

of how much stress it could be subjected to. As mentioned for the colloids in 7.3.3.1, the weakest confining stress is thought to limit the maximum shear stress the material can withstand during DST, and this is typically the confining capillary stress [26, 28]. As detailed in [Chapter 2](#), for a dilating material with particles protruding from the interface, this confining stress can be defined as the surface tension divided by the particle diameter [21, 28]. Accounting for the surface tension of water (72.8 mN/m) and the average particle size of the cornflour used (16  $\mu\text{m}$  diameter measured using microscope), this confining capillary stress was estimated to be in the region of 4000 N/m<sup>2</sup>. This was of a similar magnitude to the maximum stress measured using the rheometer.

The theoretical capillary stress of cornflour-water suspensions relative to the concentrated colloidal suspensions therefore scaled well with the ratio of the maximum stresses obtained experimentally. The theoretical capillary stress of the cornflour suspensions was approximately 15% of that for the colloidal suspensions (4000 N/m<sup>2</sup> compared to 30,000 N/m<sup>2</sup>). The experimental maximum stress of the cornflour suspensions was approximately 10% of that for the colloidal suspensions (700-1000 N/m<sup>2</sup> compared to 10,000-13,000 N/m<sup>2</sup>).

As with the colloidal suspensions, when DST occurred, large normal stress fluctuations were measured (Figure 7.22). These were found to correlate with fluctuations in the shear stress. These stress fluctuations and normal and shear stress couplings have been shown to accompany DST in literature [26, 28, 30-32].

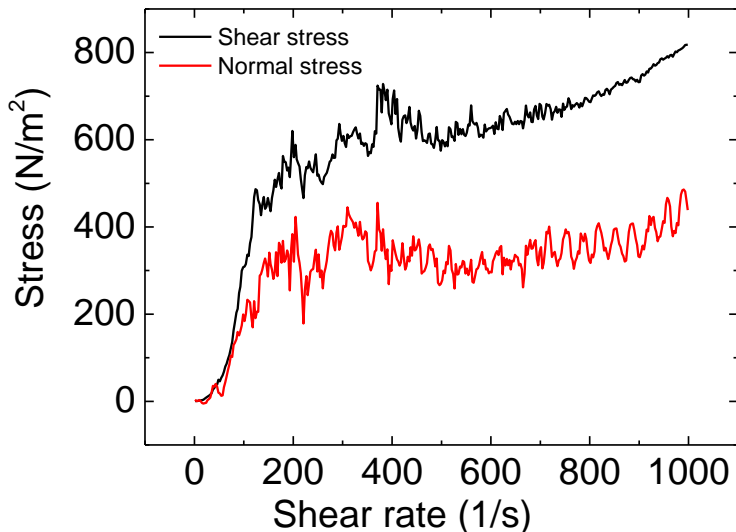


Figure 7.22- Example fluctuating normal and shear stresses during DST (0.54 cornflour mass fraction)

Overall, the strong similarities between the cornflour-water suspension and colloidal suspension rheometry results suggested strong links between the behaviour of colloidal and granular systems under shear. This agrees with the findings of [Chapter 6](#) and [Chapter 8](#).

### 7.3.3.3 Use of Rotating Cylinder Shear Cell as a Relative Rheometer

As detailed in 7.3.3.1, the results obtained from the commercial rheometer showed similar trends to the results obtained using the rotating cylinder shear cell geometries in [Chapter 4](#) and [Chapter 5](#). The use of the shear cells as basic rheometers was therefore investigated further. For this, systems with well-known properties, such as water-glycerol mixtures, were analysed.

The use of the shear cell as a relative rheometer was investigated. This gave a viscosity as that relative to another substance's viscosity, as detailed below.

The relative viscosities of various mixtures were estimated as follows:

$$\eta = \frac{\tau}{\dot{\gamma}} \quad \text{Equation 7.25}$$

Assuming a fixed shear stress/voltage (as detailed in 4.2.1.1)

$$\eta \propto \frac{1}{\dot{\gamma}} \quad \text{Equation 7.26}$$

Relative viscosity is defined as:  $\eta_r = \frac{\eta_{mixture}}{\eta_{solvent}}$  Equation 7.27

Therefore:

$$\eta_r = \frac{\left(\frac{1}{\dot{\gamma}}\right)_{mixture}}{\left(\frac{1}{\dot{\gamma}}\right)_{solvent}} = \frac{\dot{\gamma}_{solvent}}{\dot{\gamma}_{mixture}} \quad \text{Equation 7.28}$$

Here the mixture would be, for example, a mixture of water and glycerol, and the solvent would be water.

Since the average shear rate across the gap was directly proportional to the rotational rate (RPM) of the rotating cylinder, the relative viscosity could be written as:

$$\eta_r = \frac{\left(\frac{1}{RPM}\right)_{mixture}}{\left(\frac{1}{RPM}\right)_{solvent}} = \frac{RPM_{solvent}}{RPM_{mixture}} \quad \text{Equation 7.29}$$

Therefore estimations of the relative viscosity simply involved measuring the rotational rate of the inner cylinder for the two samples at a fixed voltage and comparing these.

If the shear cell shear stress/voltage calibrations detailed in 4.2.1.1 were used, the actual viscosity could also be deduced.

For these tests, known masses of water and glycerol were mixed to produce mixtures of varying percentage by weight glycerol (20, 40, 60 and 80% w/w). Samples were placed in the shear cells (5mm gap rotating inner cylinder shear cell with 9mm fill height) and subjected to steady shear at a fixed voltage/ shear stress. The RPM of the rotating inner cylinder was measured using a tachometer. This was compared to that obtained with just water in the shear cell at the same voltage. This allowed the relative viscosity to be estimated. The viscosities of water-glycerol mixtures are well reported in literature so the relative viscosities estimated via the experiments were compared to these. The viscosities of the mixtures were also obtained using the rheometer (fixed at 20°C).

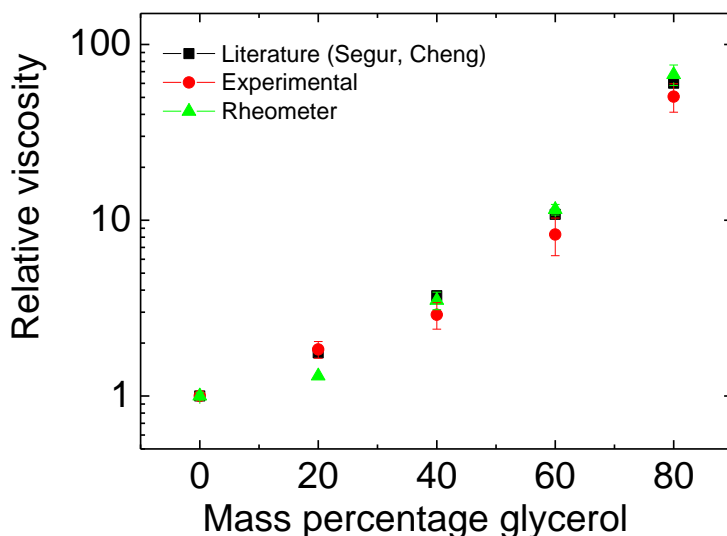


**Figure 7.23- Relative viscosity of water-glycerol mixtures: comparison between experimental work and literature. Error bars show standard deviation of repetitions.**

As shown in Figure 7.23, the experimentally deduced relative viscosities compared well to literature values (and rheometer values), particularly at the lower mass percentages [34, 35].

Overall, the rheometry work done in this section suggested robustness of the more novel work contained in other chapters of this thesis and highlighted the effectiveness of the shear cells used in this work.

## 7.4 Light Scattering to Detect Ordering

Light scattering was performed to find out whether particle ordering was occurring during the shearing of the colloidal suspensions that were used experimentally in [Chapter 4](#) and [Chapter 5](#).

### 7.4.1 Colloidal Ordering Under Shear: Background

Literature suggests the possibility that concentrated suspensions may order under shear. Studies have shown that concentrated samples ordered under flow when samples were monodisperse [36-41]. This ordering has not been found to occur in polydisperse systems [39].

To find out whether ordering was occurring during the shearing of the colloidal suspensions that were used experimentally in [Chapter 4](#) and [Chapter 5](#), light scattering was performed to see if any signs of ordering were present. Diffraction patterns obtained from shining a collimated beam of light through a sample can be used to detect ordering in samples under shear [37]. This technique was used to investigate ordering in the experiments performed in [Chapter 4](#) and [Chapter 5](#).

#### Speckle Patterns and Bragg Peaks

When light is passed through a sample, scattered light produces a speckle pattern (Figure 7.24). If the particles that are causing the scattering are stationary, the speckle pattern remains constant. If the particles that are causing the scattering are moving, the speckle pattern will constantly fluctuate due to the changing phases of the scattered light [5]. Dark regions are produced when waves of scattered light from different particles interfere destructively. Bright regions are produced when the waves interfere constructively [5].

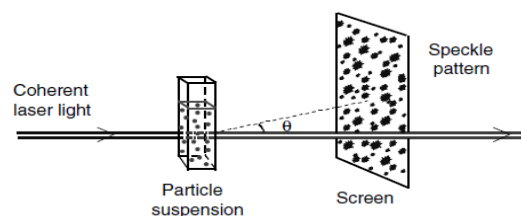
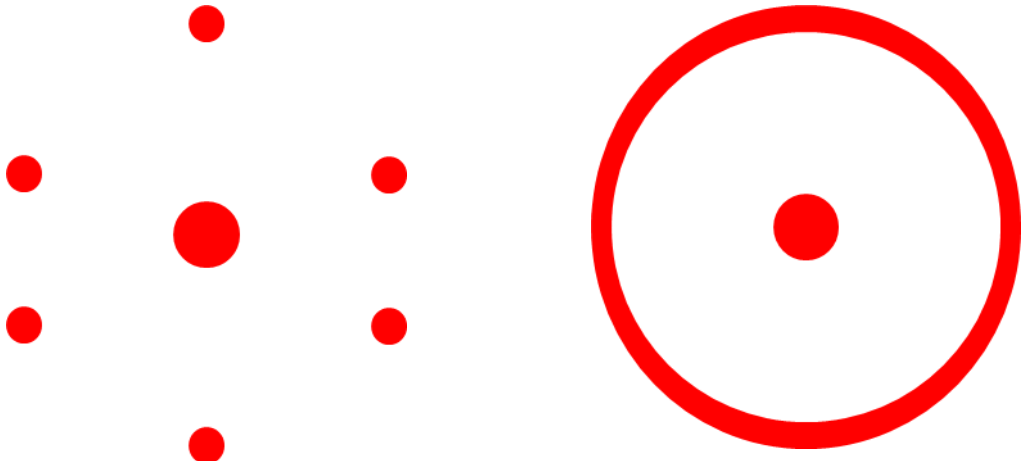


Figure 7.24- Speckle pattern [5]

If the light is passed through a single crystal domain (suggesting the material has ordered), a pattern of bright spots would be expected to emerge (Figure 7.25).

Several spots that share the same distance from the centre form a group and the exact nature of these spots (position etc.) depends on the crystal structure [42]. If the light is diffracted off multiple crystal domains with different orientations of the crystal planes, and a sufficient number of crystal domains are present, the multiple bright spots may form a ring (Figure 7.26) [42].



**Figure 7.25- Diffraction spots/ Bragg peaks for hexagonal crystal**

**Figure 7.26- Diffraction ring**

The theory behind this diffraction phenomenon comes from Bragg's law. This describes how the angle between the incident and scattered light depends on the spacing of the crystal structure and wavelength of incident light [7].

Bragg's law is:

$$2dsin\theta = n\lambda \quad \text{Equation 7.30}$$

Here d is the lattice spacing between crystal planes,  $\theta$  is the angle between incident and scattered light, n is an integer and  $\lambda$  is the wavelength of light.

The bright spots mentioned above are often referred to as Bragg peaks or Bragg spots.

In the experiments, if the colloidal suspensions ordered under shear, they would have a crystal-like structure and so the emergence of Bragg peaks or rings would be expected [43, 44].

### 7.4.2 Experimental Procedures

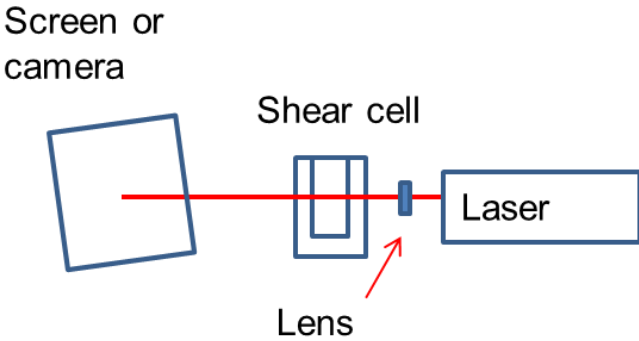


Figure 7.27- Set-up to detect colloid ordering

A laser (Thorlabs 17mW 633nm) was focussed to 0.1mm and passed through the centre of a shear cell similar to that used in [Chapter 4](#) and [Chapter 5](#). The light leaving the cell was imaged onto a screen or CCD camera (Starlight Express SXVR-H9).

Colloidal suspensions with volume fractions similar to those used in [Chapter 4](#) and [Chapter 5](#) were sheared at the maximum shear stress/voltage ( $72 \text{ N/m}^2 / 10.8\text{V}$ ). After set time intervals (after 30s, 1min, 2min, 5min), the motor was stopped and the diffraction patterns were observed either on a screen or using the camera. This allowed signs of ordering to be investigated.

### 7.4.3 Results and Discussion

In the experiments, no clear signs of ordering (Bragg peaks or rings) were seen for any of the conditions studied. Since these are strong indicators of colloid crystallisation and ordering, it could therefore be said that it was unlikely that significant ordering was occurring in the experiments.

There were, however, differences between images taken before and images taken after the samples were sheared, and these changes were notable within 30s of the shear being applied. When shear had been applied, a number of bright lines or a brighter region was seen emanating from the laser beam that passed through the sample (Figure 7.29). These were not seen prior to the material being sheared (Figure 7.28). The causes of these lines were unclear, but it was possible that some form of structural rearrangement of the particles, such as layering, was caused by the shear, as outlined below [45]. Due to the lack of Bragg peaks and diffraction rings, this structural change was, however, unlikely to be due to the colloid particles strongly ordering. The black spot seen in the screen images (Figure 7.28 and Figure 7.29) was due to a hole placed in the screen to allow the undiffracted laser beam to pass through.

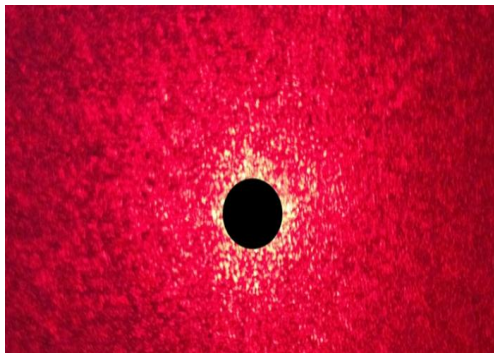


Figure 7.28- Example scattering pattern projected onto screen for unsheared  $\Phi=0.56$  sample after 1 minute

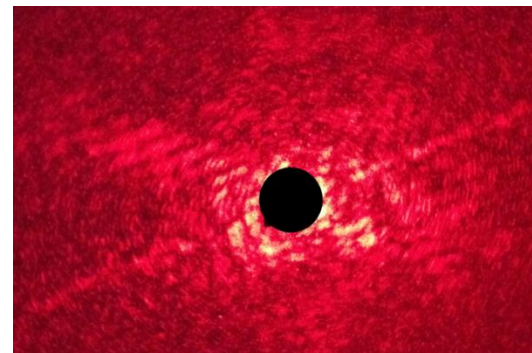
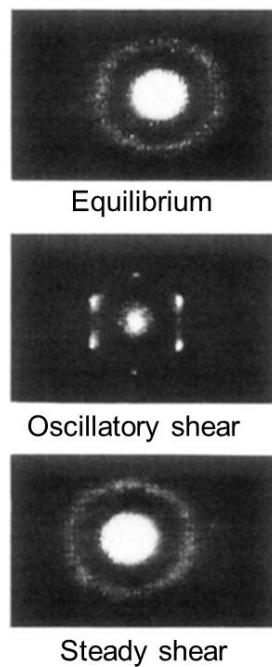


Figure 7.29- Example scattering pattern projected onto screen for sheared  $\Phi=0.56$  sample after 1 minute. Shear rate  $\sim 80\text{s}^{-1}$ .



**Figure 7.30-** Images seen for  $\Phi=0.48$   $1\mu\text{m}$  diameter PMMA particles (index matched as done in this thesis) at equilibrium, undergoing oscillatory shear and undergoing steady shear. Evidence of ordering is only found under oscillatory shear [45].

The orientation of the lines in Figure 7.29 appear to perhaps lie in the directions of where Bragg spots would be detected if the sample fully crystallised, as seen in the central image of Figure 7.30. The lines seen in Figure 7.29 may therefore be a ‘weak’ version of the Bragg spots seen in Figure 7.30. Layering of the particles may have occurred and there may have been weak orientation within the layers, causing the lines. The fact that strong ordering did not occur under steady shear was in agreement with literature [45].

The main volume fraction investigated was  $\Phi=0.56$ . Due to difficulties index matching the particles in the solvent perfectly, in more concentrated suspensions there was a notable amount of multiple scattering within the sample, making the images on the screen/camera less clear. Lower volume fractions were also investigated ( $\Phi=0.52$  and  $\Phi=0.55$ ), since colloid crystallisation under shear has been shown to occur in this range of volume fractions [21, 37, 43, 44]. Similar results were found for all volume fractions studied.

## 7.5 Conclusions

By using commercial instruments, a greater understanding of the behaviour of the colloidal suspensions used in [Chapter 4](#) and [Chapter 5](#) and the cornflour suspensions used in [Chapter 8](#) was established. The rheometry work in particular highlighted how effective the shear cells used in [Chapter 4](#) and [Chapter 5](#) were for estimating properties of the materials.

Dynamic light scattering confirmed particle sizes and showed that the colloids used were highly monodisperse. DLS showed that colloidal suspensions at the volume fractions that showed jamming behaviour in [Chapter 4](#) and [Chapter 5](#) ( $\Phi \geq 0.56$ ) had significantly slower dynamics than those that did not show jamming behaviour.

The rheometry work showed many trends that agreed with the work done with the concentrated colloidal suspensions in the shear cells in [Chapter 4](#) and [Chapter 5](#). For example, with the rheometer, DST was only seen at  $\Phi \geq 0.56$ , in agreement with the volume fractions where visible dilatancy and jamming peaks were observed using the shear cells. This suggested the means of detecting jamming in [Chapter 4](#) and [Chapter 5](#) (whether visual or with the force sensor technique) were reasonable and that DST and jamming were closely related. When DST occurred, granules and opaque material, very similar to that seen when the material dilated in the shear cells, were seen.

Another similarity to the shear cell experiment results was that as volume fraction increased, the shear rate required for the onset of DST decreased. These critical shear rates obtained from the rheometer were of a similar magnitude to those deduced for the onset of jamming using the shear cells.

The rheometry work on the cornflour suspensions showed similar trends to the work done in [Chapter 8](#), where the effects of pipe flow on concentrated cornflour suspensions were investigated. It was only at mass fractions  $\geq 0.5$  that discontinuous shear thickening was seen using the rheometer, in agreement with the mass fractions required for jamming with the pipe flow geometry in [Chapter 8](#). This suggested that the means of detecting jamming used in [Chapter 8](#) was reasonable. In agreement with the colloidal experiments, as mass/volume fraction increased, the shear rate required for the onset of DST decreased. This showed similarities between the behaviour of concentrated colloidal and granular materials under flow, agreeing with the findings of [Chapter 6](#) and [Chapter 8](#).

Light scattering suggested that the colloidal suspensions were not strongly ordering under shear, consistent with previous work in the literature.

Overall, this chapter resulted in a greater understanding of the behaviour of the materials used in the thesis and supported the work done in other chapters. The work suggested robustness of the more novel methods used, with strong links between the results from the novel equipment and commercial instruments being found. Consistency between the onset concentrations and shear rates for jamming effects in the range of different flow geometries indicates that jamming is not strongly dependent on flow geometry.

A	Area
b	Coefficient of the first cumulant
c	Coefficient of the second cumulant
CCD	Charge coupled device
D	Average diffusion coefficient
d	Lattice spacing between planes
DLS	Dynamic light scattering
E	Electric field of the scattered light
FWHM	Full width at half maximum height
$G_2(t)$	Intensity autocorrelation function
$g_2(t)$	Normalised intensity autocorrelation function
$g_1(t)$	Normalised electric field autocorrelation function
h	Sample gap height
I	Intensity
$k_B$	Boltzmann constant
n	Refractive index of the dispersion medium
n	Integer (Bragg's law)
N	Rotation rate (e.g. rotations per minute)
Pdl	Polydispersity index
q	Scattering vector
r	Radial position
R	Plate radius
$R_h$	Hydrodynamic radius
RPM	Rotations per minute
T	Absolute temperature
T	Torque
t	Time
v	Rotational velocity
X	Mass fraction
$\Phi$	Volume fraction
$\eta$	Viscosity
$\eta_r$	Relative viscosity
$\theta$	Angle between incident and scattered light
$\tau$	Delay time
$\tau$	Shear stress
$\lambda$	Wavelength of laser light
$\Gamma$	Decay rate
$\omega$	Rotational rate
$\dot{\gamma}$	Shear rate

1. van de Hulst, H.C., *Light Scattering by Small Particles*. 2nd ed. 1957, New York: Dover Publications.
2. Finsy, R., *Particle Sizing By Quasi-Elastic Light-Scattering*. Advances in Colloid and Interface Science, 1994. **52**: p. 79-143.
3. Hahn, D.W., *Light Scattering Theory*. 2009, Department of Mechanical and Aerospace Engineering: University of Florida.
4. Liou, K., *An Introduction to Atmospheric Radiation*. 2002: Academic Press.
5. Pusey, P., *Dynamic Light Scattering*, in *Neutron, X-rays and Light. Scattering Methods Applied to Soft Condensed Matter*, T.Z. P Lindner, Editor. 2002, Elsevier.
6. C. J. and G. D, *Laser Light Scattering*. 1995: Dover Publications Inc.
7. Wyn, B., *Dynamic Light Scattering- The Method and Some Applications*. 1993: Oxford University Press.
8. Provencher, S.W., *CONTIN - A General-Purpose Constrained Regularization Program For Inverting Noisy Linear Algebraic And Integral-Equations*. Computer Physics Communications, 1982. **27**(3): p. 229-242.
9. Malvern Instruments, *Measurement of Nano particles and Proteins*. 2014.
10. Malvern Instruments, *Dynamic Light Scattering Common Terms Defined*. 2011.
11. Liddle, S.M., T. Narayanan, and W.C.K. Poon, *Polydispersity effects in colloid-polymer mixtures*. Journal of Physics-Condensed Matter, 2011. **23**(19).
12. Pusey, P.N. and W. Vanmegen, *Observation Of A Glass-Transition In Suspensions Of Spherical Colloidal Particles*. Physical Review Letters, 1987. **59**(18): p. 2083-2086.
13. Friskin, B.J., *Revisiting the method of cumulants for the analysis of dynamic light-scattering data*. Applied Optics, 2001. **40**(24): p. 4087-4091.
14. Poon, W., *Colloidal Glasses*. 2004, Materials Research Society Bulletin.
15. Pusey, P.N., et al., *Colloidal Fluids, Crystals And Glasses*. Physica A, 1991. **176**(1): p. 16-27.
16. Vanmegen, W. and P.N. Pusey, *Dynamic Light-Scattering Study Of The Glass-Transition In A Colloidal Suspension*. Physical Review A, 1991. **43**(10): p. 5429-5441.
17. Barnes, H., *A Handbook of Elementary Rheology*. 2000: The University of Wales Institute for Non-Newtonian Fluid Mechanics.
18. Malvern, *School of Rheology- Rotational Rheometry*. 2012.
19. Schramm, G., *A Practical Approach to Rheology and Rheometry*. 2000: Thermo Haake Rheology.
20. Secco, R., *Fluid Viscosity Measurement*. 1999: The University of Western Ontario.
21. Mewis, J. and N. Wagner, *Colloidal Suspension Rheology*. 2012: Cambridge University Press.
22. Morrison, F., *Understanding Rheology*. 2001: OUP USA.
23. Chhabra, R. and J. Richardson, *Non-Newtonian Flow and Applied Rheology: Engineering Applications*. 2008, Butterworth-Heinemann.
24. Macosko, C., *Rheology: Principles, Measurements, and Applications*. 1994, Wiley.
25. O'Brien, V.T. and M.E. Mackay, *Stress components and shear thickening of concentrated hard sphere suspensions*. Langmuir, 2000. **16**(21): p. 7931-7938.
26. Brown, E. and H.M. Jaeger, *The role of dilation and confining stresses in shear thickening of dense suspensions*. Journal of Rheology, 2012. **56**(4): p. 875-923.

27. Fall, A., et al., *Shear thickening of cornstarch suspensions as a reentrant jamming transition*. Physical Review Letters, 2008. **100**(1).
28. Brown, E. and H. Jaeger, *Shear thickening in concentrated suspensions: phenomenology, mechanisms, and relations to jamming*. Reports on Progress in Physics, 2013. **77**(4): p. 046602.
29. Medicine, U.N.L.o. *PubChem Open Chemistry Database*. 2015; Available from: <http://pubchem.ncbi.nlm.nih.gov/>.
30. Hebraud, P. and D. Lootens, *Concentrated suspensions under flow: Shear-thickening and jamming*. Modern Physics Letters B, 2005. **19**(13-14): p. 613-624.
31. Lootens, D., et al., *Dilatant flow of concentrated suspensions of rough particles*. Physical Review Letters, 2005. **95**(26): p. 4.
32. Lootens, D., H. Van Damme, and P. Hebraud, *Giant stress fluctuations at the jamming transition*. Physical Review Letters, 2003. **90**(17).
33. Fall, A., et al., *Shear thickening of cornstarch suspensions*. Journal of Rheology, 2012. **56**(3): p. 575-591.
34. Segur, J.B. and H.E. Oberstar, *Viscosity Of Glycerol And Its Aqueous Solutions*. Industrial and Engineering Chemistry, 1951. **43**(9): p. 2117-2120.
35. Cheng, N.S., *Formula for the viscosity of a glycerol-water mixture*. Industrial & Engineering Chemistry Research, 2008. **47**(9): p. 3285-3288.
36. Campbell, C.S. and C.E. Brennen, *Computer-Simulation Of Granular Shear Flows*. Journal of Fluid Mechanics, 1985. **151**(FEB): p. 167-188.
37. Hoffman, R.L., *Discontinuous And Dilatant Viscosity Behavior In Concentrated Suspensions .1. Observation Of A Flow Instability*. Transactions of the Society of Rheology, 1972. **16**(1): p. 155-&.
38. Isa, L., et al., *Quantitative Imaging of Concentrated Suspensions Under Flow*. High Solid Dispersions, 2010. **236**: p. 163-202.
39. Sierou, A. and J.F. Brady, *Rheology and microstructure in concentrated noncolloidal suspensions*. Journal of Rheology, 2002. **46**(5): p. 1031-1056.
40. Solomon, T. and M.J. Solomon, *Stacking fault structure in shear-induced colloidal crystallization*. Journal of Chemical Physics, 2006. **124**(13).
41. Wu, Y.L., et al., *Melting and crystallization of colloidal hard-sphere suspensions under shear*. Proceedings of the National Academy of Sciences of the United States of America, 2009. **106**(26): p. 10564-10569.
42. Liu, X., *Bragg Diffraction from 2-D Nanoparticle Arrays*. 2010: University of Illinois.
43. Haw, M.D., W.C.K. Poon, and P.N. Pusey, *Direct observation of oscillatory-shear-induced order in colloidal suspensions*. Physical Review E, 1998. **57**(6): p. 6859-6864.
44. Haw, M.D., et al., *Colloidal glasses under shear strain*. Physical Review E, 1998. **58**(4): p. 4673-4682.
45. Ackerson, B.J. and P.N. Pusey, *Shear-Induced Order In Suspensions Of Hard-Spheres*. Physical Review Letters, 1988. **61**(8): p. 1033-1036.

# 8. Pipe Flow Investigation of Concentrated Suspensions

## This section will cover:

- The experimental procedures for setting up a pipe flow geometry.
  - The experimental procedures for preparing concentrated cornflour-water suspensions.
  - The experimental procedures for investigating the effects of pipe flow on concentrated suspensions.
  - The results obtained from investigating the effects of pipe flow on concentrated suspensions.



## 8.1 Summary

Due to the ubiquitous nature of pipe flow in industry, it was decided to investigate the effects of pipe flow on concentrated suspensions. Due to the large volumes of suspension required for the pipe geometries, it was not economically possible to do the experiments with the concentrated colloidal suspensions used in [Chapter 4](#) and [Chapter 5](#). It was therefore decided to use cornflour-water suspensions since they are cheap and simple to make. Despite the suspensions consisting of simple ingredients, literature has shown that they can provide interesting results and show complex rheological behaviour. It also provided the opportunity to investigate the effects of discontinuous shear thickening and jamming in a more granular material to see if there were similarities with the colloidal suspensions used in [Chapter 4](#) and [Chapter 5](#). Exploring links between colloidal and granular media under flow is an area of interest in recent literature [1-3].

The set-up involved pumping concentrated cornflour-water suspensions through cylindrical pipes, as outlined in [Chapter 3](#). Parameters such as the maximum force that could be applied to the fluid (i.e. the maximum shear stress) and shear rate (through controlling the suspension's volumetric flow rate) could be adjusted. If the force applied to the fluid became insufficient to maintain the desired shear rate, the pump stalled. Stalling therefore indicated a large increase in fluid viscosity, and so was taken as indicative of jamming occurring in the suspension.

The effects of parameters such as shear stress, shear rate, pipe diameter and pipe length were investigated. Since the results in [Chapter 5](#) suggested that confinement was important, the effects of using different pipe materials, with different stiffnesses and rigidities, were investigated.

Main findings included that jamming was only found to occur above a particular mass/volume fraction, and jamming occurred more frequently when smaller pipe diameters were used, in agreement with the work in [Chapter 5](#) that suggested that jamming was more frequent when smaller gap sizes were used. The effect of confinement was also significant. Jamming occurred less frequently when less stiff piping was used. This was in agreement with the work in [Chapter 5](#), where the use of soft walls resulted in significantly fewer jams.

Overall, this work showed similar trends to the work done with the rotating cylinder shear cell geometries used in [Chapter 4](#) and [Chapter 5](#), suggesting that the findings

were not particular to the specific flow geometry. It also showed that there are strong similarities in the behaviour of concentrated colloidal suspensions and concentrated granular suspensions under flow, as was seen in [Chapter 7](#) where a rheometer was used to investigate the effects of flow on the granular and colloidal materials that were used in this thesis.

## 8.2 Cornflour Background

For the pipe flow geometry, the behaviour of non-Brownian mixtures of granular cornflour and water was investigated [4]. Cornflour and water mixtures are perhaps the most commonly known examples of shear thickening fluids [1]. They are often referred to as ‘oobleck’ after a sticky substance called ‘oobleck’ that featured in Dr. Seuss’s book ‘Bartholomew and the Oobleck’ [5]. They have been investigated extensively in literature and key benefits of these mixtures are that they are very cheap and simple to prepare [1, 4, 6-10].

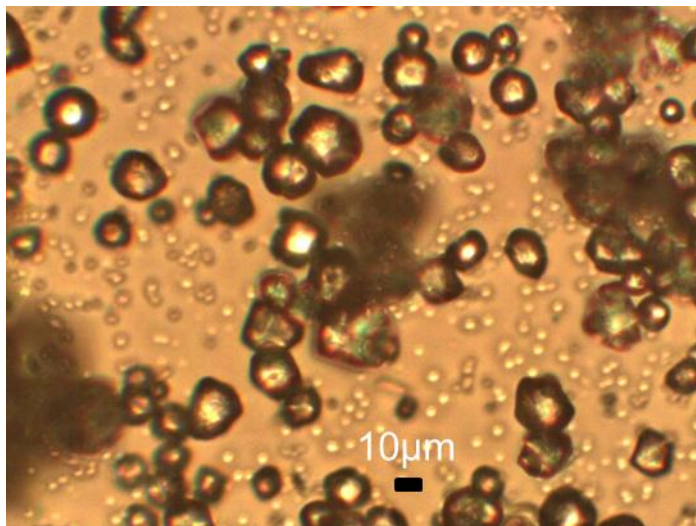


Figure 8.1- Cornflour used in experiments (40x magnification)

Cornflour (or cornstarch) is the starch of the corn (maize) grain and is obtained from the endosperm of the corn kernel. Its primary use is as a thickening agent in food preparation, particularly liquid-based foods such as soups, sauces and custards. As the cornflour is heated, molecular starch chains unravel, allowing them to entangle with other starch chains. This results in a mesh-like formation, thickening the liquid (starch gelatinisation). Cornflour is sometimes used preferentially over flour because it forms a translucent mixture, rather than an opaque one.

Cornflour particles are polydisperse, typically 10-20 $\mu\text{m}$  in diameter, and complexities can arise since they are deformable and can take in water causing them to swell (they are very hydrophilic) [6]. The cornflour used in the experiments (Sigma Aldrich Starch from Corn) was 27% amylose and 73% amylopectin by weight and was unrefined (Figure 8.1). Microscopy suggested the average particle size (diameter) was ~16 microns.

As mentioned, cornflour suspensions have been investigated extensively in literature. Samples are cheap and simple to prepare and as mentioned in [Chapter 2](#), cornflour particles are also in the optimal size region for showing signs of discontinuous shear thickening and jamming behaviour. This is where the largest stress range for the shear thickening regime can be found and the shear stress required for shear thickening is at its minimum [1]. Cornflour suspensions are interesting to study as they can show a wide range of rheological behaviour, including shear thinning behaviour at lower shear rates and concentrations and discontinuous shear thickening behaviour at higher shear rates and concentrations [11].

Literature suggests that the shear thickening of cornflour suspensions can be viewed as a ‘re-entrant jamming transition’ [8, 11, 12]. As a function of applied stress, the suspension is first in a solid-like jammed state due to it having a small yield stress. Once the yield stress is exceeded, the material becomes liquid-like. At even higher shear rates, the material becomes solid-like again as it strongly shear thickens [6]. These transitions are thought to be due to a shear banding mechanism. At low shear rates, shear localisation occurs and this flowing band grows with increasing shear rate, liquefying the material. Shear thickening is thought to occur at the end of the localisation regime, where all the material must flow. It is at this point that the material becomes solid-like.

Cornflour suspensions also highlight the important roles particle interactions and deformability can play in shear thickening. Cornflour is hydrophilic and shear thickens in water but does not shear thicken in a hydrophobic substance [13]. If the particles are heated, they soften and become deformable and will not show shear thickening [14].

### Sedimentation

It is worth noting that attempts were made to use cornflour-water suspensions in the rotating cylinder shear cell geometry in [Chapter 4](#). Due to cornflour’s large particle size and density difference with water, sedimentation occurred significantly during the time scale of the experiments. Literature suggests that it is possible to density match cornflour with Caesium Chloride solutions, however, this was decided against due to the possible impact of Caesium Chloride on the overall suspension behaviour. It has been shown to induce charges on the particles [6, 8].

Theoretical sedimentation times were calculated to confirm the greater extent of sedimentation with cornflour-water suspensions. The terminal velocity of the particles was deduced from:

$$v_{terminal} = \frac{2r^2\Delta\rho g}{9\eta} \quad \text{Equation 8.1}$$

Here  $r$  is the particle radius,  $\Delta\rho$  is the density difference between the particles and liquid,  $g$  is the acceleration due to gravity and  $\eta$  is the liquid's viscosity.

As mentioned in [Chapter 1](#), this is valid for a single particle that is experiencing no effects from other particles. The terminal velocity for a particle in a concentrated suspension will be much lower.

Calculating the terminal velocity allowed the time for a free particle in a dilute suspension at the top of the shear cell to sediment to the bottom to be deduced. For cornflour-water suspensions, this was determined to be 1.5min. This used an average particle diameter of 16 $\mu\text{m}$ , a water viscosity of 0.001 Pa.s, a cornflour density of 1570 kg/m<sup>3</sup> and a water density of 998 kg/m<sup>3</sup>.

For the colloidal suspensions used in [Chapter 4](#) and [Chapter 5](#), this sedimentation time was 2100min (0.5 $\mu\text{m}$  radius, a solvent viscosity of 0.002 Pa.s, a PMMA density of 1180 kg/m<sup>3</sup> and a solvent density of 920 kg/m<sup>3</sup>). This matched well with what was seen experimentally and confirmed that cornflour suspensions were not suitable to be used over the time scale of the rotating cylinder shear cell experiments, while the concentrated colloidal suspensions were.

Sedimentation should not have been an issue with the pipe flow geometry as the residence time of the suspension in the pipe was always notably shorter than the sedimentation time. The suspension's velocity through the pipe was also much greater than its terminal velocity.

## 8.3 Experimental Procedures

It is worth noting that the experiments that were performed were limited to the different piping that was commercially available. Obtaining the same type of pipe but with a slight difference, for example different wall thickness, was challenging. This restricted the experiments that could be performed, however, trends worth mentioning were still identified despite the limited experiments.

### 8.3.1 Materials and Apparatus

#### 8.3.1.1 Shear Cell Set-up

A syringe pump (Cole Parmer 74905-54) was used to control the flow of concentrated cornflour-water suspensions through lengths of piping (Figure 8.2). The cornflour suspension was poured into the barrel of a 2ml syringe (BD Plastipak) and this was pumped through the piping. It was necessary to construct a tapered attachment to the syringe to provide a more gradual constriction. Without this, 'self-filtration' of the suspension occurred, with the cornflour forming solid compacted build-ups in the syringe barrel. This meant that liquid could filter through small spaces in the cornflour's packing, resulting in the downstream concentration being significantly lower [15]. With the tapered attachment in place, no such phase separation occurred and the flow exiting the barrel remained homogenous and consistent with that entering the barrel. This was checked by drying the product and performing a mass balance.

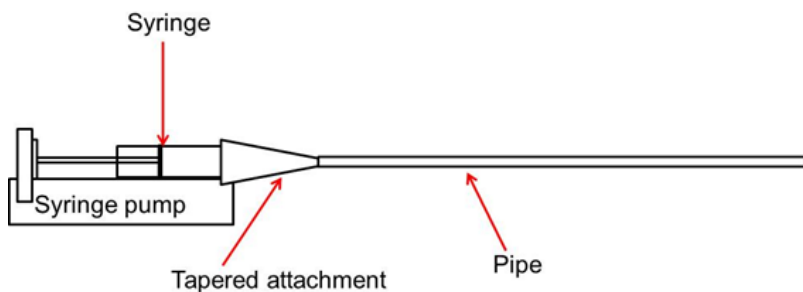


Figure 8.2- Pipe flow geometry set-up

The maximum force that could be applied by the syringe pump's bar and the bar's velocity could be adjusted (Table 8.1). The bar's velocity could be used to control the shear rate in the pipe since it controlled the volumetric flow rate of the suspension exiting the syringe barrel and entering the pipe. The maximum force that

could be applied by the bar controlled the maximum shear stress that could be applied to the fluid in order to achieve the desired flow rate. It is worth noting that only the maximum force that could be applied by the bar was known- what it was instantaneously operating at was not. During operation, the actual force applied by the bar could vary from zero up to the maximum. For the pump to run, the maximum force that could be applied by the bar and the desired flow rate (which controlled the bar's velocity) had to be set by the user.

### Jamming Indicator

If the maximum force applied by the bar was not sufficient to maintain the bar's speed at its desired level, the pump stalled. In other words, stalling occurred when the shear stress was insufficient to maintain the desired shear rate (and therefore flow rate). Stalling indicated a large increase in fluid viscosity, and so was taken as indicative of DST/jamming occurring in the suspension. Stalling therefore occurred when the maximum force applied by the syringe pump's bar was insufficient to overcome the 'temporary' force required to overcome the jam.

It was checked that no stalling occurred when the cornflour suspension was simply pumped through the syringe and its tapered attachment with no pipe present. This meant that if stalls occurred with the pipe present, the stalling was caused by flow through the pipe. When stalling occurred, the syringe pump was reset and restarted, allowing flow to continue until the next stall. The temporary reduction in stress was thought to cause the material to unjam.

**Table 8.1- Syringe pump details**

<b>Maximum linear force of bar [N] (100%)</b>	330
<b>Maximum bar speed [mm/s]</b>	3.2

Knowing the diameter of the syringe plunger (12mm for the syringe that was used in the experiments) allowed the equivalent pressure being applied by the syringe to be estimated for different maximum force applied by the bar settings (Table 8.2).

**Table 8.2- Forces and applied pressures**

Maximum linear force of bar [N]	Equivalent applied pressure [bar]
17 (5%)	1.5
34 (10%)	3.0
50 (15%)	4.4
67 (20%)	5.9
84 (25%)	7.4
340 (100%)	30

If the syringe bar was set to operate at 5% of its maximum force, the applied force to the suspension could vary from 0 to 17N throughout an experiment. If the syringe bar was set to operate at 10% of its maximum force, the applied force to the suspension could vary from 0 to 34N throughout an experiment.

### **8.3.1.2 Concentrated Cornflour-Water Suspension Preparation**

The masses of water and cornflour necessary to make a desired mass fraction of a cornflour-water suspension were deduced. These were then added and vorticed until homogeneous. It was assumed  $\rho_{\text{cornflour}}=1.57\text{g/cm}^3$  for volume fraction estimates. This was an average of various sources [4, 16, 17].

A cornflour-water composition resulting in a mass fraction  $X=0.52$  and volume fraction of  $\phi=0.41$  was used for all experiments. This composition was found to be high enough to show strong shear thickening behaviour, while still being easy to handle. At higher concentrations, some phase separation was observed in the syringe, despite the tapered attachment being present. It was found that only at mass fractions  $\geq 0.5$  did discontinuous shear thickening/jamming behaviour occur. At lower concentrations, this behaviour was not apparent. This agreed with the rheometry findings in [Chapter 7](#), suggesting this method of detecting DST/jamming was reasonable. The idea of a critical mass/volume fraction for jamming was also in agreement with what was found for the concentrated colloidal suspensions, suggesting a similarity between the colloidal and granular systems under shear.

It is worth noting that in literature, many choose to use mass fraction rather than volume fraction for describing cornflour suspensions. This is because cornflour

absorbs water, causing particle swelling, which can ultimately influence the volume fraction [6].

### **8.3.2 Steady Shear Experiments**

#### **8.3.2.1 Effect of Syringe Pump Bar Maximum Force (Shear Stress) on Jamming**

A cornflour-water suspension was poured into the syringe and attachment until the 2.5ml line was reached. This was then pumped through 50cm of straight 1mm inner diameter PVC pipe until the syringe emptied. The syringe pump was set to operate at its maximum bar speed. This resulted in a flow rate of 9.6ml/min.

The number of stalls in this time was determined for different maximum force levels/different maximum shear stresses (e.g. 5%, 10%...) that could be applied by the syringe pump's bar. The maximum force that could be applied by the bar was increased up until the point that stalling/jamming no longer occurred (due to the force applied to the fluid being sufficient to overcome all jams).

#### **8.3.2.2 Effect of Pipe Length on Jamming**

A cornflour-water suspension was pumped through 1mm inner diameter PVC pipe until the syringe emptied. The number of stalls in this time was determined for different lengths of straight pipe (10cm, 20cm and 50cm). The syringe bar's maximum force was set to operate at 5% and then 10% of the maximum force possible, at its maximum bar speed.

#### **8.3.2.3 Effect of Pipe Diameter on Jamming**

A cornflour-water suspension was pumped through 50cm of straight PVC pipe until the syringe emptied. The syringe pump was set to operate at its maximum bar speed. The number of stalls in this time was determined for different pipe inner diameters (1mm and 2mm) and for different maximum force levels (e.g. 5%, 10%...) that could be applied by the bar. The maximum force that could be applied by the bar was increased up until the point that stalling/jamming no longer occurred.

Since the volumetric flow rate remained fixed due to the fixed bar speed, increasing the pipe diameter meant the average velocity, shear rate and therefore required shear stress (assuming a fixed viscosity) through the pipe decreased.

### **8.3.2.4 Effect of Syringe Pump Bar Velocity (Shear Rate) on Jamming**

A set-up that showed strong signs of jamming behaviour at the maximum bar speed was then selected to see how changing the bar speed influenced jamming. By reducing the bar speed, the flow rate out of the syringe decreased, resulting in a lower average velocity through the pipe, a lower shear rate and therefore a lower required shear stress. For this, a cornflour-water suspension was pumped through 50cm of straight 1mm inner diameter PVC pipe until the syringe emptied. The syringe bar's maximum force was set to operate at 10% of the maximum force possible. The speed of the bar was varied and the number of stalls in the time for the syringe to empty was determined.

This was repeated for 50cm of straight 2mm inner diameter PVC pipe. These experiments were then repeated with the syringe bar's maximum force set to operate at 5% of the maximum force possible.

### **8.3.2.5 Effect of Pipe Material on Jamming**

Since DST and jamming are thought to be related to frustrated dilatancy and confinement (as detailed in [Chapter 4](#) and [Chapter 5](#)) the impact of the hardness and the rigidity/stiffness of the pipe's material was investigated. Hardness defines a material's resistance to permanent indentation, while rigidity/stiffness defines the extent to which a material resists deformation in response to an applied force [18]. The less stiff the material, the more flexible and pliable it is. In general, the harder the material is, the greater its rigidity [18]. Stiffness is related to the elastic modulus of the material.

One idea is that with soft/flexible walls, dilatancy of a suspension would not be completely frustrated, since the walls would be more likely to comply with the flow dilating, hence DST and jamming may be less extreme or less likely to occur. On the other hand, with very hard/rigid walls, dilation would be completely frustrated and the suspension would be unable to expand. In this case, complete jamming would be expected as the suspension would be unable to flow.

Since PVC is soft and flexible, the effects of harder/ more rigid materials were investigated. For this, a cornflour-water suspension was pumped through 50cm of straight 2mm inner diameter Nylon or stainless steel pipe until the syringe emptied. The syringe pump was set to operate at its maximum bar speed. The number of

stalls in this time was determined for different maximum force levels (e.g. 5%, 10%...) that could be applied by the bar. The maximum force that could be applied by the bar was increased up until the point that stalling/jamming no longer occurred.

This allowed comparisons to be made between materials with different properties.

Pipe length dependence and the effect of shear rate were also investigated for 2mm inner diameter stainless steel and Nylon. For these, the syringe bar's maximum force was set to operate at 10% of the maximum force possible.

The physical properties of the various pipes used, in terms of hardness and stiffness, are outlined in Table 8.3.

**Table 8.3- Material properties [18-20].** Durometer and Rockwell are scales used to measure material hardness. Shore A and Shore D are usually used to measure 'softer' plastics. Shore A is used for flexible materials and Shore D is used for semi-flexible materials. Rockwell is used for hard plastics and metals. Within a particular scale, the higher the number, the harder the material.

Material	Hardness	Young's Modulus/Elastic Modulus [GPa]
Flexible PVC	Durometer 55 Shore A	0.0015-0.07
Nylon	Durometer 60 Shore D	2-4
Stainless steel	Rockwell B 80-98	180-200

### **8.3.2.6 Effect of Pipe Wall Thickness/Reinforcement**

It was possible that the surface of the pipe material, rather than the material's hardness and rigidity, caused the changes in jamming found in 8.4.5. Therefore to investigate this possibility, flow through the same material but with different wall thicknesses was investigated. Since surfaces were the same, this meant that changes in jamming must have been caused by the material's resistance to deformation, rather than surface effects. Thicker walls meant the pipe was more difficult to deform and the rigidity was therefore greater. As a rule of thumb, increasing the wall thickness by a multiple increases the rigidity by the same multiple; i.e. doubling the wall thickness doubles the rigidity [21].

The 2mm inner diameter PVC pipe used previously had a wall thickness of 1mm. Flow through 50cm of 2mm inner diameter PVC pipe with 0.5mm wall thickness was now investigated. The number of stalls in the time for the syringe to empty was determined for different maximum force levels (e.g. 5%, 10%...) that could be

applied by the bar. The maximum force that could be applied by the bar was increased up until the point that stalling/jamming no longer occurred. The syringe pump was set to operate at its maximum bar speed.

In addition to changing the wall thickness, a tight fitting surrounding case for the 2mm inner diameter PVC pipe (1mm wall thickness) was made. This prevented it from deforming/expanding. Therefore, flow through 20cm of reinforced 2mm inner diameter PVC pipe was investigated. The number of stalls in the time for the syringe to empty was determined for different maximum force levels (e.g. 5%, 10%...) that could be applied by the bar. The maximum force that could be applied by the bar was increased up until the point that stalling/jamming no longer occurred. The syringe pump was set to operate at its maximum bar speed.

For all experiments, typically three to five repetitions were done. Error bars represent one standard deviation.

## 8.4 Results and Discussion

### 8.4.1 Effect of Syringe Pump Bar Maximum Force (Shear Stress) on Jamming

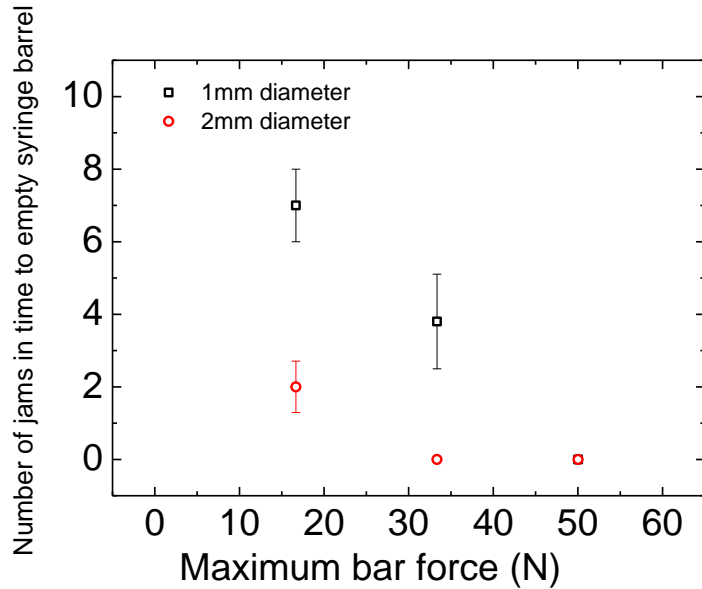


Figure 8.3- Effect of maximum bar force (shear stress) on jamming (50cm long PVC pipe at maximum flow rate; 1mm and 2mm inner diameter pipe). Error bars show standard deviation of repetitions. Time to empty syringe barrel was ~16s. Residence time in 1mm diameter pipe was ~2s. Residence time in 2mm diameter pipe was ~8s. The maximum bar force was the maximum force the bar could apply. During an experiment, the force could vary from zero to this maximum.

As the maximum force that could be applied by the syringe pump's bar was increased, the number of jams measured in the time to empty the syringe decreased, until finally no jams were measured (Figure 8.3). At lower maximum forces, jamming may have been sufficient to result in the maximum force applied by the bar (the shear stress) being insufficient to maintain the desired shear rate (due to the significantly increased viscosity caused by jamming and the maximum force being unable to 'break up' a jam).

An idea is that as the maximum force that could be applied by the bar was increased, the force became sufficient to overcome 'weaker jams' (e.g. by causing them to break up or causing the jam to yield) that previously caused stalling at lower applied forces. Eventually, the bar's force was sufficient to overcome all jams. As mentioned in 8.4.5 where the effect of pipe material is investigated, it was possible

that larger applied forces made it more likely for the walls to comply with the flow (or the particles to deform), therefore helping overcome jams.

This trend was found for both the 1mm and 2mm inner diameter pipes. These findings are discussed in more detail in 8.4.7.

#### 8.4.2 Effect of Pipe Length on Jamming

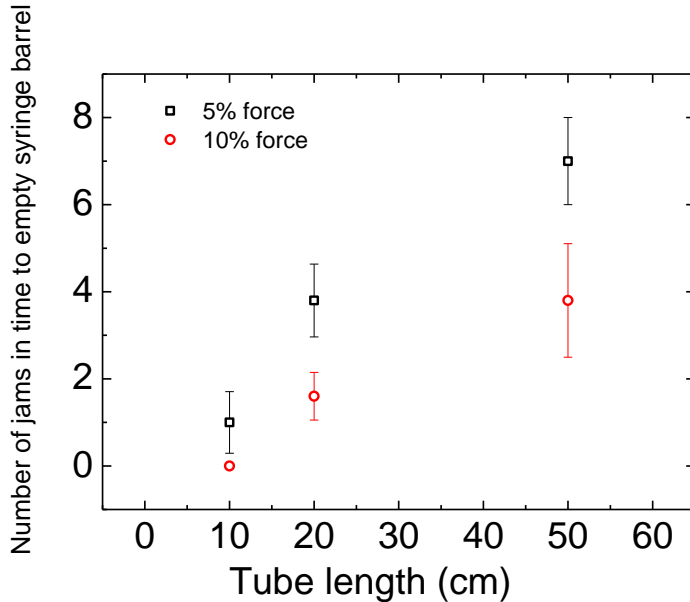


**Figure 8.4-** Effect of pipe length on jamming (5% maximum bar force (17N) at maximum flow rate with 1mm inner diameter pipe and 10% maximum bar force (34N) at maximum flow rate with 1mm inner diameter pipe). Error bars show standard deviation of repetitions. Time to empty syringe barrel was ~16s. Residence time in 50cm of 1mm diameter pipe was ~2s, residence time in 20cm of 1mm diameter pipe was ~1s and residence time in 10cm of 1mm diameter pipe was ~0.5s. The maximum bar force was the maximum force the bar could apply. During an experiment, the force could vary from zero to this maximum.

As the pipe length was increased, the number of jams in the time for the syringe to empty increased (Figure 8.4). This may have been due to the sample having a longer residence time in the pipe, resulting in a greater likelihood of jamming occurring since an element of fluid had to be sheared over a greater distance before leaving the pipe.

This was investigated again in 8.4.5, where the trend of increasing pipe length resulting in more jams was again found for different pipe materials.

### 8.4.3 Effect of Pipe Diameter on Jamming

As the pipe diameter was increased, for a fixed maximum bar force that could be applied, the number of jams in the time for the syringe to empty decreased (Figure 8.3). Since the flow rate remained fixed, the larger diameter meant the average velocity, shear rate and required shear stress through the pipe decreased and the material therefore had a longer residence time in the pipe.

Lower shear rates meant that a smaller applied stress was required to shear the material (this ‘required’ shear stress mentioned assumes no jamming, i.e. simple  $\tau = \eta\dot{\gamma}$ ) and it was therefore more likely for this to be met due to the fixed maximum stress that could be applied to the fluid.

One possible picture is that the larger diameter may have made it more difficult for particles/force transmitting clusters to span across the pipe to cause jamming, since more material was required. As pipe diameter increased, the surface to volume ratio decreased. This may have made jamming less likely as there was less surface for particles/clusters to bridge between and to confine the material. As previous chapters showed, surfaces/boundaries and the confining stresses they provide are very important in dilation and jamming [1, 6-8].

These results showed similarities to the results from the rotating cylinder geometry used with the concentrated colloidal suspensions in [Chapter 4](#) and [Chapter 5](#), where it was found that jamming occurred less frequently with larger gap sizes. With the rotating cylinder shear cells, however, the shear rate was constant with the different gap sizes.

Since the shear rate varied with the different pipe diameters, the total strain varied. The total strain a unit of fluid underwent when passing from one end of the pipe to the other was twice as large for the 1mm diameter pipe compared to the 2mm diameter pipe. Figure 8.3 was replotted as the number of jams per unit strain. While this brought the data closer together for the different pipe diameters, they did not converge (Figure 8.5). Therefore a smaller pipe diameter still results in more jams than can be explained by proportionality to the total strain suffered by the fluid.

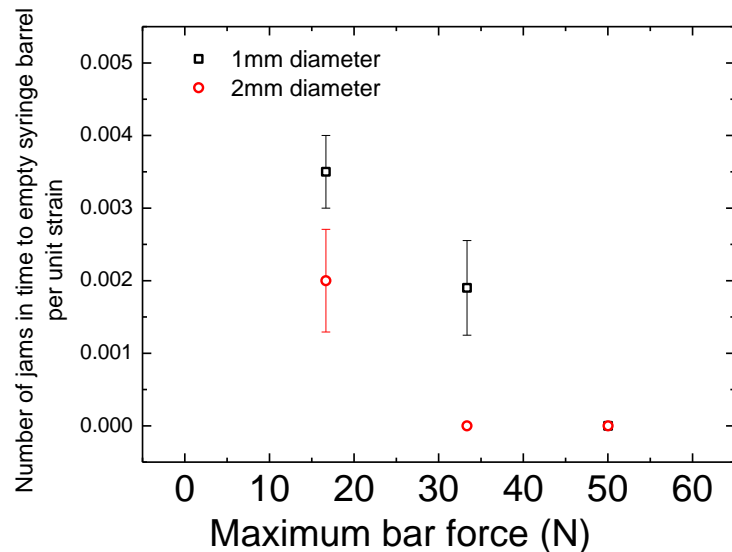


**Figure 8.5-** Effect of maximum bar force (shear stress) on jamming per unit strain (50cm long PVC pipe at maximum flow rate; 1mm and 2mm inner diameter pipe). Error bars show standard deviation of repetitions. Time to empty syringe barrel was ~16s. Residence time in 1mm diameter pipe was ~2s. Residence time in 2mm diameter pipe was ~8s. The maximum bar force was the maximum force the bar could apply. During an experiment, the force could vary from zero to this maximum.

#### 8.4.4 Effect of Syringe Pump Bar Velocity (Shear Rate) on Jamming

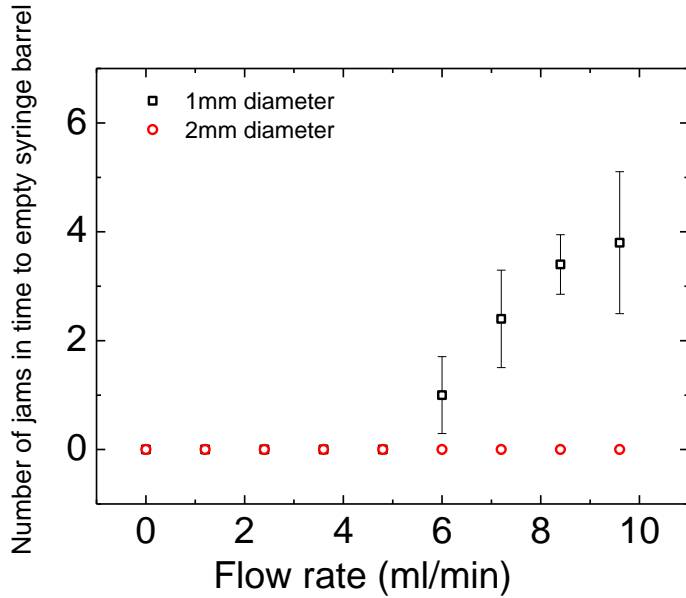


Figure 8.6- Effect of flow rate on jamming (50cm long piping at 10% maximum bar force (34N)). Error bars show standard deviation of repetitions. It is worth noting that the time to empty the syringe barrel increased as the flow rate decreased. Time to empty syringe barrel was ~16s at maximum flow rate (9.6ml/min). By 6ml/min, this had increased to ~25s. The maximum bar force was the maximum force the bar could apply. During an experiment, the force could vary from zero to this maximum.

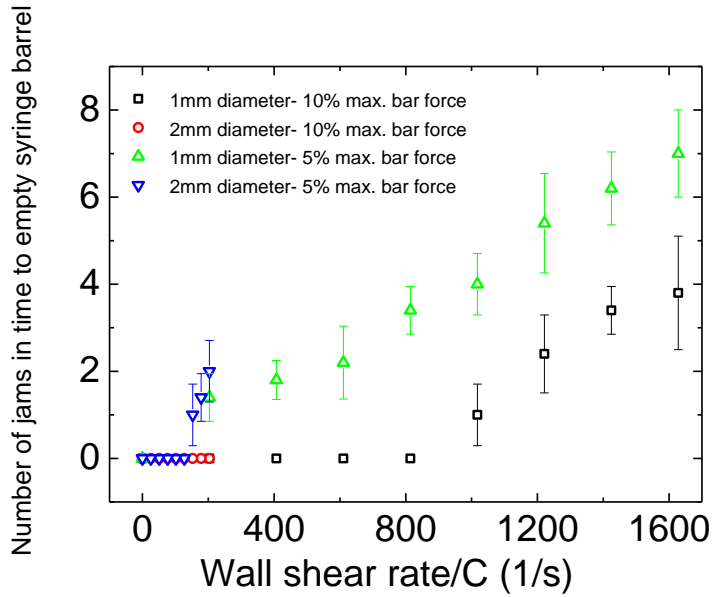


Figure 8.7- Effect of wall shear rate on jamming (50cm long piping at 10% maximum bar force (34N) and at 5% maximum bar force (17N)). Error bars show standard deviation of repetitions. Here C is a correction factor for the wall shear rate for non-Newtonian flows as detailed in 3.4.3. The maximum bar force was the maximum force the bar could apply. During an experiment, the force could vary from zero to this maximum.

Varying the bar speed, which varied the fluid's flow rate, velocity, shear rate and required shear stress had a significant impact on jamming (Figure 8.6 and Figure 8.7). At a fixed maximum bar force that could be applied, jamming was only evident beyond a critical shear rate. Increasing the shear rate further resulted in an increased number of jams. The increased number of jams with increased shear rate at a fixed maximum stress that could be applied by the syringe pump may have been due to larger shear rates requiring a larger stress to flow (particularly when strongly shear thickening). Higher shear rates therefore meant that a larger applied stress was required and it was less likely for this to be met due to the fixed maximum force that could be applied to the fluid by the syringe pump's bar. At higher shear rates, particles were also more likely to have to dilate and 'roll over' one another, and perhaps form force transmitting clusters, than at lower shear rates.

This critical shear rate beyond which jamming was measured increased as the maximum force that could be applied by the bar increased, again suggesting that increasing the maximum force that could be applied by the bar meant the force became sufficient to overcome 'weaker jams' that previously caused stalling at lower applied forces. This can be seen by comparing the 5% force and 10% maximum force plots in Figure 8.7. It is worth noting that for the 2mm diameter experiments at 10% maximum bar force, the force was always sufficient to prevent stalling at all shear rates.

The results also showed similarities to the results from the rotating cylinder geometry used with the concentrated colloidal suspensions in [Chapter 4](#) and [Chapter 5](#), where it was found that jamming only occurred beyond a critical shear rate.

In Figure 8.7, C is a correction factor for the wall shear rate for non-Newtonian flows, as detailed in 3.4.3. This was thought to be ~0.8-0.9 for the cornflour-water suspensions used in this work. The wall shear rate was calculated as follows:

$$\dot{\gamma}_{max} = \frac{8u_{avg}}{d} \quad \text{Equation 8.2}$$

Here  $u_{avg}$  is the average fluid velocity and  $d$  is the pipe diameter.

### 8.4.5 Effect of Pipe Material on Jamming

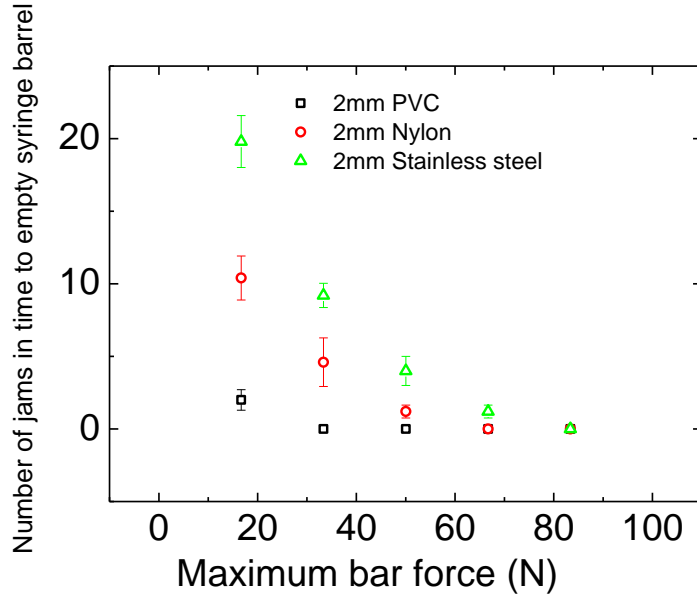


Figure 8.8- Effect of pipe material on jamming with different maximum bar forces (50cm long pipe at maximum flow rate). Error bars show standard deviation of repetitions. Time to empty syringe barrel was ~16s. Residence time in 2mm diameter pipe was ~8s. The maximum bar force was the maximum force the bar could apply. During an experiment, the force could vary from zero to this maximum.

The pipe's material had a significant impact on jamming and this was likely related to the material's hardness and rigidity, which ultimately affected the flowing suspension's confinement (Figure 8.8).

When harder/stiffer Nylon piping was used, for a fixed maximum bar force that could be applied and bar speed, more jams were measured in the time to empty the syringe, compared to when the softer/less stiff PVC piping was used. The number of jams increased further when the even harder and stiffer stainless steel pipe was used. This suggested that the material's hardness and rigidity had an important influence on jamming and this is supportive of the idea that frustrated dilatancy plays a significant role in the mechanism of discontinuous shear thickening and flow induced jamming, as outlined in [Chapter 4](#) and [Chapter 5](#).

As detailed in [Chapter 4](#) and [Chapter 5](#), discontinuous shear thickening and jamming may occur when frictional force transmitting hydroclusters span the system (e.g. across the pipe) and they must dilate in order to flow [22]. Dilatation of these hydroclusters against a frustrated system boundary may therefore lead to the large fluctuations in stress and dramatic increases in viscosity associated with discontinuous shear thickening and jamming. This could result in the maximum bar

force applied to the fluid being unable to maintain the desired shear rate (due to being unable to break up jams), hence causing the syringe pump to stall.

One picture is that when the force transmitting clusters span the pipe, the force applied to the suspension to make it flow would be redirected towards the boundaries via solid-solid frictional contacts between neighbouring particles. With flexible walls, although still frustrated, the particles would be able to dilate if the applied force was sufficient to cause the walls to expand and comply with the dilating flow. With harder/ more rigid walls, more extreme DST and even complete jamming would be expected since dilation may be completely frustrated- if walls have very little flexibility, the applied force would be insufficient for the walls to comply and the suspension would be unable to dilate at all (unless the particles themselves could sufficiently deform, which likely occurred for the stainless steel piping as detailed below). This would result in complete jamming.

This idea of the walls complying may also help partially explain why the number of jams decreased with increasing maximum bar force that could be applied. With an increased maximum bar force that could be applied, greater forces would have been applied to the walls (via the solid-solid contacts), with larger forces being more likely to be able to cause the walls to comply and allow dilation. This idea is in addition to the possibility of larger forces being sufficient to cause the jammed material to break up or the jam to yield. Perhaps overcoming/breaking up jams was caused by the walls complying.

It was found that jams occurred over a larger range of maximum bar forces as material hardness/stiffness increased (Figure 8.8). For example, when the bar's maximum force was ~70N, no jams were seen with PVC or Nylon pipe, but they were still seen with stainless steel. This was likely due to larger forces being required to cause deformation of the piping with harder/stiffer materials. Since stainless steel is so difficult to deform compared to PVC and Nylon, it was likely that particle deformation ultimately occurred in the stainless steel set-up. Cornflour's compressive modulus is estimated to be 10GPa which is significantly lower than the elastic modulus of stainless steel but higher than that of PVC and Nylon [6].

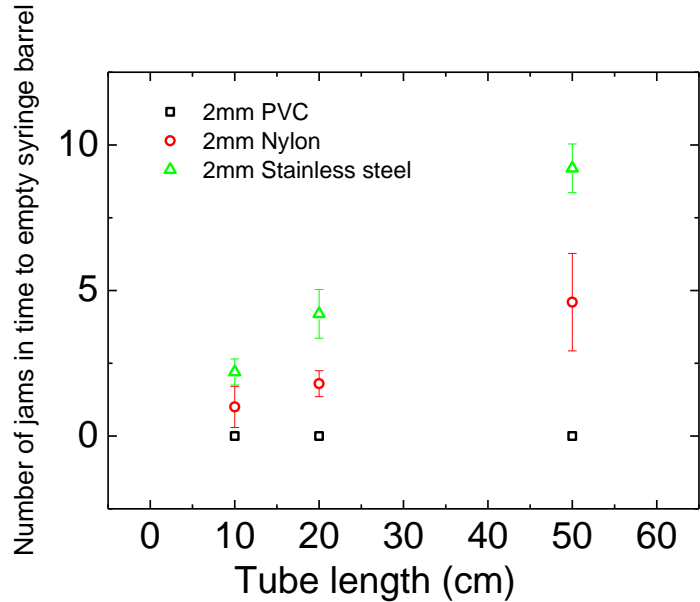


**Figure 8.9-** Effect of pipe length on jamming with different materials (10% maximum bar force (34N) force at maximum flow rate). Error bars show standard deviation of repetitions. Time to empty syringe barrel was ~16s. Residence time in 50cm of 2mm diameter pipe was ~8s, residence time in 20cm of 2mm diameter pipe was ~4s and residence time in 10cm of 2mm diameter pipe was ~2s. The maximum bar force was the maximum force the bar could apply. During an experiment, the force could vary from zero to this maximum.

The trend of increased pipe length resulting in more jams was similarly found for the different materials (Figure 8.9), as was found in 8.4.2. This suggested that this was a trend of jamming overall and was not particular to the pipe material.

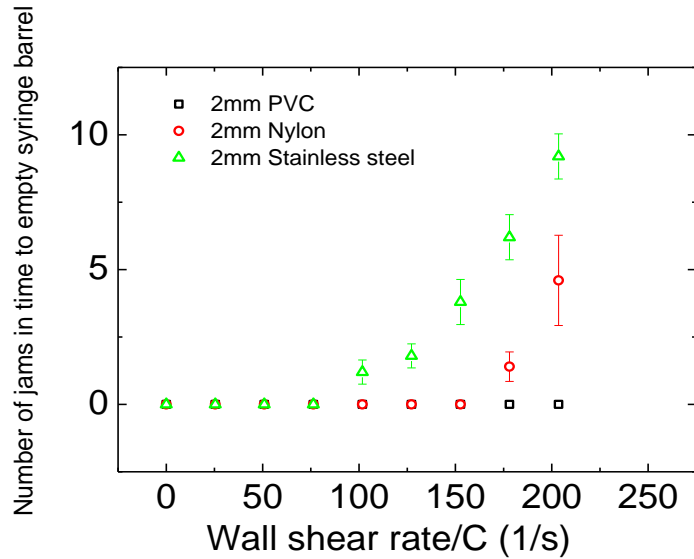


**Figure 8.10-** Effect of wall shear rate on jamming with different materials (50cm long pipe at 10% maximum bar force (34N)). Error bars show standard deviation of repetitions. It is worth noting that the time to empty the syringe barrel increased as the shear rate decreased. The maximum bar force was the maximum force the bar could apply. During an experiment, the force could vary from zero to this maximum.

Similarly, with the different materials, jamming was only evident beyond a critical shear rate and increasing the shear rate further resulted in an increased number of jams (Figure 8.10). The critical shear rate decreased as material hardness/rigidity increased. This suggested that it was ‘easier’ for the suspension to jam with harder walls. Perhaps this was due to it being more difficult for hard walls to comply with the flow.

It is worth noting that this section on the effects of pipe material on jamming should be treated as largely qualitative. Obtaining more quantitative information was difficult due to uncertainties on whether it was the particles or pipe walls that were deforming (particularly for the case of stainless steel).

#### 8.4.6 Effect of Pipe Wall Thickness/Reinforcement on Jamming

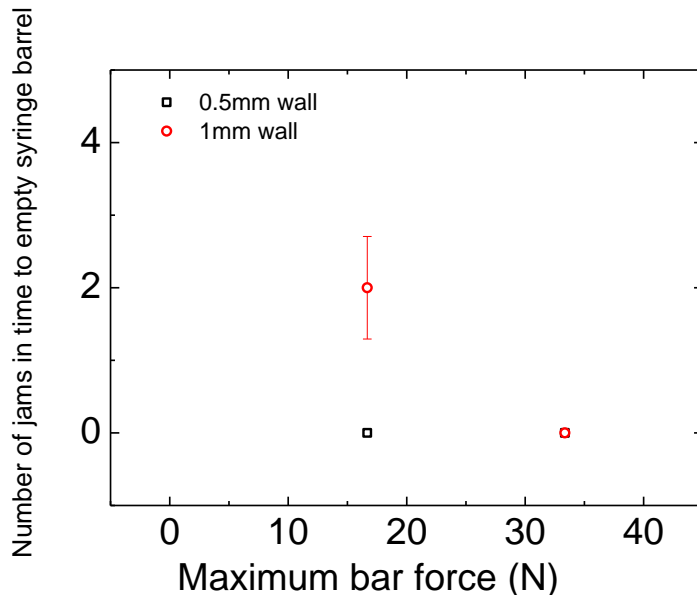


**Figure 8.11- Effect of wall thickness on jamming (50cm long PVC pipe at maximum flow rate, 2mm inner diameter). Error bars show standard deviation of repetitions. Time to empty syringe barrel was ~16s. Residence time in 2mm diameter pipe was ~8s. The maximum bar force was the maximum force the bar could apply. During an experiment, the force could vary from zero to this maximum.**

To further investigate the effect of confinement and to ensure that changes were due to confinement, rather than surface properties of the different materials, experiments with the same type of piping but with different wall thicknesses were performed, and the effect of reinforcing the pipe was investigated.

When pipes with thinner walls were used, fewer jams occurred in the time to empty the syringe (Figure 8.11). Thinner walls perhaps meant it was easier for the walls to expand/deform to comply with the suspension dilating, reducing the extent of jamming. The fact that wall thickness influenced jamming suggested that it was the pipe material's resistance to deformation, rather than its internal surface, that affected jamming. Unfortunately it was not possible to obtain 1mm inner diameter piping with different wall thicknesses, hence the limited results.

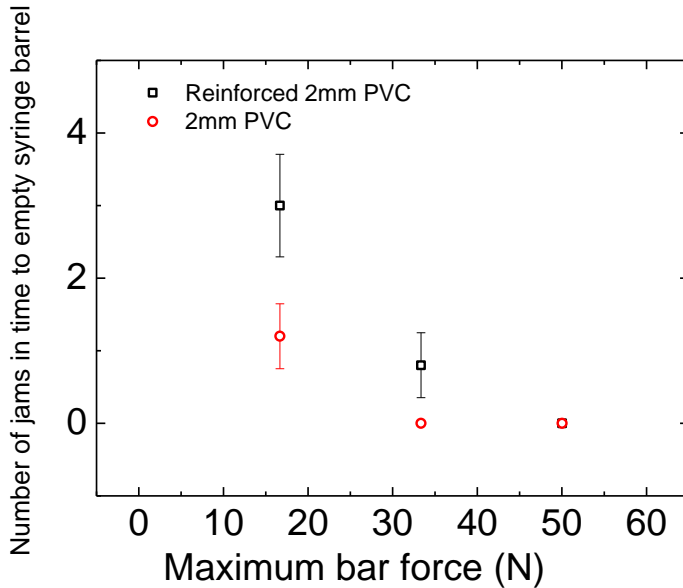


**Figure 8.12- Effect of material reinforcement on jamming (20cm long pipe at maximum flow rate).** Error bars show standard deviation of repetitions. Time to empty syringe barrel was ~16s. Residence time in 20cm of 2mm diameter pipe was ~4s. The maximum bar force was the maximum force the bar could apply. During an experiment, the force could vary from zero to this maximum.

When the PVC piping was reinforced by a tight fitting Perspex case, the number of jams at a given maximum force was greater than when no reinforcement was present (Figure 8.12). The tight casing would have made it more difficult for the pipe to deform, since there was no room for it to move or expand. The only compliance would have come from the pipe walls since they could have been compressed slightly.

Overall, the work done on confinement in 8.4.5 and 8.4.6 supported the work done in [Chapter 5](#) that showed how important an impact confinement had on jamming. In [Chapter 5](#) it was shown that soft walls resulted in significantly fewer jams compared to hard walls; this idea is similar to that found here where softer pipe walls resulted in jamming being less frequent. A consideration of confinement could therefore be

used as a possible means to prevent and control jamming. As mentioned, the work should be treated as largely qualitative. Obtaining more quantitative information was difficult due to uncertainties on whether it was the particles or pipe walls that were deforming (particularly for the case of stainless steel).

#### 8.4.7 Summary of Findings

As mentioned in 8.3.1, stalling of the syringe pump, which was indicative of jamming, occurred when the maximum force applied by the syringe pump's bar was insufficient to overcome the 'temporary' force required to overcome the jam. This meant the desired shear rate (and flow rate) could not be achieved.

This concept can be seen more clearly in Figure 8.13 and also ties the results from this chapter more closely to the results from [Chapter 5](#).

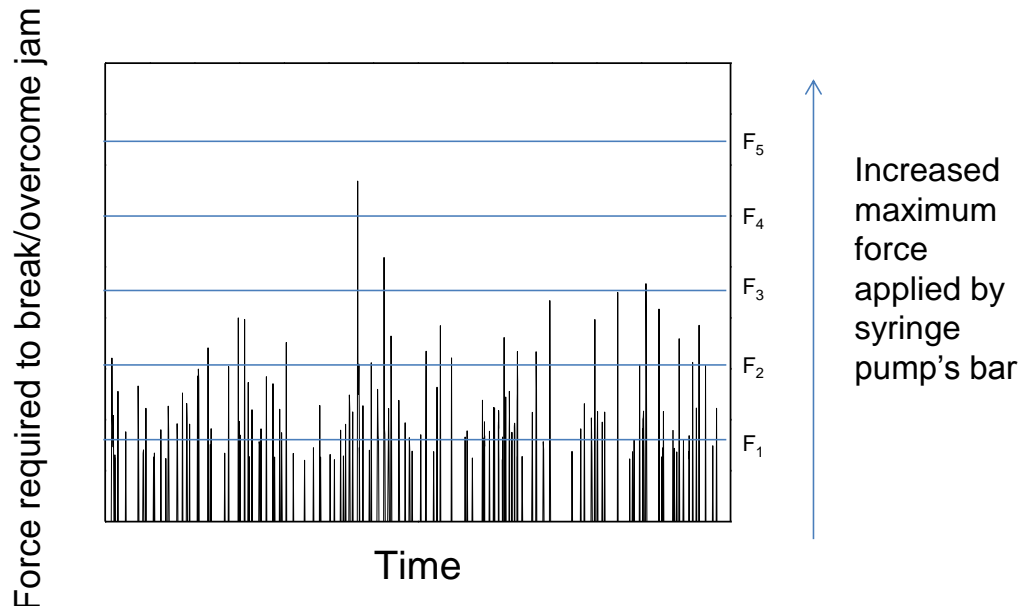


**Figure 8.13- Diagram of hypothetical varying forces required to break up/ overcome a jam with time.** Horizontal lines  $F_1$  to  $F_5$  represent the maximum force that could be applied by the syringe pump's bar at different settings. If the maximum force ( $F_{1-5}$ ) is less than the force required to overcome the jam, stalling will occur. At  $F_1$ , many stalls are observed, while at  $F_5$ , the force is sufficient to overcome all force fluctuations and no stalls are observed.

From Figure 8.13, it can be seen that at low maximum force levels (e.g.  $F_1$ ) there are a significant number of incidents where the maximum force that can be applied to the material is less than the force required to overcome jams. When this happens, the syringe pump would stall.

As the maximum force that can be applied increases, the number of incidents where the force required to break up a jam cannot be met decreases. Eventually, the maximum force applied to the material is sufficiently high that it is able to overcome all jams and no stalling occurs ( $F_5$ ).

This viewpoint is consistent with the findings of this chapter. For example, when the effect of the syringe pump bar's maximum force/ shear stress on jamming was investigated, it was found that as the maximum force that could be applied by the syringe pump's bar was increased, the number of jams measured in the time to empty the syringe decreased, until finally no jams were measured.

The increased number of jams with increasing pipe length could be explained by the longer residence time with longer pipes. For example, longer pipes would cover a greater range of time in Figure 8.13.

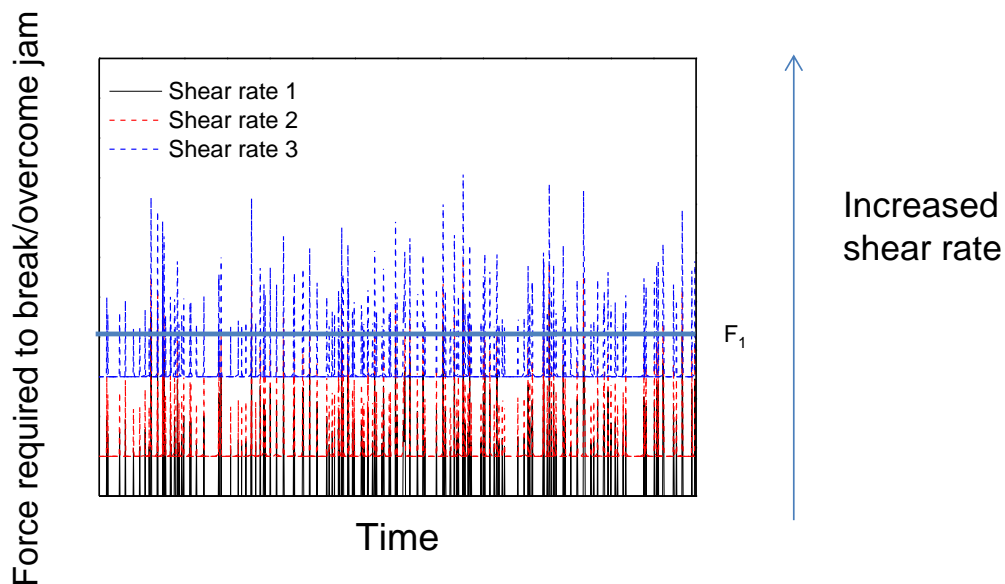


**Figure 8.14-** Diagram of hypothetical varying forces required to break up/ overcome a jam with time at different shear rates. Shear rate 1<shear rate 2< shear rate 3. Horizontal line,  $F_1$ , represents the maximum force that could be applied by the syringe pump's bar. If the maximum force ( $F_1$ ) is less than the force required to overcome the jam, stalling will occur. As shear rate increases, there are more jams with force $> F_1$ , and so more stalls.

The increased number of jams with increasing shear rate may have been due to the increased shear rate increasing the size of the force required to overcome the jam. It was possible that increasing the shear rate effectively shifted Figure 8.13 up since the larger shear rate meant that a larger shear stress was required for flow in general. It was therefore more likely for the force required to break a jam, on top of

the force required for flow in general, to be greater than the maximum force that could be applied by the syringe pump. This can be seen in Figure 8.14 where at higher shear rates, there are a greater number of jams that the force applied by the syringe pump's bar is insufficient to overcome, than at lower shear rates. This would result in more stalling at higher shear rates, as was found experimentally.

This may also explain why larger pipe diameters resulted in fewer jams. This may have been due to the reduced shear rate with larger pipes since it meant that a smaller applied stress was required to shear the material and it was therefore more likely for this to be met due to the fixed maximum stress that could be applied.

## 8.5 Conclusions

The flow of concentrated cornflour-water suspensions through pipe geometries resulted in jamming under certain conditions. The results using granular cornflour-water suspensions in the pipe geometry showed similar findings to the work done with the rotating cylinder shear cell geometries used in [Chapter 4](#) and [Chapter 5](#), where concentrated colloidal suspensions were used. This suggested that the findings were not particular to the specific flow geometry. It also showed that there are strong similarities in the behaviour of concentrated colloidal suspensions and concentrated granular suspensions under flow, as was found in [Chapter 7](#) where a rheometer was used to investigate the effects of flow on the granular and colloidal materials that were used in this thesis.

Main findings included that jamming was only found to occur above a particular mass/volume fraction, and jamming occurred more frequently when smaller pipe diameters were used, in agreement with the work in [Chapter 5](#) which suggested that jamming was more frequent when smaller gap sizes were used. The effect of confinement was also significant. Jamming occurred less frequently when less stiff piping was used. This was in agreement with the work in [Chapter 5](#), where the use of soft walls resulted in significantly fewer jams. This confirmed that confinement plays an essential role in the jamming mechanism and consideration of confinement could be used as a possible means to prevent and control jamming.

Main limitations of this chapter were the restricted number of experiments that could be performed due to the limited configurations (e.g. pipe diameters, wall thicknesses etc.) of piping that is commercially available. The work did, however, show trends worth mentioning and the work showed much agreement with the rheometer work in [Chapter 7](#). The work could be strengthened further if more varied pipes were available.

C	Correction factor
g	Acceleration due to gravity
N	Newton
R	Radius
$v_{\text{terminal}}$	Terminal velocity
X	Mass fraction
$\rho$	Density
$\eta$	Viscosity
$\phi$	Volume fraction

1. Brown, E. and H. Jaeger, *Shear thickening in concentrated suspensions: phenomenology, mechanisms, and relations to jamming*. Reports on Progress in Physics, 2013. **77**(4): p. 046602.
2. Jenkins, M.C., et al., *Does Gravity Cause Load-Bearing Bridges in Colloidal and Granular Systems?* Physical Review Letters, 2011. **107**(3).
3. Cates, M.E., M.D. Haw, and C.B. Holmes, *Dilatancy, jamming, and the physics of granulation*. Journal of Physics-Condensed Matter, 2005. **17**(24): p. S2517-S2531.
4. Brown, E. and H.M. Jaeger, *Dynamic Jamming Point for Shear Thickening Suspensions*. Physical Review Letters, 2009. **103**(8): p. 4.
5. Wagner, N.J. and J.F. Brady, *Shear thickening in colloidal dispersions*. Physics Today, 2009. **62**(10): p. 27-32.
6. Brown, E. and H.M. Jaeger, *The role of dilation and confining stresses in shear thickening of dense suspensions*. Journal of Rheology, 2012. **56**(4): p. 875-923.
7. Fall, A., et al., *Shear thickening of cornstarch suspensions as a reentrant jamming transition*. Physical Review Letters, 2008. **100**(1).
8. Fall, A., et al., *Shear thickening of cornstarch suspensions*. Journal of Rheology, 2012. **56**(3): p. 575-591.
9. White, E.E.B., M. Chellamuthu, and J.P. Rothstein, *Extensional rheology of a shear-thickening cornstarch and water suspension*. Rheologica Acta, 2010. **49**(2): p. 119-129.
10. Crawford, N.C., et al., *Shear thickening of corn starch suspensions: Does concentration matter?* Journal of Colloid and Interface Science, 2013. **396**: p. 83-89.
11. Fall, A., et al., *Shear thickening of cornstarch suspensions as a reentrant jamming transition*. Physical Review Letters, 2008. **100**(1): p. 018301.
12. Fall, A. and F. Bertrand, *Macroscopic Discontinuous Shear Thickening vs Local Shear Jamming in Cornstarch*. Soft Condensed Matter, 2015. Under review.
13. Brown, E., et al., *Generality of shear thickening in dense suspensions*. Nature Materials, 2010. **9**(3): p. 220-224.
14. Barnes, H.A., *Shear-Thickening (Dilatancy) In Suspensions Of Nonaggregating Solid Particles Dispersed In Newtonian Liquids*. Journal of Rheology, 1989. **33**(2): p. 329-366.
15. Haw, M.D., *Jamming, two-fluid behavior, and "self-filtration" in concentrated particulate suspensions*. Physical Review Letters, 2004. **92**(18).
16. Merkt, F.S., et al., *Persistent holes in a fluid*. Physical Review Letters, 2004. **92**(18).
17. von Kann, S., et al., *Nonmonotonic settling of a sphere in a cornstarch suspension*. Physical Review E, 2011. **84**(6).
18. Callister, W.D., *Materials Science and Engineering*. 7th ed. 2007: Wiley. 1000.
19. Scientific, T., *Thermo Scientific Nalgene Data Guideline*. 2014.
20. Engineering-Toolbox. *Material Property Data*. 2014.
21. Miller, C., *Tubing Rigidity- Its Relation to Size is Dramatic but often Misunderstood*. 2010, Design Criteria.
22. O'Brien, V.T. and M.E. Mackay, *Stress components and shear thickening of concentrated hard sphere suspensions*. Langmuir, 2000. **16**(21): p. 7931-7938.

## 9. Conclusions and Future Work

## This section will cover:

- Overall conclusions that can be drawn from this work.
  - Ideas for future work worth considering.



## 9.1 Conclusions

The main conclusions from this work are summarised below.

### Equipment Design and Implementation

A bespoke rotating cylinder shear cell geometry was designed for shearing concentrated suspensions. The shear cell was effective for shearing the concentrated suspensions and was designed to allow microscope images to be taken while samples were undergoing shear. The set-up was characterised to allow shear stresses and shear rates to be determined and the shear cell could effectively be used as a very basic rheometer. No reports of such an instrument are reported in literature, making this a novel design.

A novel jamming detection method was designed to help overcome limitations with visual measurement techniques. This technique measured intermittent forces in the sample being sheared in the rotating cylinder shear cell geometry that were only present when jamming occurred. This allowed quantitative data to be obtained from systems that showed jamming behaviour. This jamming force sensor could be used simultaneously with visual measurements, allowing links to be made. No similar devices have been reported in literature.

Due to the simplicity and versatility of the rotating cylinder shear cell geometry designed, it has been used by other researchers within the university for different applications with success.

### Effects of Flow on Concentrated Colloidal Suspensions

To investigate the effects of flow on concentrated colloidal suspensions, the novel shear cells and jamming detection method outlined above were used and these allowed unique data to be recorded. A combination of visual observations, basic rheometry and the novel jamming detection method resulted in a better understanding of what was actually happening in the systems, compared to if just a commercial rheometer was used.

Useful results were seen visually. Above a critical volume fraction and shear rate, macroscopically the sample could be seen dilating (volumetrically expanding) at the open surface (fluid-air interface). At these conditions, microscope observations showed that the flow appeared to slow down significantly, and this was followed by

significant cracking and breaking. These visual effects were thought to be signatures of flow induced jamming/ discontinuous shear thickening.

The onset conditions required for these visual observations coincided with the detection of jamming with the jamming force sensor. It was only beyond a critical volume fraction and shear stress/rate that jamming peaks were detected. The size of jams and number of jams for a fixed strain depended on parameters such as volume fraction, applied stress, system geometry and particle size. System confinement appeared important. Conditions where jamming occurred were mapped out, allowing ways to prevent and control jamming to be identified. An analysis of jamming distributions was performed to gain a better insight and understanding of the results. This showed that for a particular set of conditions, there was a ‘constant’ average jamming peak magnitude that was well defined.

The conditions where jamming was detected using the novel equipment matched well with where discontinuous shear thickening was measured using a commercial rheometer. This supported the idea of discontinuous shear thickening and flow induced jamming being closely related.

The studies allowed a mechanism for flow induced jamming and discontinuous shear thickening to be proposed. This involved a combination of frictional force transmitting hydrocluster formation and frustrated dilatancy.

Overall, this work resulted in an improved understanding of conditions where jamming occurs and how it may be controlled and prevented in concentrated colloidal suspensions. This could ultimately lead to a better understanding of complex flow systems and lead to more efficient processes.

#### Effects of Flow on Concentrated Granular Suspensions

Due to the ubiquitous nature of pipe flow in industry, a syringe pump pipe set-up was used to investigate the effects of pipe flow on concentrated granular cornflour-water suspensions. The effects of parameters such as shear stress, shear rate, pipe diameter and pipe length on jamming were investigated. Since the results on the concentrated colloidal suspensions suggested that confinement was important, the effects of using different pipe materials, with different stiffnesses and rigidities, were investigated.

The results showed similarities to the work done on the concentrated colloidal suspensions in the rotating cylinder geometry, with similar trends being found. For example, jamming was only found to occur above a particular mass/volume fraction. Pipe diameter and confinement appeared important. This suggested that the findings were not particular to the specific flow geometry.

The conditions where jamming was detected using the syringe pump pipe set-up compared well to where discontinuous shear thickening was measured using a commercial rheometer. This again supported the idea of discontinuous shear thickening and flow induced jamming being closely related.

Overall, the results showed that there are strong similarities in the behaviour of concentrated colloidal suspensions and concentrated granular suspensions under flow and this is an area of interest in literature.

#### Preliminary Molecular Dynamics Simulations (Appendix)

Molecular dynamics simulations were used to investigate the effects of flow on a system of hard spheres, similar to the concentrated colloidal suspensions that were investigated experimentally. The results obtained from the simulations showed similarities to the work on the concentrated suspensions, with dilation and fluctuating stresses being features under particular conditions (close to those investigated experimentally, for example in terms of volume fraction and shear rate).

The results, however, suggested that ordering of the monodisperse particles occurred under shear and this was likely influencing results. This ordering was not thought to occur experimentally. This suggested that additional particle interactions must be added to the simulations to better capture the behaviour seen experimentally. This was beyond the scope of the project but would prove a valuable piece of future work. The results did, however, show that some form of clustering was likely necessary to result in stress fluctuations and dilatancy, supporting the mechanism for flow induced jamming and discontinuous shear thickening that was proposed.

#### Overall Conclusions

By designing and using novel equipment that is not commercially available, a better understanding of the effects of flow on concentrated suspensions was achieved. The work has identified conditions where jamming/ discontinuous shear thickening

occurs and therefore has led to means to prevent and control it being identified. It has also resulted in a deeper understanding of the jamming/discontinuous shear thickening mechanism and highlights similarities in the flow behaviour of concentrated colloidal and granular materials. The findings could ultimately lead to a better understanding of complex flow systems and lead to more efficient processes.

## 9.2 Future Work

While this work has produced a lot of useful conclusions and novel ideas, it has also led to ideas for several areas of future work that may be worth considering.

A more controllable rotating cylinder shear cell would be a useful idea. In the experiments, only the supplied voltage was controlled, which ultimately controlled the shear stress. A shear cell where the rotational rate could be kept constant or changed to a set value by varying the voltage/stress could be beneficial. If the shear cell could be linked up to data acquisition equipment, perhaps to measure the rotational rate and voltage information, fluctuations in the supplied voltage to achieve a particular shear rate could, for example, be used to detect jamming. This could also be used to obtain more reliable data about how the speed of the rotating inner cylinder varied during jamming.

With the force sensor technique designed in [Chapter 5](#), it may be interesting to place multiple probes in the sample to take simultaneous measurements. Perhaps using a larger probe would also be worth considering to see if significant flow disruption influences the results.

From [Chapter 4](#) and [Chapter 5](#), more work on studying the effects of oscillatory shear could be worthwhile. Additional work on the effects of particle size and the effects of polydispersity may lead to interesting findings. Investigating the effects of rough particles or roughened shear cell walls may also be worth considering. Investigating particles with different shapes, such as rods, would be interesting. Perhaps a shear cell with a lid that could expand with the flow would be useful to allow confinement to be controlled; a set-up that allowed the lid's movement or applied forces to the lid to be measured could be beneficial.

For the work on jamming distributions in [Chapter 6](#), additional repetitions would be useful to allow more conclusive findings to be drawn.

From [Chapter 7](#), some form of in-situ light scattering equipment would be worth implementing to see how dynamics change when jamming occurs. It could also be used to detect changes in turbidity due to dilation and to probe structural changes in more detail. Using the rheometer to investigate the effects of particle size and polydispersity could be worthwhile.

For the pipe flow arrangement in [Chapter 8](#), some way of monitoring (and controlling) the actual force applied by the syringe pump's bar, rather than just the maximum force would be useful. Being able to obtain raw data from the pump would be beneficial, for example, to record the jams automatically, rather than counting them manually. Obtaining additional piping with different wall thicknesses and inner diameters would be useful to allow a more complete data set to be collected.

For all the experimental work, investigating with different materials may be interesting. Using soft and deformable particles could lead to a better understanding of the effects of confinement. Looking at different equipment scales, for example larger shear cells and pipe geometries would be interesting. Perhaps collaborating with industry to find information about systems that are causing jamming problems there would be beneficial as it could help identify larger scale issues.

# Appendix. Preliminary Molecular Dynamics Simulations of Hard Spheres under Shear

---

This section will cover:

- The basic background and theory behind the preliminary molecular dynamics simulations that were performed.
- The procedures and conditions that were used for running the simulations, including a discussion of their relevance to the conditions used experimentally in [Chapter 4](#) and [Chapter 5](#).
- The results obtained from the simulations, including a comparison with what was seen experimentally in [Chapter 4](#) and [Chapter 5](#).

## A.1 Summary

Molecular dynamics (MD) is a computer simulation method where the time evolution of a set of interacting particles is obtained by integrating their equations of motion [1-3]. In this chapter, preliminary molecular dynamics simulations of a system of hard spheres, similar to those investigated experimentally in [Chapter 4](#) and [Chapter 5](#), were performed to try to gain a better understanding of the behaviour that was observed experimentally. For the simulations, particles were assumed to interact only via hard sphere repulsion. Drag was added to simulate the solvent's effect on the particles.

The results obtained from the simulations showed similarities to the work in [Chapter 4](#) and [Chapter 5](#), with dilation and fluctuating stresses being features under particular conditions (similar to those investigated experimentally, for example in terms of volume fraction and shear rate).

The results, however, suggested that ordering of the monodisperse particles occurred under shear and this was likely influencing results. This ordering was not thought to occur experimentally ([Chapter 7](#)). This suggested that additional particle interactions must be added to the simulations to better capture the behaviour seen experimentally. This was beyond the scope of the project but would prove a valuable piece of future work.

The results did, however, show that some form of clustering was likely necessary to result in stress fluctuations and dilatancy. This agreed with the proposed mechanism for discontinuous shear thickening and jamming in [Chapter 5](#), where a mechanism involving force transmitting cluster formation and dilatancy was proposed, based on the experimental findings.

## A.2 Molecular Dynamics Background and Theory

Before proceeding with the simulations, it was necessary to understand the background, theory and concepts of molecular dynamics simulations. This section details the main areas that were considered in setting up and running the simulations.

### A.2.1 Molecular Dynamics Background

Molecular dynamics (MD) is a computer simulation method where the time evolution of a set of interacting particles is obtained by integrating their equations of motion [1-3].

Computer simulations play an important role in science and engineering research today. In the past, before the advent of high speed computers, research was largely done through a combination of traditional laboratory experiments and theory [1]. Here physical experiments were performed and the data from these were compared to models or used to create new models. This method often involved significant simplifications to produce models and theory that matched experiments well, or to make problems solvable [1, 2]. Theoretical models that were produced could only be tested in physical conditions that were easy to obtain. Many areas of interest, however, are difficult to obtain in a lab or with resources available, meaning that model verification was difficult and areas were often left unexplored.

The advent of high speed computers in the 1950s has significantly changed how much research is done today, with the introduction of computer simulations or ‘computer experiments’. In a computer experiment, a model is still provided, but the rigorous and many calculations are performed by a computer following a suitable algorithm. This has allowed further complexities to be added, allowing more realistic systems to be investigated. Systems that were previously unattainable can now be explored, resulting in a greater understanding of complex systems.

Computer simulations can be useful to verify experimental data (and vice-versa) if it has been possible to match simulation conditions closely to experimental. The results of simulations are determined solely by the nature of the model used [2]. As a result, comparison of simulation results with experimental data is a clear test of the model’s accuracy and validity. If the experimental data are reliable, discrepancies between the experimental measurements and simulation data can be attributed to

the model's failure to represent the system accurately [2]. By using computer simulations and lab experiments together, it is possible to gain a greater understanding of complex systems than if only one technique alone was used.

It was hoped that by performing molecular dynamics simulations on a system similar to that investigated experimentally in [Chapter 4](#) and [Chapter 5](#), a better understanding of the underlying experimentally observed behaviour would be achieved.

### A.2.2 Basic Molecular Dynamics Principles

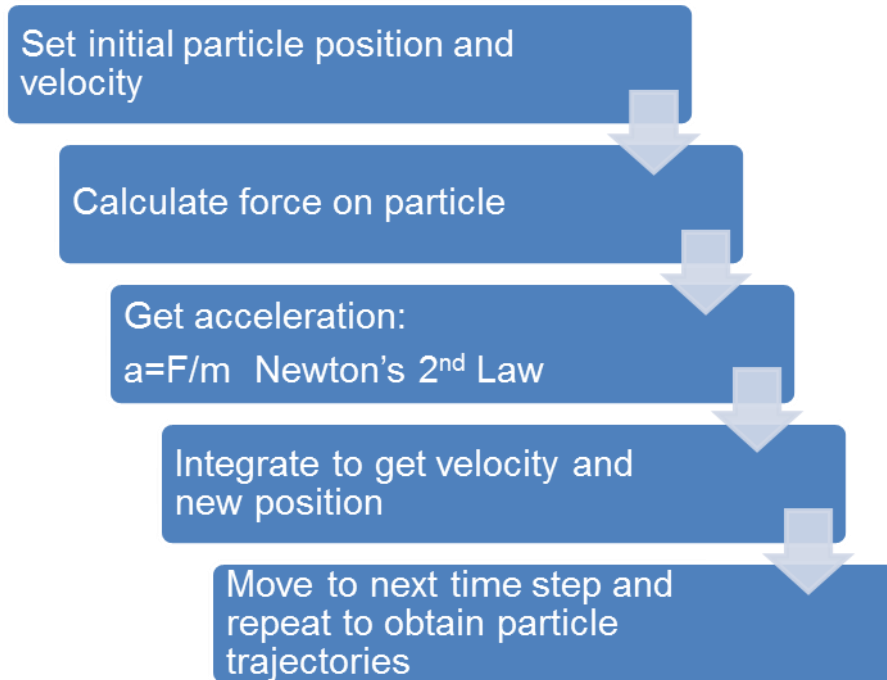


**Figure A.1- Molecular dynamics step overview**

As mentioned, molecular dynamics is a computer simulation method where the time evolution of a set of interacting particles is obtained by integrating their equations of motion [1, 2]. These equations of motion are those from the laws of classical mechanics, particularly Newton's 2<sup>nd</sup> Law of Motion.

From Newton's 2<sup>nd</sup> Law of Motion, a particle's acceleration can be deduced if its mass and the forces acting on it are known.

$$F_i = m_i a_i \quad \text{Equation A.1}$$

Here  $F_i$  is force,  $m_i$  is mass and  $a_i$  is acceleration of particle 'i'.

The force acting on a particle is determined from the particle's interactions with other particles (e.g. through hard sphere repulsion). Since the mass of the particle is also known, its acceleration can be determined.

Integration therefore allows the particle's velocity and displacement to be found:

$$v = \int a dt \quad \text{Equation A.2}$$

$$r = \int v dt \quad \text{Equation A.3}$$

Here  $v$  is velocity,  $t$  is time and  $r$  is position.

When the force is determined for each particle in the simulation, at each step over a time range, particle trajectories can be obtained from an initial set of positions and velocities. As later explained, this information can be used to obtain a range of system properties, allowing a detailed understanding of system behaviour to be evaluated.

The main steps of molecular dynamics simulations are summarised in Figure A.1.

### A.2.3 Simulation Forces

Determining the force acting on a particle is an integral part of a simulation, since determining this force is necessary to calculate the particle's acceleration according to Newton's 2<sup>nd</sup> law. The force acting on a particle can be determined from the gradient of the potential energy [1, 3]:

$$F_i = -\nabla U_i \quad \text{Equation A.4}$$

Here  $U$  is the potential energy.

A suitable function, or functions, must be used to determine the potential between particles. The potential on a particular particle involves summing the potential contribution of all other particles in the system with the particular particle. It is generally assumed that treating interactions as pair-wise additive is sufficient. This means that only two body interactions/ particle pairs are considered [1-3].

$$F_i = \sum_{j=i+1}^N F_{ij} \quad \text{Equation A.5}$$

This is due to computational costs (the evaluation of particle interactions is the most time consuming step) and is sufficient since two body interactions typically make by

far the most significant contribution to particle interactions [2]. Since particle interactions are the most time consuming calculations, the computational cost is of the order  $N^m$  where  $N$  is the number of particles and  $m$  is the number of particles being considered for interactions (typically 2) [2].

These force calculations must be repeated for each particle in the system.

The computation time can be reduced from Newton's 3<sup>rd</sup> law since:

$$F_{ij} = -F_{ji} \quad \text{Equation A.6}$$

It is worth noting that since the system studied was three dimensional, forces etc. must be determined in the x,y and z co-ordinates.

### A.2.3.1 Hard Spheres

In this work, particles were treated as approximate hard spheres. This is the simplest approximation and assumes that each particle has a physical volume prohibiting overlap with other particles [2, 4]. Regarding the lab experiments with the concentrated colloidal suspensions, as detailed in [Chapter 1](#) and [Chapter 4](#), it was reasonable to assume that the colloid particles used behaved as hard spheres.

For monodisperse particles, the hard sphere potential energy is:

$$U(r) = \begin{cases} \infty & \text{if } r \leq \sigma \\ 0 & \text{otherwise} \end{cases} \quad \text{Equation A.7}$$

Here  $r$  is the separation between particle centres and  $\sigma$  is particle diameter.

This states that all allowable configurations have zero potential energy and that the only restriction on the system is that the particles cannot interpenetrate (i.e. they are infinitely repulsive on contact) [5].

In this work, rather than treating particles as infinitely repulsive on contact, the repulsive interactions were defined as a truncated Lennard-Jones potential. This provides a more realistic representation of repulsive interaction than assuming an infinitely steep repulsion [2].

This truncated potential takes the form [2]:

$$U(r) = \begin{cases} 4\epsilon \left[ \left( \frac{\sigma}{r} \right)^{12} - \left( \frac{\sigma}{r} \right)^6 \right] + \epsilon & \text{if } r \leq 2^{\frac{1}{6}}\sigma \\ 0 & \text{otherwise} \end{cases} \quad \text{Equation A.8}$$

Here  $\epsilon$  is the magnitude of the energy minimum,  $r$  is the separation between particle centres and  $\sigma$  is particle diameter.

For the standard Lennard-Jones potential, the potential reaches a minimum ( $-\epsilon$ ) at separation  $2^{1/6}\sigma$  (Figure A.2) [2]. This separation corresponding to the minimum energy can be found by solving  $U'(r)=0$ .

Using the truncated Lennard-Jones potential to model hard sphere repulsion therefore effectively involves shifting the Lennard-Jones potential up by  $\epsilon$  and assuming the potential as zero at separations greater than or equal to  $2^{1/6}\sigma$  (Figure A.3) [2].

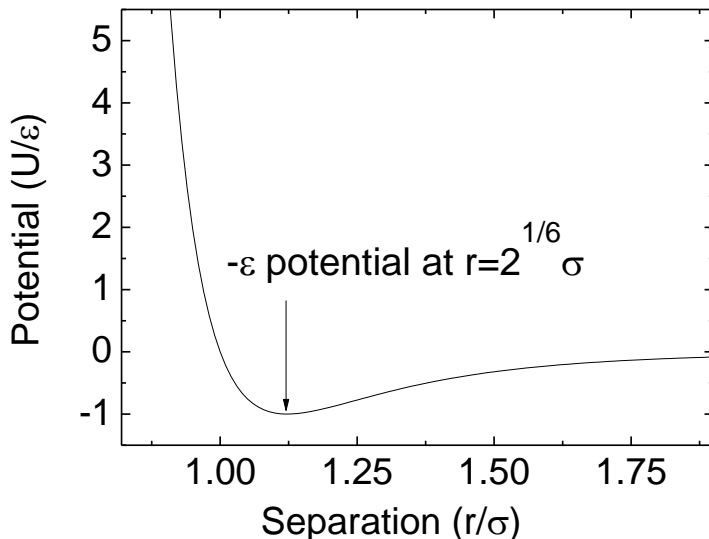
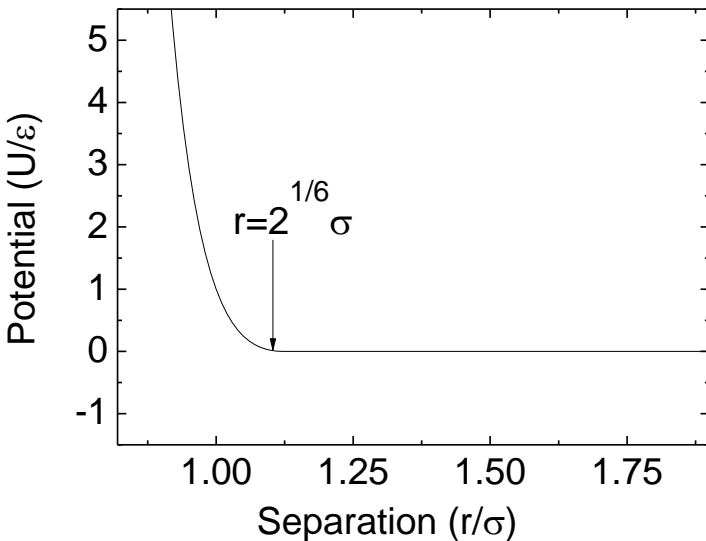


Figure A.2- Standard Lennard-Jones potential



**Figure A.3- Hard sphere potential with Lennard-Jones repulsion (i.e. the truncated Lennard-Jones potential)**

For the standard Lennard-Jones model, the  $\sim(1/r)^{12}$  term dominates at small separations when the particles are close together and experiencing repulsion. The  $\sim(1/r)^6$  term dominates at larger separations and corresponds to the attractive part. When overall attraction dominates, the potential is negative since zero energy corresponds to an infinite separation distance. When repulsion dominates, the potential is positive [1, 2].

As mentioned, the force acting on a particle can be determined from the gradient of the potential energy [1, 3]. For particle i interacting with particle j:

$$\mathbf{F}_{ij} = -\nabla U_{ij} \quad \text{Equation A.9}$$

This therefore gives (when  $r \leq 2^{1/6}\sigma$ ):

$$\mathbf{F}_{ij} = \frac{24\varepsilon}{r^2} \left[ 2 \left(\frac{\sigma}{r}\right)^{12} - \left(\frac{\sigma}{r}\right)^6 \right] \mathbf{r} \quad \text{Equation A.10}$$

### A.2.3.2 Drag Force (and Langevin Equation)

Since the system of interest involves colloid particles in a solvent, a drag force term was added to the model to represent the hydrodynamic effects of the particles' movement in the solvent.

This drag term is obtained from Stokes' law [4, 6]:

$$\mathbf{F}_D = 6\pi\eta a v \quad \text{Equation A.11}$$

Here  $\eta$  is the solvent viscosity,  $a$  is the particle radius and  $v$  is the particle velocity.

The Langevin equation expresses the force acting on a particle in a suspension as [7]:

$$Force = \frac{dp}{dt} = force\ due\ to\ other\ particles - drag\ force + random\ force$$

$$\mathbf{F}_i = \mathbf{F}_{interactions} - \delta v + \mathbf{F}_R \quad \text{Equation A.12}$$

Here  $p$  is momentum and  $\delta = 6\pi\eta a$ .

The drag force and random force represent the effects of the solvent molecules on the particles. The random force represents Brownian motion. Brownian motion is caused by thermal fluctuations in the solvent and effectively results in the particles being constantly bombarded by random impacts of solvent molecules [4]. Since the force is stochastic, over time it has an average value of zero [4, 8].

For simplicity, this random force/Brownian motion is neglected for the simulations. Given the large particle size and moderate shear rates used in the lab experiments, the effects of Brownian motion would have been negligible experimentally, as outlined in [Chapter 1](#).

This leads to:

$$\mathbf{F}_i = \mathbf{F}_{interactions} - \delta v \quad \text{Equation A.13}$$

Where:

$$\delta = 6\pi\eta a \quad \text{Equation A.14}$$

From the Stokes-Einstein equation (as detailed in [Chapter 1](#)) [4, 6]:

$$\delta = 6\pi\eta a = \frac{k_B T}{D} \quad \text{Equation A.15}$$

Here  $k_B$  is the Boltzmann constant,  $T$  is the absolute temperature and  $D$  is the diffusion coefficient.

### A.2.3.3 Newton's Third Law

As mentioned, from Newton's 3<sup>rd</sup> Law of Motion, every action has an equal and opposite reaction [2].

Therefore for every particle pair:

$$\mathbf{F}_{ij} = -\mathbf{F}_{ji} \quad \text{Equation A.16}$$

This means that the force only needs computed once for each pair of particles, significantly saving computing time [1].

### A.2.3.4 Newton's Second Law

The total force acting on a particular particle can be obtained by summing the relevant force contributions detailed [3]. Once the total force acting on a particle is known, its acceleration can be deduced from Newton's 2<sup>nd</sup> law.

$$\mathbf{F}_i = m_i \mathbf{a}_i \quad \text{Equation A.17}$$

$$\mathbf{F}_i = m_i \frac{d^2 \mathbf{r}_i}{dt^2} \quad \text{Equation A.18}$$

Calculating the trajectories of N particles therefore involves solving a set of 3N second order differential equations (x,y,z) [3]. Instead of solving 2<sup>nd</sup> order differential equations, a set of 6N first order equations are typically solved for (velocity and position in x,y,z) [3]. For this, a suitable integration method must be used.

$$\mathbf{F}_i = m_i \frac{d\mathbf{v}_i}{dt} \quad \text{Equation A.19}$$

where:

$$\mathbf{v}_i = \frac{d\mathbf{r}_i}{dt} \quad \text{Equation A.20}$$

### A.2.3.5 Other Forces

Recent literature suggests that the addition of lubrication and/or frictional forces is necessary for discontinuous shear thickening and jamming behaviour to become apparent in simulations [9-12]. This work supports the idea that DST and jamming involve a stress-induced transition from lubrication to frictional contacts. The idea suggests that at low stresses, the particles do not touch since contacts are lubricated. At higher stresses, however, the repulsive interaction that prevents contacts is overcome. This leads to networks of frictional particles forming, and is

associated with much higher viscosities [9, 12]. Further exploration of this would be an interesting area of future work. In this chapter we focus on determining whether jamming effects can be observed without lubrication and friction forces as a first step.

#### A.2.4 Finding a Suitable Integrator

Since the integration of the equations of motion is the key part of MD simulations, finding a reliable numerical integration algorithm is crucial [2, 13, 14]. A review of some of the many integrators that were investigated is given, followed by details of the integrator that was chosen and the reasoning for this choice.

Many algorithms are available and are based on finite difference methods. This involves splitting the time into time-steps ( $\Delta t$ ) and integrating the equations of motion at finite time intervals ( $t + \Delta t$ ), i.e. a continuous process is represented as discrete [2, 14].

Finite difference methods are usually based on a Taylor expansion [1]. A Taylor expansion can be used to represent a continuous function as an infinite sum of terms that are calculated from the values of the function's derivatives at a single point.

For the equations of motion:

$$\mathbf{r}(t + \Delta t) = \mathbf{r}(t) + \frac{1}{1!} \frac{d\mathbf{r}}{dt} \Delta t + \frac{1}{2!} \frac{d^2\mathbf{r}}{dt^2} \Delta t^2 + \dots \quad \text{Equation A.21}$$

$$\mathbf{v}(t + \Delta t) = \mathbf{v}(t) + \frac{1}{1!} \frac{d\mathbf{v}}{dt} \Delta t + \frac{1}{2!} \frac{d^2\mathbf{v}}{dt^2} \Delta t^2 + \dots \quad \text{Equation A.22}$$

Due to their approximations, errors are associated with finite difference methods. Since algorithms are based on a Taylor expansion, truncation errors result due to the cut-off/truncation of higher order terms. Round-off errors may also occur due to the finite number of digits used to represent a number in the code. Both can be reduced by using suitably small time-steps [1]. Errors typically get larger with time, since each result is calculated from a previously inaccurate result.

A good integrator should generally have the following properties [2, 13, 14]:

- It should satisfy known conservation laws for energy and momentum.
- It should be time-reversible (since Newton's equations of motion are).

- It should allow the use of a reasonably long time-step.
- It should duplicate the true trajectory as closely as possible.
- It should be fast and require little memory.
- It should be simple and easy to implement.

Finite difference methods can be classified as either predictor or predictor-corrector methods. In predictor methods, atom or particle co-ordinates are updated from quantities that are either known from previous time-steps or are calculated in the current time-step [2]. Euler and Verlet algorithms and their modifications are examples of predictor methods [2, 15]. These are discussed in more detail in A.2.4.1.

Predictor-corrector methods are more complex. They involve predicting new particle co-ordinates, using the predicted co-ordinates to calculate the value of some function (e.g. force) to estimate the error in the predicted values, and subsequently using this to correct the initial predictions. The Gear predictor-corrector algorithm is the most common example and it is used in the simulations here [14, 16]. It is discussed in more detail in A.2.4.2.

#### A.2.4.1 Predictor Algorithms

Some of the main predictor algorithms will briefly be detailed and discussed to allow a clear insight into why the chosen algorithm was used.

##### Euler (explicit)

Euler's method is perhaps the most common numerical integration method.

$$\mathbf{r}(t + \Delta t) = \mathbf{r}(t) + \mathbf{v}(t)\Delta t \quad \text{Equation A.23}$$

$$\mathbf{v}(t + \Delta t) = \mathbf{v}(t) + \mathbf{a}(t)\Delta t \quad \text{Equation A.24}$$

Acceleration is determined from forces on the particles at their initial position ( $\mathbf{r}(t)$ ). This allows the velocity at  $t+\Delta t$  to be deduced. The new displacement is based on the initial velocity only- this is not good if the velocity is changing (which is likely due to acceleration). The acceleration is also likely to change with time (i.e. it is not constant over the time-step). These factors make the Euler method poor [13]. It is unstable, suffering from major energy drifts, and very inaccurate unless time-steps are very small. Due to these factors, it is not a suitable integration algorithm for MD [17].

### Backward Euler (implicit)

This method is more accurate than the original Euler method. It uses the future states (velocity and acceleration at  $t+\Delta t$ ) of the system for the integration. It is too computationally expensive and not accurate or efficient enough for MD, however [17].

$$\mathbf{r}(t + \Delta t) = \mathbf{r}(t) + \mathbf{v}(t + \Delta t)\Delta t \quad \text{Equation A.25}$$

$$\mathbf{v}(t + \Delta t) = \mathbf{v}(t) + \mathbf{a}(t + \Delta t)\Delta t \quad \text{Equation A.26}$$

### Semi-Implicit Euler

This method combines the methods of Euler and Backward Euler to give a more accurate and efficient method. It is still not competitive compared to other integration methods and is rarely used [17].

$$\mathbf{r}(t + \Delta t) = \mathbf{r}(t) + \mathbf{v}(t + \Delta t)\Delta t \quad \text{Equation A.27}$$

$$\mathbf{v}(t + \Delta t) = \mathbf{v}(t) + \mathbf{a}(t)\Delta t \quad \text{Equation A.28}$$

Here the acceleration is determined by resolving the forces on the particles. This allows  $\mathbf{v}(t+\Delta t)$  to be deduced. This future velocity is then used to deduce the future position. Using a mixture of current step and next step data introduces a stabilising factor so iterations are less likely to become unstable [17].

### Original Verlet Algorithm

The original Verlet algorithm started off the ‘family’ of Verlet algorithms that now exist. These algorithms are perhaps the most widely used integration methods in molecular dynamics [2, 3].

The starting point is a Taylor expansion [2, 3, 13, 14].

$$\mathbf{r}(t + \Delta t) = \mathbf{r}(t) + \frac{1}{1!} \frac{d\mathbf{r}}{dt} \Delta t + \frac{1}{2!} \frac{d^2\mathbf{r}}{dt^2} \Delta t^2 + \dots \quad \text{Equation A.29}$$

$$\mathbf{r}(t - \Delta t) = \mathbf{r}(t) - \frac{1}{1!} \frac{d\mathbf{r}}{dt} \Delta t + \frac{1}{2!} \frac{d^2\mathbf{r}}{dt^2} \Delta t^2 + \dots \quad \text{Equation A.30}$$

Adding these (and assuming 3<sup>rd</sup> order terms and beyond are negligible) gives:

$$\mathbf{r}(t + \Delta t) = 2\mathbf{r}(t) - \mathbf{r}(t - \Delta t) + \frac{d^2\mathbf{r}}{dt^2} \Delta t^2 \quad \text{Equation A.31}$$

This is known as the Verlet algorithm. It allows the positions of particles to be advanced without determining their velocities, since it involves the direct solution of a 2<sup>nd</sup> order equation [14].

The velocity is, however, often useful (e.g. for determining kinetic and total energy etc.) and can be obtained from [14]:

$$v(t) = \frac{r(t+\Delta t) - r(t-\Delta t)}{2\Delta t} \quad \text{Equation A.32}$$

Main advantages of the Verlet algorithm include that it is easy to implement, it is time reversible and it conserves energy well, even over large time-steps. A disadvantage is that it is not self-starting- for example, at t=0, an estimate is required for its position at t=-Δt. This, however, has little impact. A more important disadvantage is that its numerical precision is not optimal [2]. It also doesn't handle velocities well; calculated velocities lag behind the calculated positions by one time-step [2]. These drawbacks have led to a number of modifications, including the Verlet Leap-Frog algorithm.

### Verlet Leap-Frog Algorithm

The Verlet- Leap-Frog algorithm is perhaps the simplest adaption of the Verlet algorithm [13]. It evaluates the velocity at half time intervals and uses these to compute the displacement [2, 13]. Unlike the original Verlet algorithm, velocity calculations are an integral part of the algorithm [2].

$$r(t + \Delta t) = r(t) + v\left(t + \frac{\Delta t}{2}\right) \Delta t \quad \text{Equation A.33}$$

$$v\left(t + \frac{\Delta t}{2}\right) = v\left(t - \frac{\Delta t}{2}\right) + a(t)\Delta t \quad \text{Equation A.34}$$

The velocity at t+Δt/2 is deduced using the velocity at the previous half time interval and the current acceleration. This is then used to determine the next position [2].

The current velocity can be determined from an average of the velocity at the next and previous half time intervals [2]:

$$v(t) = \frac{v\left(t + \frac{\Delta t}{2}\right) + v\left(t - \frac{\Delta t}{2}\right)}{2} \quad \text{Equation A.35}$$

This method is generally precise (more so than the original Verlet) since it uses differences between smaller quantities (due to half time-steps). Its disadvantages

include that the calculation of the current velocity relies on averages of the half time step velocities. Its velocity calculations lag behind the position calculations (since  $v(t+\Delta t/2)$  is required for  $v(t)$  [13]. It is also not self-starting [2].

The Verlet Leap-Frog algorithm was implemented in some of the simulations. While reasonable, it was found that the predictor-corrector method subsequently detailed was more effective (in terms of energy conservation and accuracy). The predictor-corrector method was therefore used for subsequent simulations.

### A.2.4.2 Predictor-Corrector Algorithms

#### Gear Predictor-Corrector

As mentioned, predictor-corrector methods are more complex than simply predictor methods, due to the correction stage. The Gear predictor-corrector algorithm is the most common example and is commonly used in molecular dynamics simulations [2, 16].

It involves first of all estimating the position, velocity and acceleration etc. at  $t=t+\Delta t$  using a Taylor expansion [2, 13, 14].

For position:

$$\mathbf{r}^p(t + \Delta t) = \mathbf{r}(t) + \frac{1}{1!} \frac{d\mathbf{r}}{dt} \Delta t + \frac{1}{2!} \frac{d^2\mathbf{r}}{dt^2} \Delta t^2 + \frac{1}{3!} \frac{d^3\mathbf{r}}{dt^3} \Delta t^3 + \dots \quad \text{Equation A.36}$$

Which could be written as:

$$\mathbf{r}^p(t + \Delta t) = \mathbf{r}(t) + \frac{1}{1!} \mathbf{v}(t) \Delta t + \frac{1}{2!} \mathbf{a}(t) \Delta t^2 + \frac{1}{3!} \mathbf{b}(t) \Delta t^3 + \dots \quad \text{Equation A.37}$$

Where  $\mathbf{a}(t)$  is acceleration and  $\mathbf{b}(t)$  is the 3<sup>rd</sup> order derivative. Superscript p denotes predicted values.

For velocity:

$$\mathbf{v}^p(t + \Delta t) = \mathbf{v}(t) + \frac{1}{1!} \frac{d^2\mathbf{r}}{dt^2} \Delta t + \frac{1}{2!} \frac{d^3\mathbf{r}}{dt^3} \Delta t^2 + \dots \quad \text{Equation A.38}$$

$$\mathbf{v}^p(t + \Delta t) = \mathbf{v}(t) + \frac{1}{1!} \mathbf{a}(t) \Delta t + \frac{1}{2!} \mathbf{b}(t) \Delta t^2 + \dots \quad \text{Equation A.39}$$

For acceleration:

$$\mathbf{a}^p(t + \Delta t) = \mathbf{a}(t) + \frac{1}{1!} \frac{d^3\mathbf{r}}{dt^3} \Delta t \quad \text{Equation A.40}$$

$$\mathbf{a}^p(t + \Delta t) = \mathbf{a}(t) + \frac{1}{1!} \mathbf{b}(t) \Delta t \quad \text{Equation A.41}$$

Due to the need to truncate the expansion, the predicted values are not accurate [2]. Therefore a correction procedure takes place where the predicted values are corrected.

To correct, the acceleration based on the new predicted co-ordinates at  $t=t+\Delta t$  is determined (from the force acting on the particle). This requires a re-evaluation of the force and is therefore computationally expensive [2].

The difference between this ‘corrected’ acceleration and predicted acceleration is then determined. This yields an estimate of error size in the prediction stage [14].

$$\Delta \mathbf{a}(t + \Delta t) = \mathbf{a}^c(t + \Delta t) - \mathbf{a}^p(t + \Delta t) \quad \text{Equation A.42}$$

Superscript c denotes corrected values.

The predicted values and this error estimate are then used in a correction procedure.

$$\mathbf{r}^c(t + \Delta t) = \mathbf{r}^p(t + \Delta t) + c_0 \Delta \mathbf{a}(t + \Delta t) \quad \text{Equation A.43}$$

$$\mathbf{v}^c(t + \Delta t) = \mathbf{v}^p(t + \Delta t) + c_1 \Delta \mathbf{a}(t + \Delta t) \quad \text{Equation A.44}$$

$$\mathbf{a}^c(t + \Delta t) = \mathbf{a}^p(t + \Delta t) + c_2 \Delta \mathbf{a}(t + \Delta t) \quad \text{Equation A.45}$$

etc.

$c_n$  are constants associated for position ( $n=0$ ), velocity ( $n=1$ ) and acceleration ( $n=2$ ). Suitable values of the constants have been determined by Gear [16]. The constants depend on the order of the equations being solved (here it is second order since the 2<sup>nd</sup> derivative of position is compared to the computed acceleration) and the extent of truncation [14]. The Gear predictor-corrector algorithm cannot be truncated before the third term since the algorithm depends on the evaluation of the acceleration in the corrector step. The use of higher derivatives improves the accuracy of the algorithm. In the simulations a 5<sup>th</sup> order predictor-corrector algorithm was used[14].

The Gear algorithms are slower than the Verlet algorithms, for example, but the difference in speed is not significant [2]. Although the Verlet algorithms are easier to implement than the Gear predictor-corrector algorithm, the Gear predictor-corrector algorithm is not particularly difficult to implement [2]. The Gear predictor-corrector

algorithm's main advantage over other algorithms is its accuracy [2]. For reasonably small time-steps and reasonably short simulations, a 4<sup>th</sup> or 5<sup>th</sup> order Gear algorithm (as was used in the simulations) is more accurate than the Verlet algorithms [2]. These reasons are why it was chosen for the simulations.

## A.2.5 Periodic Boundary Conditions

Molecular dynamics systems typically contain a few hundred particles arranged in a box. Due to the small sample size, a large fraction of the particles will be at/near the surface of the box, rather than being in the bulk. This is undesirable since forces experienced by particles at a surface are different from those in the bulk [1-3].

Another problem with a single box is that over time, it is likely that a particle will pass through the walls and out of the system. This has the undesirable effect of reducing the density [3].

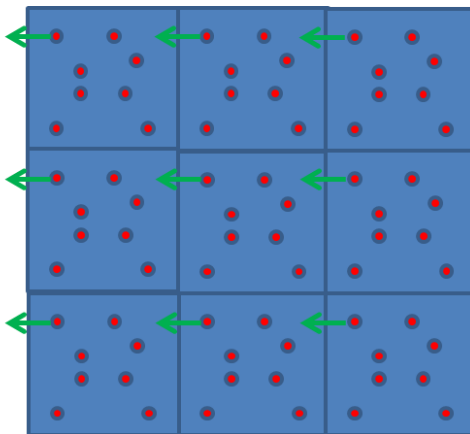


Figure A.4- Periodic boundary conditions

To overcome these problems, periodic boundary conditions are used. This involves creating an infinite lattice that replicates the cubic simulation box throughout space (Figure A.4). These replicas are all identical copies of the initial box, and each particle undergoes the same time development as its image in every other copy [2, 3].

When a particle leaves a box, its counterpart in a neighbouring box enters through the opposite face. This keeps the density constant. Since the central box is now devoid of boundaries, surface effects are eliminated [2, 3].

## A.2.6 Minimum Image Convention

Due to the periodic boundary conditions, there are an infinite number of particles which would result in infinite calculations. To overcome this problem, a minimum image convention is introduced. With this, for the purpose of calculating interaction potentials, a particle is always assumed to interact with particles that are within a certain distance from it only- i.e. it only interacts with the closest periodic images of the other N-1 particles. For example, if particle i interacts with particle j, i will only interact with the closest particle j: this may or may not be in the original simulation box [2, 3].

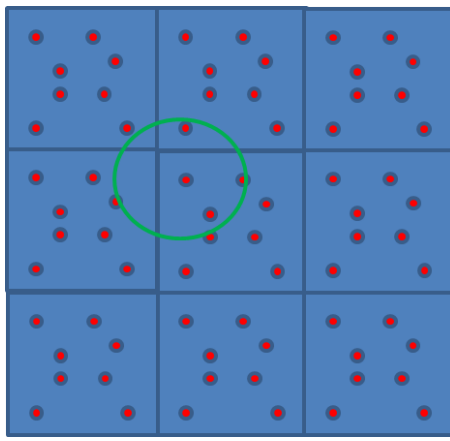


Figure A.5- Minimum image convention

Since the model used for the hard sphere interactions is short ranged, a cut-off distance is introduced. This means that only particles that lie within a sphere of radius  $R_{\text{cut}}$  from the particle of interested are considered in the particle-particle force calculations (Figure A.5). The cut-off distance can be any distance up to half the length of the simulation box. A higher cut-off would violate the minimum image convention [2, 3].

For the purposes of the simulations,  $R_{\text{cut}}=2^{1/6}$  was used since beyond this, the hard sphere interaction potential was assumed to be zero (see A.2.3.1).

## A.2.7 Applying Shear to Simulations

Moving periodic boundary conditions can be used to induce shear flow in simulations and this idea was first proposed by Lees and Edwards [18]. This makes use of ‘sliding brick’ periodic boundary conditions and can induce planar Couette flow in simulations, much like the shear regime in the shear cells used in [Chapter 4](#) and [Chapter 5](#). These Lees-Edwards periodic boundary conditions enable homogeneous simulations of shear flow to be performed where the Reynolds number is low and the velocity profile is approximately linear [2, 7, 18].

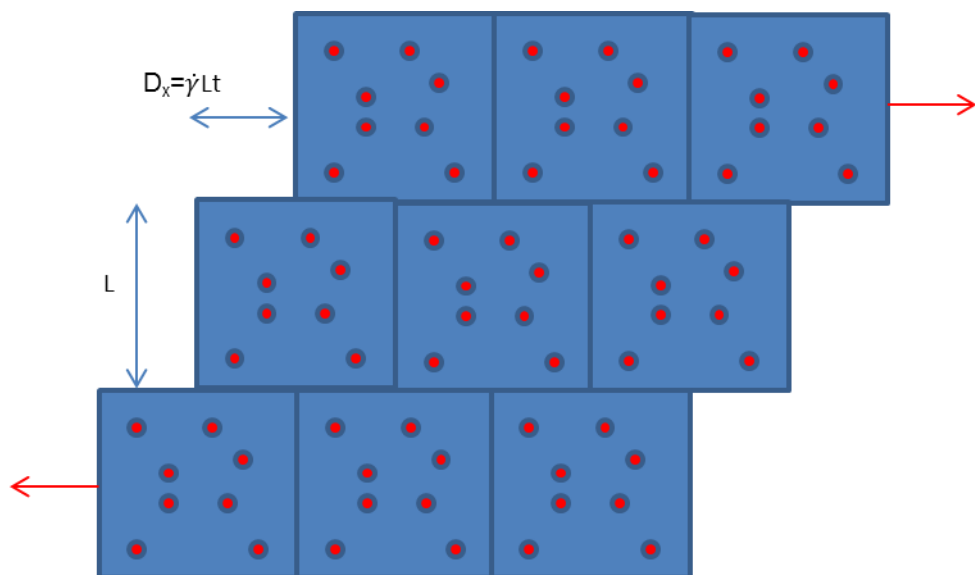
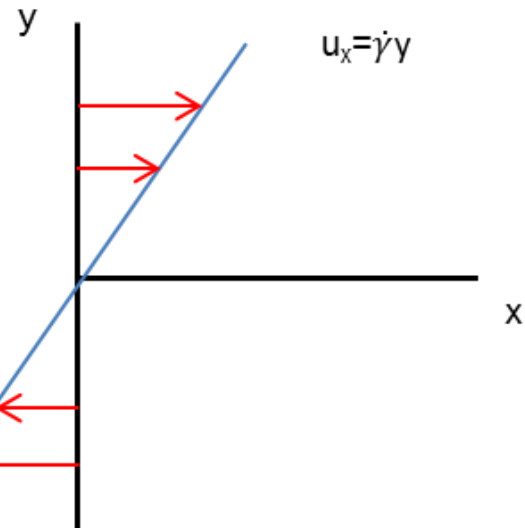


Figure A.6- Lees-Edwards sliding boundary conditions

With Lees-Edwards periodic boundary conditions, as before, the central cell is replicated infinitely in the x,y and z directions. Now boxes above the central cell move right and boxes below move left (Figure A.6). The velocities of this movement are determined by the shear rate ( $\dot{\gamma}=dv/dy$ ).

The motion of the cell images is such that their individual origins move with an x-velocity that is proportional to the y-co-ordinate of the particular cell origin [7]. In time, assuming the Reynolds number is sufficiently small and turbulence does not occur, the motion of image particles above and below a given cell, and movement of particles in and out of the cell, will induce a linear streaming velocity ( $\mathbf{u}(r)$ ) on each particle in the cell (Figure A.7) [7].



**Figure A.7- Lees-Edwards linear velocity profile**

$$\mathbf{u}(r, t) = i\dot{\gamma}y \quad \text{Equation A.46}$$

Here  $\mathbf{u}$  is velocity,  $r$  is position,  $t$  is time,  $i$  is the  $x$  direction,  $\dot{\gamma}$  is the shear rate and  $y$  is the  $y$  position.

The shift distance in a given time ( $D_x$ ) and velocity of the cells above and below the original cell ( $v_x$ ) will be:

$$D_x = \dot{\gamma}Lt \quad \text{Equation A.47}$$

$$v_x = \dot{\gamma}L \quad \text{Equation A.48}$$

Where  $L$  is the height of the box.

When a particle leaves through a  $y$ -face of the cell (i.e. the top or bottom) the image particle that replaces it will not have the same  $x$ -velocity or  $x$ -position. It is this effect that causes a stable linear streaming velocity profile to be generated [7].

Consideration of particle movement in more detail:

The laboratory velocity of a particle is the sum of two parts: the peculiar/thermal velocity ( $\mathbf{c}_i$ ) and the streaming velocity mentioned ( $\mathbf{u}(r)$ ) [7, 19].

$$\mathbf{v}_i = \dot{\mathbf{r}}_i = \mathbf{c}_i + \mathbf{u}(r_i) \quad \text{Equation A.49}$$

The streaming velocity is a function of  $y$  only, so only needs considered in  $y$ -direction boundary crossings.

By definition, the peculiar velocity of each particle and its periodic images are equal [7].

Therefore a particle moving out of the bottom of the box is replaced by its image particle at the top of the box [2, 7]:

$$\mathbf{r}_i^{new} = \mathbf{r}_i^{original} + \mathbf{j}L + i\dot{\gamma}Lt \quad \text{Equation A.50}$$

Here  $i$  is the  $x$  direction and  $j$  is the  $y$  direction.

And similarly, a particle moving out the top of the box is replaced by its image particle at the bottom of the box [7]:

$$\mathbf{r}_i^{new} = \mathbf{r}_i^{original} - \mathbf{j}L - i\dot{\gamma}Lt \quad \text{Equation A.51}$$

The change in laboratory velocity can be found from the derivative of these [7].

A main disadvantage of Lees-Edwards boundary conditions is that it takes time for the linear velocity profile to form. It therefore takes particles this amount of time to realise that shear is taking place [7]. The method is, however, sufficient for the purpose of these simulations and is widely used [2].

## A.2.8 Neighbour List, Linked Cells and Look-up Table

Periodic boundary conditions reduce computational costs since calculations involving particle separations greater than a specified cut-off distance are not included. Other ‘book-keeping’ methods are also used to reduce computational cost further.

Verlet proposed the idea of a neighbour list to reduce computation time [15]. This method involves keeping a periodically updated list of the neighbours of each particle. Therefore instead of searching repeatedly for neighbouring particles, the neighbours are found from the list and their interactions are calculated. Typically particles within a slightly extended cut-off distance are stored in the list. This therefore avoids searching for particles that are out with the contributing region. The added ‘buffer’ overcomes the problem of those particles that may move into the cut-off distance within the time steps before the list is next updated [1, 2].

Neighbour lists reduce computation substantially, particularly for systems with more than 500 particles, such as these simulations [2]. An update interval of every 10-20 steps is usually sufficient, but depends on simulation specifics. It can also be programmed to update automatically, for example when the magnitudes of the two largest displacements exceeds the buffer distance. This avoids updating the list more than necessary [2].

Another technique used for reducing computation is the linked cells method. It involves splitting the simulation box into a lattice of linked cells. At each time-step, the particles are binned into 3D cells whose length is equal to (or slightly larger) than the cut-off distance. This means that the task of finding the neighbours of a given particle is reduced to checking 27 bins: the cell the particle is in and the 26 surrounding ones [1, 2].

This technique is useful for large simulations with the number of particles exceeding 1000, since testing every pair as specified by the neighbour list becomes increasingly inefficient [2].

A combination of the neighbour list and linked cells method can be used (and is used in the simulations) to reduce computational work further and speed up simulations [1]. With this combined method, particles are only binned into cells every few time steps for the purpose of forming neighbour lists. At intermediate time steps, the neighbour lists alone are used to find neighbours. This has a significant saving over the standalone linked cells method since there are significantly fewer particles to check in a sphere of radius  $R_{\text{cut}}$  (plus buffer) than a cube of  $27 R_{\text{cut}}^3$  [1].

Although not used in the simulations, a final method worth mentioning is the ‘look-up table’ method. With this, pair-pair potentials are determined across a suitable range of separations at the start of the simulation and stored in a look-up table. Now, rather than calculating the potential for each separation during the simulation, the corresponding potential is obtained by interpolating from the look-up table [2].

## A.2.9 Time-step Considerations

Choosing a suitable time-step for the simulations is important for numerical accuracy and conserving energy. If the time-step is too large, systems can become unstable, with the total energy rising rapidly with time. This is caused by the large time-step resulting in particles overlapping (or very close to overlapping), causing a massive repulsive force between them [13, 20]. For these simulations, various time steps were investigated and one that gave stable results while still allowing simulations to run in a reasonable time was chosen.

## A.2.10 Reduced Units

Since sizes involved in molecular dynamics are very small, rather than working in atomic-scale units (such as pico, nano etc.), it is most popular to use dimensionless- or reduced- units. For this, all observable quantities are made dimensionless with respect to their characteristic values [1].

Scaling is typically done with the following parameters: particle size/diameter ( $\sigma$ ), particle mass ( $m$ ) and particle energy ( $\epsilon$ ). Values are given to these and other parameters are given in terms of these reference values [1]. The energy value used is usually chosen arbitrarily for a typical particle-particle pair potential, for example of a noble gas such as Argon. This is the magnitude of the energy minimum from the Lennard-Jones potential.

For example (\* denotes reduced/dimensionless units):

$$\text{Potential energy: } U^* = \frac{U}{\epsilon} \quad \text{Distance: } r^* = \frac{r}{\sigma} \quad \text{Time: } t^* = \frac{t}{\sigma \sqrt{\frac{m}{\epsilon}}}$$

$$\text{Shear rate: } \dot{\gamma}^* = \frac{\dot{\gamma}}{\frac{1}{\sigma \sqrt{\frac{m}{\epsilon}}}} \quad \text{Shear stress: } \tau^* = \frac{\tau}{\frac{\epsilon}{\sigma^3}} \quad \text{Viscosity: } \eta^* = \frac{\eta}{\frac{\sqrt{m\epsilon}}{\sigma^2}}$$

The hard sphere potential in dimensionless form is therefore as follows:

$$U^*(r) = \begin{cases} 4 \left[ \left( \frac{1}{r^*} \right)^{12} - \left( \frac{1}{r^*} \right)^6 \right] + 1 & \text{if } r^* \leq 2^{\frac{1}{6}} \\ 0 & \text{otherwise} \end{cases} \quad \text{Equation A.52}$$

## A.2.11 Stress Tensor

In the simulations, the stress tensor was determined and this was used for much of the analysis.

Consider a cuboid, with edges parallel to the co-ordinates directions (Figure A.8).

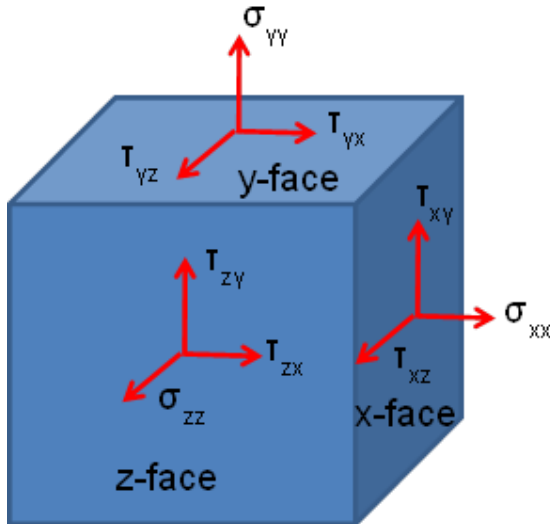


Figure A.8- Stress tensor arrangement

The faces on the cuboid are named according to the direction of their normal. Therefore there are two x-faces: one facing greater values of x and one facing lesser values of x. The same applies for the y and z directions. The force on the x-plane,  $\mathbf{F}_x$ , can be split into components parallel to the co-ordinates' directions:  $\mathbf{F}_{xx}$ ,  $\mathbf{F}_{xy}$  and  $\mathbf{F}_{xz}$ . The stress on the x-plane can be found by dividing the force on the x-plane by the area of the x-face [21]. This results in the following components:

$$\sigma_{xx} \quad \tau_{xy} \quad \tau_{xz}$$

$\sigma$  denotes a normal stress while  $\tau$  denotes a shear stress. Normal stresses are oriented normal to the plane on which they act, while shear stresses are oriented within the plane under consideration [6]. Stresses are named with the face/plane they are acting on first, followed by the direction the force is acting [21]. For example,  $\tau_{xy}$  represents a shear stress on the x-plane in the y direction.

Similarly on the y-face:

$$\tau_{yx} \quad \sigma_{yy} \quad \tau_{yz}$$

And on the z-face:

$$\tau_{zx} \quad \tau_{zy} \quad \sigma_{zz}$$

The stress tensor therefore has 9 components and takes the following form [21, 22]:

$$\boldsymbol{\sigma} = \begin{pmatrix} \sigma_{xx} & \tau_{xy} & \tau_{xz} \\ \tau_{yx} & \sigma_{yy} & \tau_{yz} \\ \tau_{zx} & \tau_{zy} & \sigma_{zz} \end{pmatrix}$$

The diagonals of the stress matrix therefore represent the normal stresses, while the remainder represent shear stresses [21]. The stresses on any plane with arbitrary orientation at a given point can be calculated from the nine stress components on the coordinate planes for that point. The stress tensor therefore completely describes the stress conditions around a point in the material [6].

In terms of sign convention, the stress on a face that is facing greater values of the co-ordinate is positive if the associated force acting in the direction of the coordinate is increasing [21].

The stress tensor is symmetric across the diagonal [6, 21, 22]. Therefore,  $\tau_{ij} = \tau_{ji}$ .

$$\boldsymbol{\sigma} = \begin{pmatrix} \sigma_{xx} & \tau_{xy} & \tau_{xz} \\ \tau_{xy} & \sigma_{yy} & \tau_{yz} \\ \tau_{xz} & \tau_{yz} & \sigma_{zz} \end{pmatrix}$$

To explain this, consider the system in two-dimensions (Figure A.9):

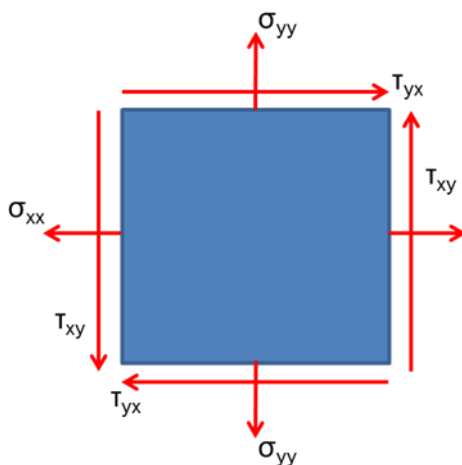


**Figure A.9- Stress tensor in 2D**

By taking moments, for equilibrium,  $\tau_{xy}$  must equal  $\tau_{yx}$  [6]. For the 3D stress tensor, the shear stresses therefore exist in complementary pairs and so the stress tensor contains 6 independent components [6, 21].

In the simulations, the stress tensor ( $P$ ) was determined from:

$$P = \sum_{i=1}^N (m_i \mathbf{v}_i \mathbf{v}_i + \sum_{j=i+1}^N \mathbf{r}_{ij} \mathbf{F}_{ij})$$

### A.2.12 Viscosity and Energy Dissipation

The shear viscosity could be estimated from the definition of viscosity ( $\eta$ ):

$$\eta = -\frac{\langle \tau_{xy} \rangle}{\dot{\gamma}} \quad \text{Equation A.53}$$

The rate of energy dissipation per unit volume could be determined from [6]:

$$\frac{\dot{E}}{V} = \tau_{xy} \times \dot{\gamma} \quad \left[ \frac{J}{m^3 s} \right] = \left[ \frac{N}{m^2} \right] \times \left[ \frac{1}{s} \right] \quad \text{Equation A.54}$$

Here  $\dot{E}$  is the rate of energy dissipation,  $V$  is the volume,  $\tau_{xy}$  is the shear stress in the  $xy$  direction and  $\dot{\gamma}$  is the shear rate.

This could be checked against the energy dissipated through drag.

This could be found by summing the drag force multiplied by the peculiar velocity for all particles (at a particular time).

$$\frac{\dot{E}}{V} = \frac{\sum_{i=1}^N \mathbf{F}_{Di} \times \mathbf{v}_i}{V} \quad \left[ \frac{J}{m^3 s} \right] = \frac{[N] \times \left[ \frac{m}{s} \right]}{[m^3]} \quad \text{Equation A.55}$$

### A.2.13 Energy

The potential energy of the system (at a given time) was determined from the truncated Lennard Jones potential for hard spheres, as detailed in A.2.3.1.

$$U(r) = \begin{cases} 4\epsilon \left[ \left( \frac{\sigma}{r} \right)^{12} - \left( \frac{\sigma}{r} \right)^6 \right] + \epsilon & \text{if } r \leq 2^{\frac{1}{6}}\sigma \\ 0 & \text{otherwise} \end{cases} \quad \text{Equation A.56}$$

The total potential energy was found by summing the potential of all particle-particle interactions.

$$E_{potential} = \sum_{i=1}^N \sum_{j=i+1}^N U_{ij} \quad \text{Equation A.57}$$

The kinetic energy of an individual particle was found from:

$$E_{kinetic\ i} = \frac{1}{2}mv_i^2 \quad \text{Equation A.58}$$

The total kinetic energy was found by summing the kinetic energy of each particle in the system.

$$E_{kinetic} = \sum_{i=1}^N \frac{1}{2}mv_i^2 \quad \text{Equation A.59}$$

The total system energy was found by summing the total potential and total kinetic energy.

$$E_{total} = E_{potential} + E_{kinetic} \quad \text{Equation A.60}$$

Under steady state, the total average energies should stay ~constant.

## A.3 Simulation Set-Up Procedures

In this section, main details of the simulation set-up and how they were run are given. The molecular dynamics codes used were originally written by Leo Lue. These were adapted and additional features were added.

### A.3.1 Simulation Properties

A molecular dynamics code written in C++ was used to perform molecular dynamics simulations. The main approach to writing the code was adapted from [2].

For the simulations, spherical particles (all with identical dimensions and mass) were initially arranged in the simulation box as an FCC lattice. Their initial velocity was set to zero. The box was split into cells in the x,y and z direction and there were 4 particles per cell. Typically, 7 cells in each direction were used, resulting in 1372 particles. The number of cells could be adjusted to produce simulations with different numbers of particles.

$$n_{particles} = 4 \times n_{cell}^{n_{dim}} \quad \text{Equation A.61}$$

Where  $n_{cell}$  is the number of cells per dimension and  $n_{dim}$  is the number of dimensions (which was three).

The number density of particles could be chosen, and this determined the dimensions of the box.

$$box\_length = \left( \frac{n_{particles}}{density} \right)^{\frac{1}{3}} \quad \text{Equation A.62}$$

This meant the number of particles was fixed for each run.

The volume fraction resulting from the number of particles and box volume could be determined from:

$$\Phi = \frac{V_{particles}}{V_{box}} = \frac{n_{particles} \times \frac{4}{3}\pi a^3}{\left( \frac{n_{particles}}{density} \right)} \quad \text{Equation A.63}$$

The shear rate and drag coefficient could be chosen and were the key control parameters that affected the simulation properties at a fixed density.

The shear rate, time-step and simulation lengths were chosen to be sufficient for a steady-state to be reached (where applicable) and for particles at the top of the box to traverse the box a sufficient number of times for well-established trends to be identified.

The simulations saved potential energy and kinetic energy data, as well as the components of the stress tensor, to a file for later processing. The system co-ordinates were saved at various time intervals to allow particle trajectories to be visualised. They were saved in .gro format and layout for ease of integration into visualisation software as detailed in A.3.2.

It is worth noting that while simulations started with particles arranged in the simulation box as an FCC lattice (i.e. ordered), similar results were obtained when the system started off with a random configuration.

### A.3.2 Simulation Visualisation

Trajectory visualisation was done using VMD (Visual Molecular Dynamics) software [23]. Scripts for VMD were written (using Tool Command Language- TCL). The scripts opened the .gro co-ordinates file obtained from the simulations and set the particles' co-ordinates for each saved time-step as a frame. The code then set the particles to a suitable shape and size and displayed the simulation box (and periodic images) if necessary (Figure A.10).

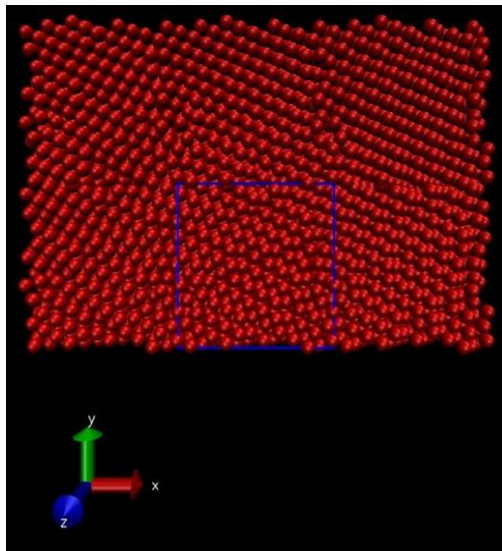
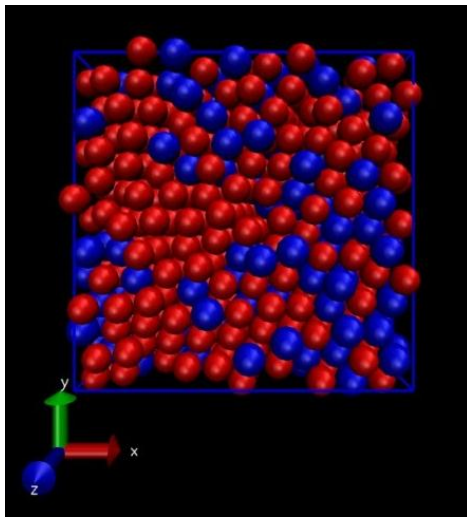


Figure A.10- VMD code resulting in simulation box and its periodic images being shown

An additional script was written to allow particles with a certain property (e.g. force acting on the particle above a certain threshold) to be coloured a particular way (Figure A.11). For this, the simulation code was adjusted to also produce a file listing, for example, the force on each particle at each time-step used in the trajectories. The VMD script obtained this additional data, assigned it to the necessary particle and coloured it accordingly. This method allowed a more detailed insight into particle behaviour during the simulations.



**Figure A.11- VMD code resulting in particles above a certain force to be coloured red, otherwise blue**

### A.3.3 Link to Experiments

Particle diameters, simulation densities/volume fractions, shear rates and drag coefficients were chosen to be as close to those used experimentally as possible.

The following parameters were used for the reduced unit reference values:

**Table A.1- Reduced unit reference values**

Particle diameter	$1 \times 10^{-6} \text{m}$
Particle mass	$6.2 \times 10^{-16} \text{kg}$
Particle energy	$1.7 \times 10^{-21} \text{J}$

The particle diameter and mass were those of the particles used experimentally (using the density of PMMA). There was uncertainty about which value of energy to use since  $\sim 1 \text{kJ/mol}$  which is commonly used in simulations refers to atoms while the

particles used in the experiment were significantly larger. This did, however, yield sensible results, so it was assumed sufficient.

By using these reference values, shear rates and drag coefficients in the region of those used in the experiments in [Chapter 4](#) and [Chapter 5](#) could now be deduced and used in the simulations.

### A.3.4 Correlation Determination

For the simulations, it was useful to see if certain parameters were correlated. For this, the Pearson Correlation Coefficient was determined.

The Pearson Correlation Coefficient ( $p$ ) measures the linear correlation between two variables [24]. It is defined as the covariance of the two variables divided by the product of their standard deviations and gives a value between +1 and -1.

$$p = \frac{\sigma_{xy}}{\sigma_x \sigma_y} \quad \text{Equation A.64}$$

Where  $\sigma_{xy}$  is the co-variance between  $x$  and  $y$ , while  $\sigma_x$  and  $\sigma_y$  are  $x$  and  $y$ 's standard deviations respectively [24].

This leads to [24]:

$$p = \frac{\sum_{i=1}^n [(y_i - \bar{y})(x_i - \bar{x})]}{\sqrt{\sum_{i=1}^n (y_i - \bar{y})^2 \sum_{i=1}^n (x_i - \bar{x})^2}} \quad \text{Equation A.65}$$

Here the bar denotes the mean.

1 suggests total positive correlation, 0 suggests no correlation, and -1 suggests total negative correlation. Table A.2 gives a 'rule of thumb' link between the value of the correlation coefficient and the strength of the relationship [24].

**Table A.2- Correlation coefficient strength guide [24]**

Coefficient magnitude	Strength of linear relationship
1.0-0.5	Strong
0.5-0.3	Moderate
0.3-0.1	Weak
0-0.1	None or very weak

## A.4 Results and Discussion

### A.4.1 Low Density Simulations

Densities corresponding to volume fractions below those where jamming occurred experimentally in [Chapter 4](#) and [Chapter 5](#) were investigated (i.e. volume fractions  $<0.56$ ). System densities ranging from 0.8 to 1 were used; these corresponded to volume fractions between 0.42-0.52. For these, the applied shear rate was varied (0.001- 0.1 in reduced units) and the stress and energy data were monitored. The systems were also inspected visually. It was found that running simulations for 3000 time units was sufficient for useful data to be recorded. Simulations with 7 cells in each direction, corresponding to 1372 particles, were used. A drag coefficient ( $6\pi\eta a$ ) of 1 was used.

Shear rates between 0.001 and 0.1 (in reduced units) corresponded to the magnitude of the shear rates encountered in the experiments in [Chapter 4](#) and [Chapter 5](#) ( $\sim 1-100\text{s}^{-1}$ ) when using the reduced unit reference values in Table A.1.

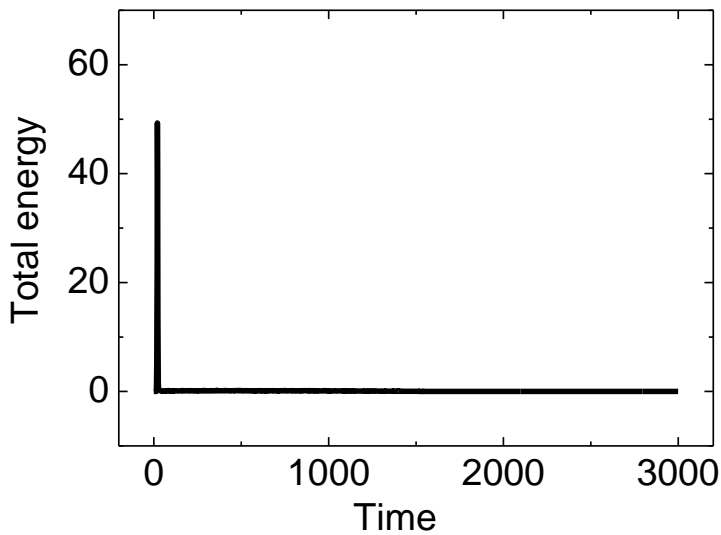
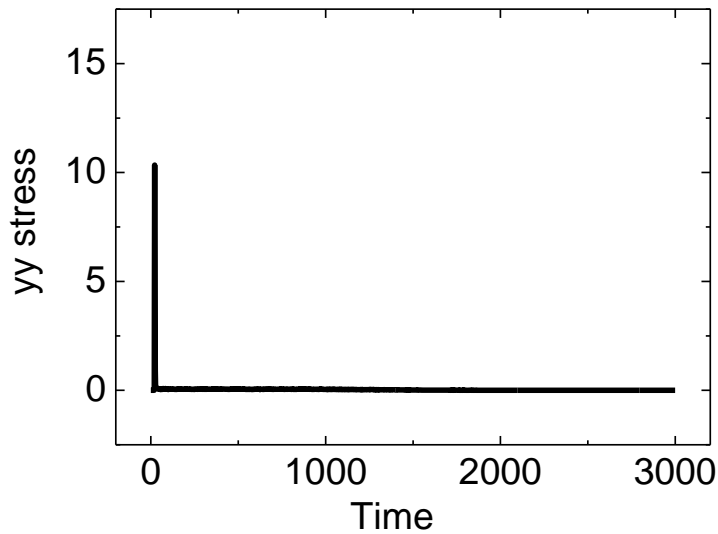


Figure A.12- Example total energy (kinetic plus potential) variation with time for  $\Phi=0.42$  and shear rate=0.01



**Figure A.13- Example stress (yy) variation with time for  $\Phi=0.42$  and shear rate=0.01. Similar was seen for the zz stress.**

With low  $\Phi$  simulations, once a steady state was reached, no fluctuations in the stress and energy data were observed (Figure A.12 and Figure A.13). Fluctuations in the yy normal stress would have corresponded to the sample pushing against the walls of the shear cells used experimentally. Fluctuations in the zz normal stress would have corresponded to the sample pushing out with the shear cell at the open surface. Stress fluctuations in these directions would therefore have indicated the sample was dilating.

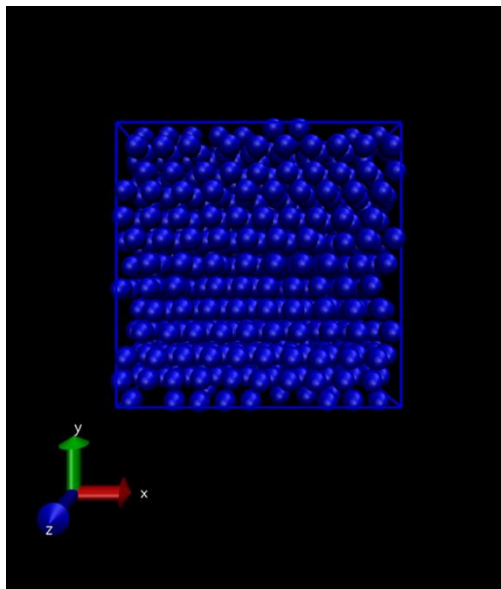
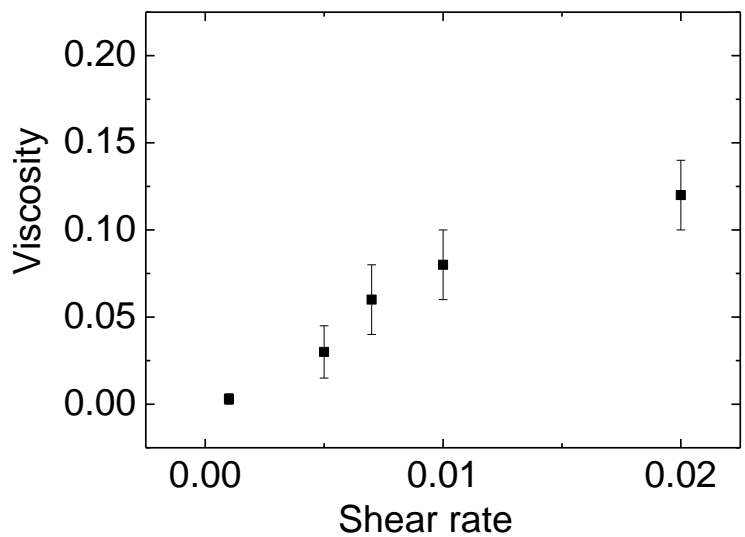


Figure A.14- Particles at  $t=3000$ ,  $\Phi=0.42$  and shear rate=0.01 example

Visually, particles behaved as expected, moving along with the flow, and eventually flowing in streamlines (Figure A.14). This was expected since colloidal suspensions have been shown to order under shear to minimise energy dissipation. This is often associated with a shear thinning response, however, shear thinning was not apparent in the simulations, as shown below [6, 25-27].

As the applied shear rate was increased, the magnitude of stresses also increased, as expected. The viscosity at a particular shear rate was found by dividing the negative of the time average of the  $xy$  shear stress by the shear rate (Equation A.53). Mild continuous shear thickening behaviour was found, which was expected for a system of the volume fractions used (Figure A.15) [6, 25, 28].



**Figure A.15-** Viscosity versus shear rate for  $\Phi=0.42$  sample at various shear rates. Error bars were from the standard deviation of data measured over different time intervals.

## A.4.2 Higher Density Simulations

Simulations were performed on higher density systems, with volume fractions now corresponding to the region where jamming was found experimentally in [Chapter 4](#) and [Chapter 5](#) ( $\Phi \geq 0.56$ ). For these, densities ranging from 1.02-1.2 were used. These corresponded to volume fraction ranging from 0.53-0.63. The applied shear rate was varied (0.001- 0.1 in reduced units) and the stress and energy data were monitored. The systems were also inspected visually. Simulations with 7 cells in each direction, corresponding to 1372 particles, were used. A drag coefficient ( $6\pi\eta a$ ) of 1 was used. It was found that running simulations for 3000 time units was sufficient for useful data to be recorded.

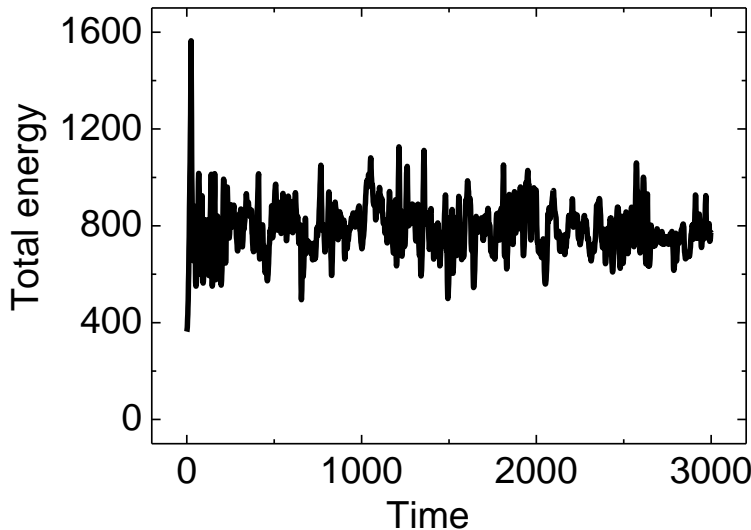


**Figure A.16- Example total energy variation with time for  $\Phi=0.58$  and shear rate=0.007 (equivalent of  $\sim 10\text{s}^{-1}$  in experiments)**

With volume fractions greater than or equal to 0.54, significant fluctuations in stress (shear and normal) and energy were observed (Figure A.16, Figure A.17 and Figure A.18). Normal stress fluctuations (Figure A.17) corresponded to the system dilating. These showed the system expanding in the yy direction (corresponding to the material pushing against the walls of the shear cell used experimentally) and the zz direction (corresponding to the sample pushing out with the shear cell at the open surface). This suggested a similarity between the experimental work in [Chapter 4](#) and [Chapter 5](#) and the simulations. The volume fraction beyond which this

behaviour was seen also corresponded closely to the critical volume fraction found experimentally.

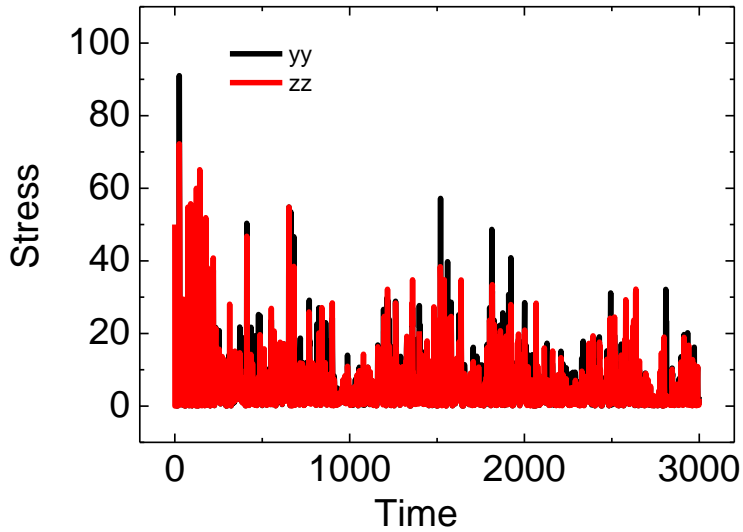


**Figure A.17-** Example normal stress (yy and zz) variation with time for  $\Phi=0.58$  and shear rate=0.007.

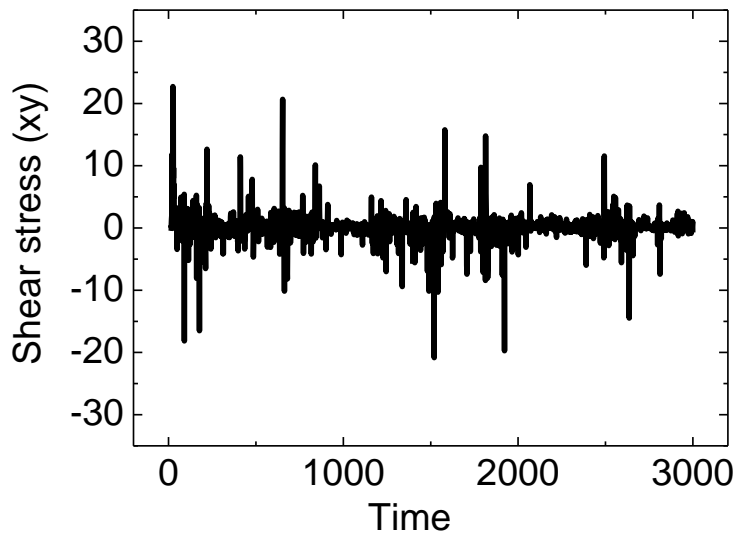


**Figure A.18-** Example shear stress variation with time for  $\Phi=0.58$  and shear rate=0.007.

Visually it was noticed that the particles no longer moved along with the flow as before. Particles now formed cluster-like regions that ‘rolled’ and ‘tumbled’ together

in the flow, often moving perpendicular to the velocity direction (Figure A.19). These regions did not follow streamlines and caused significant disruption in the flow. They had a resemblance to what was seen visually in [Chapter 4](#), where the material jammed and fractured. As detailed in A.4.6, when these clustered regions are considered in more detail, the presence of clusters corresponded to stress fluctuations. When no clusters were present, the stresses did not fluctuate. This suggested that clustering was related to the stress fluctuations and dilation.

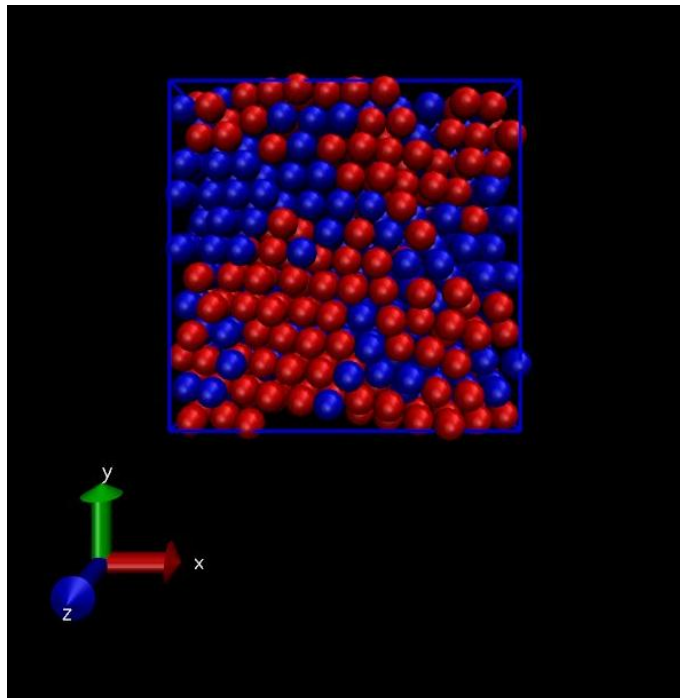


**Figure A.19- Particles at t=2710,  $\Phi=0.58$  and shear rate=0.007 example. Red denotes clustered regions (detailed in A.4.6).**

It was also noticed that the particle arrangement had a strong degree of order to it. This is considered in more detail in A.4.7.

As the applied shear rate was increased, the magnitude of the stresses also increased, as in A.4.1. For calculating the viscosity, however, the time average of the xy shear stress was positive, resulting in a negative viscosity being obtained. This irregularity was likely caused by the clustered regions, since this problem was only found to occur when they were present. Further consideration of stress variation with shear rate is given in A.4.4.

At shear rates  $\sim 0.1$ , stress fluctuations no longer occurred as before and the clustered regions were no longer seen. These shear rates (and corresponding stresses) may have been sufficient to ‘unjam’ the clusters (i.e. the maximum stress where discontinuous shear thickening and jamming can occur may have been exceeded). The system was no longer ordered at this point.

#### A.4.3 Shear and Normal Stress Coupling

The normal stress ( $\sigma_{yy}$ ) was plotted against the magnitude of the shear stress ( $\tau_{xy}$ ) to see if coupling of the stresses was evident (Figure A.20), as was seen in the rheology work in [Chapter 7](#).

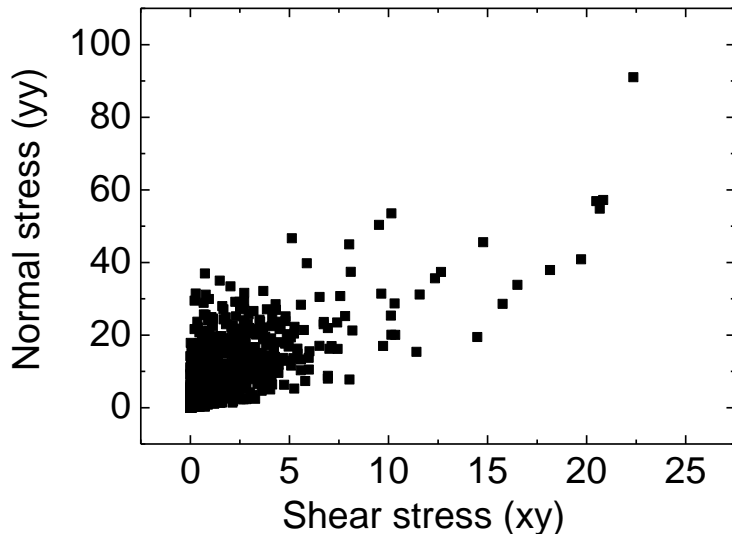


Figure A.20- Example coupling of shear and normal stresses for  $\Phi=0.58$  and shear rate=0.007.

In general it was found that as the shear stress increased, the normal stress increased: i.e. peaks in the shear stress corresponded to peaks in the normal stress. This suggested the two variables were correlated. A Pearson Correlation Coefficient (see A.3.4) was determined to investigate the strength of the correlation. For all examples studied, the coefficient varied from 0.7- 0.9. This suggested strong linear coupling between the shear and normal stresses in the systems that showed dilation, in agreement with the rheology work in [Chapter 7](#). Pearson Correlation Coefficients were determined for the shear and normal stress couplings in the rheology work and these typically varied between 0.8-0.9.

This stress coupling is in agreement with studies that found that during DST and jamming, the characteristic large fluctuations in the shear stress were strongly correlated to large normal stress fluctuations, with direct proportionality being evident [28-32]. Coupling of the shear and normal stresses is therefore regarded as a key signature of DST and jamming- for particles to shear past each other, dilation is necessary and this causes fluctuations in the normal stress [28]. Systems that do not undergo DST or jamming do not show such behaviour.

Coupling between the shear and normal stresses implies a redirection of stress by particle interactions within the bulk of the suspension [28]. Experimentally, this is thought to be due to solid-solid friction in which forces are transmitted along chains or clusters of hard particles via frictional contacts [28]. In the simulations, this was likely due to particles being brought into very close contact and their movements becoming correlated.

In systems that did not show ‘rolling’ clusters, there were no stress fluctuations and so no stress coupling was seen. This further suggested that the clusters seen in the simulations and their impact were closely related to the DST, dilatancy and jamming seen experimentally.

#### A.4.4 Effect of Shear Rate and Volume Fraction on Stress Peaks

As mentioned briefly in A.4.2, in systems that showed stress fluctuations, as the applied shear rate was increased, the magnitude of the stresses (shear and normal) increased, in terms of the average peak size and the maximum (Figure A.21). This was expected since larger stresses would have been required to achieve the higher shear rates (and more so if shear thickening). The spread of peak sizes also increased. Since the shear and normal stresses were coupled, larger shear stress fluctuations meant larger normal stress fluctuations.

As mentioned in A.4.2, at shear rates  $\sim 0.1$ , stress fluctuations no longer occurred as before and the clustered regions were no longer seen. These shear rates (and corresponding stresses) may have been sufficient to ‘unjam’ the clusters (i.e. the maximum stress where discontinuous shear thickening and jamming can occur may have been exceeded).

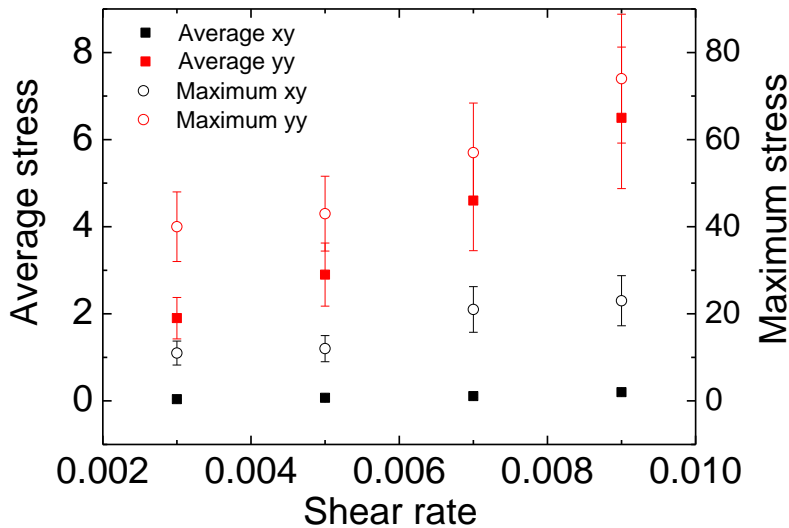
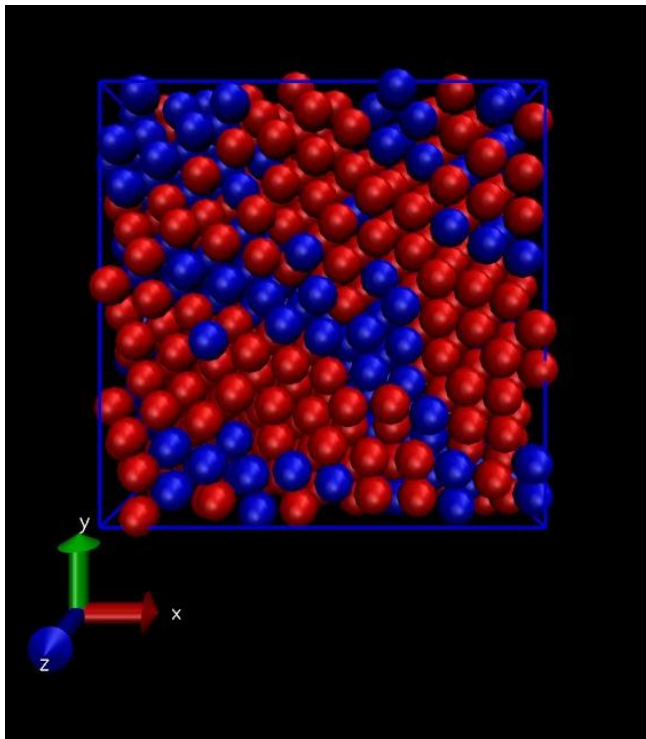


Figure A.21- Variation of average and maximum stresses with shear rate for  $\Phi=0.58$ .

As mentioned in A.4.2, it was only with volume fractions greater than or equal to 0.54, that significant fluctuations in stress were observed. By increasing the volume fraction further, larger average and maximum stresses were observed. This was likely due to the system having a higher viscosity, due to its increased density

(resulting in more energy dissipation). Therefore to achieve the shear rate that was set, higher shear stresses were required. Since the shear stress was coupled to the normal stress, this would explain why larger fluctuations in the normal stress were measured. As detailed in A.4.6.3, the larger cluster sizes and count of clusters at higher volume fractions perhaps meant that dilation was more extreme as volume fraction increased. This would have contributed to the larger stress fluctuations.

The transmission of forces through the system, and its link to the peaks, was also considered. It was found that when large peaks were present, the forces acting on regions of particles were higher than a threshold amount (e.g. close to the average) and large peaks occurred when particles with forces higher than a threshold amount spanned the system (Figure A.22). The particles experiencing larger forces were typically those in the clustered regions.



**Figure A.22- Force distribution through system example. Particles spanning the system in red had force above threshold. ( $\Phi=0.58$  and shear rate=0.007)**

The effects of shear rate and volume fraction on the simulations are considered in more detail in A.4.6.

### **A.4.5 Effect of Drag Coefficient**

The effect of the drag coefficient on simulations was investigated. A drag coefficient of 1 (in dimensionless units) was used for the majority of simulations as this approached the order of magnitude of that used experimentally. It was also suitable for the chosen time-step. When a drag coefficient greater than one was used, the system was very difficult to disrupt and an ordered layered crystal structure tended to prevail. This was likely due to increased energy dissipation due to drag, resulting in disruption due to shear having little impact. When lower drag coefficients were used, shear had more of an impact. For example, with lower drag coefficients, the maximum shear rate that could be applied before the system crashed (due to particles colliding rapidly) decreased.

Lower drag coefficients resulted in the ‘rolling’ clustered regions being less evident as lower shear rates were required to ‘unjam’ the clustered regions. The idea of the shear being sufficient to ‘unjam’ the clustered regions was mentioned briefly in A.4.2 and A.4.4.

### **A.4.6 Cluster Analysis**

#### **A.4.6.1 Cluster Definitions**

To analyse the rolling clustered regions in more detail, a code was written to analyse cluster formation in the simulations. The parameters that defined a cluster could readily be changed. The most effective definition investigated involved a combination of distance and velocity criteria being used to define a cluster.

The minimum distance between particles for particles to be counted as belonging to the same cluster was chosen so that particles in ordered layers did not count. Particles were only said to belong in a cluster if they had a radial velocity below a certain threshold. Radial velocity describes a particle’s speed straight towards or away from another particle. Since ‘rolling’ regions involved particles whose movement was correlated (i.e. they moved together in regions), they should not have been moving away from other particles in the cluster. This radial velocity threshold was determined by analysing particle velocities for particles that visually appeared to be in a cluster compared to those that were not.

The magnitude of the radial velocity between two particles was deduced from the dot product of the relative velocity vector and the unit vector in the direction of the vector between the particles:

$$v_{radial} = \frac{\mathbf{v}_{relative} \cdot \mathbf{r}}{|\mathbf{r}|} \quad \text{Equation A.66}$$

The cluster code looped through each particle-particle combination and if particles met the necessary criteria, they were designated into a cluster. Cluster data were analysed to see how factors such as shear rate and volume fraction affected cluster formation, and to see how clusters evolved with time. The effect of system size on cluster formation was also analysed. Links between clustering and features in the energy and stress data were then made.

It was noted that when only a distance between particles was used for defining clusters, when lower distance cut-off values were used (less than the average when no rolling occurred), regions that were detected were largely rolling. This suggested that regions that were rolling were more densely packed with particles. When only particles with a distance greater than this value were counted as clustering, the regions that were detected were not rolling.

Codes were written to allow clusters to be visualised using VMD (see A.3.2). This allowed clusters greater than a certain size to be coloured a certain way. This allowed the parameters that defined clusters to be checked.

#### A.4.6.2 Effect of Shear Rate on Clustering

Initially, as the shear rate was increased, the average cluster size over the simulation increased up until a maximum (Figure A.23). During this range of shear rates, the total number of clusters detected over the simulation time increased with shear rate (Figure A.24) and the spread of cluster sizes became larger. Typically when clusters were present, the code detected one or two large cluster at any one time.

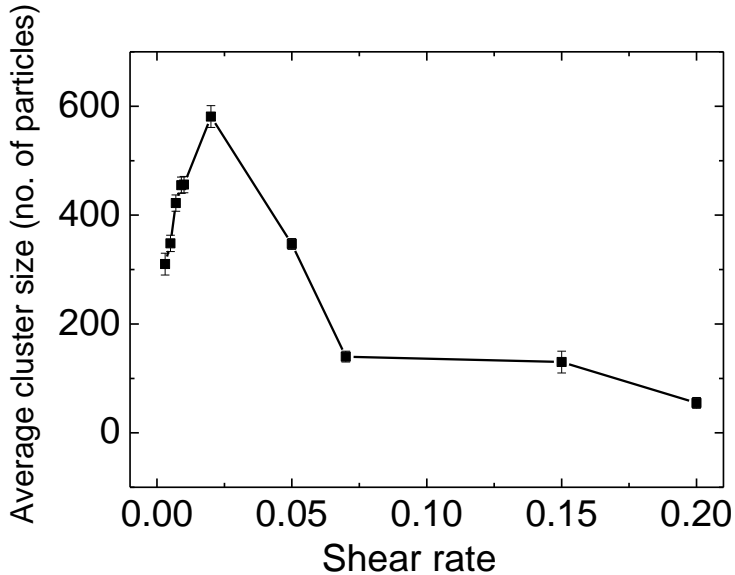


Figure A.23- Average cluster size (number of particles) variation with shear rate for  $\Phi=0.58$ . Error bars were from the standard deviation of data measured over different time intervals.

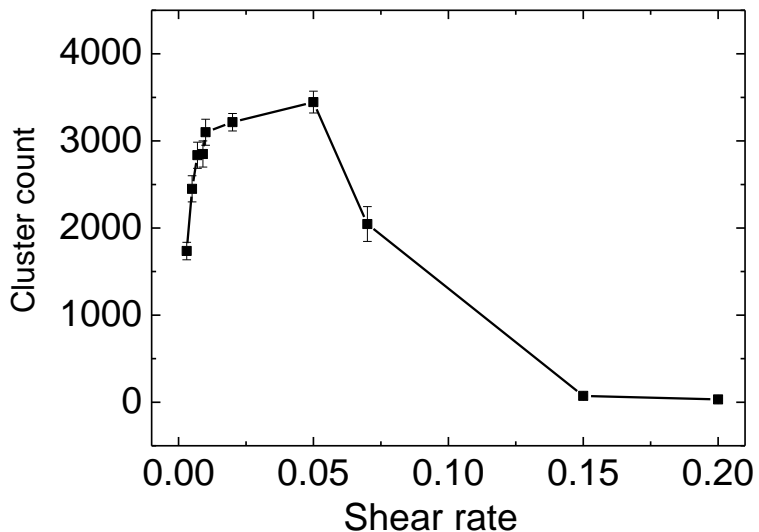
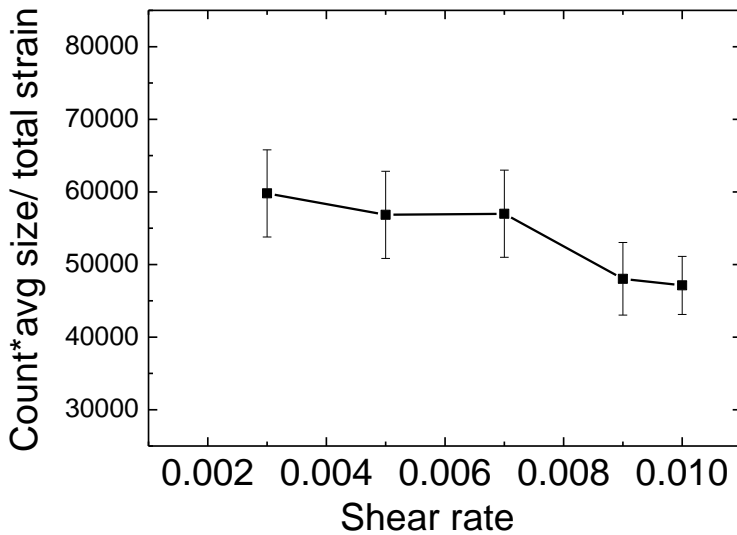


Figure A.24- Cluster count variation with shear rate for  $\Phi=0.58$ . Simulations were run for a time of 3000. Error bars were from the standard deviation of data measured over different time intervals.

When the shear rate was increased further, the average cluster size began to decrease to a point where clustering (in terms of size and cluster count) was negligible. Visually, this corresponded to when dilating regions were no longer present. This may have corresponded to the shear rate being sufficient to ‘unjam’

the system as mentioned previously. Further increases in shear rate therefore had no impact on average cluster size and count.

To get an overall extent of clustering (or jamming if a cluster is taken as analogous to a jammed region), the product of the average cluster size and cluster count in the simulation time was calculated. Since the simulation time was fixed, different shear rates meant that a different overall strain was applied to the system. Therefore the extent of clustering was divided by overall strain to see the extent of clustering per unit strain (Figure A.25).



**Figure A.25- Extent of clustering per unit strain for  $\Phi=0.58$ . At shear rates greater than this, the overall clustering extent fell towards zero.**

Interestingly, this showed that in the range of shear rates where dilation was seen and the clusters were getting larger on average, the overall clustering extent per unit strain was approximately constant.

As the shear rate was increased, the maximum and average stress peak sizes increased (as mentioned in A.4.4). Larger shear stresses would have been required to achieve the larger shear rates and as found by the cluster code, larger and more frequent dilating regions occurred at higher shear rates.

As mentioned previously, the occurrence of stress peaks corresponded to the occurrence of clusters- notably when no clusters were present, no stress peaks were present. The correlation between the extent of clustering at a given time and

size of peaks in the yy-stress was evaluated through a Pearson Correlation Coefficient.

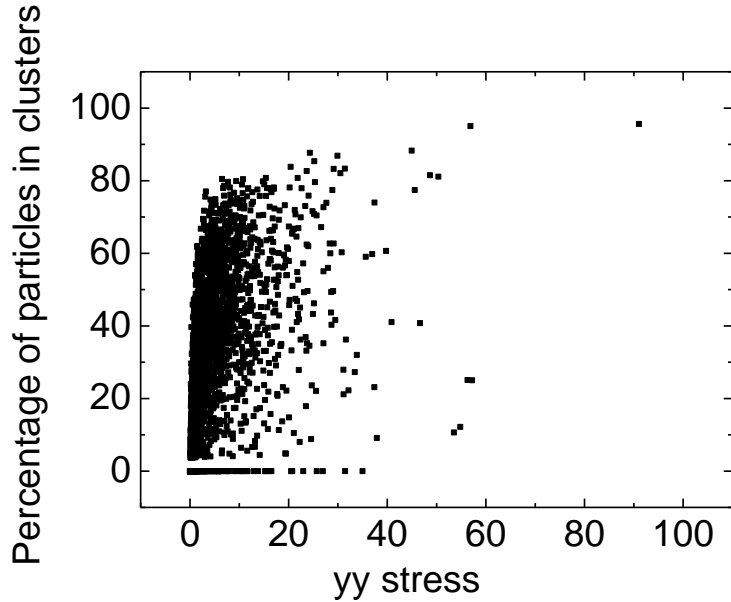


**Figure A.26- Example correlation between percentage of particles involved in clusters at given time and yy stress ( $\Phi=0.58$  and shear rate=0.007)**

The analysis showed that a moderate correlation existed between the extent of clustering and stress peaks, with the correlation coefficient ranging from 0.4-0.6 (Figure A.26). Stronger correlation is unlikely to have existed since the actual layout and orientation of the clusters would likely have been important.

Jamming is thought to occur experimentally when clusters span across the flow area in the direction of the shear gradient (y-direction in simulations), therefore resulting in dilation against the boundaries [28]. If clusters only spanned across the direction of flow, or did not span the shear gradient direction completely, jamming would not occur. This idea agreed with a visual analysis where the largest peaks were seen when clusters spanned the y-direction entirely (Figure A.27). When a notable number of clusters were present but the stress peak was not significant, clusters often did not span the system (Figure A.28).

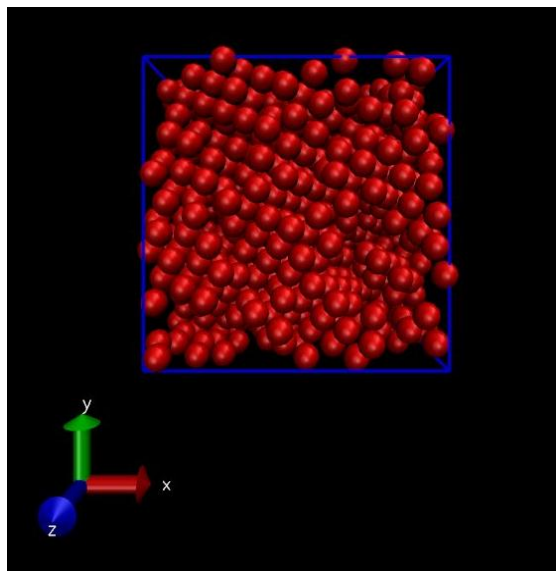


**Figure A.27-** Example of clusters spanning system, resulting in large yy stress peak

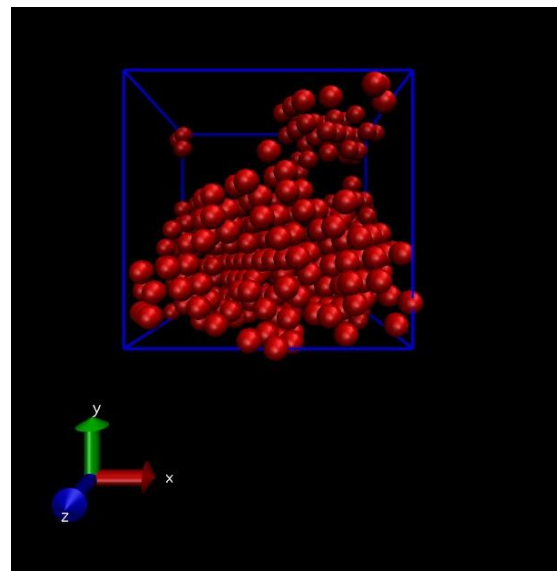


**Figure A.28-** Example of clusters spanning x direction only, resulting in small stress peak

By plotting the distributions of cluster size as a function of time and the evolution of the yy stress as a function of time, it could be seen that clusters formed and this was then followed by a stress peak. This suggested that the clusters were the cause of the stress peaks, rather than vice-versa, since the clusters were shown to grow prior the stress peak appearing. This agreed with the work in [Chapter 5](#) where it was proposed that the presence of these clustering/dilating regions caused the fluctuating stresses measured in the experiments.

### A.4.6.3 Effect of Volume Fraction on Clustering

The system density was varied to investigate the impact of volume fraction on clustering. The system density was varied from 0.8-1.2 (corresponding to volume fractions between 0.42 and 0.63) and this was performed for shear rates of 0.005 and 0.009. The effect of density on cluster size and the extent of clustering were investigated.

From the initial results before the clustering code was implemented, peaks in the stresses began to appear at  $\Phi \geq 0.54$  and dilation became visible, with the clustered regions appearing. This was close to the critical volume fraction at which jamming began to occur experimentally in [Chapter 4](#) and [Chapter 5](#).

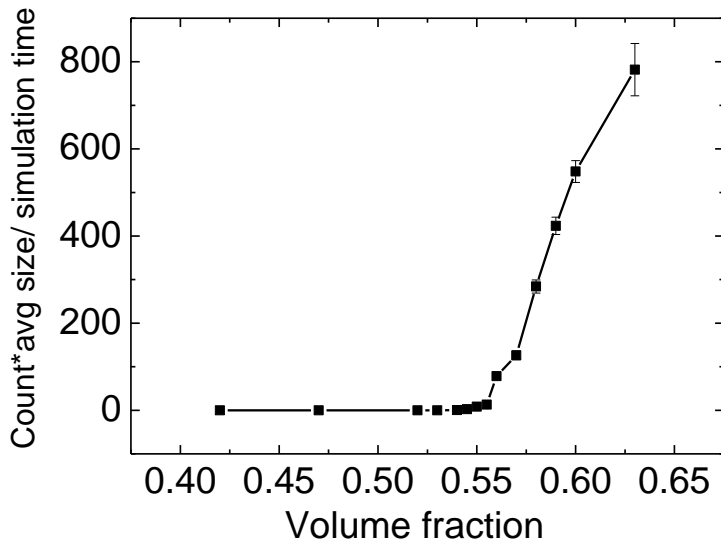


**Figure A.29- Extent of clustering variation with volume fraction (shear rate= 0.005).** Error bars were from the standard deviation of data measured over different time intervals.

With the cluster code implemented, clusters were first detected at a density of 1.03; this corresponded to a volume fraction of 0.54. The actual count of clusters during simulations of these conditions was, however, very low. As the density was increased from this, the cluster count increased gradually but at a density of 1.07 (a volume fraction of 0.56), there was a significant jump in the number of clusters. Figure A.29 shows how the overall extent of clustering (cluster count\*average size) per unit time varied with density. This showed that significant clustering was only found at volume fractions greater than or equal to 0.56, agreeing with the experimental results in [Chapter 4](#) and [Chapter 5](#).

As the volume fraction was increased beyond 0.56, the overall extent of clustering increased due to the larger cluster size and cluster count. Since the strain was fixed in these simulations (same shear rate and simulation time), this agreed with the experimental results where the energy dissipation per unit strain increased with increasing volume fraction.

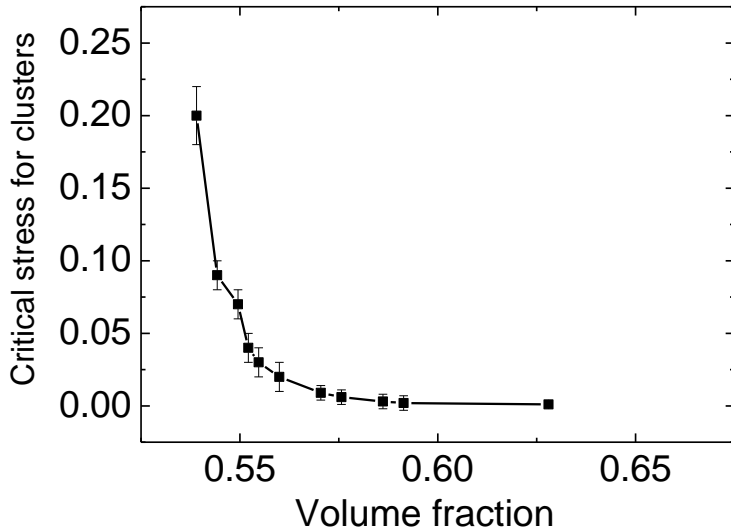


**Figure A.30- Critical stress required for clustering variation with volume fraction (shear rate= 0.005).** Error bars were from the standard deviation of data measured over different time intervals.

It was noticed that as the volume fraction was increased, the critical stress above which clusters formed decreased (Figure A.30). This agreed with the experimental results where it was found that jamming occurred at lower shear stresses and shear rates as the volume fraction increased (see [Chapter 4](#) and [Chapter 7](#)). This was likely due to particles being closer together, resulting in less effort being required for jamming and a greater likelihood of jamming occurring. This was also expected from literature [6, 28, 33].

#### A.4.6.4 Effect of System Size on Clustering

The simulation size was varied to see if system size had an influence on the clustered regions. Previously, simulations with 7 cells in each direction, corresponding to 1372 particles, were used. Now the number of cells in each direction was varied from 3 to 15. This varied the number of particles between 108 and 13500. The extent of clustering was investigated visually and through the cluster code.

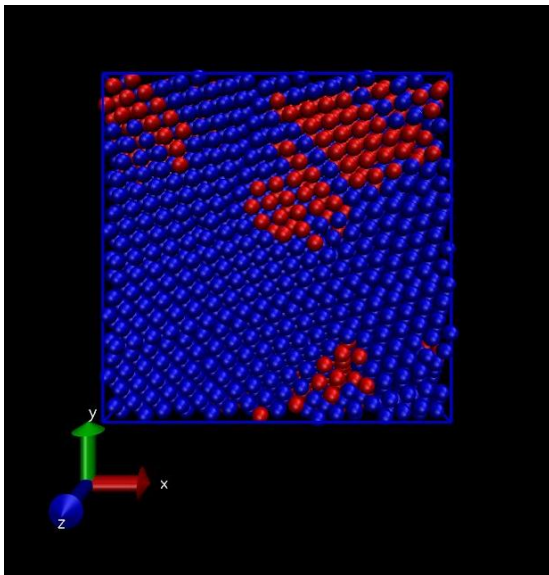


**Figure A.31- Example of clusters (red) in larger simulation. 8788 particles,  $\Phi=0.58$  and shear rate=0.005.**

For smaller simulations (7 or fewer cells in each direction), clusters often spanned the entire system and much of the system appeared to be undergoing dilation. When the number of cells was increased beyond this, the clustered regions did not occupy the entire system and non-dilating regions often existed and occupied much of the system (Figure A.31). This suggested that the clusters had a finite size and did not grow proportionally with the simulation size.

As system size increased, the average cluster size increased, but the increase in cluster size did not scale with the larger box size and particle number. For example, with 7 cells in each direction (1372 particles), the average cluster size was  $368\pm 55$ . By increasing the box size to 10 (and increasing the number of particles to 4000) the average cluster size increased to just  $498\pm 61$ . This suggested that as the simulation

size increased, there was a finite size the clusters could reach, as can be seen in Figure A.32.

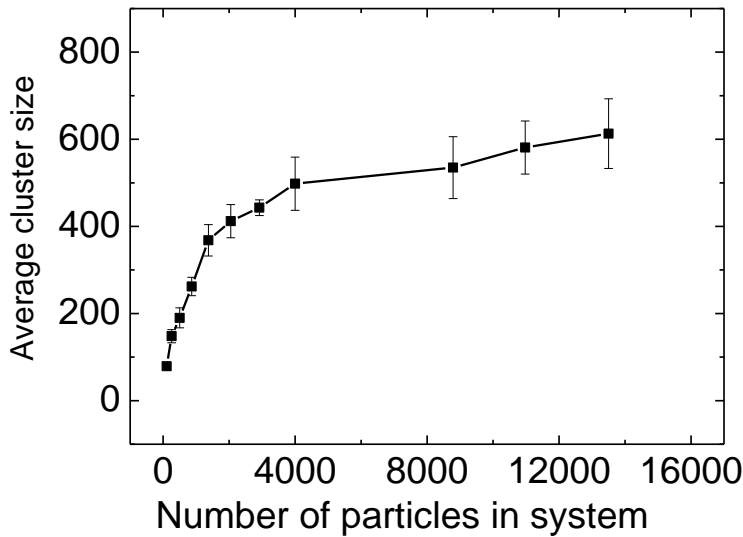


**Figure A.32- Average cluster size variation with simulation size.  $\Phi=0.58$  and shear rate=0.005.**  
Error bars were from the standard deviation of data measured over different time intervals.

The effect of system size on cluster count was investigated. As the system size increased, the count increased. The count per unit volume, however, decreased and reached a plateau (Figure A.33). This suggested that when the system size was sufficiently big, the average cluster size and count of clusters per unit volume remained approximately constant and simulation size no longer had an effect.

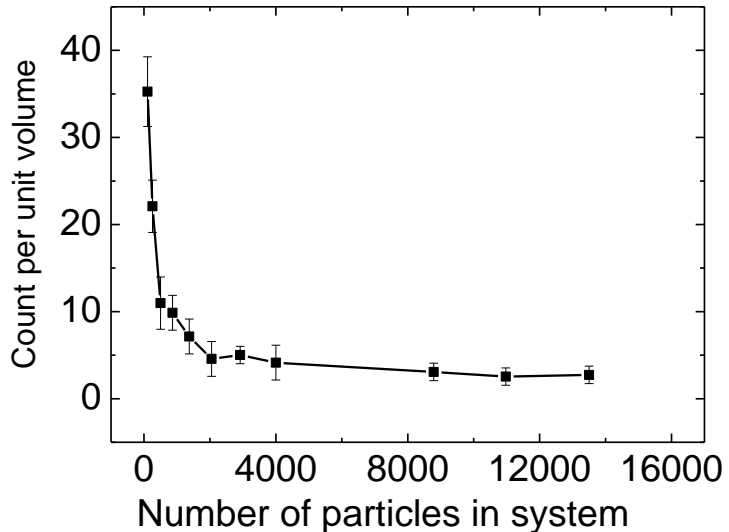


**Figure A.33- Count per unit volume variation with simulation size.  $\Phi=0.58$  and shear rate=0.005.**  
Error bars were from the standard deviation of data measured over different time intervals.

As mentioned, the majority of simulations performed were for 7 cells in each direction resulting in 1372 particles. Based on the system size analysis, this system size was deemed suitable. Further increases in system size would not have had a significant impact on the results but it would have taken a significantly longer time to run the simulations and they would have used up much more memory. This was not practical and was not deemed worthwhile.

The effect of simulation size results may also have some relevance to the experimental work done in [Chapter 4](#) and [Chapter 5](#). From the experiments, as gap size was increased, fewer but larger jamming peaks were detected. This was thought to be due to it being more difficult/less likely for force transmitting clusters to span the system and dilate. This may agree with the simulation results where it has been shown that clusters reach a finite size, and so with a larger gap, more of these finite sized clusters would be required to span the system to cause a jam.

The sizes of the stress peaks measured in the xy shear stress and yy and zz stress components were larger in the simulations when clusters spanned the system. They were therefore largest in the larger simulations when clusters spanned the system, compared to when they spanned the system in the smaller simulations. This may be linked to the fact that with bigger gaps in the shear cells, larger peaks were

detected. This may be due to larger jammed and dilating regions, hence larger forces.

Overall, trends in clustering (which corresponded to trends in stress peaks) appeared to show similarities to the experimental work done in this thesis. This suggested there may have been a link between the stress peaks and clusters seen with the simulations and the force peaks (which were thought to be signatures of jamming) that were seen experimentally in [Chapter 5](#).

#### A.4.7 Effect of Polydispersity

Until now, particles were assumed perfectly monodisperse for the simulations. Experimentally, this was unlikely to be the case since producing perfectly monodisperse particles is near impossible. As detailed in [Chapter 7](#), the dynamic light scattering analysis suggested the polydispersity of the colloids was very low and that the particles were highly monodisperse. Using the polydispersity definition based on standard deviation, the experimental colloids had a  $4 \pm 2\%$  polydispersity.

To add polydispersity to the simulations, the particle sizes were normally distributed with the standard deviation being adjustable to change the polydispersity. Simulations with particle polydispersity were run for a range of polydispersities and conditions to investigate the effect of polydispersity on the system. Percentage polydispersities ranging from 0-20% were studied. System conditions similar to those used previously (in terms of shear rate, density etc.) were investigated.

When polydispersity was added to the simulations, with polydispersity less than 9%, the results were qualitatively similar to those obtained with no polydispersity- dilating regions with significant stress peaks were obtained. Here a degree of ordering was seen in the systems, as detailed in A.4.2.

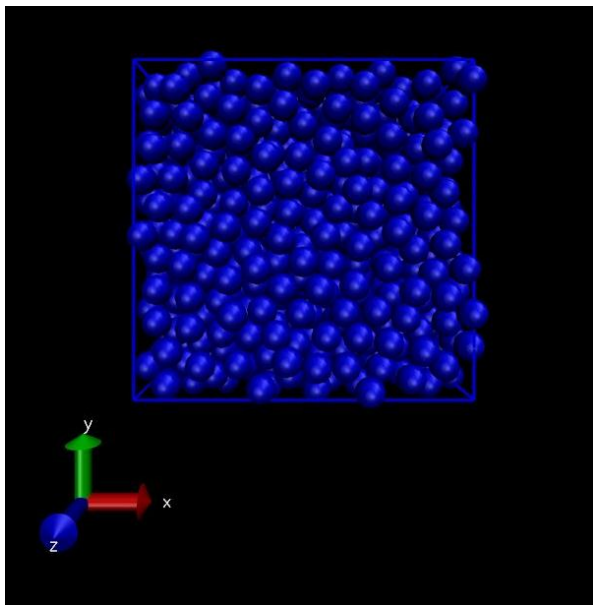


**Figure A.34-** Example of non-ordered arrangement seen with 10% polydispersity.  $\Phi=0.58$  and shear rate=0.005.

When polydispersity was  $\geq 9\%$ , no significant stress peaks and no dilating/clustered regions were seen. The system was also disordered, with no layering (Figure A.34). This suggested that polydispersity was an important factor and that the ordering seen with the low polydispersities was responsible for the effects seen.

Molecular dynamics studies have shown that relatively small amounts of polydispersity can suppress phenomena seen in monodisperse systems [34]. According to literature, shear thickening often does not appear to occur to the same extent in polydisperse suspensions [35]. They often just show continuous shear thickening or no shear thickening at all [6]. The presence of smaller particles effectively causes a viscosity reduction, since particles can pack closer together [6]. It is likely that particles with different sizes would make it more difficult for particles to span the system and would make dilation less extreme. Polydispersity can therefore be used as a method to suppress shear thickening and jamming [35].

The polydispersity of the samples used experimentally fell into the range where behaviour was similar to that with the monodisperse simulations, since experimental polydispersity was  $4 \pm 2\%$  (using the same definition). This suggested that the monodisperse analysis done previously may have been acceptable, however, as detailed in [Chapter 7](#), light scattering results suggested that the particles were not strongly ordering under shear experimentally.

As mentioned, when the particles were not ordered in the simulations, no stress peaks and dilating clusters were seen. The simulations with the ~monodisperse particles may therefore not have been a good representation of the experimental system and the effects seen may have been due to the ordering and not due to discontinuous shear thickening/jamming. It was possible that stacking faults in the ordered structure, or shear causing the ordered structure to form and melt may have been responsible for the stress fluctuations [36, 37]. This suggested that additional particle interactions, such as lubrication and friction as detailed in A.2.3.5, must be added to the simulations to better capture the behaviour seen experimentally. This was beyond the scope of the project but would prove a valuable piece of future work.

The results did, however, show that some form of clustering was likely necessary to result in stress fluctuations and dilatancy. This agreed with the proposed mechanism for discontinuous shear thickening and jamming in [Chapter 5](#), where a mechanism involving force transmitting cluster formation and dilatancy was proposed, based on the experimental findings.

## A.5 Conclusions

By performing molecular dynamics simulations on a system of hard spheres, similar to that used experimentally in [Chapter 4](#) and [Chapter 5](#), a greater understanding of the behaviour of concentrated suspensions under flow was achieved.

By treating the particles as monodisperse hard spheres and simulating the solvent through drag, results obtained from the simulations showed similarities to the work in [Chapter 4](#) and [Chapter 5](#). Dilatation and fluctuating stresses were features under particular conditions, similar to those investigated experimentally (for example in terms of volume fraction and shear rate).

The results, however, suggested that ordering of the monodisperse particles occurred under shear and this was likely influencing the results. As detailed in [Chapter 7](#), this ordering was not thought to occur experimentally. This suggested that additional particle interactions must be added to the simulations to better capture the behaviour seen experimentally. This was beyond the scope of the project but would prove a valuable piece of future work.

The results did, however, show that some form of clustering was likely necessary to result in stress fluctuations and dilatancy. This agreed with the proposed mechanism for discontinuous shear thickening and jamming in [Chapter 5](#), where a mechanism involving force transmitting cluster formation and dilatancy was proposed, based on the experimental findings.

a	Radius
a	Acceleration
D	Shift distance
D	Diffusion coefficient
Dim	Dimensions
E	Energy
F	Force
FCC	Face centred cubic
$k_B$	Boltzmann constant
L	Box height
m	Mass
MD	Molecular dynamics
N	Number of particles
n	Number
p	Momentum
P	Pearson Correlation Coefficient
r	Position or distance between two particles
t	Time
T	Temperature (absolute)
U	Potential energy
u	Velocity
v	Velocity
$\sigma$	Particle diameter
$\epsilon$	Magnitude of energy minimum
$\eta$	Viscosity
$\sigma_x$ and $\sigma_y$	x and y's standard deviation
$\sigma_{xy}$	Co-variance between x and y
$\Phi$	Volume fraction
$\sigma$	Normal stress
$\tau$	Shear stress
$\delta$	$6\pi\eta a$
$\dot{\gamma}$	Shear rate

1. Ippoliti, E., *What is Molecular Dynamics?* 2011: German Research School for Simulation Sciences.
2. Sadus, R., *Molecular Simulation of Fluids: Theory, Algorithms and Object-Orientation*. 2002, Elsevier.
3. Hinchliffe, A., *Molecular Modelling for Beginners*. 2005: Wiley.
4. Jones, R., *Soft Condensed Matter*. 2011: Oxford.
5. Hunter, G.L. and E.R. Weeks, *The physics of the colloidal glass transition*. Reports on progress in physics. Physical Society (Great Britain), 2012. **75**(6): p. 066501.
6. Mewis, J. and N. Wagner, *Colloidal Suspension Rheology*. 2012: Cambridge University Press.
7. Evans, D. and G. Morriss, *Statistical Mechanics of Nonequilibrium Liquids*. 2008: Cambridge University Press.
8. Kittel, C., *Elementary Statistical Physics*. 1964: Wiley.
9. Seto, R., et al., *Discontinuous Shear Thickening of Frictional Hard-Sphere Suspensions*. Physical Review Letters, 2013. **111**(21): p. 5.
10. Melrose, J.R. and R.C. Ball, "Contact networks" in continuously shear thickening colloids. Journal of Rheology, 2004. **48**(5): p. 961-978.
11. Melrose, J.R. and R.C. Ball, Continuous shear thickening transitions in model concentrated colloids - The role of interparticle forces. Journal of Rheology, 2004. **48**(5): p. 937-960.
12. Wyart, M. and M.E. Cates, *Discontinuous Shear Thickening without Inertia in Dense Non-Brownian Suspensions*. Physical Review Letters, 2014. **112**(9).
13. Frenkel, D. and B. Smit, *Understanding Molecular Simulation: From Algorithms to Applications*. 2 ed. 2001: Academic Press.

14. Allen, M.P. and D.J. Tildesley, *Computer Simulation of Liquids*. 1989: Oxford Science Publications.
15. Verlet, L., *Computer Experiments On Classical Fluids .I. Thermodynamical Properties Of Lennard-Jones Molecules*. Physical Review, 1967. **159**(1): p. 98-&.
16. Gear, C.W., *Numerical Initial Value Problems in Ordinary Differential Equations*. 1971: Longman Higher Education.
17. University, N., *Physics: Numerical Integration*. 2013.
18. Lees, A.W. and S.F. Edwards, *Computer Study Of Transport Processes Under Extreme Conditions*. Journal of Physics Part C Solid State Physics, 1972. **5**(15): p. 1921-&.
19. Bannerman, M.N., et al., *Collision statistics in sheared inelastic hard spheres*. Physical Review E, 2009. **79**(4).
20. Shell, S., *Principles of modern molecular simulation methods*. 2012, University of California.
21. Mackley, M., *Rheology and Processing*. 2011, Cambridge University.
22. Morrison, F., *Understanding Rheology*. 2001: OUP USA.
23. VMD- Visual Molecular Dynamics. 2014; Available from: <http://www.ks.uiuc.edu/Research/vmd/>.
24. Montgomery, C., *Applied Statistics and Probability for Engineers*. 4th ed. 2006: Wiley.
25. Wagner, N.J. and J.F. Brady, *Shear thickening in colloidal dispersions*. Physics Today, 2009. **62**(10): p. 27-32.
26. Hoffman, R.L., *Discontinuous And Dilatant Viscosity Behavior In Concentrated Suspensions .1. Observation Of A Flow Instability*. Transactions of the Society of Rheology, 1972. **16**(1): p. 155-&.
27. Hoffman, R.L., *Explanations for the cause of shear thickening in concentrated colloidal suspensions*. Journal of Rheology, 1998. **42**(1): p. 111-123.
28. Brown, E. and H. Jaeger, *Shear thickening in concentrated suspensions: phenomenology, mechanisms, and relations to jamming*. Reports on Progress in Physics, 2013. **77**(4): p. 046602.
29. Hebraud, P. and D. Lootens, *Concentrated suspensions under flow: Shear-thickening and jamming*. Modern Physics Letters B, 2005. **19**(13-14): p. 613-624.
30. Brown, E. and H.M. Jaeger, *The role of dilation and confining stresses in shear thickening of dense suspensions*. Journal of Rheology, 2012. **56**(4): p. 875-923.
31. Lootens, D., et al., *Dilatant flow of concentrated suspensions of rough particles*. Physical Review Letters, 2005. **95**(26): p. 4.
32. Lootens, D., H. Van Damme, and P. Hebraud, *Giant stress fluctuations at the jamming transition*. Physical Review Letters, 2003. **90**(17).
33. O'Brien, V.T. and M.E. Mackay, *Stress components and shear thickening of concentrated hard sphere suspensions*. Langmuir, 2000. **16**(21): p. 7931-7938.
34. Sierou, A. and J.F. Brady, *Rheology and microstructure in concentrated noncolloidal suspensions*. Journal of Rheology, 2002. **46**(5): p. 1031-1056.
35. Barnes, H.A., *Shear-Thickening (Dilatancy) In Suspensions Of Nonaggregating Solid Particles Dispersed In Newtonian Liquids*. Journal of Rheology, 1989. **33**(2): p. 329-366.
36. Wu, Y.L., et al., *Melting and crystallization of colloidal hard-sphere suspensions under shear*. Proceedings of the National Academy of Sciences of the United States of America, 2009. **106**(26): p. 10564-10569.

37. Solomon, T. and M.J. Solomon, *Stacking fault structure in shear-induced colloidal crystallization*. Journal of Chemical Physics, 2006. **124**(13).